THE USE OF ASYMPTOTIC METHODS IN BOUNDARY-LAYER AND INTERFACIAL PHENOMENA

A thesis submitted to the University of Manchester
for the degree of Doctor of Philosophy
in the Faculty of Science and Engineering

2022

Eleanor C. Johnstone
Department of Mathematics
School of Natural Sciences

Contents

Word count 41500

The University of Manchester

Eleanor C. Johnstone
Doctor of Philosophy
The Use of Asymptotic Methods in Boundary-Layer and Interfacial Phenomena
April 22, 2022

We present four studies that use asymptotic methods to understand physical phenomena in boundary-layer and interfacial flows.

First, we present solutions for the shapes of static equilibria in rectangular channels that have been perturbed by isolated ridges and grooves and by scattered bump protrusions and intrusions. We solve the Young–Laplace equation to quantify the sensitivity of the meniscus shape to the perturbations using a combination of numerical computations and asymptotic techniques for a linearised model when the amplitude of the perturbations is small relative to the channel height. For small-amplitude ridge/groove and bump perturbations, we derive an equation for the induced pressure difference over the meniscus that depends solely on the boundary data. Thus the total pressure difference over the meniscus (and therefore the mean curvature) can be found without solving the Young–Laplace equation. Mirror symmetric ridge and bump perturbations which change the volume of the channel cause a change in the mean curvature of the meniscus which leads to long-range curvature of the contact line. For ridge perturbations, we show that this long-range curvature matches onto the contact line of a droplet with the same mean curvature as the meniscus. We use this information to choose specific combinations of perturbations to engineer contact line shapes. We present preliminary results for bump intrusions/protrusions which show that the direction of deformation of a meniscus changes as it passes over a bump.

Next, we present an asymptotic description of nonlinear equilibrium and travelling-wave solutions of the Navier–Stokes equations in incompressible unsteady boundary-layer and compressible parallel boundary-layer flows. The solutions take the form of self-sustaining vortex-wave interaction-type states, known as free-stream coherent structures, with the nonlinear interaction between the vortex and the wave taking place in a layer close to the free-stream. The interaction produces streaky disturbances that can grow exponentially due to interaction with the base flow. We first extend the asymptotic theory of Deguchi and Hall (2014a) to show that free-stream coherent structures can be embedded in unsteady two-dimensional boundary layers. The time evolution of the structure is affected strongly by the unsteady base flow, and ultimately it can only persist for a finite time. Next, we describe free-stream coherent structures in compressible parallel boundary layer flows in the subsonic and moderate supersonic regimes. These flows are more industrially relevant to laminar flow control than the previously studied incompressible flows. The key result is that the equations for the nonlinear interaction of the vortex and wave in the layer near the free-stream are identical to those obtained in the incompressible problem, but the velocity field now also drives a passive thermal field. The resulting disturbances to both the velocity and temperature fields can then grow exponentially towards the wall; the maximum amplitude of the disturbances depends on the Mach number and the Prandtl number.

Declaration

I declare that, except where specific reference is made to the work of others, or where sections of the published paper in Chapter 4 have been explicitly marked as not for examination, no portion of the work referred to in the thesis has been submitted in support of an application for another degree or qualification of this or any other university or other institute of learning.

Eleanor Catherine Johnstone
April 2022

Copyright Statement

Acknowledgements

First and foremost, I would like to thank my supervisors Andrew and Oliver for their guidance, patience and enthusiasm throughout this project. It was a great privilege to be able to spend an hour talking about this work with you every week; your breadth of knowledge and contrasting viewpoints led to the many hours of engaging discussion, contemplation, inevitable confusion and ultimate understanding from which the work in this thesis emerged. Thanks also for always finding the time for me despite your many responsibilities within the department. To Phil, thank you for supervising the work in the second half of this thesis (even after I was no longer your student) and for arranging the visits to Melbourne. I have learnt so much from your perspectives on the field, on science and on life and I greatly enjoyed working with you. Thank you also for your encouragement which gave me the confidence to start a PhD in the first place.

Thanks also to those who have provided inspiration, guidance and help along the way, including (but almost certainly not limited to): my continuation examiners Alice Thompson, Raphael Assier and Peter Duck, who provided invaluable feedback on earlier drafts of the work in this thesis; the anonymous reviewers of the papers who undoubtedly greatly improved the finished manuscripts from their first drafts; Matthias Heil for his work as postgraduate director and for arranging the weekly 'Oomph Lunch' discussions which have been a real highlight of my time at Manchester; Alice Thompson and Chris Johnson for arranging such interesting seminars within the department; and Ozge Ozgakir and Anna Haley at Monash for everything you did during my visits there. I would also like to acknowledge Abigail Bown and Louise Walker for providing me with the opportunity to undertake outreach work which I have greatly enjoyed.

Finally, I am deeply thankful to my family and friends who have supported me over the past few years. I couldn't have done this without you.

Chapter 1

Introduction

A fluid is a substance that flows and can be freely deformed. Many natural phenomena and biological and industrial processes involve the behaviour of fluids; for example, the flow of blood around the body, the behaviour of magma inside the earth's core, the flow of wind past a turbine blade, the motion of an avalanche and the slow deformation of glass window panes. In this thesis, we study fluid phenomena in two specific scenarios. First, we investigate the behaviour of fluids confined in microchannels when the geometry of the channel is perturbed. These problems typically involve spatial scales of the order of millimetres. Secondly, we consider the structure underpinning many turbulent fluids (for which the velocity varies irregularly in both space and time). Turbulent flows are associated with problems involving scales of metres (for example, the turbulent flow over an aeroplane wing) through to hundreds of kilometres (for example in the ocean and atmosphere).

These problems both have important industrial applications. In recent years the unique behaviour of fluids in microchannels has been exploited to create 'micro-fluidic devices' which have been used in a wide range of industrial and scientific processes; for an overview see e.g. Stone, Stroock and Ajdari (2004), Ajaev and G. Homsy (2006), Anna (2016), and Venkatesan et al. (2020). Manufacturing such devices without imperfections is challenging due to the small scales involved (Stone, Stroock and Ajdari, 2004; Lohse, 2022), and therefore one of the key questions we may ask is how small geometric imperfections affect the flow in a confined geometry. An understanding of the effects of geometry enables exploitation of these effects as in some cases surface roughness may enhance the desired effect of the device, for example by increasing heat transfer performance (Jia et al., 2019).

Meanwhile, controlling turbulent flows is extremely important in many applications: for example, one of the key challenges to overcome in the design of aeroplanes is how to control and reduce the drag and noise production that are associated with the turbulent flow around the plane. Until quite recently, it was thought that turbulence was random and chaotic. Indeed, it may be difficult to distinguish any pattern in a body of white water or turbulent smoke from a match. The groundbreaking experiments of Kline et al. (1967) at Stanford University were the first to show that complicated turbulent flows could have structure sitting in the background. This structure effectively consisted of vortices and areas of high and low-speed flow. An understanding of the structure sitting behind the turbulence could lead to the ability to exploit and modify the turbulent flow, and hence to control drag and noise production in aeronautical settings.

To gain an understanding of these (and other) problems we wish to model the behaviour of fluids. However, physical phenomena involving the motion of fluids operate across a wide range of temporal and spatial scales and involve fluids with vastly different physical properties. Therefore, it might be expected that writing down equations to govern the motion of a general fluid is a difficult task. However, incredibly, it is believed that the motion of many fluids is governed by the same equations which are derived from conservation of mass and energy, and Newton's laws of motion (Newton, 1833).

1.1 The Navier–Stokes equations

The Navier–Stokes equations are partial differential equations which are widely used to describe the motion of viscous fluids. They are attributed to the physicists Claude-Louis Navier and George Gabriel Stokes, and were written down for the first time in the 19th century. For a general compressible flow with velocity $\mathbf{u}$, they are given by

$$\rho\left(\frac{\partial \mathbf{u}}{\partial t} + \mathbf{u}\cdot\nabla\mathbf{u}\right) = -\boldsymbol{\nabla} p + \mathbf{F} + \boldsymbol{\nabla}\cdot\left(\mu\left(\boldsymbol{\nabla}\boldsymbol{u} + (\boldsymbol{\nabla}\boldsymbol{u})^T - \frac{2}{3}(\boldsymbol{\nabla}\cdot\boldsymbol{u})\mathbf{I}\right)\right), \tag{1.1}$$

$$\frac{\partial \rho}{\partial t} + \nabla\cdot(\rho\mathbf{u}) = 0, \tag{1.2}$$

where t denotes time, ρ is the density, p is the pressure, μ is the dynamic viscosity, $\mathbf{F}$ represents any body force per unit volume acting on the fluid, $\mathbf{I}$ is the identity tensor and superscript T denotes transpose; for a derivation see e.g. Batchelor (2000). In deriving these equations it is assumed that the stress can be expressed as a linear constitutive equation involving velocity and dynamic viscosity, and that the bulk viscosity $\lambda = -\frac{2}{3}\mu$. The first equation (1.1) expresses conservation of momentum (derived from Newton's second law (Newton, 1833)) and the second equation (1.2) expresses conservation of mass. For temperature-dependent flows they are also solved subject to an energy equation, which is derived from the first law of thermodynamics and expresses conservation of energy (Stewartson, 1964), and an equation of state relating the pressure, density and temperature.

1.1.1 Boundary conditions

This discussion is based on the overview given in Batchelor (2000).

The Navier–Stokes equations must be solved subject to appropriate boundary conditions which impose that velocity and stress (force per unit area) must be continuous across any material boundary. The realisation of these conditions varies depending on the type of boundary. We describe two common scenarios relevant to the work in this thesis.

The first common type of boundary is a fluid-solid boundary. In general, at a rigid solid boundary, the fluid sticks to the surface so that continuity of velocity requires both the tangential and normal components of fluid velocity to match the velocity of the solid. The former condition is known as 'no-slip', while if the boundary is impermeable, the latter condition is known as 'no-penetration'. The no-slip condition becomes problematic at the intersection of a fluid-fluid interface with a rigid surface (a contact line). Moving contact lines can be observed in many situations, for example the spread of a droplet placed on a solid surface, or the rise of mercury in a thermometer. Thus, analysis of moving contact lines on a stationary surface with a no-slip condition leads to a paradox; mathematically, unbounded forces can be produced at the contact line (Dussan V. and Davis, 1974), leading to a singularity in the flow field. This singularity is resolved by allowing the fluid to slip along the wall (Dussan, 1976), which is known

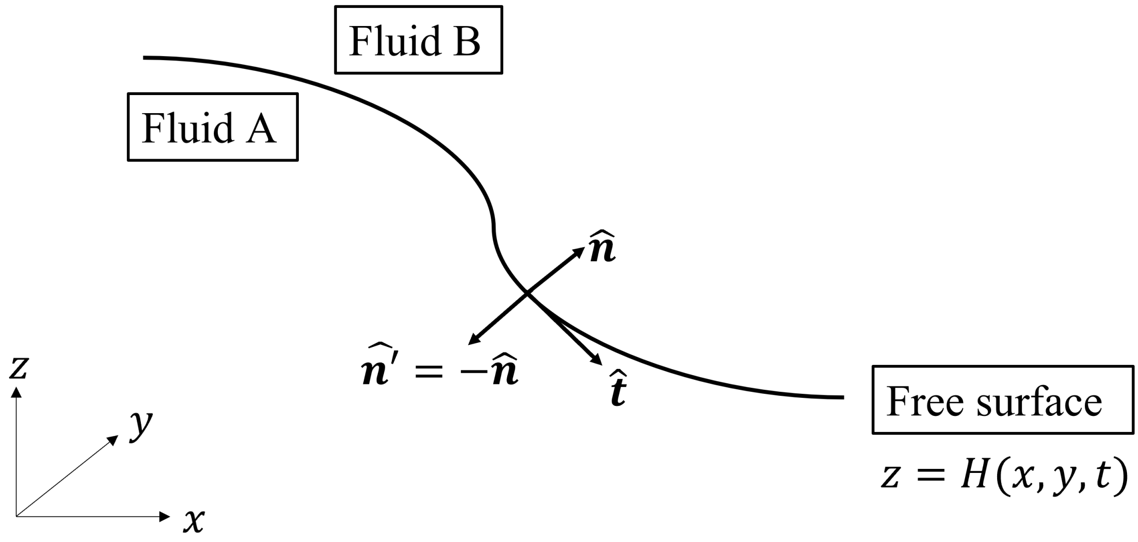

Figure 1.1: Sketch illustrating a free surface $z = H(x, y, t)$ separating fluids A and B with unit normal vectors $\hat{\boldsymbol{n}}$ and $\hat{\boldsymbol{n}}'$ respectively and unit tangent vector $\hat{\boldsymbol{t}}$.

as a ‘slip’ condition.

Meanwhile another common boundary is a fluid-fluid interface, where continuity of velocity and stress must be imposed at a known or unknown boundary. In the latter case, we have a ‘free boundary’ problem, where we are required to find the form of the boundary as part of the solution. We require two conditions: a ‘kinematic’ condition, relating the velocity of the free surface to the velocity of the bounding fluids at the free surface (continuity of velocity) and a ‘dynamic’ condition, requiring the continuity of stress across the free surface separating the two liquids.

The kinematic condition requires that there is zero rate of change of material fluid elements on the free surface due to the velocity field $\boldsymbol{u}$ acting on it; that is, fluid elements on the free surface remain on it. So if the location of free surface in space and time is described by $z = H(x, y, t)$ in Cartesian coordinates (x, y, z) (see figure 1.1), then it has zero material derivative so that

$$\frac{\mathrm{D}H}{\mathrm{D}t} = \frac{\partial H}{\partial t} + \boldsymbol{u} \cdot \boldsymbol{\nabla} H = 0. \tag{1.3}$$

Meanwhile, since stress is defined as force per unit area, to examine the dynamic condition in more detail it is first necessary to understand the forces acting at the free surface. We consider as an example a fluid-fluid interface taking the form of a liquid-vapour interface, for example, air and water. A liquid molecule within the bulk of the liquid experiences a stronger force of attraction to the liquid molecules which surround it than a liquid molecule at the free surface which is only partly surrounded by liquid molecules. Therefore the molecules at the free surface are in a higher energy state. The system works to reduce the number of these high-energy molecules, and thus the fluid system acts to minimise the area of the free surface. Surface tension σ is defined as a measure of the energy loss of a molecule at the free surface relative to a molecule in the bulk of the fluid per unit area, and has units of energy per unit area, or equivalently, force per unit length. Since surface tension only acts at the free surface, it does not appear in the Navier–Stokes equations and therefore acts only through the stress balance boundary condition.

The force acting on the interface due to surface tension can be split into a force acting normally to the interface (direction $\hat{\boldsymbol{n}}$, see figure 1.1), which is associated with the local curvature of the interface $\boldsymbol{\nabla}\cdot\hat{\boldsymbol{n}}$, and a force acting tangentially to the interface (direction $\hat{\boldsymbol{t}}$), which is associated with surface tension gradients $\boldsymbol{\nabla}\sigma$. We require continuity of stress (force/area) across the interface separating fluids A and B. Performing a force balance for the forces acting on each side of the free surface and integrating over the free surface shows that the difference between the stress (force/area) exerted on fluid A by fluid B must be balanced by the force per unit area due to surface tension. If the components of the surface forces normal to the boundary and tangential to it are considered separately, then the dynamic boundary condition says (i) the jump in normal hydrodynamic stress (force/area) across the interface must balance the force per unit area due to curvature associated with surface tension and (ii) the jump in tangential hydrodynamic stress (force/area) across the interface must balance the local surface tension gradient.

1.1.2 Solutions of the Navier–Stokes equations

To find the behaviour of a particular fluid, the task is to find the functions $\boldsymbol{u}$, p, μ, and ρ (and the temperature field for a thermodynamic flow) subject to appropriate boundary conditions for the situation. However, this is, in general, a difficult task as the Navier–Stokes equations (1.1)–(1.2) are nonlinear, and exact solutions only exist under the assumption of various simplifications which may not be physically relevant. Computer simulations can be used to find approximate solutions; however, for large or complex problems, this can require massive computing power. Moreover, it has not yet been proven that solutions of the general Navier–Stokes equations (1.1)–(1.2) always exist (Ladyzhenskaya, 2003).

However, in practice, we can obtain insights into fluid behaviour through solving reduced versions of the equations through various assumptions, simplifications and asymptotic limits for specific types of flows. As discussed above, in this thesis we consider two specific problems: the first involving fluids in microchannels and the second involving turbulent flows. These problems require us to consider two special cases of the equations: static fluid-fluid interfaces and boundary-layer flows.

1.1.3 Static fluid-fluid interfaces

For problems involving two fluids, we must solve the Navier–Stokes equations in each fluid and and apply continuity of velocity and stress at the interface separating the fluids, together with any relevant conditions at solid boundaries confining the fluid system. In a static flow the velocity $\mathbf{u}$ is set to zero and therefore in each fluid the Navier–Stokes equations (1.1)–(1.2) reduce to

$$\mathbf{F} = \boldsymbol{\nabla} p. \tag{1.4}$$

The tangential component of hydrodynamic stress of each static fluid acting on the interface is zero (which means there are no surface tension gradients from the tangential stress balance). Moreover, the jump in normal hydrodynamic stress across the interface is equivalent to a jump in pressure. Therefore for static fluids, the stress balance condition says that the pressure jump across the fluid-fluid interface must be balanced by the force per unit area due to curvature associated with surface tension. This balance is commonly known as the Young–Laplace equation after the mathematicians Thomas Young and Pierre-Simon Laplace, and is given by:

$$\Delta p = \sigma \boldsymbol{\nabla} \cdot \hat{\boldsymbol{n}}, \tag{1.5}$$

where Δp is the pressure jump across the free surface. In the absence of body forces $\boldsymbol{F}$ we solve this equation, together with any boundary conditions associated with the solid walls confining the fluid, for the shape of the free surface. The Young–Laplace equation is nonlinear; exact solutions can be found for certain fluid systems and in general, it can be solved numerically. However we can gain insights into specific features of a problem in relevant asymptotic limits.

Although we have here considered the Young–Laplace equation as deriving from Navier–Stokes with stress-balance boundary conditions at a fluid-fluid interface, this equation was written down in the early 19th century, some years before the Navier–Stokes equations. Young first introduced the idea of mean curvature and a theory describing surface tension, while Laplace later wrote down the formal analytical expression (1.5) that is known as the Young–Laplace equation. Laplace's arguments were based on hydrostatic balances in the context of capillary rise in a tube. The German mathematician Carl Friedrich Gauss is often not credited in the derivation of the Young–Laplace equation, however, he later provided a rational analytic derivation of the equation through the principle of virtual work (see Finn (2012) for details) which helped elucidate the physics of the problem and unified the qualitative arguments of Young with the mathematical arguments of Laplace.

1.1.4 Interfacial phenomena

The following discussion is based on material from De Gennes (1985), Quéré (2008) and Herminghaus, Brinkmann and Seemann (2008). For illustration, we consider three-phase solid-liquid-vapour systems.

As fluid systems become smaller, surface tension dominates gravity on scales less than the capillary length which is defined as $\sigma/\sqrt{\rho g}$, with g the magnitude of the gravitational field. Fluids dominated by surface tension exhibit a range of fascinating interfacial phenomena; many of these effects are shown in the video series G. M. Homsy (2008). As discussed above, surface tension does not appear in the Navier–Stokes equations and only appears in the stress balance boundary condition at the fluid-fluid interface. Thus in small fluid systems, the boundaries become very important. Particularly, when a fluid meets a solid boundary, wetting of the solid can occur. This wetting can take many forms, for example, a droplet on a surface could spread into a film to minimise surface energy, or could form a spherical cap sitting on the solid surface (for example, a droplet on a leaf). The difference between these states is defined by the contact angle, ϕ, between the liquid-vapour interface and the solid boundary. For $\phi > \pi/2$ the surfaces are hydrophobic while hydrophilic surfaces have

$\phi < \pi/2$. So-called superhydrophobic surfaces, when $\phi > 5\pi/6$, are desired for many industrial applications including self-cleaning surfaces (Liu and Jiang, 2012).

At the same time as he was developing his theory of surface tension and mean curvature, Young (1805) also deduced a law relating the contact angle ϕ to the surface energies of the solid-liquid, liquid-vapour and solid-vapour interfaces γ_{SL}, γ_{LV} and γ_{SV} respectively:

$$\gamma_{SV} = \gamma_{SL} + \gamma_{LV} \cos \phi. \tag{1.6}$$

This law was deduced by considering force balances at the point where the interface touches the solid (known as the contact line). The shape of a static meniscus is prescribed by the contact angle ϕ between the liquid-vapour interface and the solid, and the balance between hydrostatic pressure and pressure associated with curvature (the Young–Laplace equation (1.5)). Thus in theory, if the surface energies are known, it is possible to write down the shape of a meniscus using Young's contact angle law (1.6) and the Young–Laplace equation (1.5). However, the situation is often not quite so straightforward as the static contact angle may not take its equilibrium value.

Contact angle hysteresis

As a liquid wets a solid the contact line moves. Measurements taken from these dynamic contact lines yield so-called advancing and receding contact angles which can be different to the equilibrium contact angle observed in static systems. The observed static contact angle ϕ^* can take any value between the advancing and receding contact angles; contact angle hysteresis is defined as the difference between the advancing and receding contact angles. This range of contact angles may arise from many factors including surface roughness.

Chemical heterogeneity or surface roughness can impede contact line motion as the liquid has to overcome an energy barrier to wet the surface over the roughness. The American scientist Josiah Gibbs was the first to realise that this means surface roughness leads to pinning of the contact line on the roughness. Pinning in turn increases the interfacial area, which is energetically costly. Thus further contact line motion is resisted, and the contact angle adjusts instead to keep the system in equilibrium, and so a drop wetting a rough surface will, in general, have a contact angle ϕ^* which is different from the contact angle ϕ predicted by Young's Law (1.6). Wenzel (1936) gave an argument for rough surfaces to suggest that if the surface is hydrophobic ($\phi > \pi/2$) then in general $\phi^* > \phi$, whereas hydrophilic surfaces ($\phi < \pi/2$) have $\phi^* < \phi$. Thus the hydrophobicity/hydrophilicity of a solid is enhanced by heterogeneity. This effect can be exploited to manufacture surfaces, for example with superhydrophobic properties to be used for corrosion resistance (Darband et al., 2020). The effect of surface roughness on the system is also determined by whether the liquid wets the surface completely (Wenzel, 1936) or whether air pockets are trapped between the surface and the liquid (Cassie and Baxter, 1944). These states lead to increased and decreased hysteresis respectively.

Since most manufactured surfaces are rough, contact angle hysteresis is present in many industrial processes. However, as Herminghaus, Brinkmann and Seemann (2008) discuss, while hysteresis effects may dominate on a large scale, these effects can play a minor role in microscopic interactions and therefore it is possible to use simple theoretical models of wetting as a starting point for describing liquids on rough surfaces.

1.1.5 Boundary-layer flows

We now turn our attention to a different reduction of the Navier–Stokes equations (1.1)–(1.2) which describes flows for which the viscosity is very small. The Navier–Stokes equations (1.1)–(1.2), together with boundary conditions, contain parameters μ and ρ which can affect the behaviour of the partial differential equations and constants associated with the boundary conditions which may be dimensional. When using the equations, it is often more convenient to non-dimensionalise and carry out the analysis in terms of the smallest number of parameters possible (which is determined by the Buckingham π theorem (Buckingham, 1914)). Particularly, non-dimensionalising the Navier–Stokes equations (1.1)–(1.2) leads to the emergence of a dimensionless number known as the Reynolds number, which is characterised by the typical length scales L and flow speed U, and kinematic viscosity $\nu = \mu/\rho$ of the flow:

$$Re = \frac{\rho U L}{\mu}. \tag{1.7}$$

The Reynolds number measures the relative importance of inertial forces to viscous forces in the system and is named after Osborne Reynolds, who performed experiments in the late 1800s at the University of Manchester to characterise flows, particularly the breakdown of laminar flow, using this parameter. If the Reynolds number is large we expect viscous effects to be negligible throughout much of the fluid, whereas we expect viscous effects to be important for small Reynolds number.

At high Reynolds numbers Re, the flow is essentially inviscid. If we solve the Navier–Stokes equations with dynamic viscosity $\mu \to 0$, i.e. $Re \to \infty$, then the highest-derivative terms are lost from the momentum equation (1.1). However at the boundary, the flow must still satisfy no-slip boundary conditions; we now have too many boundary conditions to satisfy. This observation, and the theory to deal with it, was developed by the German physicist Ludwig Prandtl in the early 20th century. To allow the flow to satisfy the no-slip boundary conditions, a thin viscous layer is introduced close to the boundary where the tangential velocity adjusts from the boundary velocity to its inviscid value; this is known as a boundary layer. We then solve for the flow in an outer region where viscous effects are neglected. The scalings of the flow variables in each layer are found by comparing the relative sizes of terms in the equations of motion; in the boundary layer, inertial and viscous terms must balance. The solutions are matched using the method of matched asymptotic expansions.

It is important to note that singular regions can also develop away from boundaries. In general, we need to introduce a smoothing viscous layer anywhere where we obtain a discontinuity in a velocity distribution derived from the inviscid equations.

1.1.6 Boundary-layer phenomena

In general, the Navier–Stokes equations behave well for small Reynolds numbers and in many cases, unique solutions can be shown to exist. However, at high Reynolds numbers, the nonlinear $\mathbf{u} \cdot \boldsymbol{\nabla} \mathbf{u}$ term gains in significance and the flow can become turbulent. This process was first observed by Osborne Reynolds in 1883 using his now-famous apparatus which still exists at the University of Manchester.

As discussed above, subsequent experiments (beginning with the study by Kline et al. (1967)) have indicated that there is structure underpinning turbulent flows; for an overview of the types of structures observed see e.g. Robinson (1991) and Jiménez (2018). Since the initial study by Kline et al. (1967) in the mid-20th century, massive advances in computing power have enabled new insights into solutions of the Navier–Stokes equations (1.1)–(1.2) through direct numerical simulations. Particularly, fully nonlinear solutions of the Navier–Stokes equations at finite Reynolds numbers have been found which exhibit features of the coherent structures observed in turbulent flow; these solutions have been found numerically in a wide range of situations including channel flows (e.g. Nagata (1990), Kawahara and Kida (2001), and Wang, Gibson and Waleffe (2007)) and pipe flows (e.g. Faisst and Eckhardt (2003) and Wedin and Kerswell (2004)). These states are often known as "self-sustaining processes" (SSP).

The basic physics of the SSP states is understood to be a self-sustaining tripartite interaction of vortices and waves. The description that follows is based on the work of Waleffe (1997) in the context of shear flows, which itself has its origins in earlier work by Benney (1984) on the nonlinear evolution of a three-dimensional mean shear flow.

To illustrate the physics of the system, we first take Cartesian coordinates (x, y, z) in the parallel, normal and spanwise directions respectively relative to a solid wall. In a shear flow with streamwise velocity $U(y)$, the introduction of a perturbation in the wall-normal direction (for example, a cross-stream jet) leads to streamwise rolls (pairs of counter-rotating vortices) $\boldsymbol{u} = (0, v(y, z), w(y, z))$. These rolls redistribute the background mean shear flow by lifting slow fluid up and pulling fast fluid down, which creates a pattern of x-independent "streaks" $u(y, z)$ of high and low-speed flow. These streaks are named for the patterns seen in the experiments of Kline et al. (1967), where hydrogen bubbles released in the near-wall region of turbulent shear flows made streaky patterns. The streaky flow is unstable, leading to the growth of a 'streak-sloshing' wavy mode. However, the instability of the streak removes energy from the streak, so could accelerate the transition back to the laminar state. Therefore, to sustain the nonlinear interaction, there must be feedback from the streak instability to regenerate the rolls which is driven by a three-dimensional nonlinear mechanism. This process is depicted in figure 1.2. Thus it is possible to obtain exact solutions of the Navier–Stokes equations consisting of wavy streaks flanked by staggered, counter-rotating streamwise vortices, as shown in the inset to figure 1.2 which is from Waleffe (2003).

Computationally-generated nonlinear SSP equilibrium solutions of the Navier Stokes equations are often known as 'exact coherent structures' since they are exact solutions

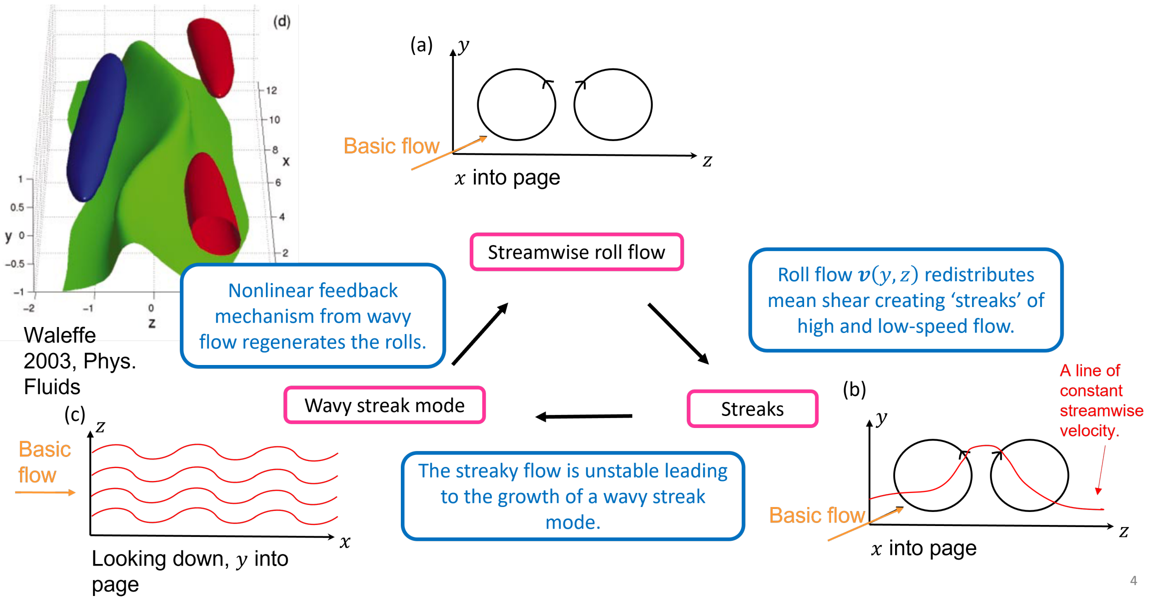

Figure 1.2: The self-sustaining tripartite interaction of vortices and waves forming coherent structures. The top graph (a) shows a streamwise roll flow $\boldsymbol{u} = (0, v(y,z), w(y,z))$ with the basic shear flow $U(y)$ into the page. Graph (b) shows the development of streaks $u(y,z)$, which leads to a wavy streak mode shown in (c) where the red lines denote lines of constant velocity. The inset figure (d) is from Waleffe (2003) which shows isosurfaces for the streamwise velocity (green) and the streamwise vorticity (red/blue) so that the wavy streak flow is coloured green and the red and blue colours are used for the counter-rotating vortices.

that exhibit some of the coherent motions observed in turbulent flow. The modes split up into what are termed upper and lower branch modes; the branches arise as a saddle–node bifurcation as the Reynolds number is increased, as explained by (Wang, Gibson and Waleffe, 2007), with the lower branch states (associated with low drag flows) relating to fully turbulent flows while the upper branch states (associated with high drag flows) relating to bypass transition as discussed by e.g. Schneider et al. (2008). Note that this terminology is at odds with the usual one for linear stability theory. Thus exact coherent structures are thought to form the unstable 'scaffold' on which turbulent flows evolve; for an overview see, for example, Graham and Floryan (2021). The upper branch states associated with high Reynolds number nonlinear transition are not the focus of the studies in this thesis and we shall instead concentrate on the lower branch states which are thought to provide a route to understanding the structure underpinning turbulent flows.

Computation of SSP states at high Reynolds numbers becomes difficult because the layer where the nonlinear interaction between the wave, roll and streak occurs, in which the flow changes rapidly, becomes vanishingly small and thus the flow can be difficult to resolve in this layer. At the same time as SSP states were being found numerically by Nagata (1990) and others, Hall and Smith (1991) developed a high-Reynolds number asymptotic theory for a vortex-wave interaction mechanism describing a three-point coupling between a wave and a roll-streak flow in much the same manner as the SSP states described above; however, the theory was applied to boundary-layer transition where it was shown to not be particularly relevant. Some twenty laters later, Hall and Sherwin (2010) showed that vortex-wave interaction theory describes lower-branch SSP states at finite Reynolds number with remarkable accuracy compared to the computationally-generated solutions of Wang, Gibson and Waleffe (2007). With current computing power, the asymptotic approach is much more viable at high Reynolds numbers than the computations. To understand the vortex-wave interaction mechanism it is first helpful to first understand another boundary-layer phenomenon that can arise in oscillatory boundary layers.

Oscillatory boundary layers: steady streaming

This discussion is based on the work of Stuart (1966), the review by Riley (2001) and the overview in Batchelor (2000) for incompressible flows, and the reader is referred to these texts for full mathematical details.

Consider a system with Cartesian coordinates (x, y, z) in the parallel, normal and spanwise directions respectively with respect to a solid wall. If the solid boundary is oscillating with sinusoidal motion then an oscillatory boundary layer occurs because the fluid velocity must match the solid velocity at the interface. Then the external velocity field in the free-stream will have a non-zero tangential velocity relative to the boundary, $u = \text{Real}(U(x)\mathrm{e}^{-i\omega t})$, where $U(x)$ varies with position on the boundary. This solution is used as a boundary condition to find the boundary-layer solution, which shows that the amplitude of the streamwise velocity u varies rapidly across the boundary layer.

Then, if $U'(x) \neq 0$, i.e. the inviscid outer flow has non-zero tangential variation, then by the continuity equation (1.2), throughout the boundary layer, there is a non-zero transverse velocity in the direction normal the boundary. Solving for this transverse velocity (see e.g. Batchelor (2000)) shows that this results in an average net transport of momentum in the tangential and transverse directions to the boundary; these time-averaged transport terms are called wave-induced Reynolds stresses. The transport of momentum is an inherently nonlinear effect and is dependent on the amplitude of the oscillation.

Because the amplitude of the streamwise velocity u varies rapidly across the boundary layer, the Reynolds stresses also vary across the boundary layer. The varying stress induces a non-zero average force on the fluid in the boundary layer. This generates steady motion of the fluid. This induced velocity does not decay to zero at the edge of the boundary layer so an outer ‘steady streaming’ flow is generated.

Vortex-wave interaction theory

This discussion is based on the papers by Hall and Smith (1991) and Hall and Sherwin (2010); the reader is referred to these papers for full mathematical details.

Based on the discussion of steady-streaming above, we now explain the vortex-wave interaction mechanism. We again take Cartesian coordinates (x, y, z) in the parallel, normal and spanwise directions respectively with respect to a solid wall. Firstly, consider a streamwise vortex flow: this is a shear flow $(u(y), 0, 0)$ which is modified to produce a spanwise-periodic velocity field $\boldsymbol{u}(y, z)$. As for the description of SSP states, the streamwise velocity component u is the streak while the v, w components are the streamwise roll, and the streamwise rolls and downstream streaks then make a streamwise vortex. At high Reynolds numbers Re, the Navier–Stokes equations (1.1)–(1.2) admit an exact solution with the streaky flow $u = O(1)$ and the streamwise rolls $v \sim w \sim Re^{-1}$; these scalings are based on the scalings for Taylor vortices derived by Taylor (1923) in the small gap/thin boundary layer limit. Since at high Reynolds numbers the roll velocity components v, w are tiny compared to the streak u, any small interference or forcing of these components can have a large effect on the total velocity $\boldsymbol{u}$ and this is essentially the idea behind the vortex-wave interaction mechanism, with the forcing provided by a wave.

Inviscid waves propagating on a flow have a singularity where the phase speed of the wave matches the speed of the background flow. To smooth out this singularity, a thin, viscous critical layer centred around the singularity is introduced (Lin, 1955). Thus the system now has a thin viscous oscillatory layer that is bounded on both sides by inviscid fluid; this is analogous to an oscillatory boundary layer from which we can get steady streaming effects as described above.

As in the steady streaming process, the rapid variation of wave amplitude across the critical layer generates wave Reynolds stresses which vary across the layer generating mean motion. However, the critical layer is bounded on both sides by fluid, which changes the situation somewhat. As discussed above in §1.1, at any fluid interface we require continuity of stress and velocity. However, an analysis of the momentum equation for velocity parallel to the critical layer shows that the mean motion generated by the wave Reynolds stresses leads to a jump in mean stresses parallel to the critical layer, which must be balanced by a jump in roll shear. Meanwhile, an analysis of the momentum equation for velocity normal to the critical layer shows that the streaming motion also generates a centripetal acceleration of the wave which is balanced by a jump in roll pressure; for a full mathematical description of this analysis see Hall and Sherwin (2010). These jumps must be accommodated by the roll velocity field in the bulk of the flow, and thus the wave forcing drives the roll flow. The streak can then be unstable to a wave so that the system is fully interactive.

Vortex-wave interaction theory provides a high-Reynolds-number description of lower-branch SSP states at finite Reynolds number, and results are in excellent agreement with numerical results; see, for example, Hall and Sherwin (2010). The strength of the agreement is somewhat surprising as high Reynolds number theory is often not particularly useful for the description of boundary layer processes and linear stability when compared to numerical simulations at finite Reynolds numbers. It is so far unclear as to why the agreement is so good.

Free-stream coherent structures

There are other types of exact coherent structures which are not described by the inviscid vortex-wave interaction theory. Free-stream coherent structures are a specific type of exact coherent structure that were first described in the context of the incompressible parallel asymptotic suction boundary layer by Deguchi and Hall (2014a), in which the roll–wave–streak interaction is confined to take place in a viscous layer at the edge of the boundary layer. They are thus quite distinct from the exact coherent structures seen in the main part of the boundary layer, however, are similar in that many waves interact to produce a single spanwise periodic flow outside the critical layer. Note that although they are called free-stream coherent structures, they are still associated with a boundary layer at a wall.

In the free-stream coherent structure solutions, the waves driving the interaction are viscous rather than inviscid so that equations governing the wave, roll and streak cannot be separated and the nonlinear interaction mechanism between the wave, roll and streak cannot be explicitly described by the critical layer/steady streaming theory for inviscid waves. Instead, the crucial point is that the existence of the layer where the nonlinear interaction takes place is fixed by the boundary-layer form of the basic flow, i.e. the exponential decay of the basic flow to its free-stream form.

The interaction in this viscous layer, which is of approximately the same thickness as the (non-dimensional) boundary-layer thickness, produces global disturbances to the flow field, hence it is termed the ‘production layer’. In this layer, the flow satisfies the reduced Navier-Stokes equations at unit Reynolds number and the roll-wave-streak interaction is driven by the nonlinearity in these equations. Although the full Navier–Stokes equation still have to be solved, there is a large saving compared to the full computational approach which becomes progressively more computationally demanding as the Reynolds number increases.

The roll–wave–streak flow exiting the production layer towards the wall adjusts to become compatible with the basic flow, hence this layer is termed the 'adjustment layer'. Here, the roll and wave flow decay. However, the streaks, i.e. the x-independent disturbance to the streamwise velocity field, can continue to grow towards the wall in the region beneath the production layer before taking their maximum amplitude in a near-wall layer, which again is of boundary-layer thickness. Thus the free-stream coherent structures couple the nonlinear interaction in the free-stream to the disturbances at the wall, and thus allow for a way for disturbances to get from outside the boundary layer to the wall.

The asymptotic theory to describe these solutions, which was first developed by Deguchi and Hall (2014a), is in excellent agreement with numerical solutions found by Kreilos, Gibson and Schneider (2016) and Deguchi and Hall (2014a). The production-layer problem has since been shown to be generic to a wide range of flows, including two-dimensional spatially-growing boundary layers (Deguchi and Hall, 2015a) and planar jets (Deguchi and Hall, 2018). Ozcakir, Hall and Tanveer (2019) have also found analogous states in pipe flow.

1.2 Thesis structure

The rest of this thesis is presented in journal format; the papers have been written as part of my studies and three of the four have been published in journals that have a history of publishing work in fluid dynamics. Each paper has an introduction and discussion, and self-contained appendices and bibliography.

The first part of this thesis will use the methods described above to show the effect of channel geometry on static menisci in confined channels. Here we present a study of static equilibrium solutions which form the initial state of low capillary number (defined as the ratio of viscous drag forces to surface tension forces) dynamical flows.

Chapter 2 shows how we can quantify and describe the sensitivity of static menisci in confined channels to imperfections in geometry taking the form of isolated ridges and grooves running the length of the channel. We are interested in knowing the shape of the meniscus in the perturbed channel and the contact line displacement. The key result of the work is that small-amplitude perturbations that change the volume of the channel induce a change in the mean curvature of the meniscus, which results in long-range curvature of the contact line; we can find this long-range curvature by matching onto a catenoid/droplet with the same total pressure difference. Thus, we can predict the far-field behaviour of the contact line a priori just using the boundary data.

Chapter 3 considers the same problem but with forcing in the form of isolated bump protrusions and intrusions scattered on the channel walls. This paper has not been published as work is still ongoing, however, we present some preliminary results for small-amplitude perturbations which show that the location of the meniscus relative to the bump affects the direction and amplitude of deformation, and the direction of deformation smoothly deforms as a meniscus advances over a bump in a quasi-static manner.

We were originally motivated to study menisci in perturbed channels because of the effects of channel imperfections seen in the Hele–Shaw problem for air fingers and bubbles, as described by Tabeling, Zocchi and Libchaber (1987), Thompson, Juel and Hazel (2014), and Franco-Gómez et al. (2016, 2018). There, the surface roughness of the channel walls was found to change the set of stable solutions however it was unclear how the perturbations acted to select a particular set. The simplified model of a static meniscus in a channel was intended to provide some insight into how to implement the boundary conditions around the perturbation and how these might be affected by dynamics. However, the static problem has proved to be interesting and subtle in its own right.

The second part of this thesis uses the methods discussed above to describe non-linear free-stream coherent structure-type equilibrium and travelling-wave solutions of the Navier–Stokes equations.

In Chapter 4 we show how to obtain free-stream coherent structures in two-dimensional unsteady incompressible flows (as an extension of two-dimensional spatially-varying flows discussed in Deguchi and Hall (2015a)). We show that unsteady flows can be added to the class of incompressible flows which support free-stream coherent structures.

In Chapter 5 we consider compressible flows (which are more industrially relevant to drag control than incompressible flows). The key result is that the asymptotic theory describing exact coherent structures in incompressible flows can be applied to compressible flows. Since in incompressible flows this theory agrees well with numerical SSP solutions of the Navier–Stokes equations, our study indicates that similar mechanisms underpinning turbulent flows may be present in compressible flows.

In Chapter 6 we draw together some conclusions.

Chapter 2

The effect of isolated ridges and grooves on static menisci in rectangular channels

This chapter contains a paper was written as part of my studies at the University of Manchester. It appears as:

E. C. Johnstone, A. L. Hazel and O. E. Jensen (2022). "The effect of isolated ridges and grooves on static menisci in rectangular channels". *J. Fluid Mech.* 935, A32.

The paper has a self-contained introduction, discussion, appendices and bibliography. Following the paper there are three additional appendices which provide detail of some aspects of the problem that were not presented in the paper for publication.

Statement of Contributions

EJ performed the asymptotic analysis, numerical computations and analysis to obtain the required data to answer the research question, wrote the paper and was responsible for the paper throughout the publication process. AH and OJ provided advice, guidance and supervision throughout all stages of the process, suggested ideas and direction of the research and provided editorial suggestions. Additionally OJ wrote the second half of appendix F.

J. Fluid Mech. (2022), *vol.* 935, A32, doi:10.1017/jfm.2022.26

The effect of isolated ridges and grooves on static menisci in rectangular channels

Eleanor C. Johnstone[1],†, **Andrew L. Hazel**[1] **and Oliver E. Jensen**[1]

[1]Department of Mathematics, University of Manchester, Manchester M13 9PL, UK

(Received 28 May 2021; revised 13 December 2021; accepted 7 January 2022)

We present theoretical and numerical results that demonstrate the sensitivity of the shape of a static meniscus in a rectangular channel to localised geometric perturbations in the form of narrow ridges and grooves imposed on the channel walls. The Young–Laplace equation is solved for a gas/liquid interface with fixed contact angle using computations, analytical arguments and semi-analytical solutions of a linearised model for small-amplitude perturbations. We find that the local deformation of the meniscus's contact line near a ridge or groove is strongly dependent on the shape of the perturbation. In particular, small-amplitude perturbations that change the channel volume induce a change in the pressure difference across the meniscus, resulting in long-range curvature of its contact line. We derive an explicit expression for this induced pressure difference directly in terms of the boundary data. We show how contact lines can be engineered to assume prescribed patterns using suitable combinations of ridges and grooves.

Key words: contact lines, capillary flows

1. Introduction

The behaviour of fluids when the dominant force is surface tension underpins many fundamental physical and industrially valuable processes, including microfluidics and inkjet printing (Yang, Yang & Hong 2005; He *et al.* 2017; Calver *et al.* 2020); directional transport of liquids in biological processes (Prakash, Quéré & Bush 2008; Zheng *et al.* 2010; Ju *et al.* 2012; Comanns *et al.* 2015; Xu & Jensen 2017; Bhushan 2019); engineering applications such as water harvesting (Brown & Bhushan 2016; Xu *et al.* 2016; Li *et al.* 2017); and the behaviour of fluids in low-gravity situations (Passerone 2011). Moreover, from a purely theoretical point of view, such systems have been known to exhibit a plethora of complex behaviours associated with contact-line dynamics, such as contact-angle

† Email address for correspondence: eleanor.johnstone@manchester.ac.uk

hysteresis (Dussan 1979; Gao & McCarthy 2006; Eral, 't Mannetje & Oh 2013) and the 'stick-slip' phenomenon (Picknett & Bexon 1977; Bourges-Monnier & Shanahan 1995; Shanahan 1995; Stauber *et al.* 2014). However, the behaviour that we study here is that of a very simple static system, which forms the 'basic state' for many of these dynamical problems. Specifically, we seek to quantify and describe the sensitivity of menisci in confined channels to imperfections in geometry. Understanding such sensitivity is important in the industrial and biological processes described above, where natural or manufactured surfaces are in general not perfectly smooth. Indeed, the sensitivity of microfluidic devices to small imperfections has hampered their usefulness in an industrial setting (Zhou *et al.* 2012; Calver *et al.* 2020). On the other hand, the structuring of channels by parallel grooves has also been shown to improve the efficacy of microfluidic devices: for example, railed microfluidic channels have been used to create superhydrophobic surfaces (Yoshimitsu *et al.* 2002; Emami *et al.* 2013), to guide and assemble microstructures inside fluidic channels (Chung *et al.* 2008), and in primary cell culture technology to control the deposition and location of cells within microfluidic devices (Khademhosseini *et al.* 2004; Howell *et al.* 2005; Khademhosseini *et al.* 2005; Park *et al.* 2006; Lee, Hung & Lee 2007; Manbachi *et al.* 2008; Khabiry *et al.* 2009; Mobasseri *et al.* 2015). Stone, Stroock & Ajdari (2004) also provide a general discussion of the role of channel geometry in controlling fluids in microchannels. Anna (2016) and Ajaev & Homsy (2006) give a more general discussion of the modelling and applications of drops and bubbles in microchannels and confined channels.

It has been known since Wenzel (1936) that menisci in channels are sensitive to imperfections in the channel geometry. Wenzel's work demonstrating the effect of wall roughness on contact-line wettability using simple energy conservation arguments was further extended for porous surfaces by Cassie & Baxter (1944) and Cassie (1948). Quasi-static effects such as contact-line hysteresis (at finite microscopic contact angle) and the stick-slip phenomenon were first observed by Johnson & Dettre (1964), who studied the wettability of a drop on a rough surface where the roughness was in the form of concentric circular grooves. By moving the contact line very slowly over the obstacles, they observed multiple axisymmetric equilibria. Huh & Mason (1977) studied surfaces with more complex roughness, including cross, hexagonal and radial grooves. They used the linearised Young–Laplace equation to find a relationship between the contact angle and hysteresis/stick-slip behaviour. Surfaces with periodic roughness (Cox 1983) and random roughness (Jansons 1985) were also found to induce contact-angle hysteresis and stick-slip behaviour in the limit of zero capillary number. More recently, rough surfaces with Gaussian-type defects have been shown to influence significantly contact-line dynamics in the contexts of droplet spreading (Espín & Kumar 2015), droplet sliding (Park & Kumar 2017), and droplet evaporation and imbibition (Pham & Kumar 2017, 2019). Jansons (1985) made the further observation that the location of the contact line influenced its future position, leading to irreversibility of the wetting process. Stick-slip behaviour can also be induced by defects caused by changes in wettability or temperature (Ajaev, Gatapova & Kabov 2020).

Concus & Finn (1969), Fowkes & Hood (1998) and Reyssat (2014) showed that for static liquid–vapour interfaces in a wedge, the existence of solutions depends on the angle of the wedge and the contact angle between the liquid–vapour and solid–liquid interfaces. Instead of imposing perturbations on the channel walls geometrically, it is also possible to perturb the meniscus by changing the contact angle locally on the upper and lower channel walls. Boruvka & Neumann (1978) considered a meniscus in contact with a stripwise heterogeneous wall in which each strip has a different equilibrium contact angle. They showed that locally near the wall, the contact-line curvature becomes unbounded at the point where the contact angle changes. The jump in contact angle is analogous to a ridge or groove perturbation with corners; here the displacement of the contact line can be unbounded in some circumstances (Concus & Finn 1969; Weislogel & Lichter 1998; King, Ockendon & Ockendon 1999). In what follows, we consider smooth (differentiable everywhere) wall perturbations with no sharp corners.

At low flow speeds, the motion of drops and bubbles in confined devices follows a series of near-equilibrium configurations and thus the static problem discussed here can also be used to provide insight into the effect of wall roughness on these problems. Channel imperfections are known to have a significant effect on the set of observable stable solutions for air fingers and bubbles propagating in a Hele-Shaw channel. This effect has been seen with a cusp at the tip of a bubble/finger created by a needle (Hong & Family 1988); a tiny bubble at the tip of a bubble/finger (Maxworthy 1986); anisotropy by etching of the plates (Ben-Jacob *et al.* 1985; Dorsey & Martin 1987); and channel occlusions (Hazel *et al.* 2013; Thompson, Juel & Hazel 2014). Wall roughness has also been seen to affect the 'tip-splitting' effect seen by propagating interfaces (Tabeling, Zocchi & Libchaber 1987; Franco-Gómez *et al.* 2016, 2018). It is unclear so far how the wall roughness contributes to the selection of a particular set of solutions.

In this study, we consider a static liquid–vapour interface in a rectangular channel and introduce imperfections to the upper and lower walls in the form of narrow ridges and grooves running the length of the channel. We are interested in how the meniscus shape changes due to the perturbations and, in particular, how the perturbations displace the contact line (defined as the intersection of the meniscus with the channel walls). We consider two classes of perturbations: those that change the volume of the channel, and those that preserve it. A key result is that small-amplitude perturbations that change the volume of the channel induce a change in the pressure difference across the meniscus, and thus change the mean curvature of the meniscus. This change is a long-range effect that is felt along the whole contact line.

In § 2 we present the governing nonlinear Young–Laplace equation and boundary conditions. In § 2.1 we derive and solve a linear model to find the shape of the meniscus for perturbations of small amplitude. The linearised problem shows that the change in mean curvature of the meniscus (i.e. the change in pressure difference over the meniscus) due to small perturbations is given by the Helmholtz equation. In § 3, we derive an explicit expression for the change in pressure difference that is directly proportional to the integral of the perturbations around the contact line, which corresponds to the change in channel volume. We also solve for the fully nonlinear mean curvature of the meniscus numerically using Surface Evolver (Brakke 1992).

We present results for both the linear and nonlinear models in § 4. We show that for channel-volume-changing perturbations, the meniscus away from the local perturbation matches onto a catenoid that must have the same constant mean curvature as the meniscus, which can be worked out *a priori* from the boundary data. We also show that perturbations that are offset from each other on the two walls – for example, forming weakly corrugated channels – can be used to engineer patterns in the contact line because each perturbation causes a deflection of both the upper and lower contact lines. The deflection mechanism acts differently depending on whether the total perturbation is channel-volume-changing or channel-volume-preserving. We conclude with a short discussion in § 5.

2. Model

Consider a static liquid–vapour interface having uniform mean curvature in a rectangular channel with non-dimensional edge lengths $2L$, $2W$ and 1 in the x, y and z directions,

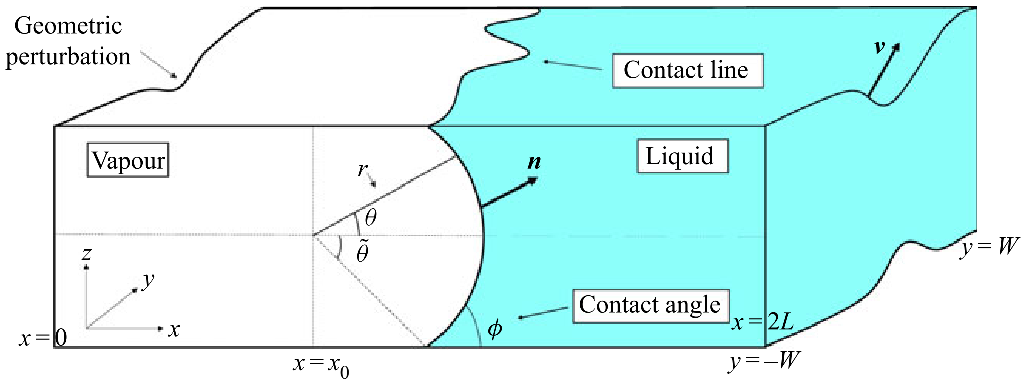

Figure 1. A static liquid–vapour meniscus in a rectangular channel $0 \leq x \leq 2L$, $-W \leq y \leq W$ and $-\frac{1}{2} + B_-(y) \leq z \leq \frac{1}{2} + B_+(y)$. The shape of the meniscus is described using a cylindrical polar coordinate system (r, θ, y) centred at $(x, y, z) = (x_0, 0, 0)$ where x_0 is fixed by the volume of liquid in the channel. The meniscus is located in the channel such that the unperturbed state has $r = R = 1/(2\cos\phi)$, with ϕ the solid–liquid contact angle on the upper and lower walls. The solid–liquid contact angle on the side walls is $\pi/2$.

respectively; see figure 1. We assume that the channel is sufficiently small that gravitational effects can be ignored, i.e. that the height of the horizontal channel is much smaller than the capillary length scale $\sqrt{\gamma_{LV}/\rho g}$, where γ_{LV} is the liquid–vapour surface tension, ρ is the liquid density, and g is the acceleration due to gravity. The contact angle between the liquid–vapour and solid–liquid interfaces on the upper and lower walls of the channel is fixed to be ϕ, where $0 \leq \phi < \pi/2$. We impose that the meniscus meets the side walls at $y = \pm W$ normally, with contact angle $\pi/2$, so that in the absence of wall perturbations, the interface takes the shape of an arc of a cylinder. To describe this, we adopt cylindrical polar coordinates (r, θ, y), with $r = 0$ fixed at the centre of curvature of the unperturbed meniscus. We define the maximum value of θ, which specifies the contact-line location in the unperturbed state, by $\tilde{\theta} = \pi/2 - \phi$ (see figure 1). Then the base state is given by $r = R \equiv 1/(2\sin\tilde{\theta})$, for $\theta \in [-\tilde{\theta}, \tilde{\theta}]$ and $y \in [-W, W]$. Cartesian and polar coordinates are related by $(x, y, z) = (x_0 + r\cos\theta, y, r\sin\theta)$, where x_0 is defined by the volume of liquid V_L in the channel, as

$$x_0 = 2L - \frac{R}{2}\cos\tilde{\theta} - \frac{V_L}{2W} - R^2\tilde{\theta}. \tag{2.1}$$

We denote the dimensionless pressure of the liquid phase (scaled on surface tension over channel depth) to be p_L, relative to zero pressure in the gas phase, so that in the unperturbed configuration $p_L = -1/R$.

The upper (+) and lower (−) walls of the channel are then perturbed so that they are described by $z = \pm\frac{1}{2} + B_\pm(y)$. The perturbations take the form of ridges and grooves that could be created, for example, using a pulsed laser (Xing *et al.* 2014), or using moulded fabrication with standard soft lithography techniques (Chung *et al.* 2008). We do not assume contact-angle hysteresis, but we assume that surfaces are homogeneous and smooth, allowing us to address interactions between the wall perturbations and the meniscus at the microscopic level. We non-dimensionalise all surface tensions on the liquid–vapour surface tension γ_{LV} so that the meniscus has unit surface tension.

We specify the interface location relative to the base state so that the surface of the meniscus is described in terms of the unknown radial perturbation $F(y, \theta)$ and the angular change in location of the contact lines on the upper and lower walls $\Phi_\pm(y)$:

$$r = R + F(y, \theta), \quad \theta \in [-\tilde{\theta} + \Phi_-(y), \tilde{\theta} + \Phi_+(y)], \quad y \in [-W, W]. \tag{2.2}$$

We measure the pressure difference across the meniscus as the liquid pressure minus the gas pressure, where without loss of generality we assume that the gas pressure is zero. Thus we write $\Delta p = -R^{-1} + (p_L)_p$, where $(p_L)_p$ is the change in pressure of the liquid phase due to the channel perturbations. This is constrained by the requirement that the volume of liquid V_L does not change under any perturbation to the channel geometry. Then, defining the unit normal $\boldsymbol{n}$ of the meniscus to point into the liquid phase, as shown in figure 1, the equilibrium state is specified by the Young–Laplace equation, relating the uniform mean curvature of the interface to the pressure difference across the meniscus Δp as

$$\Delta p = -\nabla \cdot \boldsymbol{n}|_{r=R+F} = -\frac{1}{\Lambda} + \left(\frac{(R+F)F_y}{\Lambda}\right)_y + \frac{1}{R+F}\left(\frac{F_\theta}{\Lambda}\right)_\theta, \tag{2.3}$$

where $\Lambda \equiv \sqrt{(R+F)^2(1+F_y^2)+F_\theta^2}$.

We solve the Young–Laplace equation (2.3) subject to the volume constraint and the following boundary conditions. First, we constrain the contact line to lie on the perturbed channel walls, so that

$$z = (R+F(y,\theta))\sin\theta = \pm\tfrac{1}{2} + B_\pm(y) \quad \text{at } \theta = \pm\tilde{\theta} + \Phi_\pm(y). \tag{2.4}$$

Second, we impose a fixed contact angle ϕ through the geometrical argument that if $\boldsymbol{v}_\pm$ are unit normals to the upper and lower channel walls pointing out of the channel (as shown in figure 1), then

$$\boldsymbol{n}\cdot\boldsymbol{v}_\pm = \cos\phi \quad \text{at } \theta = \pm\tilde{\theta} + \Phi_\pm(y), \quad \text{where } \boldsymbol{v}_\pm = \pm\frac{-B'_\pm(y)\,\hat{\boldsymbol{y}} + \hat{\boldsymbol{y}}}{\sqrt{1+B'_\pm(y)^2}}. \tag{2.5}$$

Finally, the meniscus meets the side walls normally, so that

$$F_y(\pm W, \theta) = 0. \tag{2.6}$$

2.1. *Linear model*

We linearise the problem when wall perturbations are small relative to the channel depth by writing $B_\pm(y) = \epsilon\, b_\pm(y)$, where ϵ is defined as the maximum amplitude of the perturbation, and $b_\pm(y) = O(1)$ as $\epsilon \to 0$. We use the parametrisation of the interface given in the nonlinear model (2.2), with the assumption that the perturbation to the radius and the change in location of the contact lines are also $O(\epsilon)$, so that $F(y,\theta) = \epsilon f(y,\theta)$ and $\Phi_\pm(y) = \epsilon\,\Theta_\pm(y)$. Then the interface is parametrised as

$$r = R + \epsilon f(y,\theta), \quad \theta \in \left[-\tilde{\theta} + \epsilon\,\Theta_-(y), \tilde{\theta} + \epsilon\,\Theta_+(y)\right], \quad y \in [-W, W]. \tag{2.7}$$

We assume that the change in the pressure difference due to the perturbation is also $O(\epsilon)$, so that $(p_L)_p = \epsilon p$ and $\Delta p = -R^{-1} + \epsilon p$.

Assuming that $f(y,\theta)$ and all its derivatives are $O(1)$ as $\epsilon \to 0$, after linearisation, the leading-order approximation to the Young–Laplace equation (2.3) is the Helmholtz equation

$$\frac{1}{R^2} f + \frac{1}{R^2} f_{\theta\theta} + f_{yy} = p, \quad y \in [-W, W], \ \theta \in [-\tilde{\theta}, \tilde{\theta}]. \tag{2.8}$$

The boundary condition (2.4) constraining the contact line to lie on the upper and lower channel walls becomes

$$f(y, \pm\tilde{\theta}) \sin\tilde{\theta} \pm f_\theta(y, \pm\tilde{\theta}) \cos\tilde{\theta} = \pm b_\pm(y), \tag{2.9}$$

whilst the leading-order approximation to boundary condition (2.5) is

$$f_\theta(y, \pm\tilde{\theta}) - R\,\Theta_\pm(y) = 0. \tag{2.10}$$

In deriving (2.10), the neglected $O(\epsilon^2)$ terms include those involving the derivative of the boundary data, $\epsilon^2 b'_\pm(y)$. These terms will formally become $O(\epsilon)$ if $b'_\pm(y) = O(\epsilon^{-1})$; this puts an additional constraint on the boundary data for the linearised model to be valid. In particular, this constraint suggests that we cannot use a linearised model for very sharp perturbations with large gradients regardless of their amplitude; this will be discussed in § 3.2. The final boundary condition (2.6) becomes

$$f_y(\pm W, \theta) = 0. \tag{2.11}$$

The problem is closed with the condition that the volume of liquid V_L is invariant with respect to changes in channel volume. This leads to the condition

$$\int_{-W}^{W} \int_{-\tilde{\theta}}^{\tilde{\theta}} f(y, \theta)\, \mathrm{d}\theta\, \mathrm{d}y = \left(\frac{V_L}{2RW} + \frac{\tilde{\theta}}{2\sin\tilde{\theta}} - \frac{\cos\tilde{\theta}}{2} \right) \int_{-W}^{W} (b_+(y) - b_-(y))\, \mathrm{d}y. \tag{2.12}$$

Finally, the linearised contact-line displacement on the upper and lower walls $x_\pm(y)$ is found by Taylor expanding the solution for $x = r\cos\theta$ at $\theta = \pm\tilde{\theta} + \epsilon\,\Theta_\pm(y)$:

$$x_\pm(y) = x_0 + R\cos\tilde{\theta} + \epsilon\, x_p^\pm(y) + O(\epsilon^2), \quad x_p^\pm(y) = f(y, \pm\tilde{\theta}) \cos\tilde{\theta} \mp f_\theta(y, \pm\tilde{\theta}) \sin\tilde{\theta}. \tag{2.13a,b}$$

For the specific case of zero contact angle ($\phi = 0$), when the meniscus meets the walls tangentially, there is no contribution to boundary condition (2.10) at $O(\epsilon)$. An expansion to powers of $O(\epsilon^2)$ is needed to obtain (2.10), as explained in Appendix A.

3. Methods

3.1. *Pressure-volume relationship*

We show that small-amplitude perturbations that change the volume of the channel must cause the mean curvature of the meniscus to change. Noting the self-adjointness of the Helmholtz operator and boundary conditions (2.8)–(2.11), we derive in Appendix B an explicit expression for this $O(\epsilon)$ pressure difference at the meniscus, and find that it has a similar dependence on the boundary data as the induced volume change,

$$p = \frac{1}{4WR^2 \sin(\tilde{\theta})} \int_{-W}^{W} (b_+(y) - b_-(y))\, \mathrm{d}y. \tag{3.1}$$

Thus in the linear problem with channel-volume-changing perturbations (for which $\int_{-W}^{W} (b_+(y) - b_-(y))\, \mathrm{d}y \neq 0$), the forcing for the Helmholtz equation (2.8) can be deduced *a priori* from the volume change encoded in the boundary data.

3.2. *Solutions for Gaussian perturbations*

We now restrict our attention to Gaussian perturbations of the form

$$B_{\pm}(y) = a^{\pm}\epsilon \exp(-(y-y_c^{\pm})^2/s^2), \quad \text{so} \quad b_{\pm}(y) = a^{\pm} \exp(-(y-y_c^{\pm})^2/s^2), \tag{3.2}$$

where $y_c^{\pm}$ and s control the location and width of the perturbation, respectively, and the prefactor $a^{\pm}$, which can take value $+1$ or -1 on either wall, determines the orientation of the perturbation, i.e. whether it is a ridge or a groove. For the purposes of illustration, we assume that the perturbation on the lower wall is a ridge so that $a^{-} = 1$. Then after fixing s, we consider two specific types of geometry: channel-volume-preserving configurations with $\int_{-W}^{W}(b_{+}(y) - b_{-}(y))\,\mathrm{d}y = 0$ (corresponding to a groove on the upper wall); and channel-volume-changing configurations with $\int_{-W}^{W}(b_{+}(y) - b_{-}(y))\,\mathrm{d}y < 0$ (corresponding to a ridge on the upper wall). The former preserve the pressure of the liquid phase, whereas the latter, which decrease the volume of the channel, cause an increase in the magnitude of the liquid pressure. If $y_c^{\pm} = 0$, then the channel-volume-preserving and channel-volume-changing configurations are mirror-antisymmetric and mirror-symmetric, respectively, about $z = 0$.

We solve the full nonlinear problem to find the shape of the interface using the open-source software Surface Evolver (Brakke 1992), which uses a gradient-descent method to converge to a surface with minimum energy from a given initial guess and subject to constraints to enforce the boundary conditions and the volume condition; for details, see Appendix C. Meanwhile, we solve the linear problem (2.8)–(2.12) using second-order-accurate finite differences; see Appendix D for more details. As seen in § 2.1, the linear model can be expected to break down when $b'_{\pm}(y) = O(\epsilon^{-1})$. For the Gaussian boundary data (3.2), this occurs if $s^2 = O(\epsilon)$, which limits how narrow the perturbation can be.

3.3. *Analytic solution for symmetric perturbations*

For the special case of aligned perturbations ($y_c^{\pm} = 0$), we can obtain an analytic solution to the linear problem (2.8)–(2.12) via separation of variables, with a Fourier discretisation across the width of the channel in the y direction because of the y dependence of the boundary conditions on the upper and lower walls. Denoting mirror antisymmetric (channel-volume-preserving) and mirror-symmetric (channel-volume-changing) solutions by 'MAS' and 'MS' subscripts, respectively, the series solution is given by

$$f_{\substack{MAS\\MS}}(y,\theta) = R^2 p + \sum_{n=0}^{\infty} A_n^{\substack{MAS\\MS}} \left(\mathrm{e}^{\lambda_n \theta} \mp \mathrm{e}^{-\lambda_n \theta}\right) \cos\left(\frac{n\pi y}{W}\right), \tag{3.3}$$

where the exponential coefficient λ_n is given by

$$\lambda_n = \sqrt{\left(\frac{n\pi R}{W}\right)^2 - 1}. \tag{3.4}$$

Thus there is a critical value of n, specific to the contact angle (through $2R\cos\phi = 1$) and the width of the channel, at which the sum switches from having oscillatory dependence in θ to exponential dependence in θ. The coefficients $A_n^{\substack{MAS\\MS}}$ are given by

$$A_n^{\substack{MAS\\MS}} = \frac{\pm a_n}{\left(\sin\tilde{\theta} + \lambda_n \cos\tilde{\theta}\right) \mathrm{e}^{\lambda_n \tilde{\theta}} \mp \left(\sin\tilde{\theta} - \lambda_n \cos\tilde{\theta}\right) \mathrm{e}^{-\lambda_n \tilde{\theta}}} \quad \begin{cases} n \geqslant 0 \text{ (MAS)}, \\ n \geqslant 1 \text{ (MS)}, \end{cases} \tag{3.5}$$

$$a_0^{MAS} = \frac{1}{2W} \int_0^W b_-(y)\, \mathrm{d}y, \quad a_n = \frac{1}{W} \int_0^W b_-(y) \cos\left(\frac{n\pi y}{W}\right) \mathrm{d}y, \quad n \geqslant 1. \tag{3.6}$$

The coefficient A_0^{MS} is found using the volume condition (2.12) to be

$$A_0^{MS} = \frac{\left(\dfrac{V_L}{2RW} + \dfrac{\tilde{\theta}}{2\sin\tilde{\theta}} - \dfrac{\cos\tilde{\theta}}{2}\right) \displaystyle\int_{-W}^{W} (b_+(y) - b_-(y))\, \mathrm{d}y - 4WR^2 \tilde{\theta}\, p}{4W \sin\tilde{\theta}}. \tag{3.7}$$

For the Gaussian boundary data (3.2), the coefficients of the convergent series are defined by

$$a_n = \frac{s\sqrt{\pi}}{2W} \exp\left(-\frac{s^2}{4}\left(\frac{n\pi}{W}\right)^2\right) \mathrm{Re}\left\{\mathrm{i}\, \mathrm{erfi}\left(-\frac{\mathrm{i}W}{s} - \frac{n\pi s}{2W}\right)\right\}, \quad n \geqslant 1. \tag{3.8}$$

The function $\mathrm{erfi}(z) = -\mathrm{i}\,\mathrm{erf}(\mathrm{i}z)$ is the imaginary error function so that for real u and v, $\mathrm{i}\,\mathrm{erfi}(-\mathrm{i}u + v) = \mathrm{erf}(u + \mathrm{i}v)$.

Numerical solutions below are obtained by truncating (3.3) at $n = n_c$ such that terms with coefficients smaller than 10^{-16} were discarded.

4. Results

We present results for the displacement of the static meniscus and the contact line induced by Gaussian perturbations (3.2). We first assume that the perturbations are aligned so that $y_c^{\pm} = 0$.

4.1. *Aligned perturbations*

Figure 2 shows 'baseline' linear solutions $f(y, \theta)$ for the two prototype channel-volume-preserving and -changing configurations, together with displacement of the upper and lower contact lines due to the perturbation, $x_p^{\pm}(y)$ (as given in (2.13*a*,*b*)), computed using the series solution (3.3). In the channel-volume-preserving case (figure 2*a*), the response of the meniscus and contact line is localised around the perturbations in the y direction, whereas in the channel-volume-changing case (figure 2*b*), the perturbations induce a larger-amplitude response that is felt across the entire depth and width of the channel. In the former case, the contact-line shape appears to mirror the curvature of the wall perturbation, but it is smoother in the latter case. Thus a small ridge or groove placed in the centre of the channel can cause non-local bending of the contact line through its impact on the pressure field (3.1). Note that we can build new small-amplitude solutions as linear combinations of the two solutions shown, and can therefore describe the behaviour of the contact line as the perturbations are varied between the two configurations.

The effect of varying perturbation amplitude and width on the contact-line displacement is presented in figure 3. Both volume-preserving (figure 3*a*) and volume-changing (figure 3*b*,*c*) perturbations result in a local displacement of the contact line in the centre of the channel that depends on the shape of the perturbations, with narrower

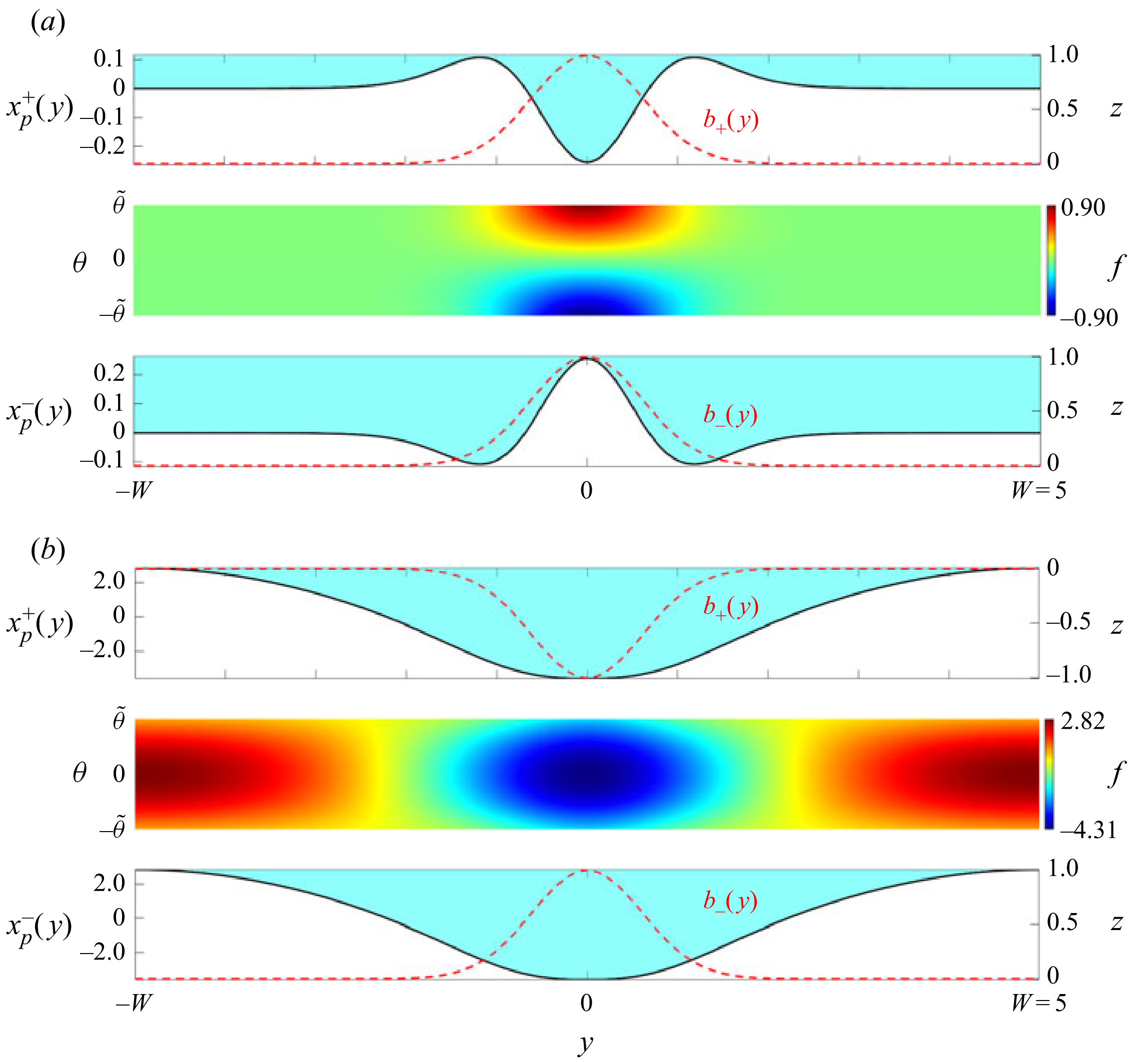

Figure 2. The displacement of the upper and lower contact lines due to the perturbation $x_p^{\pm}(y)$ (black solid lines, left axis) and change in meniscus shape $f(y,\theta)$ (heat map) due to Gaussian perturbations $b_{\pm}(y)$ proportional to $b(y) = \exp(-y^2/0.75)$ (red dashes, right axis), for a channel with half-width $W = 5$ and contact angle $\phi = 15^\circ$. As in figure 1, the liquid and vapour sides of the contact-line displacement are shown with blue and white shading, respectively, for (*a*) channel-volume-preserving perturbation ($b_- = b_+ = b$); and (*b*) channel-volume-changing perturbation ($b_- = -b_+ = b$). The heat maps denote the change in radius r due to the perturbations, with green denoting no change in the meniscus location. Positive values of f show the meniscus extending into the liquid phase.

or larger-amplitude perturbations eliciting a greater displacement. Linear and nonlinear predictions of the upper contact-line displacement $x_p^+(y)$ show good agreement for perturbations that are approximately 1 % of the channel depth (figure 3*a*,*b*). (Numerical evidence in figure 10 below suggests that the contact-line displacement increases like $\log(1/s)$ for finite contact angle as the perturbation width s becomes very small, when the linear model breaks down.) Larger perturbations, of approximately 10 % of channel depth, are shown in figure 3(*c*) for the volume-changing case. Here a greater discrepancy between linear and nonlinear predictions is evident, although the shape of the contact-line perturbations at the edges of the channel is accurately described by the linear model. A long-wave analysis for $s \ll W$ shows that the solution in the far-field has a quadratic dependence on y in the form $f_A(y,\theta) = C_1(\theta)\,(W - |y|)^2 + C_2(\theta)$. We substitute this ansatz into the Helmholtz equation (2.8) and solve the resulting coupled ODEs for $C_1(\theta)$ and $C_2(\theta)$ with modified 'far-field' boundary conditions. These are obtained by setting

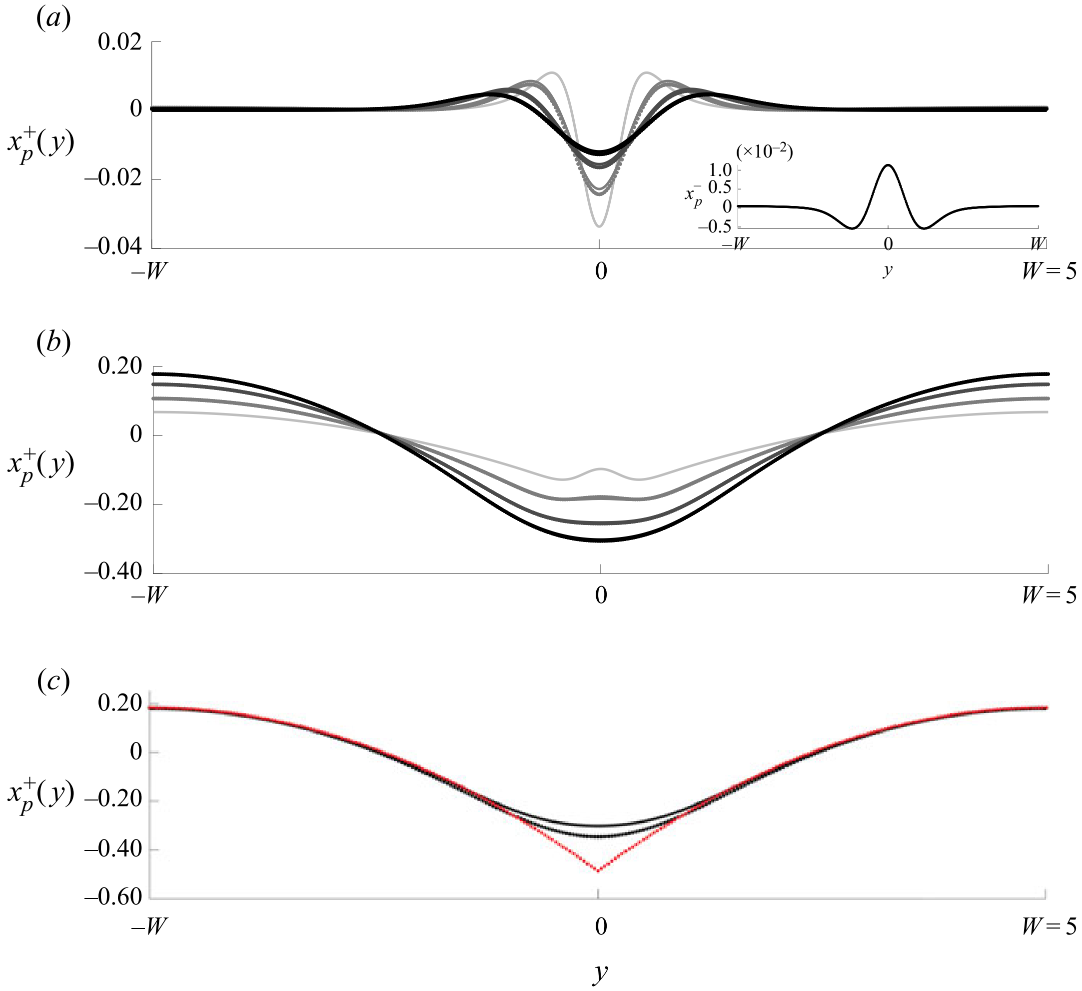

Figure 3. The displacement of the upper contact line in channels of half-width $W = 5$, for perturbations with amplitude $\epsilon = 0.01$ (*a*,*b*) and $\epsilon = 0.1$ (*c*), for channel-volume-preserving perturbations (*a*) and channel-volume-changing perturbations (*b*,*c*). The contact angle is $\phi = 85^\circ$. Panels (*a*,*b*) show wall perturbations of varying width, with darker colours indicating wider perturbations, with s^2 varying from 0.75 (black), through 0.5 and 0.25, to 0.1 (light grey); (*c*) shows $s^2 = 0.75$ only. Solid lines denote the displacement calculated via the linear solution, i.e. $x_p^+(y)$ from (2.13*a*,*b*), for all values of s; circles (thicker lines) denote the nonlinear displacement $(x_{cl} - x_0 - R\cos\tilde{\theta})/\epsilon$, where x_{cl} is the contact-line data computed in Surface Evolver for $s^2 \geqslant 0.25$. Inset: the nonlinear lower contact-line displacement for volume-preserving perturbations, for $s^2 = 0.75$. The red dots in (*c*) denote the quadratic linear far-field solution (4.1), with $C \approx 0.18$.

$b_\pm(y) = 0$ in (2.9) since the amplitude of Gaussian perturbations $b_\pm(y)$ is negligibly small for $y \sim W$ and $|y - y_c| \gg s$. Then substituting the solution for $f_A(y, \theta)$ in (2.13*a*,*b*) shows that the approximation to the displacement of the contact line far from the perturbations is given by

$$\hat{x}_p^+(y;\tilde{\theta}) \approx \left(\frac{p\sin(\tilde{\theta})}{\cos(\tilde{\theta})\sin(\tilde{\theta}) + \tilde{\theta}}\right)(W - |y|)^2 + C, \tag{4.1}$$

where the translational constant C cannot be found using the volume condition and instead is found empirically by comparison with the value of the full solution (3.3) at $y = \pm W$. This linear 'far-field solution', which is valid when $|y - y_c| \gg s$, is shown in figure 3(*c*) and gives an excellent fit to the nonlinear data.

Recalling from (3.1) that $p = O(W^{-1})$, the linear far-field solution (4.1) for volume-changing perturbations suggests that if the channel is sufficiently wide, so that

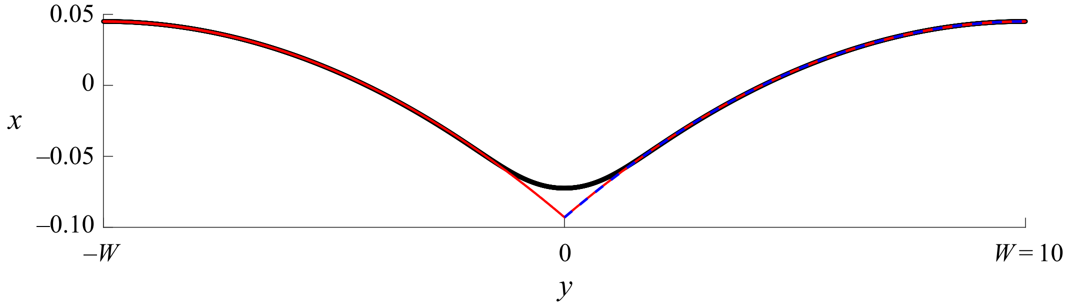

Figure 4. The nonlinear contact-line displacement for a channel of half-width $W = 10$, with contact angle $\phi = 45^\circ$ and perturbations to the channel wall of amplitude $\epsilon = 0.01$ and $s^2 = 1$. The thick black solid line denotes the nonlinear upper contact-line data computed in Surface Evolver, x_{cl}. The red line denotes the quadratic linear far-field solution (4.1), $x_0 + R\cos\tilde{\theta} + \epsilon\,\hat{x}_p^+(y)$, with $C \approx 0.18$. The blue dashes denote the arc of a circle of radius R_d, where R_d is determined as part of the solution to the boundary-value problem described in Appendix E with $\Delta p \approx -1.4167$ found from Surface Evolver.

$W \sim O(\epsilon^{-1})$, then the far-field contact-line displacement could become $O(1)$, violating the small displacement assumption of the linear model. We therefore need to revisit the far-field quadratic approximation (4.1), which should correspond to the arc of a circle having curvature equivalent to that of a large, flat ‘pancake’ catenoid confined between unperturbed plates having the same mean curvature, i.e. the same mean pressure difference Δp as the meniscus. The radius R_d of the circular arc that matches onto the contact line is found by computing a catenoid with the same pressure difference Δp, as evaluated in Appendix E. Figure 4 shows how the computed far-field shape of the contact line is captured well by both the linear far-field solution (4.1) and the circular arc computed from the catenoid solution.

In summary, the pressure change induced by the net volume changes of the wall perturbations generates curvature of the contact line away from the perturbations, whereas other geometric features of the perturbations influence contact-line shapes locally. We therefore expect that the same far-field behaviour should exist if the perturbations are not aligned, as we shall test in the next section.

4.2. *Non-aligned perturbations*

We now consider perturbations that are not aligned, i.e. $y_c^{\pm} \neq 0$. We consider specifically configurations of perturbations that are sufficiently far apart to be considered as isolated perturbations.

We compute the non-aligned solutions to the linear model using second-order-accurate central finite differences (Appendix D), with step sizes $\Delta y = 0.05$ in the y direction and $\Delta\theta = 0.03$ in the θ direction. Figure 5 shows solutions to the linear problem for perturbations that have been separated so that $b_{\pm}(y)$ are centred at $\pm y_c$. The separation of the channel-volume-preserving perturbations causes the contact line to bend away from the side wall; this deflection of the upper and lower contact lines occurs due to the presence of a perturbation on either the upper or lower wall. Isolated ridges and grooves cause the contact lines to move towards the liquid and vapour phases, respectively. In contrast, channel-volume-changing perturbations (figure 5*c*,*d*) induce non-local bending of the contact line in the far-field, which can again be described using arcs of circles.

We wish to understand the deflection mechanism so that we may choose perturbations to engineer specific contact-line shapes. In the channel-volume-preserving case (figure 5*a*,*b*), let α be the gradient of the contact-line displacement in the centre of the channel, between

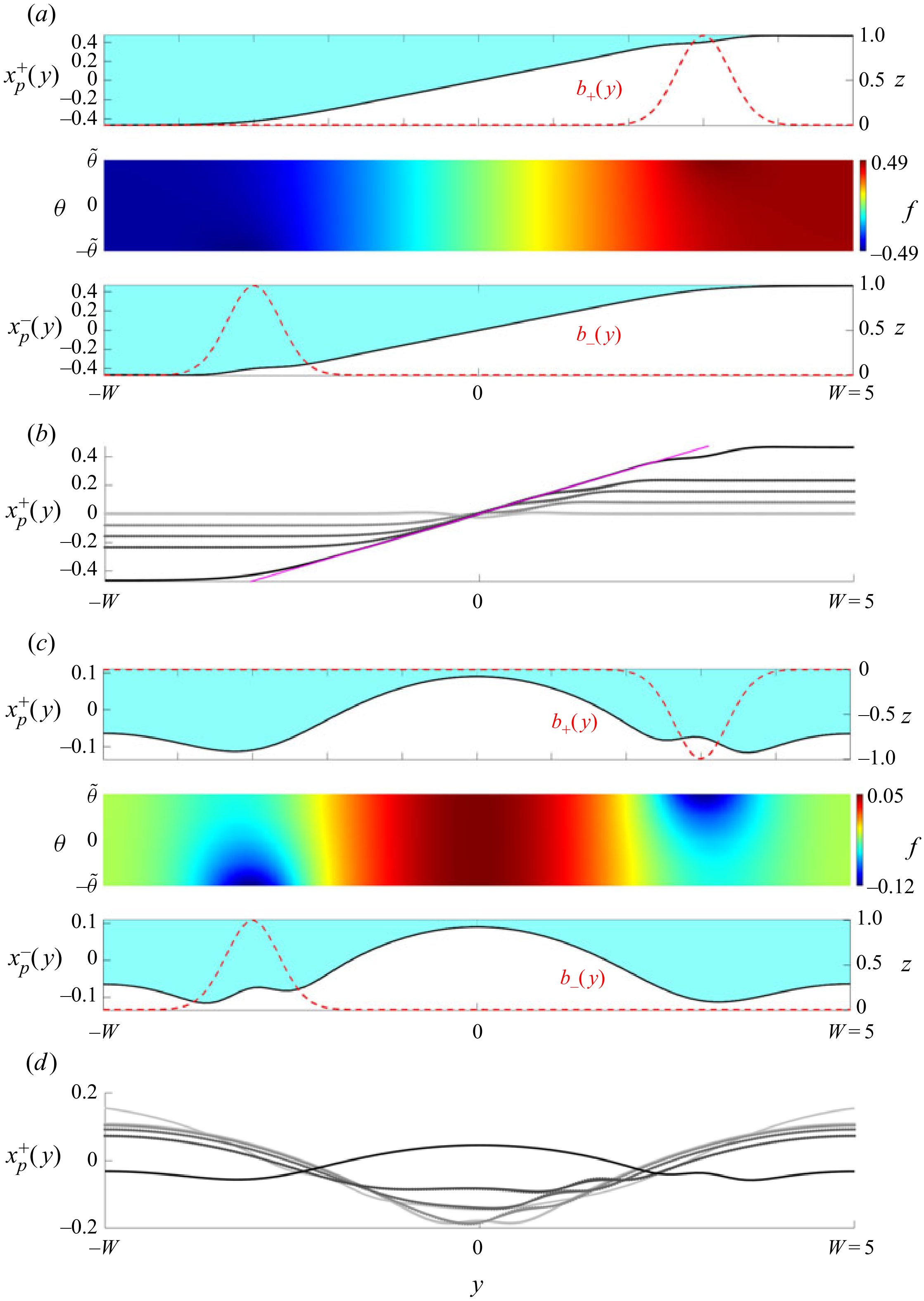

Figure 5. The linear solution $f(y, \theta)$ and upper contact-line displacement for channel-volume-preserving (*a*,*b*) and channel-volume-changing (*c*,*d*) perturbations, for channel half-width $W = 5$ and contact angle $\phi = 85^\circ$. The upper and lower wall perturbations are given by $B_\pm(y) = 0.01 \exp((y - y_c^\pm)^2/0.25)$. In (*a*,*c*) $y_c^\pm = \pm 3$, while (*b*,*d*) show contact-line displacement x_p^+ for separations varying from $y_c^\pm = \pm 3$ (black) through $\pm(1.5, 1, 0.5)$ to $y_c^\pm = 0$ (light grey). Solid lines denote the displacement calculated via the linear solution $x_p^+(y)$ from (2.13*a*,*b*); circles (thicker lines) denote the nonlinear displacement $(x_{cl} - x_0 - R\cos\tilde{\theta})/\epsilon$, where x_{cl} is the upper contact-line data computed in Surface Evolver. The pink line in (b) is the line $x = \alpha y$, where the slope α is given in (4.2).

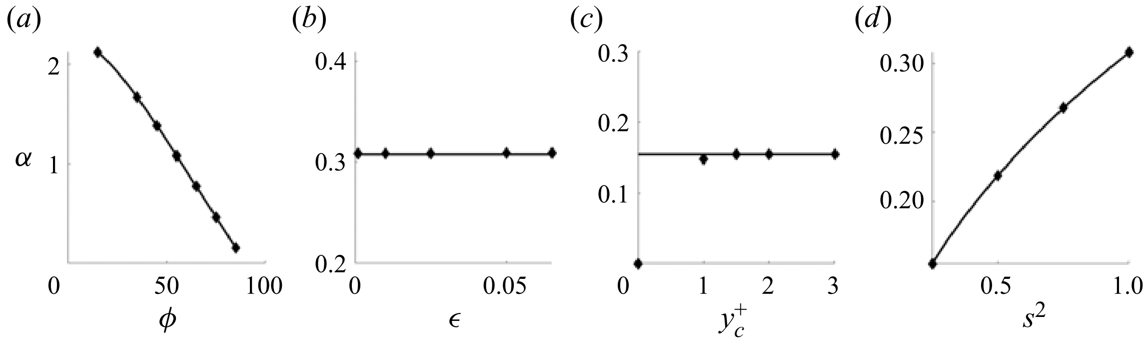

Figure 6. The slopes α of the upper contact-line displacement $x_p^+(y)$ in the centre of the channel for channel-volume-preserving perturbations. (*a*) Varying contact angle $15^\circ \le \phi \le 85^\circ$ with separation $y_c^+ = 3$, perturbation width $s = 0.5$, and perturbation amplitude $\epsilon = 0.01$. (*b*) Varying amplitude $0.001 \le \epsilon \le 0.065$ with $y_c^+ = 3$, $s = 1$ and $\phi = 85$. (*c*) Varying separation $0 \le y_c^\pm \le 3$ with $s = 0.5$, $\epsilon = 0.01$ and $\phi = 85$. (*d*) Varying square perturbation width $0.25 \le s^2 \le 1$ with $y_c^+ = 3$, $\phi = 85$ and $\epsilon = 0.01$. The solid lines denote the values of α calculated using (4.2). The diamonds denote the numerical values of α calculated empirically from the contact-line data.

the perturbations. For perturbations of sufficiently small amplitude, α is approximately equal to the angle of deflection, i.e. the angle that the contact line makes with the horizontal. We can obtain an approximation for α by considering the solution in the neighbourhood of an isolated ridge or groove: consider the Helmholtz equation (2.8), with zero pressure difference p (to obtain contact-line solutions with uniform gradient). Then the problem for a single isolated ridge or groove perturbation $b_+(y)$ on the upper wall, centred at some $y = y_c$, will admit a solution of the Helmholtz equation with $f(y, \theta) = 0$ for $y_c - y \gg s$ and $f(y, \theta) \approx \alpha(y - y_c)\cos\theta$ for $y - y_c \gg s$. Exploiting the self-adjointness of the Helmholtz operator and boundary conditions using the method given in Appendix B with a test function $g(\theta) = \cos\theta$, we obtain

$$\alpha \approx \frac{1}{R^2}\frac{1}{\cos\tilde{\theta}\,\sin\tilde{\theta} + \tilde{\theta}}\int_{-\infty}^{\infty} b_+(y)\,\mathrm{d}y, \tag{4.2}$$

where the integral is taken over the full width of the isolated perturbation b_+. Thus we anticipate that for Gaussian perturbations, the parameters that most affect the deflection will be the volume of the perturbation and the contact angle. While the linear theory allows for an $O(\epsilon)$ contact-line displacement in the x direction, the displacement $\epsilon\alpha y$ of the deflected solution can in principle become $O(1)$ in a sufficiently wide channel (if $y - y_c = O(\epsilon^{-1})$); thus the solution can in principle be matched to a straight meniscus for which the x displacement is larger. Figure 6 shows the values of α found empirically, together with the theoretical prediction (4.2), for varying perturbation separation, width, amplitude and contact angle. There is excellent agreement with the theoretical predictions except for small y_c^+, i.e. as long as the perturbations are not too close together; this is expected because it violates the assumption that the perturbations can be treated as isolated ridges and grooves.

4.3. *Weakly corrugated channels*

Based on the discussion above, we now consider the linear model for channels with a series of small-amplitude ridges and grooves on the upper wall to form weakly corrugated

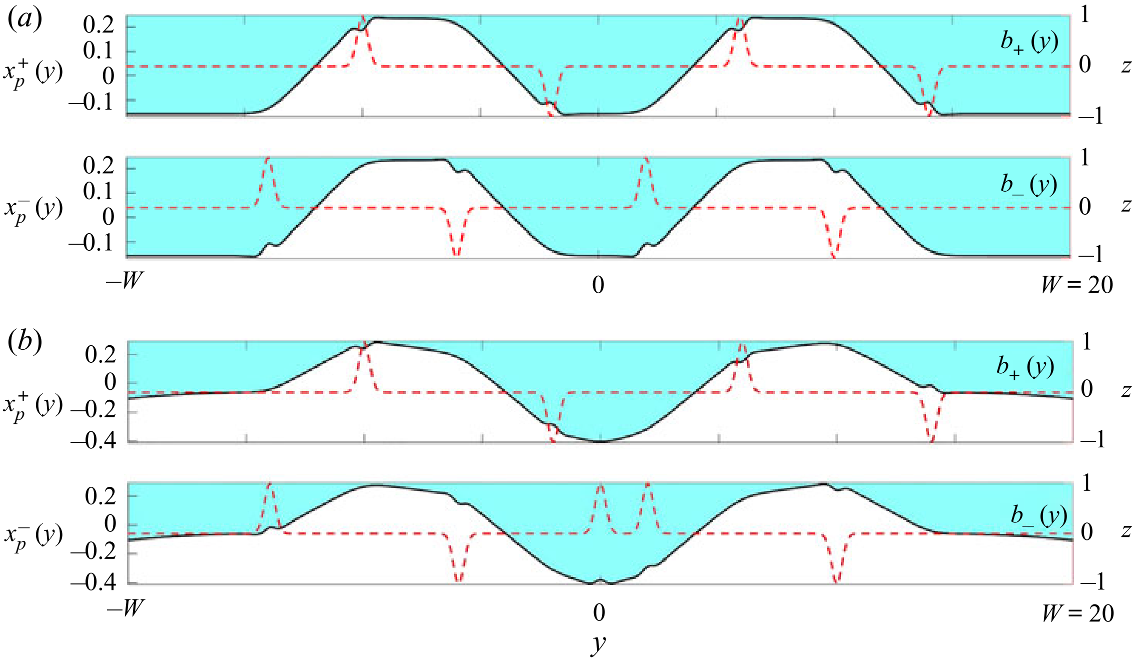

Figure 7. The upper and lower contact lines (left axis, solid black line), together with the perturbations (right axis, dashed red line) for (*a*) a channel-volume-preserving configuration and (*b*) a channel-volume-changing configuration in a channel of half-width $W = 20$. The perturbations are defined by (4.3), with ridges on the lower wall at $y = -14, 2$, grooves on the lower wall at $y = -6, 10$, ridges on the upper wall at $y = -2, 14$ and grooves on the upper wall at $y = -10, 6$. The perturbation in (*b*) has an extra ridge on the lower wall at $y = 0$ to make it channel-volume changing. All perturbations have width $s^2 = 0.1$ and the contact angle is $\phi = 85°$.

channel walls. Thus we consider perturbations of the form

$$b_\pm(y) = \sum_{k=0}^{K} a_k^\pm \exp(-(y - y_{c_k}^\pm)^2/s^2), \tag{4.3}$$

where $y_{c_k}^\pm$ are the locations of the ridges and grooves on the upper and lower walls, and $a_k^\pm = \pm 1$ depending on whether ridges or grooves are chosen. We assume that the ridges and grooves are spaced sufficiently so that we can treat each perturbation as a single isolated ridge or groove that causes deflection of the contact line in the way described above, so that we can predict the deflection angle due to each ridge and groove using (4.2). Figure 7 shows the upper and lower contact-line displacements $x_p^\pm(y)$ for a weakly corrugated channel with alternating ridges and grooves on each wall so that the contact lines take the shape of a letter 'M'. The contact-line displacement for the channel-volume-preserving configuration is shown in figure 7(*a*); this solution describes a meniscus with zero induced mean curvature, thus the contact-line displacement is flat in the far-field and has sections of varying slope. Because each perturbation can be treated in isolation, the gradient of each slope is described by (4.2). Again, ridges push the contact line towards the liquid phase, and grooves allow the contact line to move towards the vapour phase. The contact-line slope varies smoothly, and again the shape of the contact line is affected by an obstacle on either wall so that it takes, for example, a ridge/groove on the lower wall followed by a ridge/groove on the upper wall to reverse the gradient of the contact line.

In figure 7(*b*), we consider the same series of grooves and ridges and then add an extra ridge on the lower wall at $y = 0$ so that the configuration is now channel-volume-changing. Qualitatively, the shape is unchanged but the change in mean curvature is now non-zero.

Thus the 'sections' of contact line between each ridge and groove are now locally parabolic; each parabola is a local approximation to the arc of a circle that forms the contact line of a catenoid with the same mean curvature as the static meniscus.

There are, of course, a plethora of possible smoothly-varying contact-line shapes that can be made using channel-volume-changing/preserving configurations, for small-amplitude perturbations (up to approximately 10 % of the channel height). It is possible to specify these shapes *a priori* using just the boundary data, using either (4.2) for the required gradients in the channel-volume-preserving case, or (3.1) to deduce the pressure of the catenoid with circular contact line that matches onto the parabolas in the channel-volume-changing case, together with the known direction in which the contact line will move for either ridges or grooves.

5. Discussion

In this study, we have quantified the displacement of the contact line of a static meniscus in a rectangular channel arising from the presence of isolated ridges and grooves imposed on the channel walls. We have shown that small-amplitude perturbations that change the channel volume induce a change in the mean curvature of the meniscus, inducing long-range curvature of the contact line, via (3.1). For very wide channels, this curvature matches onto the arc of a catenoid whose radius is found by matching the pressure differences. Meanwhile, small-amplitude isolated non-aligned perturbations that do not change the channel volume generate a contact-line shape that is approximately piecewise linear. We derived an approximation to the deflection angle between adjacent linear segments (4.2), showing a dependence on the volume of the groove or ridge. This makes it possible in principle to engineer contact-line shapes by choosing the location and order of the ridges and grooves.

We validated predictions of the linearised model against fully nonlinear solutions obtained using Surface Evolver. However it remains unclear at present how the closed-form results (3.1) and (4.2), derived using the self-adjointness of the Helmholtz equation, might be extended to the nonlinear regime. While these predictions of the induced pressure and deflection angle show dependence on the volume of ridges or grooves, they mask more subtle dependence on the precise shape of the perturbations. For example, when there is no induced pressure change, the contact-line displacement near a ridge or groove mirrors approximately the curvature of the wall shape (figure 2*a*), which is a bounded function for the Gaussian wall perturbations chosen here. Sharper perturbations, having derivatives varying on very short length scales, can be expected to lead to dramatically different outcomes, as outlined in Appendix F. We avoided these extreme cases here by ensuring that $b_{\pm}(y)$ is analytic and not too narrow.

A natural extension of this study is to consider perturbations with curvature in two directions (such as isolated bumps). These too can be expected to generate long-range deflections of the contact line. However, nonlinear effects (associated with large amplitudes or sharp asperities) will likely need to be taken into account in order to capture effects such as contact-line hysteresis, arising as the contact line is moved slowly backwards and forwards over the bump. Similarly, the approach taken here could equally be extended to consider the sensitivity of the meniscus to changes in the contact angle arising from coating portions of the channel wall with suitable chemicals. In practice, however, a continuous gradient of contact angle may be much more difficult to achieve experimentally than smoothly-varying perturbations, which may appear naturally in an industrial or biological setting. The present study considered perturbing a 'straight' meniscus with zero Gaussian curvature; a further generalisation that merits investigation is to consider a curved base state, to accommodate contact angles at lateral walls that deviate from $\pi/2$.

The solution structures identified here will support future studies of gas/liquid interfaces moving at low capillary numbers through domains having isolated geometric features, be these engineered in order to achieve a specific outcome or naturally occurring roughness. We have shown that even when these features are smooth, isolated and of small amplitude, significant long-range deflections of the meniscus are possible.

Declaration of interests. The authors report no conflict of interest.

Author ORCIDs.
Eleanor C. Johnstone https://orcid.org/0000-0002-2166-5859;
Andrew L. Hazel https://orcid.org/0000-0003-1130-0554;
Oliver E. Jensen https://orcid.org/0000-0003-0172-6578.

Appendix A. Linearised problem for zero contact angle

When $\phi = 0$, the linearised boundary condition (2.10) vanishes, requiring expansion up to $O(\epsilon^2)$. We write the interface location as

$$r = R + \epsilon f_1(y, \theta) + \epsilon^2 f_2(y, \theta) + O(\epsilon^3), \tag{A1}$$
$$\theta \in \left[-\tilde{\theta} + \epsilon\, \Theta_{1-}(y) + \epsilon^2\, \Theta_{2-}(y),\ \tilde{\theta} + \epsilon\, \Theta_{1+}(y) + \epsilon^2\, \Theta_{2+}(y)\right],$$

where $R = \frac{1}{2}$. The pressure difference Δp is assumed to be $\Delta p = -R^{-1} + \epsilon p_1 + \epsilon^2 p_2 + \cdots$. After linearising the Young–Laplace equation (2.3), the $O(\epsilon)$ expression gives the equation for f_1 as

$$\frac{1}{R^2} f_1 + \frac{1}{R^2} f_{1\theta\theta} + f_{1yy} = p_1. \tag{A2}$$

Similarly, the $O(\epsilon)$ terms in the linearisation of boundary conditions (2.4) and (2.6) give the boundary conditions on f_1 as

$$f_1\left(y, \pm\frac{\pi}{2}\right) = b_\pm(y), \quad f_{1y}(\pm W, \theta) = 0. \tag{A3a,b}$$

The equation relating the change in meniscus shape $f(y, \theta)$, to the contact-line location $\Theta_{1\pm}(y)$, can be found at $O(\epsilon^2)$:

$$f_{1\theta}\left(y, \pm\frac{\pi}{2}\right) = R\, \Theta_{1\pm}(y). \tag{A4}$$

Therefore we recover exactly the conditions (2.9) and (2.10) with $\phi = 0$. The volume constraint (2.12) and independent pressure condition (3.1) remain the same.

Appendix B. The pressure in the linear problem

For the linearised problem, we can derive an independent equation for the pressure by using the fact that the Helmholtz operator is self-adjoint. Consider the linear problem

(2.8)–(2.12) and a smooth, twice-differentiable test function $g(\theta) : [-\tilde{\theta}, \tilde{\theta}] \to \mathbb{R}$, such that

$$R^{-2}[g'' + g] = a \in \mathbb{R}, \quad g(\pm\tilde{\theta}) = \gamma_{\pm}, g'(\pm\tilde{\theta}) = \zeta_{\pm}. \tag{B1a–c}$$

We multiply the Helmholtz equation (2.8) by g, and then integrate over the domain $D = [-\tilde{\theta}, \tilde{\theta}] \times [-W, W]$. Then, defining $\tilde{\nabla} = (\partial_y, R^{-1}\partial_\theta)$, we obtain

$$\int_D af + \tilde{\nabla} \cdot (g\tilde{\nabla}f - f\tilde{\nabla}g)\, \mathrm{d}A = \int_D gp\, \mathrm{d}A. \tag{B2}$$

Rewriting the divergence terms on the left-hand side as integrals over closed curves, we then integrate and apply the boundary conditions at the side walls, (2.11), and the boundary conditions on g to give

$$\int_D af\, \mathrm{d}A + R^{-2}\int_{-W}^{W} [-\gamma_- f_\theta(y, -\tilde{\theta}) + \zeta_- f(y, -\tilde{\theta}) + \gamma_+ f_\theta(y, \tilde{\theta}) - \zeta_+ f(y, \tilde{\theta})]\, \mathrm{d}y$$
$$= \int_D gp\, \mathrm{d}A. \tag{B3}$$

We now pick a test function $g(\theta) = \cos\theta$ (so that $a = 0$) and apply the boundary conditions (2.9) on f, which leads to an independent equation for the pressure:

$$p = \frac{1}{4WR^2 \sin(\tilde{\theta})} \int_{-W}^{W} [b_+(y) - b_-(y)]\, \mathrm{d}y. \tag{B4}$$

We also use this method to derive an approximation to the deflection angle α as given in (4.2). To derive this relationship, we again use a test function $g(\theta) = \cos\theta$, but we take 'far-field' boundary conditions across an isolated wall perturbation of $f_y \to 0$ for $(y - y_c)/s \to -\infty$, and $f_y \to \alpha\cos\theta$ for $(y - y_c)/s \to \infty$.

Appendix C. Solving the nonlinear problem with Surface Evolver

We implement the nonlinear problem using Surface Evolver (Brakke 1992), which uses a gradient-descent method to iterate towards a surface of minimum energy. The energy of the triangulated surface is defined as a scalar function of all the vertex coordinates. The iterative process forces the vertices into a configuration that is closer to an energy minimum, subject to any global constraints on the surface or local constraints on the vertices. For the problem outlined in § 2, the only force acting on the liquid–vapour interface is surface tension, thus we minimise the surface energy of the meniscus. The constraints are the boundary conditions (2.4)–(2.6) together with the volume constraint.

The boundary conditions on the upper and lower channel walls, (2.5) and (2.6), are implemented by fixing the energy of the channel walls. We define the (non-dimensional) surface tension due to the presence of the solid wall as $\gamma_S = \gamma_{SL}/\gamma_{LV} - \gamma_{SV}/\gamma_{LV}$, where γ_{SL} and γ_{SV} are solid–liquid and solid–vapour surface tensions. Then if α_w is the contact angle at the solid–liquid and liquid–vapour interface, by Young's equation, $\gamma_S = -\cos\alpha_w$, and the wall energy is

$$E_{wall} = \iint_{wall} -\cos\alpha_w\, \mathrm{d}S. \tag{C1}$$

Thus to specify the boundary conditions (2.5) and (2.6), we fix the wall energies by imposing contact angles $\alpha_w = \phi$ on the upper and lower walls at $z = \pm 1/2 + B_\pm(y)$, and $\alpha_w = \pi/2$ on the side walls at $y = \pm W$ (so that the energy of the side walls is zero).

In practice, for computational efficiency, only the liquid–vapour interface is triangulated and refined. Then the wall energy integral (C1) for the upper and lower walls is rewritten as a line integral using Stokes' theorem: if $\boldsymbol{w} = (w_x, w_y, w_z)$ is such that $(\nabla \times \boldsymbol{w}) \cdot \boldsymbol{v}_\pm = -\cos(\phi)$ (where again $\boldsymbol{v}_\pm$ is the unit outward normal to the upper and lower channel walls), then defining ∂_{wall} as the boundary of the wall, the wall energy is

$$E_{wall} = \oint_{\partial_{wall}} \boldsymbol{w} \cdot \mathrm{d}\boldsymbol{r}. \tag{C2}$$

For the upper and lower walls described by $z = \pm 1/2 + B_\pm(y)$, we can choose, for example, $w_x = w_z = 0$ and $w_y = -x \cos\phi \sqrt{1 + B_\pm(y)^2}$. The integral around the closed curve is implemented internally by Surface Evolver along the edges specified by the user, with their orientation defined such that the unit normal is outward-pointing.

Boundary condition (2.4) is imposed by constraining the contact-line vertices to lie on the upper wall of the channel. This is a local condition on each vertex.

The fixed volume of liquid V_L is handled in Surface Evolver as a global constraint on the possible energy configurations that the surface can take; that is, it removes one degree of freedom from the problem.

The mesh refinement is handled by Surface Evolver using a basic subdivision; we also equiangulate the mesh after each iteration. We converge to an energy minimum using the following process.

(i) Iterate on a fixed mesh until the solution is accurate to a specified tolerance.
(ii) Refine the mesh and check the difference between the energy on the new mesh and the old mesh. While the difference is greater than a specified tolerance, repeat step (i).

We use a tolerance of 10^{-6} for the accuracy of the solution on each mesh and the energy difference between meshes. We ensure that a global minimum has been reached by using a second-order gradient-descent method to check for positive eigenvalues near the equilibrium.

Appendix D. Numerical solution of the linear problem

We solve the linear problem (2.8)–(2.12) with Gaussian boundary data $b_\pm(y) = \pm\exp(-(y - y_c^\pm)^2/s^2)$ in a rectangular domain $-W \leq y \leq W$, $-\tilde{\theta} \leq \theta \leq \tilde{\theta}$. For general $y_c^\pm$, we integrate the Helmholtz equation (2.8) using second-order-accurate central finite differences with step lengths Δy and $\Delta\theta$ in the y and θ directions, respectively. We denote the value of the solution f at $y = k\Delta y$, $\theta = j\Delta k$ by f_k^j for $0 \leq k \leq M + 1$, $0 \leq j \leq N + 1$, so that $y = W$ is approximated by $(M + 1)\,\Delta y$ and $\theta = \tilde{\theta}$ is approximated by $(N + 1)\,\Delta\theta$. We discretise the Helmholtz equation (2.8) on the interior of the grid as

$$\frac{1}{\Delta y^2} f_{k+1}^j + \frac{1}{\Delta y^2} f_{k-1}^j + \frac{1}{\Delta\theta^2 R^2} f_k^{j+1} + \frac{1}{\Delta\theta^2 R^2} f_k^{j-1} + \left(\frac{1}{R^2} - \frac{2}{\Delta\theta^2 R^2} - \frac{2}{\Delta y^2}\right) f_k^j = p,$$
$$(1 \leq k \leq M,\ 1 \leq j \leq N). \tag{D1}$$

We use the boundary conditions (2.9) and (2.10) to show that

$$2\Delta\theta \sin(\theta_{N+1}) f_k^{N+1} - 2\Delta\theta\, b_+(y_k) + (3f_k^{N+1} - 4f_k^N + f_k^{N-1}) \cos(\theta_{N+1}) = 0, \tag{D2}$$

$$2\Delta\theta \sin(\theta_0) f_k^0 + 2\Delta\theta\, b_-(y_k) + (3f_k^0 - 4f_k^1 + f_k^2) \cos(\theta_0) = 0; \tag{D3}$$

meanwhile, the Neumann boundary conditions (2.11) give

$$-3f_0^j + 4f_1^j - f_2^j = 0, \quad 3f_{M+1}^j - 4f_M^j + f_{M-1}^j = 0 \quad \text{for } 1 \leq j \leq N. \tag{D4a,b}$$

We then obtain a system of $(N+1)(M+1)$ equations that we solve subject to the volume constraint (2.12), which we discretise using Simpson's rule.

The discretised system is solved using a direct solver that takes advantage of the sparsity in the matrix structure. The grid size is chosen so that the solution to the discretised finite difference system at each grid point is accurate to three decimal places compared to the truncated analytical series solution, which is known at each grid point to high accuracy (truncated terms had size $O(10^{-16})$, see § 3.3).

Appendix E. The catenoid problem: governing equations and solution

Consider a catenoid with solid–liquid contact angle $0 \leq \phi < \pi/2$ in a rectangular channel. Note that we use the term 'catenoid' here to describe the general shape of the interface as an 'inverted droplet'; however, it need not be a surface of zero mean curvature. The catenoid interface is described by arc-angle coordinates $(r(t), z(t), \theta(t))$ for $-t_0 \leq t \leq t_0$ and is axisymmetric with respect to the azimuthal angle φ in cylindrical polar coordinates (r, φ, z). We take $t = 0$ to be at $z = 0$ as shown in figure 8 so that $(r(0), z(0), \theta(0)) = (r_0, 0, \pi/2)$. Meanwhile, the channel walls are at $t = \pm t_0$ so that $(r(t_0), z(t_0), \theta(t_0)) = (R_d, 1/2, \phi)$ and $(r(-t_0), z(-t_0), \theta(-t_0)) = (R_d, -1/2, \pi - \phi)$. The catenoid is symmetric about $z = 0$, therefore without loss of generality we can consider the interface from $0 \leq t \leq t_0$. Then r and z depend implicitly on t as

$$\frac{\mathrm{d}r}{\mathrm{d}t} = \cos\theta, \quad \frac{\mathrm{d}z}{\mathrm{d}t} = \sin\theta, \quad 0 \leq t \leq t_0, \tag{E1a,b}$$

$$r(0) = r_0, \ r(t_0) = R_d, \quad z(0) = 0, \ z(t_0) = \tfrac{1}{2}. \tag{E2a–d}$$

The unit normal to the interface pointing into the vapour phase at $\varphi = $ const. is given by $\hat{\boldsymbol{n}} = \sin\theta\,\hat{\boldsymbol{r}} - \cos\theta\,\hat{\boldsymbol{z}}$. Thus the Young–Laplace equation is

$$\Delta p = \boldsymbol{\nabla}\boldsymbol{\cdot}\hat{\boldsymbol{n}} = \cos\theta\,\frac{\partial\theta}{\partial r} + \frac{\sin\theta}{r} + \sin\theta\,\frac{\partial\theta}{\partial z} = \frac{\mathrm{d}\theta}{\mathrm{d}t} + \frac{\sin\theta}{r}, \tag{E3}$$

so that the final equation in the system is

$$\frac{\mathrm{d}\theta}{\mathrm{d}t} = \Delta p - \frac{\sin\theta}{r}, \quad 0 \leq t \leq t_0, \tag{E4}$$

$$\theta(0) = \frac{\pi}{2}, \quad \theta(t_0) = \phi. \tag{E5a,b}$$

The ODEs (E1) and (E4), together with the boundary conditions, form a boundary-value problem for the arc-angle components r, z, θ.

A large-radius asymptotic solution ($r_0 \gg 1$) to this system can be found by writing

$$r(t) = r_0 + r_1(t) + \frac{r_2(t)}{r_0} + \cdots, \quad \theta(t) = \theta_0(t) + \frac{\theta_1(t)}{r_0} + \cdots, \tag{E6a,b}$$

$$z(t) = z_0(t) + \frac{z_1(t)}{r_0} + \cdots, \quad \Delta p = (\Delta p)_0 + \frac{(\Delta p)_1}{r_0} + \cdots, \tag{E7a,b}$$

$$t_0 = L_0 + \frac{1}{r_0}L_1 + \cdots. \tag{E8}$$

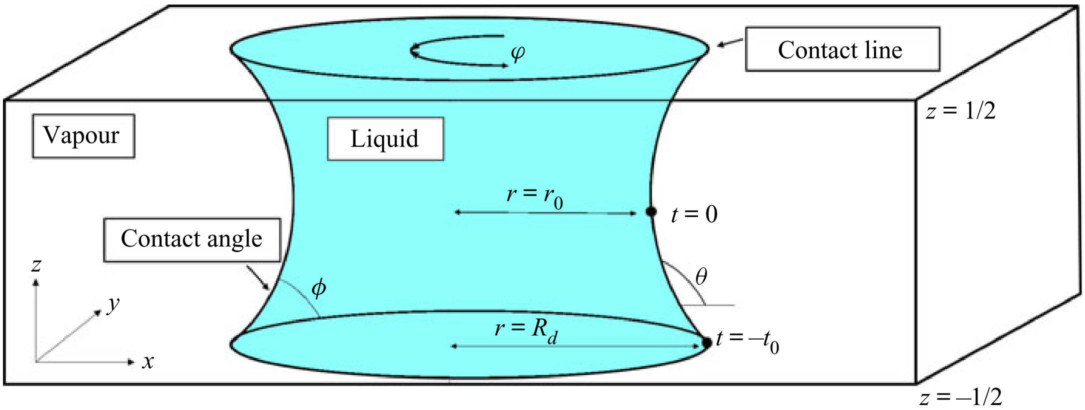

Figure 8. A catenoid in a rectangular channel with height $-\frac{1}{2} \leq z \leq \frac{1}{2}$ and solid–liquid contact angle ϕ.

Solving the leading-order problem, we find from the leading-order approximation ($\theta_0 = (\Delta p)_0 t + \pi/2$, $z_0 = (\sin((\Delta p)_0 t))/(\Delta p)_0$) that the pressure difference across the catenoid is

$$(\Delta p)_0 = -2\cos\phi, \tag{E9}$$

which is consistent with the pressure difference of the unperturbed static liquid–vapour meniscus in the rectangular channel, while the leading-order approximation to the catenoid radius and the endpoint of the curve t_0 is

$$r_1(t) = \frac{\cos((\Delta p)_0 t)}{(\Delta p)_0} - \frac{1}{(\Delta p)_0}, \quad L_0 = \frac{2\phi - \pi}{2}. \tag{E10a,b}$$

Solving the $O(r_0^{-1})$ problem, we find that

$$(\Delta p)_1 = \frac{\sin\tilde{\theta}\cos\tilde{\theta} + \tilde{\theta}}{2\sin\tilde{\theta}}. \tag{E11}$$

Thus, eliminating r_0 from truncated expansions for $r(t_0)$ and Δp, the expression

$$R_d \approx \frac{(\Delta p)_1}{\Delta p - (\Delta p)_0} + r_1(L_0) \tag{E12}$$

gives the large-radius approximation for the catenoid for any given Δp.

We can also solve for catenoids with smaller radii numerically. First, we eliminate t to obtain a nonlinear boundary-value problem where the unknown radius R_d is to be determined as part of the solution for given Δp and ϕ:

$$\frac{\mathrm{d}\theta}{\mathrm{d}z} = \frac{\Delta p}{\sin\theta} - \frac{1}{r}, \quad \frac{\mathrm{d}r}{\mathrm{d}z} = \frac{\cos\theta}{\sin\theta}, \tag{E13a,b}$$

$$r\left(\tfrac{1}{2}\right) = R_d, \quad \theta(0) = \frac{\pi}{2}, \quad \theta\left(\tfrac{1}{2}\right) = \phi. \tag{E13c–e}$$

We solve this problem numerically using the MATLAB routine ‘bvp4c’ (Kierzenka & Shampine 2001), thus for any static meniscus with a given pressure difference (mean curvature) and contact angle, we can find the radius R_d of the circular contact line of the catenoid that has the same pressure difference (mean curvature). The relationship between pressure difference and catenoid radius is shown in figure 9. It matches closely the asymptote (E12) for $R_d \gg 1$.

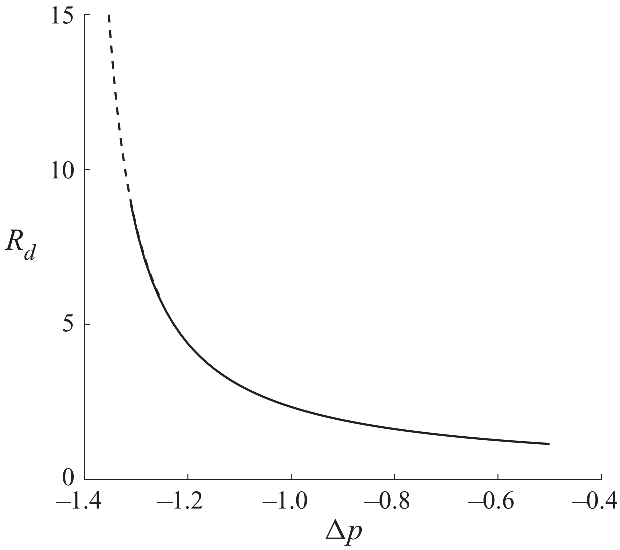

Figure 9. The maximum radius R_d of a catenoid for varying pressure difference Δp, for a contact angle $\phi = 45^\circ$. The solid line denotes the numerical solution for R_d. The dashed line denotes the asymptotic solution (E12). The location of the asymptote is at $\Delta p = -2\cos(\pi/4) \approx -1.414$.

The large-radius catenoid solution describes the curved meniscus shape (4.1) far from the wall perturbation, as we now demonstrate. The circular contact line is described locally by a parabola. To see this, take a catenoid with a contact line of radius R_d centred on $x = x_0$, $y = W$. Its contact line lies along $(x - x_0)^2 + (y - W)^2 = R_d^2$. Because the solution is translationally invariant, x_0 may be chosen such that the catenoid passes through $x = 0$, $y = y_c$. When $W \ll R_d$ and the centre of the catenoid lies in $x > 0$, we may describe the base of the contact line using

$$x = x_0 - \sqrt{R_d^2 - (W - y)^2} \tag{E14a}$$

$$\approx x_0 - R_d\left(1 - \frac{(W-y)^2}{2R_d^2} + \cdots\right) \approx C_0 + \frac{1}{2R_d}(W - y)^2, \tag{E14b}$$

with C_0 a constant. Therefore the contact-line displacement can be matched to (4.1) by choosing

$$\epsilon p = \frac{\cos\tilde{\theta}\sin\tilde{\theta} + \tilde{\theta}}{2R_d \sin\tilde{\theta}} = \frac{(\Delta p)_1}{R_d}, \tag{E15}$$

and therefore approximates the contact line in $y_c < y \leq W$ when $|y - y_c| \gg s$. This pressure–radius relationship is consistent with the leading-order relationship found via the asymptotic expansion (E11), with $r_0 \approx R_d$.

We can then assess the limit $W \sim \epsilon^{-1}$, for which the linearisation approximation of § 2.1 formally breaks down. Recall that the contact-line displacement $\epsilon x_p^{\pm}$ is $O(\epsilon p W^2)$ with $p = O(1/W)$ (from (3.1)), so that the contact-line displacement is $O(1)$, and $p = O(\epsilon)$ for $W \sim \epsilon^{-1}$. However, the contact line retains a radius of curvature that is large compared to W ($R_d = O(1/\epsilon^2)$, from (E12) with $\Delta p - (\Delta p)_0 = \epsilon p$), allowing the parabolic approximation (E14) to be used. Thus the parabolic description (4.1) remains appropriate in this limit (figure 4), because of the structure of the catenoid solution. In contrast, larger-amplitude wall perturbations will cause R_d to fall towards the size of W, pushing the contact line towards a more circular shape away from perturbations.

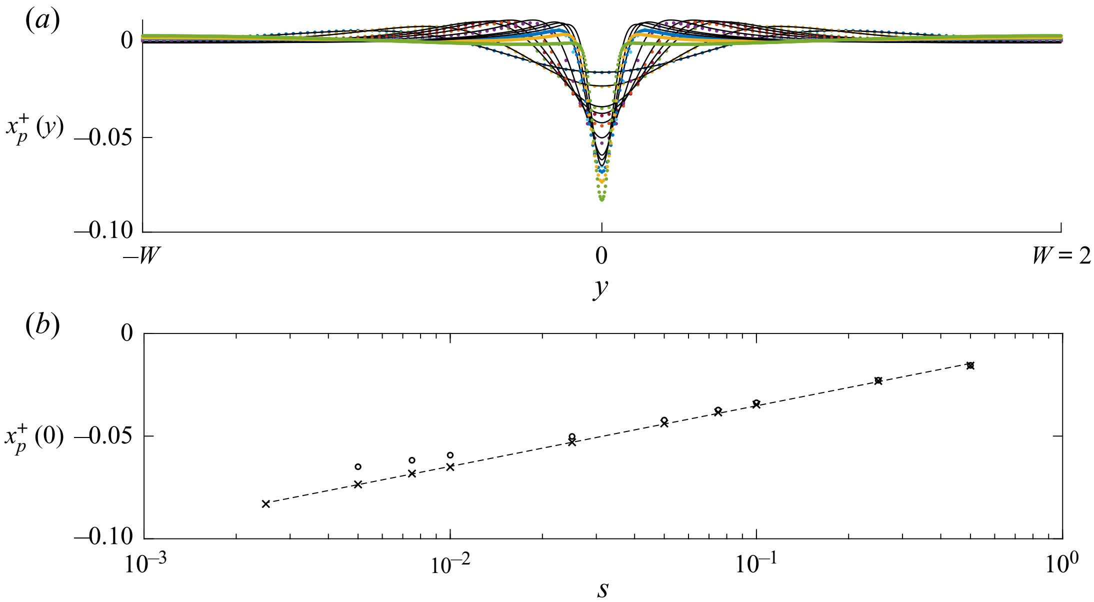

Figure 10. (a) The upper contact-line displacement $\hat{x}_p^+(y)$ for a channel-volume-preserving Gaussian perturbation $B_\pm(y) = 0.01\exp(-y^2/s^2)$, with s^2 taking values 0.0025, 0.005, 0.0075, 0.01, 0.025, 0.05, 0.075, 0.1, 0.25 and 0.5. The black lines denote the linear solution, computed using the series solution (3.3), while the coloured dots denote the Surface Evolver solution. The contact angle is $\phi = 85^\circ$, and the channel half-width is $W = 2$. (b) The upper contact-line displacement at $y = 0$, $\hat{x}_p^+(0)$, with a logarithmic scale on the x axis (values of s). The crosses denote the values of $\hat{x}_p^+(0)$ computed using the Surface Evolver solution; the circles are the corresponding values for the linear solution. The dashed line is $x_p^+(0) = 0.0128\log s - 0.0057$.

Appendix F. Sharp ridges and grooves

It is well known that a sharp wedge or groove can drive large contact-line displacements (Concus & Finn 1969), and so far we have restricted attention to Gaussian perturbations (3.2) having width s no smaller than $O(\epsilon^{1/2})$, where ϵ is the wall-perturbation amplitude.

We now examine empirically what happens to the contact-line solution for the Gaussian perturbations $b_\pm(y) = \exp(-y^2/s^2)$ with $s \to 0$. Figure 10(a) shows the upper contact-line solutions for a channel-volume-preserving perturbation with decreasing s^2, with the narrowest computed perturbation having $s^2 = 0.0025$ in a channel of half-width $W = 2$. Linear solutions computed using the series solution (3.3) are compared to Surface Evolver solutions, which are converged to an accuracy of 10^{-8} using the process outlined in Appendix C. The amplitude of the contact-line displacement increases as the perturbations become narrower; the linear model underpredicts the nonlinear Surface Evolver solution, indicating that nonlinear effects become important as the perturbations become sharper, particularly once s^2 approaches $\epsilon = 0.01$. We also note that the far-field solution does not quite have zero curvature (as the linear model predicts for a channel-volume-preserving perturbation); this again is a nonlinear effect. Plotting the maximum displacement of the contact line at $y = 0$ (figure 10b) shows that the amplitude of the displacement scales like $\log(1/s)$, suggesting that blowup may be possible even for analytic boundary forcing.

A more extreme response can be expected for smaller contact angles and less smooth forcing. Consider the case in which the ridge or groove has small amplitude and narrower width (not necessarily Gaussian, but effectively satisfying $s^2 \ll \epsilon$). More specifically, setting s to zero, suppose that the lower wall shape (b_-), say, has a discontinuity in a derivative at $y = 0$, such that $b_-(y) = 0$ for $y < 0$, and $b_-(y) = y^\gamma$ for $y > 0$. Then $\gamma = 0$

corresponds to a step in b_-, $\gamma = 1$ corresponds to a corner (a discontinuity in slope) and $\gamma = 2$ corresponds to a jump in the curvature of the wall. The linearised curvature of the nearby gas–liquid interface, described in general by the Helmholtz equation (2.8), can be expected to be approximated in the neighbourhood of the discontinuity by $\nabla^2 f \approx 0$. In the fully wetting case, for example, with $\tilde{\theta} = \pi/2$, b_- imposes f along the wall ($\theta = -\pi/2$) via (2.9), and the wall normal derivative f_n determines the contact-line displacement via (2.13*a*,*b*). Introduce polar coordinates (ϱ, ϑ) centred on $y = 0$, such that $\vartheta = 0$ ($\vartheta = \pi$) lies along the wall for $y > 0$ ($y < 0$), and consider first the case of a step ($\gamma = 0$). Then $f(\varrho, \vartheta) = -(1 - \vartheta/\pi)$ provides a local solution to Laplace's equation subject to the forcing condition $b_-(y) = H(y)$, where H is a Heaviside function. The corresponding wall normal derivative f_n is then proportional to $1/y$, indicating that the contact line will be displaced in opposite directions on either side of a step. Further cases follow by integrating with respect to y, so that $f_n \propto \log|y|$ for $\gamma = 1$ (the contact line will be displaced along the axis of a corner) and $f_n \propto y \log|y| - y$ for $\gamma = 2$. These approximate solutions suggest that a very sharp step or a corner in wall shape, even if smoothed over a very short length scale s, will cause substantial deflection of the contact line (violating the linearisation approximation), while a jump in wall curvature will bend the contact line sufficiently for it to have infinite slope with respect to y, while remaining continuous.

In summary, and as indicated by figure 10, nonlinear effects will have a leading-order role close to the ridge or groove whenever the wall shape is sufficiently sharp.

References

Ajaev, V.S., Gatapova, E.Ya. & Kabov, O.A. 2020 Interaction of advancing contact lines with defects on heated substrates. *Phys. Rev.* E **101** (2), 022801.

Ajaev, V.S. & Homsy, G.M. 2006 Modeling shapes and dynamics of confined bubbles. *Annu. Rev. Fluid Mech.* **38**, 277–307.

Anna, S.L. 2016 Droplets and bubbles in microfluidic devices. *Annu. Rev. Fluid Mech.* **48**, 285–309.

Ben-Jacob, E., Godbey, R., Goldenfeld, N.D., Koplik, J., Levine, H., Mueller, T. & Sander, L.M. 1985 Experimental demonstration of the role of anisotropy in interfacial pattern formation. *Phys. Rev. Lett.* **55** (12), 1315–1318.

Bhushan, B. 2019 Bioinspired water collection methods to supplement water supply. *Phil. Trans. R. Soc. Lond.* A **377** (2150), 20190119.

Boruvka, L. & Neumann, A.W. 1978 An analytical solution of the Laplace equation for the shape of liquid surfaces near a stripwise heterogeneous wall. *J. Colloid Interface Sci.* **65** (2), 315–330.

Bourges-Monnier, C. & Shanahan, M.E.R. 1995 Influence of evaporation on contact angle. *Langmuir* **11** (7), 2820–2829.

Brakke, K.A. 1992 The Surface Evolver. *Exp. Maths* **1** (2), 141–165.

Brown, P.S. & Bhushan, B. 2016 Bioinspired materials for water supply and management: water collection, water purification and separation of water from oil. *Phil. Trans. R. Soc. Lond.* A **374** (2073), 20160135.

Calver, S.N., Gaffney, E.A., Walsh, E.J., Durham, W.M. & Oliver, J.M. 2020 On the thin-film asymptotics of surface tension driven microfluidics. *J. Fluid Mech.* **901**, A6.

Cassie, A.B.D. 1948 Contact angles. *Discuss. Faraday Soc.* **3**, 11–16.

Cassie, A.B.D. & Baxter, S. 1944 Wettability of porous surfaces. *Trans. Faraday Soc.* **40**, 546–551.

Chung, S.E., Park, W., Shin, S., Lee, S.Ah. & Kwon, S. 2008 Guided and fluidic self-assembly of microstructures using railed microfluidic channels. *Nat. Mater.* **7** (7), 581–587.

Comanns, P., Buchberger, G., Buchsbaum, A., Baumgartner, R., Kogler, A., Bauer, S. & Baumgartner, W. 2015 Directional, passive liquid transport: the Texas horned lizard as a model for a biomimetic. *J. R. Soc. Interface* **12** (109), 20150415.

Concus, P. & Finn, R. 1969 On the behavior of a capillary surface in a wedge. *Proc. Natl Acad. Sci. USA* **63** (2), 292–299.

Cox, R.G. 1983 The spreading of a liquid on a rough solid surface. *J. Fluid Mech.* **131**, 1–26.

Dorsey, A.T. & Martin, O. 1987 Saffman–Taylor fingers with anisotropic surface tension. *Phys. Rev.* A **35**, 3989–3992.

Dussan, E.B. V 1979 On the spreading of liquids on solid surfaces: static and dynamic contact lines. *Annu. Rev. Fluid Mech.* **11** (1), 371–400.
Emami, B., Hemeda, A.A., Amrei, M.M., Luzar, A., Gad-el Hak, M. & Vahedi Tafreshi, H. 2013 Predicting longevity of submerged superhydrophobic surfaces with parallel grooves. *Phys. Fluids* **25** (6), 062108.
Eral, H.B., 't Mannetje, D.J.C.M. & Oh, J.M. 2013 Contact angle hysteresis: a review of fundamentals and applications. *Colloid Polym. Sci.* **291** (2), 247–260.
Espín, L. & Kumar, S. 2015 Droplet spreading and absorption on rough, permeable substrates. *J. Fluid Mech.* **784**, 465–486.
Fowkes, N.D. & Hood, M.J. 1998 Surface tension effects in a wedge. *Q. J. Mech. Appl. Maths* **51** (4), 553–561.
Franco-Gómez, A., Thompson, A.B., Hazel, A.L. & Juel, A. 2016 Sensitivity of Saffman–Taylor fingers to channel-depth perturbations. *J. Fluid Mech.* **794**, 343–368.
Franco-Gómez, A., Thompson, A.B., Hazel, A.L. & Juel, A. 2018 Bubble propagation in Hele-Shaw channels with centred constrictions. *Fluid Dyn. Res.* **50** (2), 021403.
Gao, L. & McCarthy, T.J. 2006 Contact angle hysteresis explained. *Langmuir* **22** (14), 6234–6237.
Hazel, A.L., Pailha, M., Cox, S.J. & Juel, A. 2013 Multiple states of finger propagation in partially occluded tubes. *Phys. Fluids* **25** (6), 021702.
He, B., Yang, S., Qin, Z., Wen, B. & Zhang, C. 2017 The roles of wettability and surface tension in droplet formation during inkjet printing. *Sci. Rep.* **7** (1), 1–7.
Hong, D.C. & Family, F. 1988 Bubbles in the Hele-Shaw cell: pattern selection and tip perturbations. *Phys. Rev.* A **38** (10), 5253–5259.
Howell, P.B. Jr., Mott, D.R., Fertig, S., Kaplan, C.R., Golden, J.P., Oran, E.S. & Ligler, F.S. 2005 A microfluidic mixer with grooves placed on the top and bottom of the channel. *Lab on a Chip* **5** (5), 524–530.
Huh, C. & Mason, S.G. 1977 Effects of surface roughness on wetting (theoretical). *J. Colloid Interface Sci.* **60** (1), 11–38.
Jansons, K.M. 1985 Moving contact lines on a two-dimensional rough surface. *J. Fluid Mech.* **154**, 1–28.
Johnson, R.E. & Dettre, R.H. 1964 Contact angle hysteresis. III. Study of an idealized heterogeneous surface. *J. Phys. Chem.* **68** (7), 1744–1750.
Ju, J., Bai, H., Zheng, Y., Zhao, T., Fang, R. & Jiang, L. 2012 A multi-structural and multi-functional integrated fog collection system in cactus. *Nat. Commun.* **3** (1), 1–6.
Khabiry, M., Chung, B.G., Hancock, M.J., Soundararajan, H.C., Du, Y., Cropek, D., Lee, W.G. & Khademhosseini, A. 2009 Cell docking in double grooves in a microfluidic channel. *Small* **5** (10), 1186–1194.
Khademhosseini, A., Yeh, J., Eng, G., Karp, J., Kaji, H., Borenstein, J., Farokhzad, O.C. & Langer, R. 2005 Cell docking inside microwells within reversibly sealed microfluidic channels for fabricating multiphenotype cell arrays. *Lab on a Chip* **5** (12), 1380–1386.
Khademhosseini, A., Yeh, J., Jon, S., Eng, G., Suh, K.Y., Burdick, J.A. & Langer, R. 2004 Molded polyethylene glycol microstructures for capturing cells within microfluidic channels. *Lab on a Chip* **4** (5), 425–430.
Kierzenka, J. & Shampine, L.F. 2001 A BVP solver based on residual control and the Matlab PSE. *ACM Trans. Math. Softw.* **27** (3), 299–316.
King, J.R., Ockendon, J.R. & Ockendon, H. 1999 The Laplace–Young equation near a corner. *Q. J. Mech. Appl. Maths* **52** (1), 73–97.
Lee, P.J., Hung, P.J. & Lee, L.P. 2007 An artificial liver sinusoid with a microfluidic endothelial-like barrier for primary hepatocyte culture. *Biotechnol. Bioengng* **97** (5), 1340–1346.
Li, J., Zhou, X., Li, J., Che, L., Yao, J., McHale, G., Chaudhury, M.K. & Wang, Z. 2017 Topological liquid diode. *Sci. Adv.* **3** (10), eaao3530.
Manbachi, A., Shrivastava, S., Cioffi, M., Chung, B.G., Moretti, M., Demirci, U., Yliperttula, M. & Khademhosseini, A. 2008 Microcirculation within grooved substrates regulates cell positioning and cell docking inside microfluidic channels. *Lab on a Chip* **8** (5), 747–754.
Maxworthy, T. 1986 Bubble formation, motion and interaction in a Hele-Shaw cell. *J. Fluid Mech.* **173**, 95–114.
Mobasseri, A., Faroni, A., Minogue, B.M., Downes, S., Terenghi, G. & Reid, A.J. 2015 Polymer scaffolds with preferential parallel grooves enhance nerve regeneration. *Tissue Engng Part A* **21** (5–6), 1152–1162.
Park, J. & Kumar, S. 2017 Droplet sliding on an inclined substrate with a topographical defect. *Langmuir* **33** (29), 7352–7363.

Park, J., Toner, M., Yarmush, M.L. & Tilles, A.W. 2006 Microchannel bioreactors for bioartificial liver support. *Microfluid Nanofluid* **2** (6), 525–535.
Passerone, A. 2011 Twenty years of surface tension measurements in space. *Microgravity Sci. Technol.* **23** (2), 101–111.
Pham, T. & Kumar, S. 2017 Drying of droplets of colloidal suspensions on rough substrates. *Langmuir* **33** (38), 10061–10076.
Pham, T. & Kumar, S. 2019 Imbibition and evaporation of droplets of colloidal suspensions on permeable substrates. *Phys. Rev. Fluids* **4** (3), 034004.
Picknett, R.G. & Bexon, R. 1977 The evaporation of sessile or pendant drops in still air. *J. Colloid Interface Sci.* **61** (2), 336–350.
Prakash, M., Quéré, D. & Bush, J.W.M. 2008 Surface tension transport of prey by feeding shorebirds: the capillary ratchet. *Science* **320** (5878), 931–934.
Reyssat, E. 2014 Drops and bubbles in wedges. *J. Fluid Mech.* **748**, 641–662.
Shanahan, M.E.R. 1995 Simple theory of ‘stick-slip’ wetting hysteresis. *Langmuir* **11** (3), 1041–1043.
Stauber, J.M., Wilson, S.K., Duffy, B.R. & Sefiane, K. 2014 On the lifetimes of evaporating droplets. *J. Fluid Mech.* **744**, R2.
Stone, H.A., Stroock, A.D. & Ajdari, A. 2004 Engineering flows in small devices: microfluidics toward a lab-on-a-chip. *Annu. Rev. Fluid Mech.* **36**, 381–411.
Tabeling, P., Zocchi, G. & Libchaber, A. 1987 An experimental study of the Saffman–Taylor instability. *J. Fluid Mech.* **177**, 67–82.
Thompson, A.B., Juel, A. & Hazel, A.L. 2014 Multiple finger propagation modes in Hele-Shaw channels of variable depth. *J. Fluid Mech.* **746**, 123–164.
Weislogel, M.M. & Lichter, S. 1998 Capillary flow in an interior corner. *J. Fluid Mech.* **373**, 349–378.
Wenzel, R.N. 1936 Resistance of solid surfaces to wetting by water. *Ind. Engng Chem.* **28** (8), 988–994.
Xing, Y., Deng, J., Lian, Y., Zhang, K., Zhang, G. & Zhao, J. 2014 Multiple nanoscale parallel grooves formed on Si_3N_4/TiC ceramic by femtosecond pulsed laser. *Appl. Surf. Sci.* **289**, 62–71.
Xu, F. & Jensen, O.E. 2017 Trapping and displacement of liquid collars and plugs in rough-walled tubes. *Phys. Rev. Fluids* **2** (9), 094004.
Xu, T., Lin, Y., Zhang, M., Shi, W. & Zheng, Y. 2016 High-efficiency fog collector: water unidirectional transport on heterogeneous rough conical wires. *ACS Nano* **10** (12), 10681–10688.
Yang, A.-S., Yang, J.-C. & Hong, M.-C. 2005 Droplet ejection study of a picojet printhead. *J. Micromech. Microengng* **16** (1), 180–188.
Yoshimitsu, Z., Nakajima, A., Watanabe, T. & Hashimoto, K. 2002 Effects of surface structure on the hydrophobicity and sliding behavior of water droplets. *Langmuir* **18** (15), 5818–5822.
Zheng, Y., Bai, H., Huang, Z., Tian, X., Nie, F.-Q., Zhao, Y., Zhai, J. & Jiang, L. 2010 Directional water collection on wetted spider silk. *Nature* **463** (7281), 640–643.
Zhou, J., Khodakov, D.A., Ellis, A.V. & Voelcker, N.H. 2012 Surface modification for PDMS-based microfluidic devices. *Electrophoresis* **33** (1), 89–104.

Appendix

2.A Towards a nonlinear pressure-volume relationship

One question that we did not address in the above paper was whether the relationship between the change in channel volume and the change in pressure difference over the meniscus holds in the general nonlinear case, i.e. for a ridge of any amplitude. Here we formulate the question in variational terms although we do not offer a definitive answer.

Let $\mathcal{S}_\delta^*$ be a channel described in Cartesian coordinates (x, y, z). Let the cross-section of the channel at $x = x_0$ be $D_\delta(x_0)$. Denote the boundary of this cross section, which is the walls of the channel at $x = x_0$, by $\partial_{D_\delta}(x_0)$. The cross-section and its boundary are then defined parametrically as

$$D_\delta(x_0) = \{\hat{\boldsymbol{r}} : \hat{\boldsymbol{r}} = \hat{\boldsymbol{r}}_{D_\delta}(x_0; y, z) = (x_0, y, z)\}, \tag{2.A.1}$$

$$\partial_{D_\delta}(x_0) = \{\hat{\boldsymbol{r}} : \hat{\boldsymbol{r}} = \hat{\boldsymbol{r}}_{\partial_{D_\delta}}(x_0; t) = (x_0, y_{\partial_{D_\delta}}(x_0; t), z_{\partial_{D_\delta}}(x_0; t)),\ t \in [0, 1]\}. \tag{2.A.2}$$

At a fixed $x = x_0$, we find the cross-sectional area of the channel, A_δ^*. Firstly,

$$\iint_{D_\delta(x_0)} \mathrm{d}y\ \mathrm{d}z = \iint_{D_\delta(x_0)} \frac{1}{2}\boldsymbol{\nabla} \cdot (y, z)\ \mathrm{d}y\ \mathrm{d}z \tag{2.A.3}$$

$$= \int_{\partial D_\delta(x_0)} \frac{1}{2}(y\ \mathrm{d}z - z\ \mathrm{d}y) \tag{2.A.4}$$

using the two-dimensional divergence theorem with outward-facing unit normal vectors to the boundary $\partial_{D_\delta(x_0)}$. Then using the parametrisation of the boundary (2.A.2), the cross-sectional area is found to be

$$A_\delta^*(x_0) = \iint_{D_\delta(x_0)} \mathrm{d}y\ \mathrm{d}z = \frac{1}{2}\int_{t=0}^{1} \Big(z'_{\partial_{D_\delta}}(x_0; t) y_{\partial_{D_\delta}}(x_0; t) - y'_{\partial_{D_\delta}}(x_0; t) z_{\partial_{D_\delta}}(x_0; t)\Big)\ \mathrm{d}t, \tag{2.A.5}$$

where prime denotes derivative with respect to t. Thus, the volume of the channel $\mathcal{S}^*_\delta$ is given by

$$V^*_\delta = \int_{x=-L}^{L} A^*_\delta(x)\ \mathrm{d}x, \tag{2.A.6}$$

where $2L$ is the length of the channel.

Now let $\mathcal{S}_\delta$ be a free surface of minimum energy, which is in contact with the channel $\mathcal{S}^*_\delta$. We define the surface parametrically so that

$$S_\delta = \left\{\hat{\boldsymbol{r}} : \hat{\boldsymbol{r}} = \hat{\boldsymbol{r}}_{S_\delta}(y,z) = \Big(x_{\mathcal{S}_\delta}(y,z), y, z\Big)\right\}. \tag{2.A.7}$$

Let the contact line Σ_δ be defined as the intersection of the free surface $\mathcal{S}_\delta$ and the channel walls S^*_δ. Then the contact line is defined parametrically by

$$\Sigma_\delta = \left\{\hat{\boldsymbol{r}} : \hat{\boldsymbol{r}} = \hat{\boldsymbol{r}}_{\Sigma_\delta}(t) = \Big(x_{\mathcal{S}_\delta}\Big(y_{\Sigma_\delta}(t), z_{\Sigma_\delta}(t)\Big), y_{\Sigma_\delta}(t), z_{\Sigma_\delta}(t)\Big),\ t \in [0,1]\right\}. \tag{2.A.8}$$

The energy of the free surface $E_{\mathcal{S}_\delta}$ is given by its area, which is defined as

$$E_{\mathcal{S}_\delta} = \iint_{\sigma_\delta} \left\| \frac{\partial \hat{\boldsymbol{r}}_{\mathcal{S}_\delta}}{\partial y} \times \frac{\partial \hat{\boldsymbol{r}}_{\mathcal{S}_\delta}}{\partial z} \right\|\ \mathrm{d}y\ \mathrm{d}z. \tag{2.A.9}$$

The domain of integration σ_δ is the region in the (y, z) plane that corresponds with the surface S_δ, i.e. it is bounded by the projection of the contact line Σ_δ onto two-dimensional space. After applying the principle of virtual work, the first variation of energy $E^1_{\mathcal{S}_\delta}$ with respect to arbitrary displacement functions $\xi(y,z)$, $\eta(y,z)$ in the normal and tangent directions to the free surface respectively is given by (Finn, 2012):

$$\begin{aligned} E^1_{\mathcal{S}_\delta} = &\iint_{\sigma_\delta} \xi(y,z)(-2H_\delta + \lambda_\delta)\ \left\| \frac{\partial \hat{\boldsymbol{r}}_{\mathcal{S}_\delta}}{\partial x} \times \frac{\partial \hat{\boldsymbol{r}}_{\mathcal{S}_\delta}}{\partial y} \right\|\ \mathrm{d}y\ \mathrm{d}z \\ &+ \int_{t=0}^{1} \eta(y_{\Sigma_\delta}(t), z_{\Sigma_\delta}(t))\ \|\hat{\boldsymbol{r}}'_{\Sigma_\delta}(t)\|\ \mathrm{d}t, \end{aligned} \tag{2.A.10}$$

where H_δ is the mean curvature of the free surface $\mathcal{S}_\delta$ and λ_δ is the Lagrange multiplier for the constraint imposed that the volume of fluid in the channel is constant. The free surface $\mathcal{S}_\delta$ is a surface of minimum energy and therefore we solve for $E^1_{\mathcal{S}_\delta} = 0$, which gives (Finn, 2012) $\lambda_\delta = 2H_\delta$ and

$$\int_{t=0}^{1} \eta(y_{\Sigma_\delta}(t), z_{\Sigma_\delta}(t))\ \|\hat{\boldsymbol{r}}'_{\Sigma_\delta}(t)\|\ \mathrm{d}t = 0. \tag{2.A.11}$$

Now assume that the channel $\mathcal{S}^*_\delta$ differs slightly in geometry from some other channel $\mathcal{S}^*$. We linearise back to this geometry. So,

- on the free surface $\mathcal{S}_\delta$,

$$\begin{aligned}\hat{\boldsymbol{r}}_{\mathcal{S}_\delta}(y,z) &= \hat{\boldsymbol{r}}_{\mathcal{S}}(y,z) + \delta\hat{\boldsymbol{r}}_{\mathcal{S}_p}(y,z),\\ &= \Big(x_{\mathcal{S}}(y,z),y,z\Big) + \delta\Big(x_{\mathcal{S}_p}(y,z),y,z\Big),\end{aligned} \tag{2.A.12}$$

- on the contact line,

$$\begin{aligned}\hat{\boldsymbol{r}}_{\Sigma_\delta}(t) &= \hat{\boldsymbol{r}}_{\Sigma}(t) + \delta\hat{\boldsymbol{r}}_{\Sigma_p}(t),\\ &= \Big(x_\Sigma(t), y_\Sigma(t), z_{\mathcal{S}}(x_\Sigma(t), y_\Sigma(t))\Big) + \delta\Big(x_{\mathcal{S}_p}(y_{\Sigma_p}(t), z_{\Sigma_p}(t)), y_{\Sigma_p}(t), z_{\Sigma_p}(t)\Big),\end{aligned} \tag{2.A.13}$$

- on the channel walls, at $x = x_0$,

$$\begin{aligned}\hat{\boldsymbol{r}}_{\partial_{D_\delta}}(x_0;t) &= \hat{\boldsymbol{r}}_{\partial_D}(x_0;t) + \delta\hat{\boldsymbol{r}}_{\partial_{D_p}}(x_0;t),\\ &= \Big(x_0, y_{\partial_D}(x_0;t), z_{\partial_D}(x_0;t)\Big) + \delta\Big(x_0, y_{\partial_{D_p}}(x_0;t), z_{\partial_{D_p}}(x_0;t)\Big).\end{aligned} \tag{2.A.14}$$

So $y_{\partial_{D_p}}(x_0;t)$, $z_{\partial_{D_p}}(x_0;t)$ is the perturbation we apply to the channel walls at $x = x_0$.

- the mean curvature and Lagrange multipler are linearised;

$$H_\delta = H + \delta H_p; \quad \lambda_\delta = \lambda + \delta\lambda_p. \tag{2.A.15}$$

Then the first variation of energy is given by

$$\begin{aligned}E^1_{\mathcal{S}_\delta} = &\iint_\sigma \xi(y,z)(-2H+\lambda)\left\|\frac{\partial\hat{\boldsymbol{r}}_{\mathcal{S}}}{\partial y}\times\frac{\partial\hat{\boldsymbol{r}}_{\mathcal{S}}}{\partial z}\right\|\,\mathrm{d}y\,\mathrm{d}z\\ &+\int_{t=0}^1 \eta(y_\Sigma(t), z_\Sigma(t))\,\|\hat{\boldsymbol{r}}'_\Sigma(t)\|\,\mathrm{d}t\\ &+\delta\iint_\sigma \xi(y,z)(-2H_p+\lambda_p)\left\|\frac{\partial\hat{\boldsymbol{r}}_{\mathcal{S}}}{\partial y}\times\frac{\partial\hat{\boldsymbol{r}}_{\mathcal{S}}}{\partial z}\right\|\,\mathrm{d}y\mathrm{d}z\\ &+\delta\iint_\sigma \xi(y,z)(-2H+\lambda)\left(\left\|\frac{\partial\hat{\boldsymbol{r}}_{\mathcal{S}_p}}{\partial y}\times\frac{\partial\hat{\boldsymbol{r}}_{\mathcal{S}}}{\partial z}\right\|+\left\|\frac{\partial\hat{\boldsymbol{r}}_{\mathcal{S}}}{\partial y}\times\frac{\partial\hat{\boldsymbol{r}}_{\mathcal{S}_p}}{\partial z}\right\|\right)\,\mathrm{d}y\,\mathrm{d}z\\ &+\delta\int_{t=0}^1 \eta\Big(y_\Sigma(t), z_\Sigma(t)\Big)\|\hat{\boldsymbol{r}}'_{\Sigma_p}(t)\|\,\mathrm{d}t\\ &+\delta\int_{t=0}^1\left(\frac{\partial\eta\Big(y_\Sigma(t),z_\Sigma(t)\Big)}{\partial y_\Sigma}y_{\Sigma_p}(t)+\frac{\partial\eta\Big(y_\Sigma(t),z_\Sigma(t)\Big)}{\partial z_\Sigma}z_{\Sigma_p}(t)\right)\|\hat{\boldsymbol{r}}'_\Sigma(t)\|\,\mathrm{d}t.\end{aligned} \tag{2.A.16}$$

So since the free surface is a surface of minimum energy, the first variation of energy must be equal to zero for all variations ξ and η. Therefore, at $O(1)$ this gives

$$\lambda = 2H, \qquad \int_{t=0}^{1} \eta(y_\Sigma(t), z_\Sigma(t)) \, \|\hat{\boldsymbol{r}}'_\Sigma(t)\| \, \mathrm{d}t = 0. \tag{2.A.17}$$

Then using these constraints, setting the $O(\delta)$ terms to zero gives

$$\begin{aligned}&\iint_\sigma \xi(y,z)(-2H_p + \lambda_p) \left\| \frac{\partial \hat{\boldsymbol{r}}_{\mathcal{S}}}{\partial y} \times \frac{\partial \hat{\boldsymbol{r}}_{\mathcal{S}}}{\partial z} \right\| \, \mathrm{d}y \mathrm{d}z \\ &+ \int_{t=0}^{1} \left(\frac{\partial \eta\Big(y_\Sigma(t), z_\Sigma(t)\Big)}{\partial y_\Sigma} y_{\Sigma_p}(t) + \frac{\partial \eta\Big(y_\Sigma(t), z_\Sigma(t)\Big)}{\partial z_\Sigma} y_{\Sigma_p}(t) \right) \|\hat{\boldsymbol{r}}'_\Sigma(t)\| \, \mathrm{d}t = 0.\end{aligned} \tag{2.A.18}$$

Meanwhile, by linearising (2.A.5) and (2.A.6) we find that the channel volume is given by

$$V_\delta^* = V^* + V_p^* = V^* + \frac{\delta}{2} \int_{x=-L}^{L} \int_{t=0}^{1} \left(z'_{\partial_D} y_{\partial_{D_p}} + z'_{\partial_{D_p}} y_{\partial_D} - y'_{\partial_D} z_{\partial_{D_p}} - y'_{\partial_{D_p}} z_{\partial_D} \right) \mathrm{d}t \ \mathrm{d}x \tag{2.A.19}$$

$$= V^* + \delta \int_{x=-L}^{L} \int_{t=0}^{1} \left(z'_{\partial_D} y_{\partial_{D_p}} - y'_{\partial_D} z_{\partial_{D_p}} \right) \mathrm{d}t \ \mathrm{d}x \tag{2.A.20}$$

$$= V^* + \delta \int_{x=-L}^{L} \int_{t=0}^{1} \left(z'_{\partial_{D_p}} y_{\partial_D} - y'_{\partial_{D_p}} z_{\partial_D} \right) \mathrm{d}t \ \mathrm{d}x, \tag{2.A.21}$$

where again prime denotes derivative with respect to t, and we have used integration by parts in t to obtain the final two integrals.

Now define two statements:

Statement P: The mean curvature of S is the same as the mean curvature of S_δ, so $H = H_\delta = \lambda = \lambda_\delta$.

Corollary 1: By setting the mean curvature change to zero,

$$H_p = \lambda_p = 0.$$

Corollary 2: By setting the first variation of the energy to zero, η is in the set $\mathcal{J}$ such that

$$\int_{t=0}^{1} \left(\frac{\partial \eta\Big(y_\Sigma(t), z_\Sigma(t)\Big)}{\partial y_\Sigma} y_{\Sigma_p}(t) + \frac{\partial \eta\Big(y_\Sigma(t), z_\Sigma(t)\Big)}{\partial z_\Sigma} y_{\Sigma_p}(t) \right) \|\hat{\boldsymbol{r}}'_\Sigma(t)\| \, \mathrm{d}t = 0. \tag{2.A.22}$$

Corollary 3: By setting the $O(1)$ terms of the first variation of the energy to zero, $\mathcal{J}$ is a subset of the set $\mathcal{K}$, where $\mathcal{K}$ is the set of functions η such that

$$\int_{t=0}^{1} \eta(y_\Sigma(t), z_\Sigma(t)) \, \|\hat{\boldsymbol{r}}'_\Sigma(t)\| \, \mathrm{d}t = 0. \tag{2.A.23}$$

Statement Q: The volume of channel S^* is the same as the volume of channel S^*_δ, so $V^* = V^*_\delta$.

Corollary 4: By setting the volume change $V^*_p = 0$, the channel variations $y_{\partial_{D_p}}$ and $y_{\partial_{D_p}}$ belong to a set $\mathcal{M}$ such that

$$\int_{x=-L}^{L} \int_{t=0}^{1} \left(z'_{\partial_{D_p}} y_{\partial_D} - y'_{\partial_{D_p}} z_{\partial_D} \right) \, \mathrm{d}t \, \mathrm{d}x = 0. \tag{2.A.24}$$

We then wish to say something about the statements P and Q, i.e, we wish to find the relationship between the sets $\mathcal{J}$ and $\mathcal{M}$. We want to prove that if $\eta \in \mathcal{J}$ then $P \implies Q$, because this would prove that variations which do not cause the mean curvature to change also do not cause the channel volume to change. We need to prove this statement for every possible $\eta \in \mathcal{J}$, where $\mathcal{J} \subset \mathcal{K}$ so that "every possible η" means η such that $\int_{t=0}^{1} \eta(y_\Sigma(t), z_\Sigma(t)) \, \|\hat{\boldsymbol{r}}'_\Sigma(t)\| \, \mathrm{d}t = 0$.

Or equivalently, if the channel volume changes in a certain specified way, what can we say about the set $\mathcal{J}$? The problem is that knowing the functions in the set $\mathcal{J}$ requires knowledge of the position of the perturbed contact line, which is not something we know *a priori*. That is, we need to know the position of the gradient of η. This may be made simpler by considering specific geometries however it is difficult to say anything in general.

2.B Long-wave analysis

We elaborate here on the long-wave analysis that leads to the form of the far-field solution (equation (4.1) in Chapter 2). We start with the Helmholtz equation

$$\frac{1}{R^2}f + \frac{1}{R^2}f_{\theta\theta} + f_{yy} = p, \tag{2.B.1}$$

with boundary conditions

$$f(y, \pm\tilde{\theta})\sin\tilde{\theta} \pm f_\theta(y, \pm\tilde{\theta})\cos\tilde{\theta} = \pm b_\pm(y), \tag{2.B.2}$$

$$f_y(\pm W, \theta) = 0. \tag{2.B.3}$$

We consider a perturbation $b_\pm(y) = \pm\exp(-y^2/s^2)$ that is varying over a very wide length scale so that $s = O(W)$. Note that to simplify the analysis we assume that the perturbations are centred at $y = 0$ (i.e. aligned); the analysis follows the same way for non-aligned perturbations. We introduce a strained parameter $S = s/W$ so that $S = O(1)$. Then if the perturbation is varying on an $O(W)$ length scale in y, we also need to introduce a strained variable for y, $Y = y/W$, so that the perturbation is varying on an $O(1)$ length scale in Y. The Helmholtz equation becomes

$$\frac{1}{R^2}f + \frac{1}{R^2}f_{\theta\theta} + \frac{1}{W^2}f_{YY} = p, \tag{2.B.4}$$

with boundary conditions

$$f(Y, \pm\tilde{\theta})\sin\tilde{\theta} \pm f_\theta(y, \pm\tilde{\theta})\cos\tilde{\theta} = \pm b_\pm(Y), \tag{2.B.5}$$

$$\frac{1}{W}f_Y(\pm 1, \theta) = 0. \tag{2.B.6}$$

If $1/W^2 = O(\epsilon)$ it is possible to obtain a disordered series expansion of the Young–Laplace equation, since the Helmholtz equation in the strained coordinates (2.B.4) is the $O(\epsilon)$ expansion of the Young–Laplace equation where we have neglected $O(\epsilon^2)$ terms. So we also need to expand f with the restriction that $W^2 \ll \epsilon^{-1}$. A Taylor expansion of the droplet solution (equation (E.14b) in Chapter 2) shows that $f \propto (W - |y|)^2$, suggesting that if $y = WY$ then $f \sim O(W^2)$ in the far field. Therefore, we expand f in powers of W^2 with $p = O(1)$:

$$f = W^2 f_0 + f_1 + \frac{1}{W^2}f_2 + \dots, \tag{2.B.7}$$

$$p = p_0 + \frac{1}{W^2}p_1 + \dots. \tag{2.B.8}$$

Leading-order problem

The leading-order problem at $O(W^2)$ is

$$\frac{1}{R^2}f_0 + \frac{1}{R^2}\frac{\partial^2 f_0}{\partial\theta^2} = 0, \tag{2.B.9}$$

where $f_0 = f_0(Y,\theta)$ and with boundary conditions

$$f_0(Y,\pm\tilde{\theta})\sin\tilde{\theta} \pm f_{0\theta}(Y,\pm\tilde{\theta})\cos\tilde{\theta} = 0, \tag{2.B.10}$$

$$f_{0Y}(\pm 1,\theta) = 0. \tag{2.B.11}$$

This leads to the solution

$$f_0(Y,\theta) = C_1(Y)\sin\theta + C_2(Y)\cos\theta, \tag{2.B.12}$$

where $C_1(Y)$ and $C_2(Y)$ are functions to be found. Then applying the boundary conditions (2.B.10) at $\theta = \pm\tilde{\theta}$ leads to $C_1(Y) = 0$. So we have,

$$f_0(Y,\theta) = C_2(Y)\cos\theta, \tag{2.B.13}$$

$$\frac{\mathrm{d}C_2}{\mathrm{d}Y} = 0 \text{ at } Y = \pm 1. \tag{2.B.14}$$

The leading-order problem does not have enough information to determine C_2 therefore we need to solve the next-order problem to determine a solvability condition.

Second order problem

At $O(1)$ we have

$$\frac{1}{R^2}f_1 + \frac{1}{R^2}\frac{\partial^2 f_1}{\partial\theta^2} = p_0 - \frac{\partial^2 f_0}{\partial Y^2}, \tag{2.B.15}$$

with boundary conditions

$$f_1(Y,\pm\tilde{\theta})\sin\tilde{\theta} \pm f_{1\theta}(Y,\pm\tilde{\theta})\cos\tilde{\theta} = \pm b_{\pm}(Y), \tag{2.B.16}$$

$$f_{1Y}(\pm 1,\theta) = 0. \tag{2.B.17}$$

We obtain the solution

$$\begin{aligned} f_1(Y,\theta) = {} & D_1(Y)\cos\theta + D_2(Y)\sin\theta \\ & - \frac{R^2(\theta\sin\theta + \cos\theta)}{2}\frac{\mathrm{d}^2 C_2}{\mathrm{d}Y} + \frac{b_+(Y) + b_-(Y)}{2}\sin\theta + R^2 p_0. \end{aligned} \tag{2.B.18}$$

After applying the boundary conditions (2.B.16) at $\theta = \pm\tilde{\theta}$, we obtain a solvability condition for $C_2(Y)$:

$$\frac{\mathrm{d}^2 C_2}{\mathrm{d}Y} = K_1 + K_2\ g(Y), \tag{2.B.19}$$

$$K_1 = \frac{2\sin\tilde{\theta}\ p_0}{\tilde{\theta} + \sin\tilde{\theta}\cos\tilde{\theta}},\ \ K_2 = -\frac{1}{R^2}\frac{1}{\tilde{\theta} + \sin\tilde{\theta}\cos\tilde{\theta}}, \tag{2.B.20}$$

$$g(Y) = b_+(Y) - b_-(Y), \tag{2.B.21}$$

subject to boundary conditions (2.B.14) (from the leading order problem)

$$\frac{\mathrm{d}C_2}{\mathrm{d}Y} = 0 \text{ at } Y = \pm 1. \tag{2.B.22}$$

So integrating once (with ξ a dummy variable) we obtain

$$\frac{\mathrm{d}C_2}{\mathrm{d}Y} = \int_{\xi=\nu_1}^{Y} (K_1 + K_2\ g(\xi))\ \mathrm{d}\xi, \tag{2.B.23}$$

with ν_1 arbitrary. We then apply the side wall boundary conditions (2.B.17). Imposing $C_2'(1) = 0$ and $C_2'(-1) = 0$ we obtain

$$2K_1 + K_2 \int_{-1}^{1} g(\xi)\ \mathrm{d}\xi = 0. \tag{2.B.24}$$

We then put everything back into original variables, using $y = WY$ and (2.B.20)–(2.B.21), to recover the independent pressure condition, (equation (3.1) from Chapter 2):

$$p_0 = \frac{1}{4WR^2\sin\tilde{\theta}} \int_{-W}^{W} (b_+(y) - b_-(y))\ \mathrm{d}y. \tag{2.B.25}$$

We can now integrate (2.B.23) to find $C_2(Y)$. We can only apply one of the side-wall boundary conditions (2.B.17), therefore we solve the problem in two halves for $Y \geq 0$ and $Y \leq 0$, then at the end, we can write a complete solution in terms of $|Y|$.

For $Y \geq 0$, we find

$$C_2(Y) = \int_{\eta=a_1}^{Y} \int_{1}^{\eta} (K_1 + K_2\ g(\xi))\ \mathrm{d}\xi\ \mathrm{d}\eta, \tag{2.B.26}$$

with a_1 is a constant to be found from the volume condition (from the expansion of equation (2.12) in the Chapter 2 paper). Similarly for $Y \leq 0$ we obtain

$$C_2(Y) = \int_{\eta=a_2}^{Y} \int_{-1}^{\eta} (K_1 + K_2\ g(\xi))\ \mathrm{d}\xi\ \mathrm{d}\eta, \tag{2.B.27}$$

$$= \int_{\eta=-a_2}^{|Y|} \int_{1}^{\eta} (K_1 + K_2\ g(\xi))\ \mathrm{d}\xi\ \mathrm{d}\eta, \tag{2.B.28}$$

with a_2 a constant. The solutions must match for $Y = 0$ so we need $a_1 = -a_2$. Then, after expanding and putting everything back into original variables, we have

$$f \approx W^2 f_0 = W^2 C_2\left(\frac{y}{W}\right)\cos\theta. \tag{2.B.29}$$

After finding C_2 by substituting for K_1, K_2 and $g(Y)$ in (2.B.26) using (2.B.20)–(2.B.21), we obtain the full solution for $y \in [-W, W]$:

$$f \approx \left(\frac{\sin\tilde{\theta}\, p_0}{\tilde{\theta} + \sin\tilde{\theta}\cos\tilde{\theta}}(|y| - W)^2\right)\cos\theta \tag{2.B.30}$$

$$- \left(\frac{1}{R^2}\frac{1}{\tilde{\theta} + \sin\tilde{\theta}\cos\tilde{\theta}}\int_{\eta=q_1}^{|y|}\int_1^{\eta}(b_+(\xi) - b_-(\xi))\ \mathrm{d}\xi\ \mathrm{d}\eta\right)\cos\theta, \tag{2.B.31}$$

where q_1 is a constant to be found from the volume condition. The contact line displacement is given by equation (2.13b) in Chapter 2:

$$\begin{aligned}\hat{x}_p^{\pm}(y) &= f(y, \pm\tilde{\theta})\cos\tilde{\theta} \mp f_\theta(y, \pm\tilde{\theta})\sin\tilde{\theta} \\ &\approx \left(\frac{\sin\tilde{\theta}\, p_0}{\tilde{\theta} + \sin\tilde{\theta}\cos\tilde{\theta}}(|y| - W)^2\right) \\ &- \left(\frac{1}{R^2}\frac{1}{\tilde{\theta} + \sin\tilde{\theta}\cos\tilde{\theta}}\int_{\eta=q_1}^{|y|}\int_1^{\eta}(b_+(\xi) - b_-(\xi))\ \mathrm{d}\xi\ \mathrm{d}\eta\right).\end{aligned} \tag{2.B.32}$$

Note that this is consistent with the far-field solution (equation (4.1) from Chapter 2) because that solution was obtained by assuming the perturbations $b_\pm$ were negligibly small in the far field.

2.C Sensitivity of the system to a wavy perturbation

Although we have considered static equilibrium solutions, for small-amplitude perturbations we may wish to consider the stability of the solutions to small-amplitude wavy perturbations. Consider the linear system described in §2.1 of Chapter 2,

$$\frac{1}{R^2}f + \frac{1}{R^2}f_{\theta\theta} + f_{yy} = p, \tag{2.C.1}$$

with boundary conditions

$$f(y, \pm\tilde{\theta}) \sin\tilde{\theta} \pm f_\theta(y, \pm\tilde{\theta}) \cos\tilde{\theta} = \pm b_\pm(y), \tag{2.C.2}$$

$$f_y(\pm W, \theta) = 0. \tag{2.C.3}$$

Let $Q(y, \theta)$ be a solution to this system. We perturb this solution by writing

$$f = Q(y, \theta) + \Re(\delta q(\theta) e^{iky}), \quad \delta \ll 1, \tag{2.C.4}$$

that is, we impose a wavy perturbation in the y direction and we look for instabilities. Substituting into the Helmholtz equation (2.C.1) and equating terms of $O(\delta)$, we solve

$$\begin{aligned} &\frac{1}{R^2}q'' + \left(\frac{1}{R^2} - k^2\right) q = 0, \\ &q(-\tilde{\theta}) \sin\tilde{\theta} - q'(-\tilde{\theta}) \cos\tilde{\theta} = 0, \quad q(\tilde{\theta}) \sin\tilde{\theta} + q'(\tilde{\theta}) \cos\tilde{\theta} = 0, \end{aligned} \tag{2.C.5}$$

where prime denotes derivative. We have two cases to consider.

First, if $k^2R^2 - 1 \leq 0$ then integrating and applying the boundary conditions (2.C.5) leads to $q(\theta) = 0$ unless $k = 0$. In this case $q(\theta) = C \cos\theta$, with C a constant, which is expected since $\cos\theta$ is an eigenmode of the system.

If $k^2R^2 - 1 > 0$ then the general solution is

$$q = Ae^{\lambda\theta} + Be^{-\lambda\theta}, \tag{2.C.6}$$

where A and B are constants and $\lambda = \sqrt{k^2R^2 - 1}$. Applying the boundary conditions (2.C.5) and adding the resulting equations leads to

$$(A + B)(\cosh(\lambda\tilde{\theta}) \sin\tilde{\theta} + \lambda \sinh(\lambda\tilde{\theta}) \cos\tilde{\theta}) = 0, \tag{2.C.7}$$

which requires $A = -B$ because by solving for $\cos(\lambda\tilde{\theta})$ we see that the second bracket cannot equal zero for $\tilde{\theta} \in (0, \pi/2)$. Thus,

$$q = C \sinh(\sqrt{k^2R^2 - 1}\ \theta) \tag{2.C.8}$$

Applying the boundary conditions (2.C.5) leads to

$$C(\sinh(\lambda\tilde{\theta}) \sin\tilde{\theta} + \lambda \cosh(\lambda\tilde{\theta}) \cos\tilde{\theta}) = 0. \tag{2.C.9}$$

Again, the second bracket cannot equal zero for $\tilde{\theta} \in (0, \pi/2)$ so that we must take $C = 0$. So, other than the previously known eigenmode $\cos\theta$, there are no non-trivial solutions of the system. Thus we conclude that any solution is stable to a wavy perturbation imposed on it; this includes long-wavelength perturbations.

Chapter 3

The effect of isolated bumps on static menisci in rectangular channels

This chapter contains a draft of a paper containing work that forms part of my studies at the University of Manchester and is currently ongoing. The paper has a self-contained introduction, discussion, appendices and bibliography. Following the paper there is an additional appendix which provides detail of an aspect of the problem that is not considered in the main body of work.

Statement of Contributions

EJ derived the model, performed the asymptotic analysis and the numerical computations, created the figures and wrote the paper. AH and OJ provided advice, guidance and supervision throughout all stages of the process, suggested ideas and direction of the research and provided editorial suggestions.

The effect of isolated bumps on static menisci in rectangular channels

Eleanor C. Johnstone, Andrew L. Hazel & Oliver E. Jensen

Abstract

A static liquid-vapour interface is confined in a large aspect-ratio rectangular channel which is perturbed with localised bump protrusions and intrusions on the upper and lower walls. Preliminary results for the response of the interface to the perturbations are found by solving the Young–Laplace equation for the interface shape in a nonlinear framework using Surface Evolver (Brakke, 1992) and in a linear framework for small-amplitude perturbations (relative to the height of the channel) using asymptotic methods. We show that axisymmetric channel-volume-preserving bump perturbations do not change the mean curvature of the meniscus, whereas channel-volume-changing perturbations induce a change in the pressure difference over the meniscus, and thus the mean curvature, and lead to long-range curvature of the contact line and meniscus across the channel. We compute 'quasi-static' solutions for a meniscus moving over a bump by computing equilibrium solutions at varying channel volumes. Preliminary results indicate that the meniscus bulges as it approaches the bump, and then the direction of the bulging and the shape of the contact line change as the meniscus moves over the bump via a smooth transition. Unlike the ridge problem (Johnstone, Hazel, and Jensen, 2022), the shape of the meniscus changes depending on its location relative to the bump. The limitations of the methods used are discussed, and a plan for further work is given.

1 Introduction

The use of microfluidic devices to control and manipulate fluids has had an impact across many areas of science and industry in recent years; for an overview, see, for example, Stone, Stroock, and Ajdari (2004), Ajaev and Homsy (2006), Anna (2016), and Venkatesan et al. (2020). The small spatial scales involved mean that surface tension effects dominate behaviour, and thus fluids in confined microchannels behave quite differently from unbounded flows. Such configurations can therefore be sensitive to small imperfections in the geometry of the channel; Pravinraj and Patrikar (2018) and Jia et al. (2019) discuss how these effects may help or hinder the desired effect of the device. The effects of surface roughness on microfluidic devices have been extensively studied in a variety of specific scenarios, for example, as a control variable to manipulate the motion of droplets in microfluidic channels (Shastry, Case, and Bohringer, 2005), in oil-water displacement (Bera et al., 2018) and electrokinetic flow in microchannels (Bhattacharyya and Nayak, 2010).

Insights into the effect of geometry on pressure-driven and surface-tension driven flows in microchannels can be gained through an understanding of the static equilibrium state, as this forms the base state for the low capillary number dynamical problem. Recently Johnstone, Hazel, and Jensen (2022) have shown that isolated ridges and grooves can cause significant bending of the contact line of a meniscus in a rectangular channel; the choice of ridges and grooves can be chosen to manipulate the contact line to form specific shapes. However, in reality, surface roughness may not be homogeneous across the length of the channel. We now examine what happens to a static meniscus in a perturbed rectangular channel when the perturbations take the form of small localised bumps.

The history of investigating the behaviour of fluid interfaces in the presence of surface roughness originates with the studies of Wenzel (1936), Cassie and Baxter (1944), and Cassie (1948) who studied the macroscopic effects of a drop sitting on a rough surface. There then followed a series of studies examining the effect of various configurations of surface roughness on droplet wettability, including concentric circular grooves (Johnson and Dettre, 1964), cross, radial and hexagonal grooves (Huh and Mason, 1977) and, most relevant to this study, periodic roughness (Cox, 1983) and random roughness (Jansons, 1985). The latter studies found that periodic and random roughness induced stick-slip behaviour and contact line hysteresis, leading to irreversibility of the wetting process. The study by Jansons (1986) further highlights the role of roughness in inducing complex stick-slip behaviour; a slip condition for fluid flow over rough surfaces was later derived by Miksis and Davis (1994).

In this study, we examine the effect of bump protrusions on a static liquid-vapour interface in a rectangular channel. By changing the liquid volume we obtain a series of quasi-static solutions for the interface shape.

We present the nonlinear Young–Laplace model governing the interface shape in §2; this model is then linearised for small-amplitude perturbations resulting in the governing equation for the interface shape being the Helmholtz equation. In §3 we show how to solve the nonlinear model using Surface Evolver (Brakke, 1992) which uses a gradient-descent method to converge to a surface of minimum energy subject to constraints on the contact angle (through the surface energy) and the liquid volume. The linear model is solved via a finite-difference scheme. For the linear model, we also derive a condition for the pressure difference across the meniscus induced by the perturbations which depends solely on the boundary data and can therefore be found independently of the interface shape. However, in contrast to the analogous result obtained for ridge perturbations, the change in pressure due to the perturbations is not, in general, proportional to the change in channel volume induced by the perturbations. However, cases where the perturbations on the upper and lower wall are identical still result in zero change in channel volume and zero induced pressure difference.

We present preliminary results for the deformation of the meniscus and the shape of the contact line for channel-volume-preserving and channel-volume-changing configurations of axisymmetric bumps in §4. We compute 'quasi-static' solutions at varying channel volumes to examine the behaviour of the meniscus as it moves over the bump. The results indicate that the amplitude of deformation of the meniscus increases as the meniscus approaches

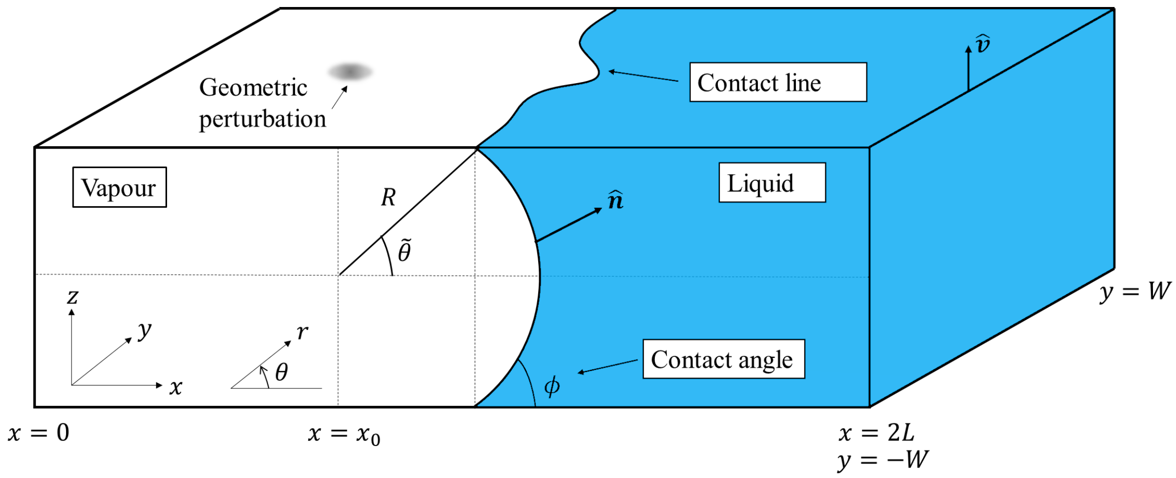

Figure 1: Sketch showing a static meniscus in a rectangular channel $0 \leq x \leq 2L$, $-W \leq y \leq W$, $-1/2 + B_-(x, y) \leq z \leq 1/2 + B_+(x, y)$ with axisymmetric bump perturbations $B_\pm(x, y)$ on the upper and lower walls. The shape of the meniscus is described using cylindrical polar coordinates (r, θ, z) with origin at $(x, y, z) = (x_0, 0, 0)$.

the bump. Then, through smooth deformation of the meniscus shape, the direction of deformation flips as the meniscus crosses the bump. The location of the perturbed contact line relative to its unperturbed location also swaps as the contact line passes over the bump. As in the ridge problem, channel-volume-preserving configurations which do not change the mean curvature of the meniscus lead to contact lines with zero curvature in the far-field, whereas channel-volume-changing configurations have contact lines that curve across the channel. We present some conclusions in §5 and a plan to develop the work further.

2 Model

We consider rectangular containers with edge lengths (which are non-dimensionalised on the channel height) $2L$, $2W$ and 1 in the x, y and z directions respectively (see figure 1), where the height of the channel is sufficiently small compared to the capillary lengthscale so that gravitational effects can be ignored. We fill these containers with a fixed volume of liquid to a static equilibrium position so that we obtain a uniform curvature liquid-vapour interface. For simplicity we take the pressure in the gas phase to be zero, then the pressure difference over the interface is given by the liquid pressure p_L, which is a dimensionless quantity when scaled on surface tension over channel depth. On the upper and lower walls of the channel, we impose a fixed contact angle ϕ between the liquid-vapour and solid-liquid interface where $0 \leq \phi < \pi/2$. On the side walls, we impose a contact angle $\pi/2$. Then the base equilibrium state is the arc of a cylinder of radius R with contact lines on the upper and lower walls at $x = x_0 + R\cos\tilde{\theta}$, where $\tilde{\theta} = \frac{\pi}{2} - \phi$ is the maximum value of the polar angle so that $R\sin\tilde{\theta} = 1/2$. We introduce cylindrical polar coordinates (r, θ, y) such that $(x, y, z) = (x_0 + r\cos\theta,\ y,\ r\sin\theta)$, where x_0 is related to the volume of liquid $V_L^{x_0}$ in the channel as

$$x_0 = 2L - \frac{R}{2}\cos\tilde{\theta} - \frac{V_L^{x_0}}{2W} - R^2\tilde{\theta}. \tag{2.1}$$

Then the base state is given by $r = R \equiv 1/(2\sin\tilde{\theta})$, for $\theta \in [-\tilde{\theta},\ \tilde{\theta}\,]$ and $y \in [-W,\ W]$, with $p_L = -1/R$.

We then assume that the upper (+) and lower (−) walls have bump perturbations described by $z = \pm\frac{1}{2} + B_{\pm}(x, y)$. We examine how the meniscus interacts with the wall perturbations at the microscopic level; that is, we do not assume contact angle hysteresis. We consider a series of equilibrium solutions where each solution is defined by the volume of liquid $V_L^{x_0}$. Thus the interface location is specified by perturbations to the radial and angular polar coordinates relative to the base state with origin at $x = x_0$:

$$r = R + F(y, \theta; x_0), \quad \theta \in [\tilde{\theta} + \Phi_-(y; x_0),\ \tilde{\theta} + \Phi_+(y; x_0)], \quad y \in [-W, W]. \tag{2.2}$$

Assuming that the gas pressure always stays zero, for each liquid volume $V_L^{x_0}$ we solve for the pressure difference across the meniscus $p_L^{x_0} = -R^{-1} + (p_L)_p^{x_0}$, where $(p_L)_p^{x_0}$ is the change in pressure of the liquid phase due to the channel perturbations for the equilibrium solution associated with the base state with origin at $x = x_0$. We find this by solving the Young–Laplace equation, which relates the uniform mean curvature of the interface to the pressure difference across the meniscus $p_L^{x_0}$, using the unit normal which points into the liquid phase $\hat{\boldsymbol{n}}^{x_0}$:

$$\Delta p^{x_0} = -\nabla \cdot \hat{\boldsymbol{n}}^{x_0}|_{r=R+F^{x_0}} = -\frac{1}{\mathscr{L}} + \left(\frac{(R+F^{x_0})F_y^{x_0}}{\mathscr{L}}\right)_y + \frac{1}{R+F^{x_0}}\left(\frac{F_\theta^{x_0}}{\mathscr{L}}\right)_\theta, \tag{2.3}$$

where $\mathscr{L} \equiv \sqrt{(R+F^{x_0})^2(1+F_y^{x_0\,2}) + F_\theta^{x_0\,2}}$, $F^{x_0} = F(y,\theta;x_0)$ and

$$\hat{\boldsymbol{n}}^{x_0} = \frac{[(R+F^{x_0})\cos\theta + F_\theta^{x_0}\sin\theta]\hat{\boldsymbol{x}} + [(R+F^{x_0})\sin\theta - F_\theta^{x_0}\cos\theta]\hat{\boldsymbol{z}} - (R+F^{x_0})F_y^{x_0}\hat{\boldsymbol{y}}}{\mathscr{L}}. \tag{2.4}$$

We impose boundary conditions that the contact line must touch the perturbed channel walls,

$$\Big(R + F(y,\theta;x_0)\Big)\sin\theta = \pm\frac{1}{2} + B_\pm\Big(x_0 + (R+F(y,\theta;x_0))\cos\theta, y\Big) \quad \text{at } \theta = \pm\tilde{\theta} + \Phi_\pm(y;x_0). \tag{2.5}$$

Note here that we have to include the x-dependence of the wall shape through the polar coordinate parametrisation; that is, we evaluate the shape of the wall at the (unknown) contact line location.

Next, to impose a contact angle ϕ on the upper and lower channel walls we firstly let $\hat{\boldsymbol{v}}_\pm$ be the unit normals to the upper and lower channel walls pointing out of the channel. So,

$$\hat{\boldsymbol{v}}_\pm = \pm\frac{-\dfrac{\partial B_\pm}{\partial x}\hat{\boldsymbol{x}} - \dfrac{\partial B_\pm}{\partial y}\hat{\boldsymbol{y}} + \hat{\boldsymbol{z}}}{\sqrt{1 + \left(\dfrac{\partial B_\pm}{\partial x}\right)^2 + \left(\dfrac{\partial B_\pm}{\partial y}\right)^2}}, \tag{2.6}$$

where $B_\pm = B_\pm(x,y)$. Then we define $\hat{\boldsymbol{v}}_\pm^{x_0}$ to be the unit normal evaluated at the point where the contact line of the meniscus associated with the base state at origin $x = x_0$ touches the wall. That is, we evaluate $\hat{\boldsymbol{v}}_\pm$ at $x = x_0 + (R + F(y,\theta;x_0))\cos\theta$, with $\theta = \pm\tilde{\theta} + \Phi_\pm(y;x_0)$.

Then, the contact angle condition is given by

$$\hat{\boldsymbol{n}}^{x_0} \cdot \hat{\boldsymbol{v}}_{\pm}^{x_0} = \cos\phi \text{ at } \theta = \pm\tilde{\theta} + \Phi_{\pm}(y; x_0), \tag{2.7}$$

where $\hat{\boldsymbol{n}}^{x_0}$ (given by (2.4)) is evaluated at $\theta = \pm\tilde{\theta} + \Phi_{\pm}(y; x_0)$. The contact-line displacement on the upper and lower walls $x_{\pm}(y; x_0)$ is given by

$$x_{\pm}(y; x_0) = x_0 + \Big(R + F^{x_0}(y, \pm\tilde{\theta} + \Phi_{\pm}^{x_0}(y)\Big) \cos\Big(\pm\tilde{\theta} + \Phi_{\pm}^{x_0}(y)\Big). \tag{2.8}$$

To impose a contact angle $\pi/2$ on the side walls, we require

$$F_y(\pm W, \theta; x_0) = 0. \tag{2.9}$$

Finally, we impose that changes to channel volume due to the perturbations do not change the liquid volume $V_L^{x_0}$.

2.1 Linear model

We consider perturbations of small maximum amplitude ϵ relative to (non-dimensional) unit channel depth, so that $B_{\pm}(x, y) = \epsilon b_{\pm}(x, y)$, where $b_{\pm}(x, y) = O(1)$ as $\epsilon \to 0$. We linearise the nonlinear model (2.2) with the assumption that, for each fixed liquid volume $V_L^{x_0}$, the resulting radial perturbations and change in contact line location are also $O(\epsilon)$ and the perturbations lead to an $O(\epsilon)$ change in pressure difference across the meniscus. Thus, we write $(p_L)_p^{x_0} = \epsilon p^{x_0}$, so that $p_L^{x_0} = -R^{-1} + \epsilon p^{x_0}$, with $F(y, \theta; x_0) = \epsilon f(y, \theta; x_0)$ and $\Phi_{\pm}(y; x_0) = \epsilon\Theta_{\pm}(y; x_0)$, so that the interface location is given by

$$r = R + \epsilon f(y, \theta; x_0), \quad \theta \in \Big[-\tilde{\theta} + \epsilon\,\Theta_-(y; x_0),\ \tilde{\theta} + \epsilon\,\Theta_+(y; x_0)\Big], \quad y \in [-W, W]. \tag{2.10}$$

As in the the case of ridge perturbations (Johnstone, Hazel, and Jensen, 2022), the leading order approximation to the Young–Laplace equation (2.3) is the Helmholtz equation

$$\frac{1}{R^2} f^{x_0} + \frac{1}{R^2} f^{x_0}_{\theta\theta} + f^{x_0}_{yy} = p^{x_0}, \quad y \in [-W, W],\ \theta \in [-\tilde{\theta}, \tilde{\theta}], \tag{2.11}$$

where $f^{x_0} = f(y, \theta; x_0)$. At $O(\epsilon)$, the boundary condition (2.5) constraining the contact line to lie on the upper and lower walls is

$$R \cos\tilde{\theta}\ \Theta_\pm(y) \pm f(y, \pm\tilde{\theta}; x_0) \sin\tilde{\theta} = b_\pm(x_0 + R\cos\tilde{\theta}, y), \tag{2.12}$$

while the $O(\epsilon)$ expansion of boundary condition (2.7) fixing the contact angle is

$$\cos\tilde{\theta} \left(f_\theta(y, \pm\tilde{\theta}; x_0) + R \left.\frac{\partial b_\pm}{\partial x}\right|_{(x_0 + R\cos\tilde{\theta}, y)} - R\,\Theta_\pm(y; x_0) \right) = 0. \tag{2.13}$$

Combining (2.12)–(2.13) gives a single condition for the solution f^{x_0} in terms of the boundary data:

$$f(y, \pm\tilde{\theta}; x_0) \sin\tilde{\theta} \pm f_\theta(y, \pm\tilde{\theta}; x_0) \cos\tilde{\theta} = \pm b_\pm(x_0 + R\cos\tilde{\theta}, y) \mp R\cos\tilde{\theta} \left.\frac{\partial b_\pm}{\partial x}\right|_{(x_0 + R\cos\tilde{\theta}, y)}. \tag{2.14}$$

The linearised contact-line displacement on the upper and lower walls $x_\pm(y; x_0)$ is found by Taylor expanding the displacement equation (2.8) for $x = x_0 + r\cos\theta$ at $\theta = \pm\tilde{\theta} + \epsilon\Theta_\pm(y; x_0)$:

$$x_\pm(y; x_0) = x_0 + R\cos\tilde{\theta} + \epsilon x_p^\pm(y; x_0) + O(\epsilon^2), \tag{2.15}$$

$$x_p^\pm(y; x_0) = f(y, \pm\tilde{\theta}; x_0) \cos\tilde{\theta} \mp f_\theta(y, \pm\tilde{\theta}; x_0) \sin\tilde{\theta} \mp R\sin\tilde{\theta} \left.\frac{\partial b_\pm}{\partial x}\right|_{(x_0 + R\cos\tilde{\theta}, y)}. \tag{2.16}$$

The side wall boundary condition (2.9) becomes

$$f_y(\pm W, \theta; x_0) = 0. \tag{2.17}$$

We note that although we have imposed side wall boundary conditions (2.17) on f^{x_0}, the contact line displacement $x_p^{\pm}(y;x_0)$ does not necessarily have zero y-derivative; this is because through linearisation we have projected the contact line displacement onto a flat wall which results in an extra gradient term appearing. However if we insist that the bumps are not located close to the side walls in wide channels, then the gradient of the bump will be negligibly small for $y = \pm W$.

The system (2.11), (2.14), (2.17) has infinitely many solutions because if $h(\theta, y)$ is a solution, then $h + \lambda \cos\theta$ is also a solution for any $\lambda \in \mathbb{R}$. Therefore to fix one solution we finally insist that the volume of liquid $V_L^{x_0}$ is invariant with respect to changes in channel volume; for a full derivation see appendix A. This condition is

$$\int_{-W}^{W} \int_{-\tilde{\theta}}^{\tilde{\theta}} f^{x_0}(y,\theta)\ \mathrm{d}\theta\ \mathrm{d}y = \frac{1}{R} \int_{-W}^{W} \int_{x_0 + R\cos\tilde{\theta}}^{2L} (b_+(x,y) - b_-(x,y))\ \mathrm{d}x\ \mathrm{d}y = \mathscr{V}^{x_0}, \tag{2.18}$$

where $\mathscr{V}^{x_0}$, which is a constant for each x_0, is the change in vapour volume due to the perturbations for a fixed liquid volume $V_L^{x_0}$.

2.1.1 Zero contact angle

When the contact angle ϕ on the upper and lower walls is zero (so that $\tilde{\theta} = \pi/2$), the meniscus meets the walls tangentially. The problem remains the same however an expansion to powers of $O(\epsilon^2)$ is needed to obtain boundary condition (2.13) which then says:

$$f_\theta\left(y, \pm\frac{\pi}{2}; x_0\right) + R\frac{\partial b_\pm}{\partial x}\bigg|_{(x_0,y)} - R\,\Theta_\pm(y;x_0) = 0. \tag{2.19}$$

2.1.2 Finding the pressure from the boundary data

We can exploit the fact that the Helmholtz equation is self-adjoint to derive an independent equation for the change in pressure difference over the meniscus due to small-amplitude perturbations for which the linear model is valid.

For each fixed x_0, we multiply the Helmholtz equation (2.11) in the domain $D = [-W, W] \times [-\tilde{\theta}, \tilde{\theta}]$ by a smooth, twice differentiable test function $g^{x_0}(\theta) = g(\theta; x_0) : [-\tilde{\theta}, \tilde{\theta}] \to \mathbb{R}$ such that

$$R^{-2}[(g^{x_0})'' + g^{x_0}] = a^{x_0} \in \mathbb{R}; \quad g(\pm\tilde{\theta}; x_0) = \gamma_{\pm}^{x_0}, \quad g'(\pm\tilde{\theta}; x_0) = \zeta_{\pm}^{x_0}, \tag{2.20}$$

where $a^{x_0}, \gamma_{\pm}^{x_0}$ and $\zeta_{\pm}^{x_0}$ are constants associated with each function g^{x_0}. After integrating over the domain D, we obtain

$$\int_D a^{x_0} f^{x_0} + \tilde{\nabla} \cdot (g^{x_0} \tilde{\nabla} f^{x_0} - f^{x_0} \tilde{\nabla} g^{x_0}) \, \mathrm{d}A = \int_D g^{x_0} p^{x_0} \, \mathrm{d}A, \tag{2.21}$$

where $\tilde{\nabla} = (\partial_y, R^{-1}\partial_\theta)$ is the rescaled divergence operator. After application of the two-dimensional divergence theorem and the boundary conditions on g^{x_0}, we obtain

$$\begin{aligned} \int_D a^{x_0} f^{x_0} \, \mathrm{d}A + R^{-2} \int_{-W}^{W} [-\gamma_{-}^{x_0} f_{\theta}^{x_0}(y, -\tilde{\theta}) + \zeta_{-}^{x_0} f^{x_0}(y, -\tilde{\theta}) + \gamma_{+}^{x_0} f_{\theta}^{x_0}(y, \tilde{\theta}) - \zeta_{+}^{x_0} f^{x_0}(y, \tilde{\theta})] \, \mathrm{d}y \\ = \int_D g^{x_0} p^{x_0} \, \mathrm{d}A. \end{aligned} \tag{2.22}$$

The choice of test function $g(\theta; x_0) = \cos\theta$ conveniently leads to $a^{x_0} = 0$, $\gamma_{\pm}^{x_0} = \cos\tilde{\theta}$ and $\zeta_{\pm}^{x_0} = \mp \sin\tilde{\theta}$ for all x_0). After applying the boundary conditions (2.14) on f^{x_0}, we obtain an independent equation for the pressure:

$$\begin{aligned} p^{x_0} = {} & \frac{1}{4WR^2 \sin(\tilde{\theta})} \int_{-W}^{W} \left\{ b_+(x_0 + R\cos\tilde{\theta}, y) - b_-(x_0 + R\cos\tilde{\theta}, y) \right\} \, \mathrm{d}y \\ & - \frac{1}{4WR^2 \sin(\tilde{\theta})} \int_{-W}^{W} \left\{ R\cos\tilde{\theta} \left(\left.\frac{\partial b_+}{\partial x}\right|_{(x_0 + R\cos\tilde{\theta}, y)} - \left.\frac{\partial b_-}{\partial x}\right|_{(x_0 + R\cos\tilde{\theta}, y)} \right) \right\} \, \mathrm{d}y. \end{aligned} \tag{2.23}$$

So the pressure can be determined before solving for the equilibrium solution and it depends on the amplitude of the perturbation and its gradient.

2.1.3 Pressure-volume relationship

Comparing the volume condition (2.18) and the independent pressure condition (2.23), we now see that, unlike in the ridge problem, there is no link between the induced pressure difference over the meniscus being zero and the change in channel volume due to the perturbations being zero. However, special cases of perturbations with $b_+ = b_-$ will still lead to zero induced pressure difference and zero change in channel volume, whereas perturbations with $b_+ = -b_-$ will lead to both a change in channel volume and a change in pressure difference across the meniscus (and therefore the perturbations will change the mean curvature of the meniscus).

3 Methods

For the remainder of this study, we consider Gaussian perturbations of the form

$$B_-(x,y) = \epsilon \exp\left(-\frac{(x-x_c^-)^2}{s} - \frac{y^2}{s}\right), \quad b_-(x,y) = \exp\left(-\frac{(x-x_c^-)^2}{s} - \frac{y^2}{s}\right), \tag{3.1}$$

$$B_+(x,y) = \epsilon a \exp\left(-\frac{(x-x_c^+)^2}{s} - \frac{y^2}{s}\right), \quad b_+(x,y) = a \exp\left(-\frac{(x-x_c^+)^2}{s} - \frac{y^2}{s}\right), \tag{3.2}$$

where ϵ is the maximum amplitude of the bump, $a = \pm 1$ to define the orientation of the bump on the upper wall, s defines the width of the perturbations, and the parameter $x_c^{\pm}$ controls their location in the x direction. For the remainder of this study we take $x_c^+ = x_c^-$.

3.1 Nonlinear problem: Surface Evolver solution

We use Surface Evolver (Brakke, 1992) to solve the nonlinear problem. We mesh an initial guess for the wetted surface, comprising the solid-liquid and liquid-vapour interfaces, by specifying the vertices, edges (connecting vertices) and facets (enclosed by edges) of the initial wetted surface. For computational efficiency, we mesh the surface from $-W \leq y \leq 0$ as the problem is symmetric about $y = 0$. For this problem the initial guess specifies the solid-liquid interfaces exactly since these are known and approximates the unknown liquid-vapour interface by a flat plane; we have found that this is sufficient for convergence. Then, the surface is parametrised by the set of vertex coordinates $\boldsymbol{X}$, and the total energy of the surface is a function $E(\boldsymbol{X})$ which we work to minimise subject to constraints.

The first constraint imposes that vertices on the solid-liquid interface must stay in contact with the solid surface; this is a local condition on each vertex $X_i \in \boldsymbol{X}$. We implement this condition by specifying the level set that each vertex must lie on. This condition removes one degree of freedom from the problem for each constrained vertex.

Second, we fix the volume of liquid enclosed by the wetted surface; this is a global constraint and implementation is handled internally by Surface Evolver once the liquid volume is specified. Denoting the wetted surface of the channel (the blue surfaces in figure 1) by S, the volume of liquid $V_L^{x_0}$ is calculated in terms of S using the three-dimensional divergence theorem: defining a vector $\boldsymbol{F}$ such that $\boldsymbol{\nabla} \cdot \boldsymbol{F} = 1$,

$$V_L^{x_0} = \iiint_{V_L^{x_0}} 1 \; \mathrm{d}V = \iiint_{V_L^{x_0}} \boldsymbol{\nabla} \cdot \boldsymbol{F} \; \mathrm{d}V = \iint_S \boldsymbol{F} \cdot \hat{\boldsymbol{v}} \; \mathrm{d}A, \tag{3.3}$$

where as described in §2, $\hat{\boldsymbol{v}}$ is the outward pointing unit normal to the wetted surface S and the most convenient choice is $\boldsymbol{F} = x\hat{\boldsymbol{x}}$. (In Surface Evolver, $\boldsymbol{F} = z\hat{\boldsymbol{z}}$ ensures that volumes are calculated by projecting surfaces onto the plane $z = 0$, so in practice we solve the problem rotated by 90°.) The global volume condition removes one degree of freedom from the problem.

In addition, we wish to impose a contact angle on the solid-liquid interface. We specify a contact angle α_w on the wetted surface S through the surface energy E_s of the wall,

$$E_S = \iint_S -\cos\alpha_w \; \mathrm{d}A. \tag{3.4}$$

Thus, we fix the surface energy of the facets comprising the solid-liquid interface. Each facet has a surface tension which is one unless the user specifies otherwise. After specifying the contact angle, the calculation of surface energy is handled internally by Surface Evolver: the contribution to the total energy is the sum of all the facet areas times their respective surface tensions. Thus, this constraint does not change the number of degrees of freedom in the problem. We denote that wetted sections of the upper and lower walls at $z = \pm 1/2 + B_\pm(x, y)$ by $S_\pm$, and the wetted sections of the side walls at $y = \pm W$ by $S_{\pm W}$ respectively. We take $\alpha_w = \phi$ on $S_\pm$ and $\alpha_w = \pi/2$ on $S_{\pm W}$ (so that the energy of the side walls is zero).

We then iterate towards a surface of minimum energy; details of the iteration process are given in appendix B. We converge to an energy minimum by iteratively refining the mesh and using quadratic convergence methods to converge the solution on this mesh to within a specified tolerance. The process stops when the difference in surface energy between solutions on consecutive meshes is within a specified tolerance. We use a tolerance of 10^{-7} for the accuracy of the solution on each mesh and the difference between the surface energy of the equilibrium solutions between meshes. We check for positive eigenvalues of the Hessian of the energy function $E(\boldsymbol{X})$ near the equilibrium to ensure a minimum has been reached.

3.2 Linear problem: finite difference scheme for solutions

For each liquid volume V^{x_0}, we implement a second-order-accurate central finite-difference scheme to integrate the linearised system (2.11), (2.14), (2.17) and (2.18). We discretise the system on a five-point stencil for a rectangular grid for $-W \leq y \leq W$, $-\tilde{\theta} \leq \theta \leq \tilde{\theta}$. Therefore $\theta = j\Delta\theta = \theta_j$ for $0 \leq j \leq M+1$, $y = k\Delta y = y_k$ for $0 \leq k \leq N+1$, where the grid size is $\Delta\theta = 2\tilde{\theta}/(M+1)$ and $\Delta y = 2W/(N+1)$. Then the solution at each grid point is $f^{x_0}(y_k, \theta_j) = f_j^k$, where the x_0 superscript notation is dropped for clarity.

On the interior of the grid, the discretisation of the Helmholtz equation (2.11) is

$$\frac{1}{R^2}\frac{1}{\Delta\theta^2}f_{j-1}^k + \frac{1}{R^2}\frac{1}{\Delta\theta^2}f_{j+1}^k + \frac{1}{\Delta y^2}f_j^{k-1} + \frac{1}{\Delta y^2}f_j^{k+1} + \left(\frac{1}{R^2} - \frac{2}{R^2}\frac{1}{\Delta\theta^2} - \frac{2}{\Delta y^2}\right)f_j^k = p^{x_0},$$
$$1 \leq j \leq M, 1 \leq k \leq N, \tag{3.5}$$

where p^{x_0} is found for the Gaussian perturbations (3.1)–(3.2) from the independent pressure condition (2.23).

The Robin boundary conditions (2.14) and Neumann boundary conditions (2.17) are implemented at the edges of the grid; at the corners both boundary conditions are valid but we implement the more restrictive Robin condition (2.14). Thus at the edges of the grid,

$$\sin\tilde{\theta} f_0^k - \cos\tilde{\theta}\,\frac{-3f_0^k + 4f_1^k - f_2^k}{2\Delta\theta} = K_-(y_k), \quad 0 \le k \le N+1, \tag{3.6}$$

$$\sin\tilde{\theta} f_{M+1}^k + \cos\tilde{\theta}\,\frac{f_{M-1}^k - 4f_M^k + 3f_{M+1}^k}{2\Delta\theta} = K_+(y_k), \quad 0 \le k \le N+1, \tag{3.7}$$

$$\frac{-3f_j^0 + 4f_j^1 - f_j^2}{2\Delta y} = 0, \quad 1 \le j \le M, \tag{3.8}$$

$$\frac{f_j^{N-1} - 4f_j^N + 3f_j^{N+1}}{2\Delta y} = 0, \quad 1 \le j \le M, \tag{3.9}$$

where

$$K_\pm^{x_0}(y) = \pm b_\pm(x_0 + R\cos\tilde{\theta}, y) \mp R\cos\tilde{\theta}\left.\frac{\partial b_\pm}{\partial x}\right|_{(x_0+R\cos\tilde{\theta},y)}. \tag{3.10}$$

Finally, as discussed in §2.1, without the volume condition the Helmholtz equation (2.11) together with the boundary conditions (2.14), (2.17) has infinitely many solutions, and we thus close the system with the volume condition (2.18).

In the ridge problem (Johnstone, Hazel, and Jensen, 2022) we implemented the volume condition using quadrature by replacing one line of the matrix with the discretised volume constraint. However, this approach does not work in the current problem as the degree of freedom in the continuous problem does not directly translate to the discrete problem, as the matrix of coefficients of the discretised system is near singular but has a zero eigenvalue only in the limit of Δy, $\Delta\theta \to 0$. This discrepancy could occur because the finite difference scheme used is not conserving fluxes however we have not had time to investigate this further.

As discussed in §2, $\cos\theta$ is an eigenmode of the continuous problem, which is removed via the volume condition. Therefore to implement the volume condition we write

$$\tilde{f}_j^k = f_j^k + \lambda \cos\theta_j, \tag{3.11}$$

where $\lambda \in \mathbb{R}$ is a free variable. We substitute this solution into the discretised equations (3.5)–(3.9). The inclusion of the free variable λ provides the degree of freedom necessary to impose the volume constraint which we implement via trapezium rule:

$$\begin{aligned} &\int_{-W}^{W}\int_{-\tilde{\theta}}^{\tilde{\theta}} f^{x_0}(y,\theta)\ \mathrm{d}\theta\ \mathrm{d}y \\ &\approx \frac{W}{(N+1)}\frac{\tilde{\theta}}{(M+1)}\left(f_0^0 + 2\sum_{j=1}^{M} f_j^0 + f_{M+1}^0 + 2\sum_{k=1}^{N}\left(f_0^k + 2\sum_{j=1}^{M} f_j^k + f_{M+1}^k\right)\right. \\ &\qquad\qquad \left. + f_0^{N+1} + 2\sum_{j=1}^{M} f_j^{N+1} + f_{M+1}^{N+1}\right). \end{aligned} \tag{3.12}$$

The discretised system comprises $(M+2)(N+2)+1$ equations: MN for the Helmholtz equation (3.5), together with $2(M+N+2)$ for the boundary conditions (3.6)–(3.9), and one for the volume condition (3.12). The matrix of coefficients is of size $((M+2)(N+2)+1) \times ((M+2)(N+2)+1)$. The first $(M+2)(N+2)$ rows and columns of the matrix have a block structure, with each block being of size $(M+2)\times(M+2)$, and with $(N+2)$ block rows and $(N+2)$ block columns. The matrix of coefficients is given in Appendix C for a very simplified case with $M = N = 1$.

We solve the system using a direct solver which takes advantage of the sparsity in the matrix structure. We use a grid with $M = 37$ interior grid points in the θ direction and $N = 2003$ interior grid points in the y direction.

4 Results

We present preliminary results for solutions of the linear and nonlinear models to show the effect of small-amplitude Gaussian perturbations ($b_\pm(x,y)$ as described in (3.1)–(3.2)) on the

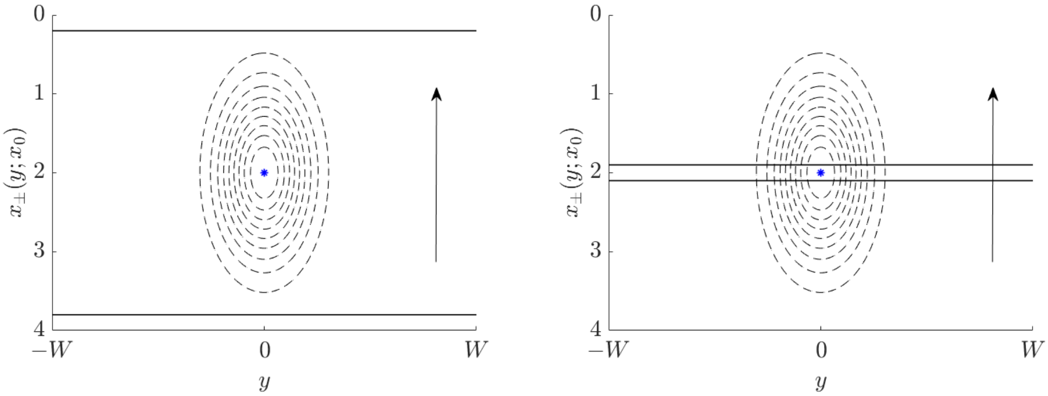

(a) $V_L^{x_0} \approx 1.85$ and $V_L^{x_0} \approx 37.85$ (b) $V_L^{x_0} \approx 18.85$ and $V_L^{x_0} \approx 20.85$

Figure 2: The location of the unperturbed contact line for (a) figures 3–4 and (b) figures 5–6 with $s_x = s_y = 1$, $x_c^{\pm} = 2$, $W = 5$, $L = 2$ and $\phi = 85$. The black solid lines denote the unperturbed contact line location. The black dashed lines denote amplitude contours of the perturbation $b_{\pm}(x, y)$ at 10% intervals. The blue dot denotes the centre of the perturbation. The arrow denotes the direction of increasing liquid volume.

shape of the meniscus and contact line. We generate quasi-static solutions by solving the linear and nonlinear problems for increasing values of the liquid volume $V_L^{x_0}$ from (2.18), corresponding to decreasing values of x_0 (see figure 1). We show solutions for mirror anti-symmetric ($b_+ = b_-$) channel-volume-preserving and mirror-symmetric ($b_+ = -b_-$) channel-volume-changing perturbations, with the centre of the bumps on the upper and lower wall at $x_c^{\pm} = 2$ which is in the middle of the channel.

We first consider two pairs of solutions for menisci situated behind and in front of the bump; the locations of the unperturbed contact lines for each pair are shown in figure 2. In figures 3 and 4, we show the upper and lower contact lines, together with the radial perturbation f^{x_0} to the meniscus, for menisci situated far behind and far in front of the bump (corresponding to initial contact line locations shown in figure 2a). Note that we plot the contact lines from the viewpoint of looking down on the channel with decreasing x-values on the vertical axis corresponding to the direction of increasing channel volume as shown in figure 1. The solutions retain the characteristics of the ridge problem (Johnstone, Hazel, and Jensen, 2022). We see a smooth deformation of the meniscus and contact line with zero curvature in the far-field for channel-volume-preserving perturbations (figure 3) since the perturbations have not induced a change in pressure difference, i.e. mean curvature. Meanwhile, the meniscus and contact line are curved in the far-field for channel-volume-changing perturbations (figure 4).

We note that there is a slight disagreement between the Surface Evolver and linear solutions in the location of the contact line for the channel-volume-changing perturbations (figure 4). Examination of the linear solution for varying M and N shows that the error does not decrease with grid size, therefore is not due to imposing the volume condition via the trapezium rule (as described in §3.2). However, this volume condition, and the governing Helmholtz equation (2.11) and boundary conditions (2.12)–(2.14), are only correct to $O(\epsilon)$, which is larger than the error seen in the contact line location. Thus it is likely that the discrepancy in contact line locations is within the error of the approximation.

The red colour in the heat map indicates an increase in radius r so that the meniscus is pushed into the liquid phase, whereas blue colours correspond to the meniscus moving towards the vapour phase. The maximum amplitude of the change in meniscus shape f^{x_0} is slightly greater behind the bump (figures 3a, 4a) than in front of it (figures 3b, 4b). Bump intrusions cause the contact line to move in a different direction from the protrusions. Moreover, the direction of displacement of both the meniscus and the contact lines flips as the meniscus crosses the bump.

Solutions for menisci that are closer to the centre of the bump (figures 5 and 6) show that the maximum amplitude of the radial perturbation f^{x_0} is significantly greater just behind the bump (figures 5a, 6a) than just in front of it (figures 5b, 6b). Thus the meniscus bulges as it approaches the bump, but experiences less deformation as it passes over the top. However, this change in amplitude is not reflected in the amplitude of the contact line displacement, which remains similar on both sides of the bump.

To examine this further, in figures 8 and 9 we plot the upper and lower contact lines, together with the radial perturbation f^{x_0} to the meniscus, as the meniscus travels over the

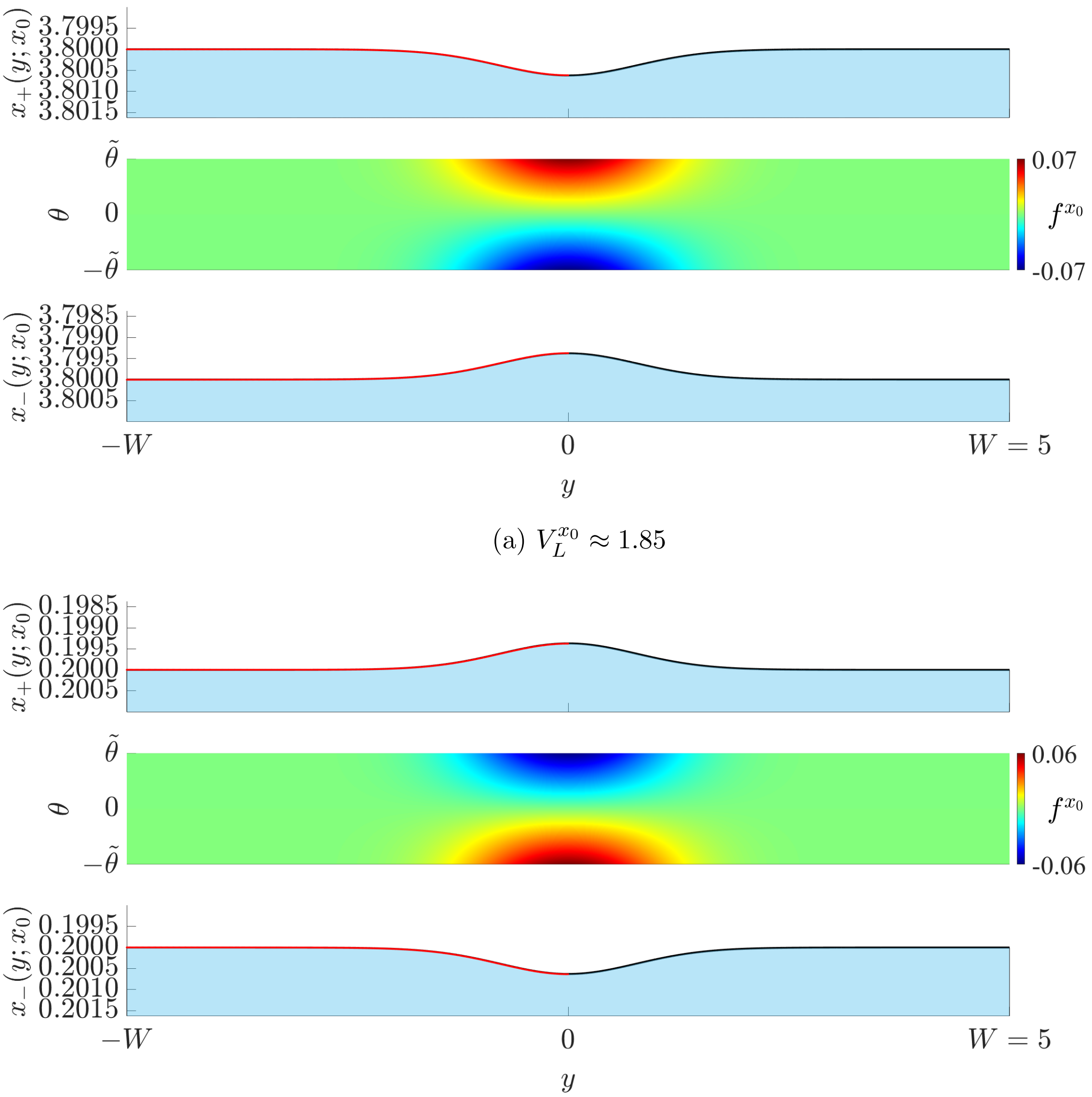

(a) $V_L^{x_0} \approx 1.85$

(b) $V_L^{x_0} \approx 37.85$

Figure 3: The upper and lower contact line displacement $x_\pm(y)$ (black/red line plots), together with the radial perturbation f^{x_0} to the meniscus (heat map), for mirror anti-symmetric channel-volume-preserving Gaussian perturbations with $a = 1$, $s_x = s_y = 1$, $x_c^\pm = 2$, $W = 5$, $L = 2$, $\phi = 85$, and $\epsilon = 0.01$. The contact lines are plotted as viewed looking down on the channel, with the liquid shaded blue as shown in figure 1. The black line denotes the linear solution, $x_\pm$ from (2.15), and the red line denotes the Surface Evolver solution computed in a half channel $-W \leq y \leq 0$. In the heat map, positive and negative values indicate deformation towards the liquid and vapour respectively. Figures (a) and (b) are for $x_0 + R\cos\tilde{\theta} = 3.8$ and 0.2, which correspond to liquid volumes $V_L^{x_0} \approx 1.85$, $V_L^{x_0} \approx 37.85$ respectively.

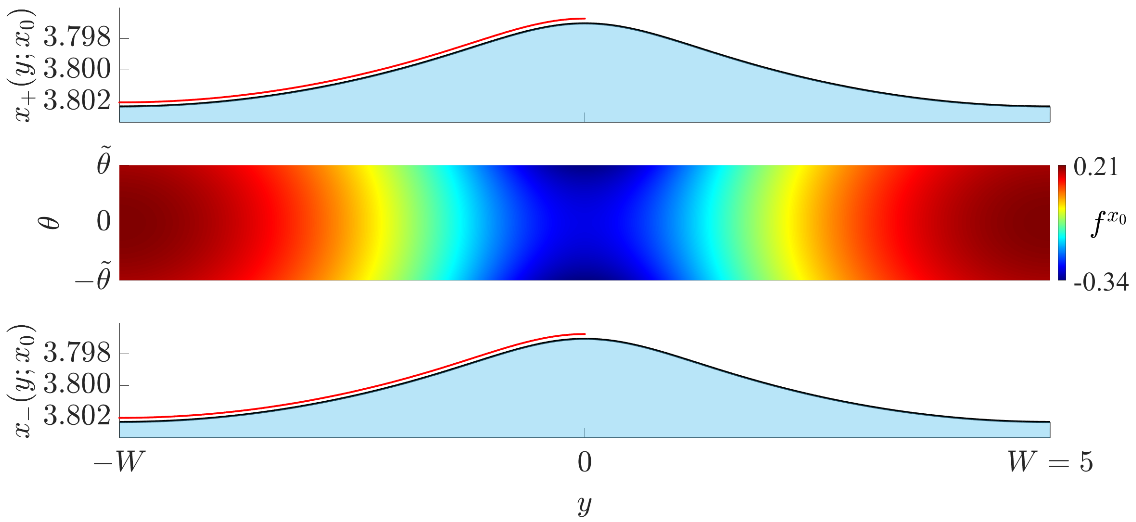

(a) $V_L^{x_0} \approx 1.85$

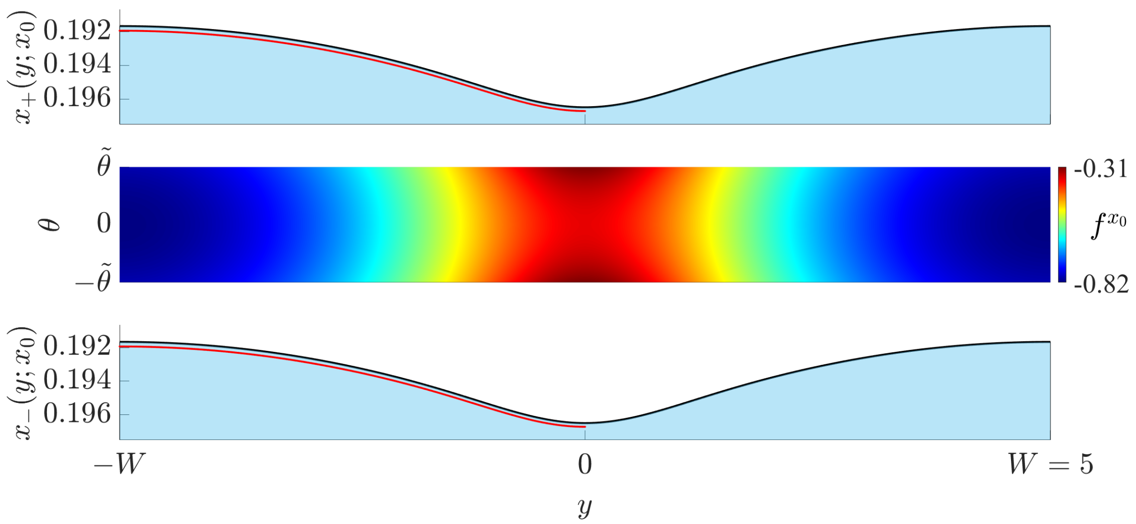

(b) $V_L^{x_0} \approx 37.85$

Figure 4: The upper and lower contact line displacement $x_\pm(y)$ (black/red line plots), together with the radial perturbation f^{x_0} to the meniscus (heat map), for mirror symmetric channel-volume-changing Gaussian perturbations with $a=-1$, $s_x=s_y=1$, $x_c^\pm=2$, $W=5$, $L=2$, $\phi=85$, and $\epsilon=0.01$. The contact lines are plotted as viewed looking down on the channel, with the liquid shaded blue as shown in figure 1. The black line denotes the linear solution, $x_\pm$ from (2.15), and the red line denotes the Surface Evolver solution computed in a half channel $-W \leq y \leq 0$. In the heat map, positive and negative values indicate deformation towards the liquid and vapour respectively. Figures (a) and (b) are for $x_0+R\cos\tilde{\theta}=3.8$ and 0.2, which correspond to liquid volumes $V_L^{x_0}\approx 1.85$, $V_L^{x_0}\approx 37.85$ respectively.

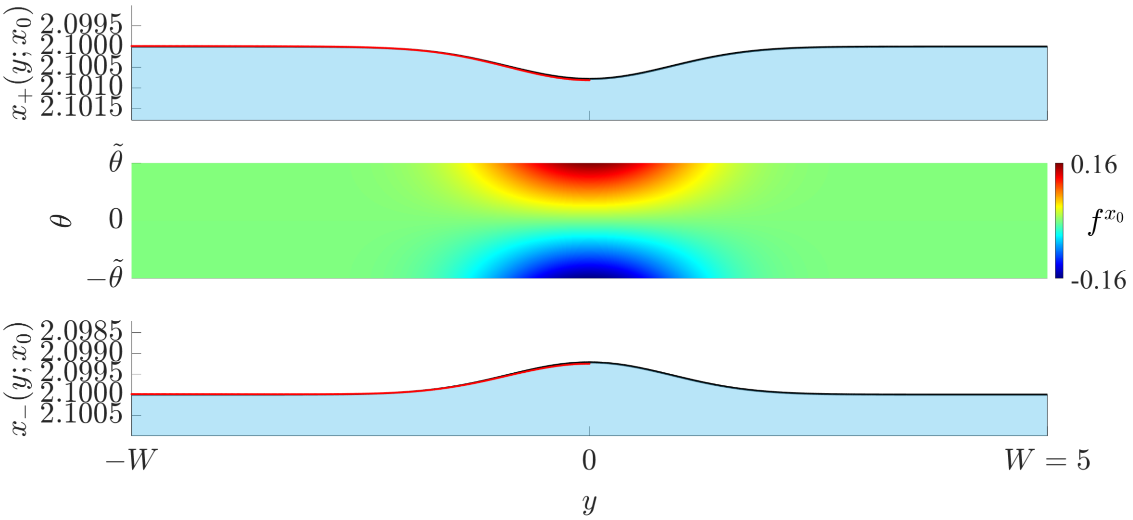

(a) $V_L^{x_0} \approx 18.85$

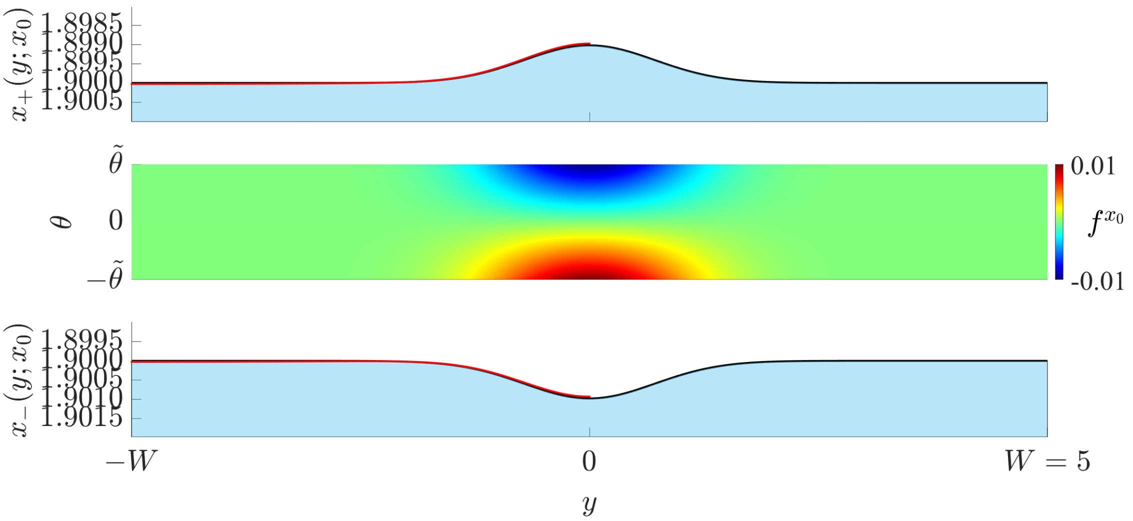

(b) $V_L^{x_0} \approx 20.85$

Figure 5: The upper and lower contact line displacement $x_\pm(y)$ (black/red line plots), together with the radial perturbation f^{x_0} to the meniscus (heat map), for mirror anti-symmetric channel-volume-preserving Gaussian perturbations with $a = 1$, $s_x = s_y = 1$, $x_c^\pm = 2$, $W = 5$, $L = 2$, $\phi = 85$, and $\epsilon = 0.01$. The contact lines are plotted as viewed looking down on the channel, with the liquid shaded blue as shown in figure 1. The black line denotes the linear solution, $x_\pm$ from (2.15), and the red line denotes the Surface Evolver solution computed in a half channel $-W \leq y \leq 0$. In the heat map, positive and negative values indicate deformation towards the liquid and vapour respectively. Figures (a) and (b) are for $x_0 + R\cos\tilde{\theta} = 2.1$ and 1.9, which correspond to liquid volumes $V_L^{x_0} \approx 18.85$, $V_L^{x_0} \approx 20.85$ respectively.

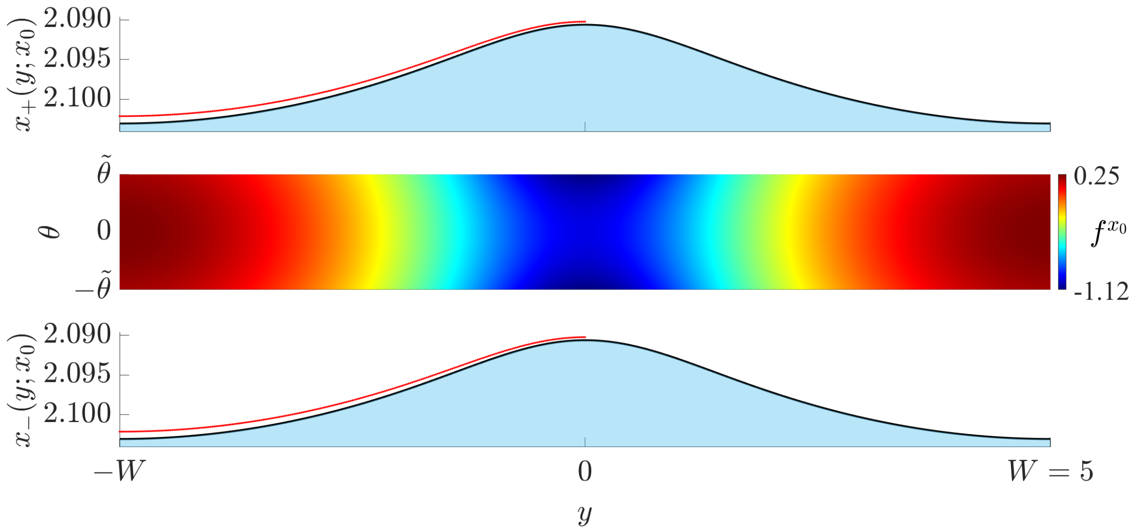

(a) $V_L^{x_0} \approx 18.85$

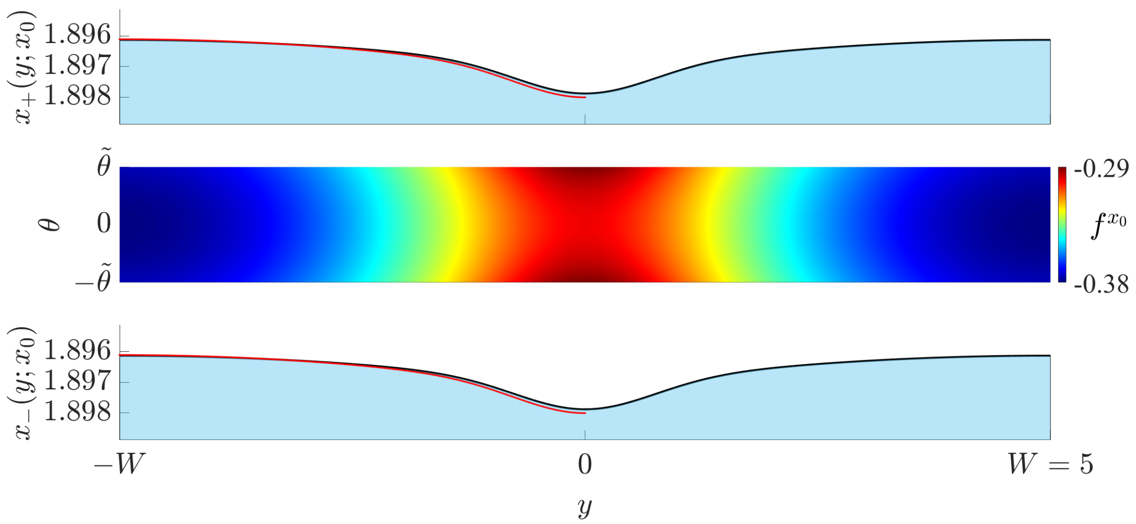

(b) $V_L^{x_0} \approx 20.85$

Figure 6: The upper and lower contact line displacement $x_\pm(y)$ (black/red line plots), together with the radial perturbation f^{x_0} to the meniscus (heat map), for mirror symmetric channel-volume-changing Gaussian perturbations with $a = -1$, $s_x = s_y = 1$, $x_c^\pm = 2$, $W = 5$, $L = 2$, $\phi = 85$, and $\epsilon = 0.01$. The contact lines are plotted as viewed looking down on the channel, with the liquid shaded blue as shown in figure 1. The black line denotes the linear solution, $x_\pm$ from (2.15), and the red line denotes the Surface Evolver solution computed in a half channel $-W \leq y \leq 0$. In the heat map, positive and negative values indicate deformation towards the liquid and vapour respectively. Figures (a) and (b) are for $x_0 + R\cos\tilde{\theta} = 2.1$ and 1.9, which correspond to liquid volumes $V_L^{x_0} \approx 18.85$, $V_L^{x_0} \approx 20.85$ respectively.

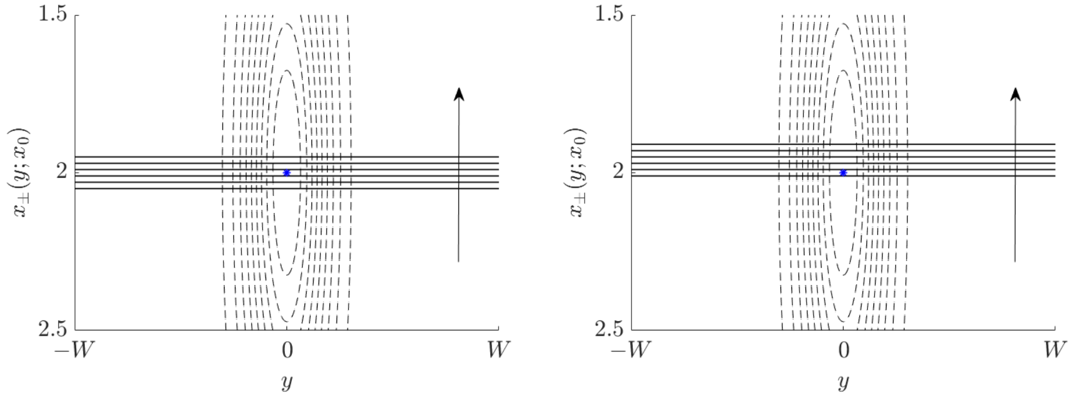

(a) $V_L^{x_0} \approx 19.35$ to 20.35.

(b) $V_L^{x_0} \approx 19.75$ to 20.75.

Figure 7: The location of the unperturbed contact line for (a) figure 8 and (b) figure 9. The black solid lines denote the unperturbed contact line location. The black dashed lines denote amplitude contours of the perturbation $b_\pm(x, y)$ at 10% intervals. The blue dot denotes the centre of the perturbation. The arrow denotes the direction of increasing liquid volume.

centre of the bump; the configurations are shown in figure 7. The figures show the smooth change in the direction of the contact line displacement as the meniscus travels over the bump.

First, we note that the change in sign of the radial perturbation f^{x_0} does not occur as the meniscus passes over the centre of the bump at $x = 2$. As the meniscus travels over the bump, the meniscus continues to bulge in the same direction, although the amplitude of deformation decreases until there is eventually negligible deformation, at which point the meniscus starts to bulge in the opposite direction so that we obtain the results seen in figures 5 and 6. However, the change in direction of the displacement of the contact line occurs for smaller liquid volumes than the change in direction of the deformation of the meniscus. The expansion of the contact line solution in (2.15) contains gradients of the boundary data $b_\pm(x)$. This term is due to the calculation of the contact line location as a projection onto a flat plane. The derivative changes sign for $x < x_c^\pm$ and $x > x_c^\pm$. Therefore, even while the sign of radial perturbation f^{x_0} has not changed, this term causes the direction of the contact line displacement to change.

From figures 8 and 9, we also see that the contact line shape and amplitude of displacement of the contact line are not symmetric on each side of the bump. Again, this is because the change in sign of the radial perturbation f^{x_0} does not occur directly over the top of the bump, but the change in sign of the gradient term in the contact line equation (2.15) does.

5 Dicussion

We have presented preliminary results for the deformation of a meniscus due to small-amplitude isolated Gaussian bumps on the walls of a rectangular channel. We restricted our attention to mirror anti-symmetric channel-volume-preserving and mirror-symmetric channel-volume-changing perturbations. We derived a linear argument to show that the pressure induced by the former perturbations is zero, leading to solutions with zero far-field mean curvature. The predictions of the contact line and meniscus shape from a linear model are confirmed by computations of the full nonlinear solution using Surface Evolver (Brakke, 1994).

Furthermore, our results indicate that the deformation of the meniscus as it travels over the bump is not symmetric on each side of the bump. The amplitude of the deformation of the meniscus increases as it approaches the bump so that the meniscus bulges. Then as the meniscus crosses the centre of the bump the amplitude of deformation decreases and becomes almost negligible. The direction of deformation then changes and grows in amplitude again as the liquid volume is increased further.

We obtained the Surface Evolver solutions by meshing the entire liquid-vapour interface. This could lead to issues with larger-amplitude, sharper or more complex perturbation shapes where meshing with triangles could become computationally expensive. An alternative implementation would be to mesh only the liquid-vapour interface and include the energy and volume contributions of the un-meshed surfaces via line integrals using Stokes' theorem; see appendix 3.A for more details. However, this is a difficult problem for the bump perturbations discussed here and we have not been able to find a solution.

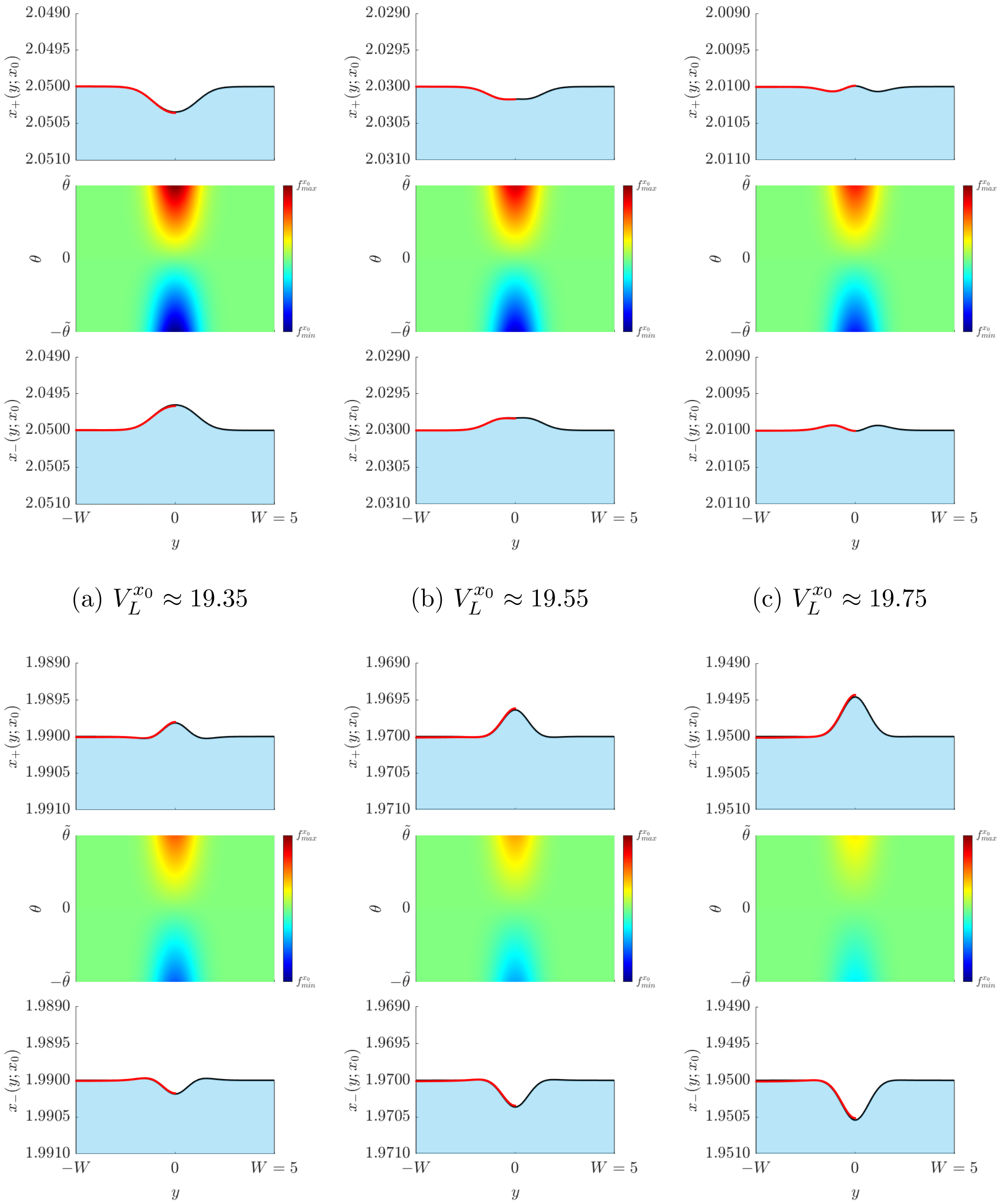

(a) $V_L^{x_0} \approx 19.35$ (b) $V_L^{x_0} \approx 19.55$ (c) $V_L^{x_0} \approx 19.75$

(d) $V_L^{x_0} \approx 19.95$ (e) $V_L^{x_0} \approx 20.15$ (f) $V_L^{x_0} \approx 20.35$

Figure 8: The upper and lower contact line displacement $x_{\pm}(y)$ (black/red line plots)(black/red line plots), together with the radial perturbation f^{x_0} to the meniscus (heat map), for mirror anti-symmetric channel-volume-preserving Gaussian perturbations with $a = 1$, $s_x = s_y = 1$, $x_c^{\pm} = 2$, $W = 5$, $L = 2$, $\phi = 85$, and $\epsilon = 0.01$. The black and red lines denote the linear and Surface Evolver solutions respectively. Figures (a)–(f) are for $x_0 + R\cos\tilde{\theta} = 2.05, 2.03, 2.01, 1.99, 1.97$ and 1.95, which correspond to liquid volumes $V_L^{x_0} \approx 19.35, 19.55, 19.75.19.95, 20.15$ and $V_L^{x_0} \approx 20.35$ respectively. On the colourbar $f^{x_0}_{min} = -0.12$, $f^{x_0}_{max} = 0.12$.

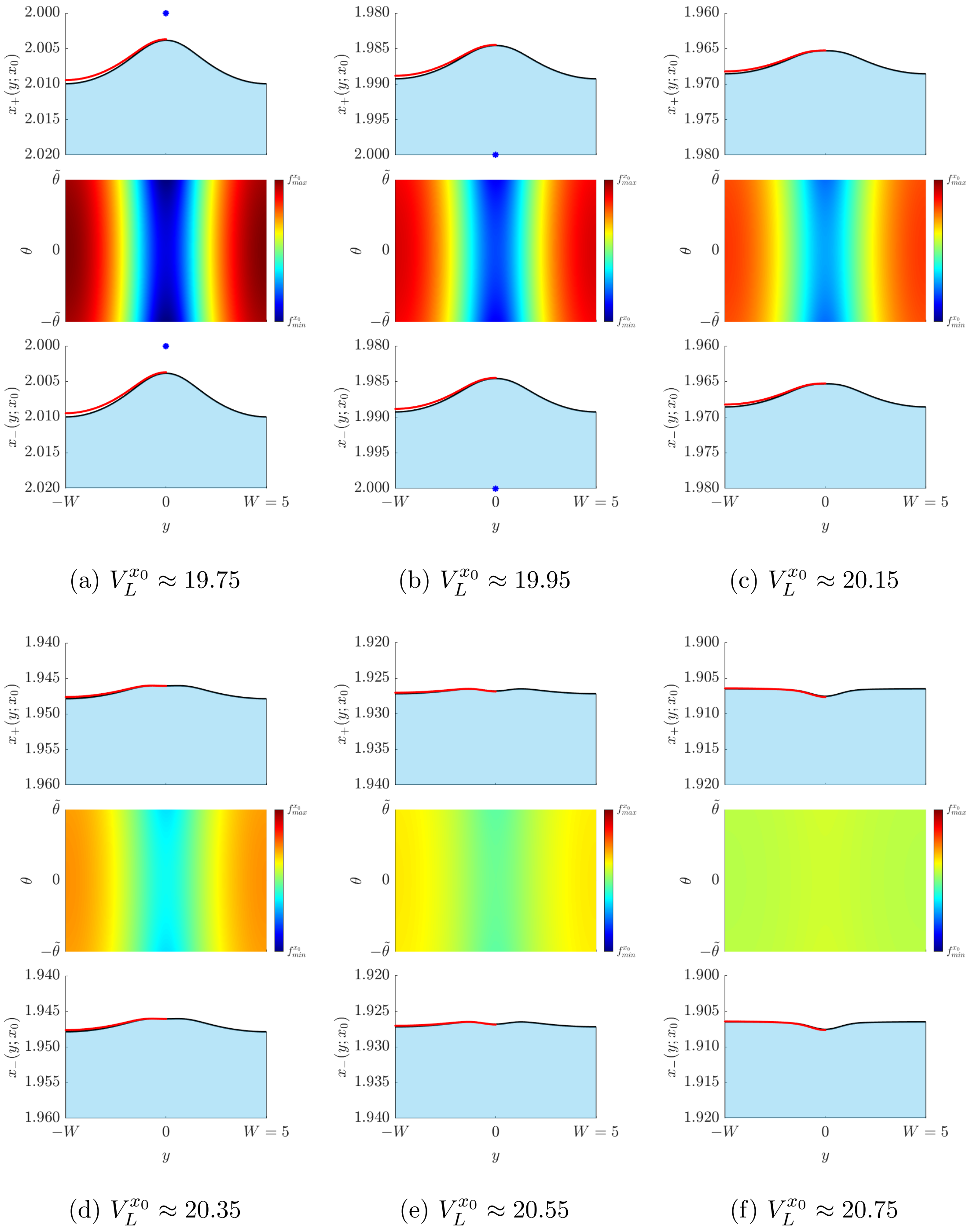

Figure 9: The upper and lower contact line displacement $x_{\pm}(y)$ (black/red line plots), together with the radial perturbation f^{x_0} to the meniscus (heat map), for mirror symmetric channel-volume-changing Gaussian perturbations with $a = -1$, $s_x = s_y = 1$, $x_c^{\pm} = 2$, $W = 5$, $L = 2$, $\phi = 85$, and $\epsilon = 0.01$. The black and red lines denote the linear and Surface Evolver solutions respectively. Figures (a)–(f) are for $x_0 + R\cos\tilde{\theta} = 2.01, 1.99, 1.97, 1.95, 1.93$ and 1.91, which correspond to liquid volumes $V_L^{x_0} \approx 19.75, 19.95, 20.15, 20.35, 20.55$ and $V_L^{x_0} \approx 20.75$ respectively. The blue dot denotes the centre of the bump. On the colourbar $f_{min}^{x_0} = -0.75$, $f_{max}^{x_0} = -0.03$.

Obtaining solutions to the nonlinear problem using Surface Evolver was challenging and therefore due to time constraints, we have only presented preliminary results here for a narrow range of parameters. There is thus ample scope for future work which will initially consist of three parts. First, we wish to understand in more detail the deformation of the meniscus as it travels over the bump, including the bulging effect and the asymmetry as a function of the liquid volume. Next, we wish to examine the system for a wider range of parameters. Specifically, we wish to focus on the effect of the width of the bump and its location in the y-direction. In the ridge problem (Johnstone, Hazel, and Jensen, 2022), changing the location of the ridge caused a scattering effect which led to large-amplitude displacement of the contact line even for small-amplitude perturbations; we might expect to see similar behaviour here. Finally, we wish to extend this analysis by considering arrays of isolated bumps, which are a more realistic representation of the surface roughness found in industrial and biological problems. Understanding this surface roughness is important in developing models of dynamic contact angles and hysteresis effects.

Finally, we would also like to investigate the zero contact angle dynamical problem for low capillary numbers. This relates to the Bretherton problem (Bretherton, 1961), which investigates the steady motion of an air finger in a tube using lubrication theory. The motion of the finger deposits thin fluid films on the walls of the channel. It would be intriguing to consider how the presence of a bump affects the shape of the meniscus and the films.

Acknowledgements

We would like to thank Professor Simon Cox from the University of Aberystwyth for his advice about computing the nonlinear Surface Evolver solutions.

References

Wenzel, R. N. (1936). "Resistance of solid surfaces to wetting by water". *Industrial & Engineering Chemistry* 28.8, pp. 988–994.

Cassie, A. B. D. and Baxter, S. (1944). "Wettability of porous surfaces". *Trans. Faraday Soc.* 40 (0), pp. 546–551.

Cassie, A. B. D. (1948). "Contact angles". *Discuss. Faraday Soc.* 3 (0), pp. 11–16.

Bretherton, F. P. (1961). "The motion of long bubbles in tubes". *J. Fluid Mech.* 10.2, pp. 166–188.

Johnson, R. E. and Dettre, R. H. (1964). "Contact Angle Hysteresis. III. Study of an Idealized Heterogeneous Surface". *J. Physical Chemistry* 68.7, pp. 1744–1750.

Huh, C. and Mason, S. (1977). "Effects of surface roughness on wetting (theoretical)". *J. Colloid and Interface Science* 60.1, pp. 11–38.

Cox, R. G. (1983). "The spreading of a liquid on a rough solid surface". *J. Fluid Mech.* 131, pp. 1–26.

Jansons, K. M. (1985). "Moving contact lines on a two-dimensional rough surface". *J. Fluid Mech.* 154, pp. 1–28.

Jansons, K. M. (1986). "Moving contact lines at non-zero capillary number". *J. Fluid Mech.* 167, pp. 393–407.

Brakke, K. A. (1992). "The Surface Evolver". *Experimental Mathematics* 1.2, pp. 141–165.

Brakke, K. A. (1994). "Surface Evolver Manual". *Mathematics Department, Susquehanna Univerisity, Selinsgrove, PA.*

Miksis, M. J. and Davis, S. H. (1994). "Slip over rough and coated surfaces". *J. Fluid Mech.* 273, pp. 125–139.

Stone, H. A., Stroock, A. D., and Ajdari, A. (2004). "Engineering flows in small devices: microfluidics toward a lab-on-a-chip". *Annu. Rev. Fluid Mech.* 36, pp. 381–411.

Shastry, A., Case, M. J., and Bohringer, K. (2005). “Engineering surface roughness to manipulate droplets in microfluidic systems”. *18th IEEE International Conference on Micro Electro Mechanical Systems, 2005. MEMS 2005.* IEEE, pp. 694–697.

Ajaev, V. S. and Homsy, G. (2006). “Modeling shapes and dynamics of confined bubbles”. *Annu. Rev. Fluid Mech.* 38, pp. 277–307.

Bhattacharyya, S. and Nayak, A. (2010). “Combined effect of surface roughness and heterogeneity of wall potential on electroosmosis in microfluidic/nanofuidic channels”. *J. Fluids Eng.* 132.4.

Anna, S. L. (2016). “Droplets and bubbles in microfluidic devices”. *Annu. Rev. Fluid Mech.* 48, pp. 285–309.

Bera, B., Hauner, I., Qazi, M., Bonn, D., and Shahidzadeh, N. (2018). “Oil-water displacements in rough microchannels”. *Phys. Fluids* 30.11, p. 112101.

Pravinraj, T. and Patrikar, R. (2018). “Modeling and characterization of surface roughness effect on fluid flow in a polydimethylsiloxane microchannel using a fractal based lattice Boltzmann method”. *AIP Advances* 8.6, p. 065112.

Jia, J., Song, Q., Liu, Z., and Wang, B. (2019). “Effect of wall roughness on performance of microchannel applied in microfluidic device”. *Microsystem Technologies* 25.6, pp. 2385–2397.

Venkatesan, S., Jerald, J., Asokan, P., and Prabakaran, R. (2020). “A comprehensive review on microfluidics technology and its applications”. *Recent Advances in Mechanical Engineering*, pp. 235–245.

Johnstone, E. C., Hazel, A. L., and Jensen, O. E. (2022). “The effect of isolated ridges and grooves on static menisci in rectangular channels”. *J. Fluid Mech.* 935, A32.

Appendix A Volume Constraint

To find the volume constraint we first find the volume of the perturbed channel, then we find the volume of the vapour in the perturbed channel. Then we use the fact that the volume of vapour plus the volume of liquid must equal the channel volume to obtain a condition for the interface location.

A.1 Volume of the perturbed channel

The volume of the perturbed channel is given by

$$\begin{aligned}\hat{V}_C &= \int_{-W}^{W}\int_{0}^{2L}\int_{-\frac{1}{2}+B_-(x,y)}^{\frac{1}{2}+B_+(x,y)} \mathrm{d}z\ \mathrm{d}x\ \mathrm{d}y \\ &= \int_{-W}^{W}\int_{0}^{2\,L} \left(1 + B_+\left(x,y\right) - B_-\left(x,y\right)\right) \mathrm{d}x\,\mathrm{d}y. \end{aligned} \tag{A.1}$$

After linearisation, the expansion of the channel volume to $O(\epsilon)$ is

$$\hat{V}_C = 4\,W L + \epsilon \int_{0}^{2\,L}\int_{-W}^{W} \left(b_+\left(x,y\right) - b_-\left(x,y\right)\right) \mathrm{d}y\,\mathrm{d}x. \tag{A.2}$$

A.2 Volume of vapour in the perturbed channel

We find the volume of vapour in the perturbed channel for a meniscus with liquid volume $V_L^{x_0}$; that is, a meniscus with contact location specified relative to unperturbed location at $x = x_0$. Using the three-dimensional divergence theorem, the volume of vapour $\hat{V}_V$ in the perturbed channel is given by

$$\begin{aligned}\iiint_{\hat{V}_V} \mathrm{d}V &= \iiint_{\hat{V}_V} \boldsymbol{\nabla}\cdot\left(z\hat{\boldsymbol{z}}\right)\,\mathrm{d}V, \\ &= \iint_{S_{\hat{V}_V}} \left(z\hat{\boldsymbol{z}}\right)\cdot\hat{\boldsymbol{N}}\ \mathrm{d}\Sigma, \end{aligned} \tag{A.3}$$

where $S_{\hat{V}_V}$ is the surface enclosing the vapour volume $\hat{V}_V$ and $\hat{\boldsymbol{N}}$ is the outward pointing unit normal to this surface. As shown in figure 1, the surface $S_{\hat{V}_V}$ is comprised of six parts: the end wall at $x = 0$, the side walls at $y = \pm W$, the upper and lower walls at $z = \pm\frac{1}{2} + B_{\pm}(x, y)$ and the liquid-vapour interface at $r = R + F^{x_0}(y, \theta)$. Only the upper/lower walls and the liquid-vapour interface contribute to the volume calculation since on the other parts of the surface $z\hat{\boldsymbol{z}} \cdot \hat{\boldsymbol{N}} = 0$.

We first consider the surface integral on the upper wall. This surface is parametrised by

$$(x, y, z) \mapsto \boldsymbol{g}_+(x, y) = \left(x, y, \frac{1}{2} + B_+(x, y)\right), \tag{A.4}$$

$$0 \le x \le x_+(y), \quad -W \le y \le W, \tag{A.5}$$

where $x_+^{x_0}(y) = x_0 + \left(R + F^{x_0}(y, \tilde{\theta} + \Phi_+^{x_0}(y)\right) \cos\left(\tilde{\theta} + \Phi_+^{x_0}(y)\right)$ is the location of the upper contact line. So the volume contribution from the surface integral (A.3) over the upper wall is

$$\hat{V}_{V+} = \int_{y=-W}^{W} \int_{x=0}^{x_+^{x_0}(y)} \left(\frac{1}{2} + B_+(x, y)\right) \hat{\boldsymbol{z}} \cdot \hat{\boldsymbol{N}} \left| \frac{\partial \boldsymbol{g}_+}{\partial x} \times \frac{\partial \boldsymbol{g}_+}{\partial y} \right| \,\mathrm{d}x\,\mathrm{d}y, \tag{A.6}$$

where on the upper wall

$$\hat{\boldsymbol{N}} = \frac{-\dfrac{\partial B_+}{\partial x}\hat{\boldsymbol{x}} - \dfrac{\partial B_+}{\partial y}\hat{\boldsymbol{y}} + \hat{\boldsymbol{z}}}{\sqrt{1 + \left(\dfrac{\partial B_+}{\partial x}\right)^2 + \left(\dfrac{\partial B_+}{\partial y}\right)^2}}. \tag{A.7}$$

After linearising, the expansion to $O(\epsilon)$ is

$$\begin{aligned}
\hat{V}_{V+} &= \int_{y=-W}^{W} \int_{x=0}^{x_0+R\cos\tilde{\theta}+\epsilon(f^{x_0}(y,\tilde{\theta})\cos\tilde{\theta}-\Theta_+^{x_0}(y)R\sin\tilde{\theta})} \left(\frac{1}{2}+\epsilon b_+(x,y)\right) \,\mathrm{d}x\,\mathrm{d}y \\
&= W(x_0+R\cos\tilde{\theta}) \\
&+ \epsilon\left(\int_{-W}^{W} \frac{-\Theta_+^{x_0}(y)R\sin\tilde{\theta}}{2} + \frac{f^{x_0}(y,\tilde{\theta})\cos\tilde{\theta}}{2}\,\mathrm{d}y + \int_{-W}^{W}\int_{0}^{x_0+R\cos\tilde{\theta}} b_+(x,y)\,\mathrm{d}x\,\mathrm{d}y\right).
\end{aligned} \tag{A.8}$$

Similarly, the volume contribution from the surface integral (A.3) over the lower wall is

$$\begin{aligned}
\hat{V}_{V-} &= W(x_0+R\cos\tilde{\theta}) \\
&+ \epsilon\left(\int_{-W}^{W} \frac{\Theta_-^{x_0}(y)R\sin\tilde{\theta}}{2} + \frac{f^{x_0}(y,-\tilde{\theta})\cos\tilde{\theta}}{2}\,\mathrm{d}y - \int_{-W}^{W}\int_{0}^{x_0+R\cos\tilde{\theta}} b_-(x,y)\,\mathrm{d}x\,\mathrm{d}y\right).
\end{aligned} \tag{A.9}$$

Finally we consider the surface integral over the liquid-vapour interface, which is parametrised in cylindrical polar coordinates $(x,y,z)=(x_0+r\cos\theta,\ y,\ r\sin\theta)$ by

$$(x,y,z)\mapsto \boldsymbol{g}_{LV}(y,\theta) = \left(x_0+\Big(R+F^{x_0}(y,\theta)\Big)\cos\theta, y, \Big(R+F^{x_0}(y,\theta)\Big)\sin\theta\right), \tag{A.10}$$

$$-W\le y\le W, \quad -\tilde{\theta}+\Phi_-^{x_0}(y)\le\theta\le\tilde{\theta}+\Phi_+^{x+0}(y). \tag{A.11}$$

In the cylindrical polar coordinate system that describes the liquid-vapour interface, $\hat{\boldsymbol{z}} = \sin\theta\hat{\boldsymbol{r}}+\cos\theta\hat{\boldsymbol{\theta}}$, so that the volume contribution from the surface integral (A.3) over the liquid-vapour interface is

$$\hat{V}_{V_{LV}} = \int_{y=-W}^{W}\int_{\theta=-\tilde{\theta}+\Phi_-^{x_0}(y)}^{\tilde{\theta}+\Phi_+^{x_0}(y)} \Big(R+F^{x_0}(y,\theta)\Big)\sin\theta(\sin\theta\hat{\boldsymbol{r}}+\cos\theta\hat{\boldsymbol{\theta}})\cdot\hat{\boldsymbol{N}}\left|\frac{\partial\boldsymbol{g}_{LV}}{\partial y}\times\frac{\partial\boldsymbol{g}_{LV}}{\partial\theta}\right|\,\mathrm{d}\theta\,\mathrm{d}y, \tag{A.12}$$

where on the liquid-vapour interface,

$$\hat{\boldsymbol{N}} = \frac{(R+F^{x_0})\hat{\boldsymbol{r}} - F^{x_0}_{\theta}\hat{\boldsymbol{\theta}} - (R+F^{x_0})F^{x_0}_{y}\hat{\boldsymbol{y}}}{\mathscr{L}}, \tag{A.13}$$

, with $\mathscr{L} \equiv \sqrt{(R+F^{x_0})^2(1+F^{x_0\,2}_{y}) + F^{x_0\,2}_{\theta}}$. After linearising, the expansion to $O(\epsilon)$ is

$$\begin{aligned}
\hat{V}_{V_{LV}} &= \int_{y=-W}^{W}\int_{\theta=-\tilde{\theta}+\epsilon\Theta^{x_0}_{-}(y)}^{\tilde{\theta}+\epsilon\Theta^{x_0}_{+}(y)} R^2\sin^2\theta + \epsilon R\sin\theta\left(2f^{x_0}(y,\theta)\sin\theta - \cos\theta\frac{\partial f^{x_0}(y,\theta)}{\partial\theta}\right)\,\mathrm{d}\theta\,\mathrm{d}y \\
&= 2R^2W(-\cos\tilde{\theta}\sin\tilde{\theta}+\tilde{\theta}) \\
&+ \epsilon R\int_{-W}^{W}\int_{-\tilde{\theta}}^{\tilde{\theta}} -\sin\theta\left(\cos\theta\frac{\partial f^{x_0}(y,\theta)}{\partial\theta} - 2f^{x_0}(y,\theta)\sin\theta\right)\,\mathrm{d}\theta\,\mathrm{d}y \\
&- \epsilon R^2\sin^2\tilde{\theta}\int_{-W}^{W}\left(\Theta^{x_0}_{-}(y) - \Theta^{x_0}_{+}(y)\right)\,\mathrm{d}y.
\end{aligned} \tag{A.14}$$

So to $O(\epsilon)$, the total volume of vapour is given by $\hat{V}_V = \hat{V}_{V+} + \hat{V}_{V-} + \hat{V}_{V_{LV}}$. Using the fact that $2R\sin\tilde{\theta} = 1$, and using integration by parts on the $f^{x_0}_{\theta}$ term in the integral over θ yields

$$\begin{aligned}
\hat{V}_V = 2W&\left(\frac{R\cos\tilde{\theta}}{2} + R^2\tilde{\theta} + x_0\right) + \epsilon R\int_{-W}^{W}\int_{-\tilde{\theta}}^{\tilde{\theta}} f(y,\theta)\,\mathrm{d}\theta\,\mathrm{d}y \\
&+ \epsilon\int_{-W}^{W}\int_{0}^{x0+R\cos\tilde{\theta})}(b_+(x,y) - b_-(x,y))\,\mathrm{d}x\,\mathrm{d}y.
\end{aligned} \tag{A.15}$$

A.3 The volume condition

We find the volume condition by imposing $\hat{V}_c = \hat{V}_V + V^{x_0}_L$. At $O(1)$, this gives the equation for the liquid volume (2.1),

$$V^{x_0}_L = 4WL - 2Wx_0 - RW\cos\tilde{\theta} - 2WR^2\tilde{\theta}. \tag{A.16}$$

Meanwhile at $O(\epsilon)$, we obtain the volume constraint (2.18):

$$\int_{-W}^{W}\int_{-\tilde{\theta}}^{\tilde{\theta}} f^{x_0}(y,\theta)\ \mathrm{d}\theta\ \mathrm{d}y = \frac{1}{R}\int_{-W}^{W}\int_{x_0+R\cos\tilde{\theta}}^{2L}(b_+(x,y)-b_-(x,y))\ \mathrm{d}x\ \mathrm{d}y. \tag{A.17}$$

Appendix B Iterating to a minimum energy configuration in Surface Evolver

The technical details presented here are based on the material given in Brakke (1994). Evolver iterates through configurations of vertices $\mathbf{X}$ to minimise the total energy $E(\boldsymbol{X})$ of the surface subject to the constraints described above; without gravitational energy, this is just the surface energy so Evolver works to minimise the area of the wetted surface. The iteration step reduces the energy whilst obeying any imposed constraints.

Each iteration causes a small perturbation $\Delta\boldsymbol{X}$ to the configuration of vertices $\boldsymbol{X}$. The resulting energy is approximated by a multivariate Taylor expansion:

$$E(\boldsymbol{X}+\Delta\boldsymbol{X}) = E(\boldsymbol{X}) + \boldsymbol{G}^T\Delta\boldsymbol{X} + \frac{1}{2}(\Delta\boldsymbol{X})^T H\Delta\boldsymbol{X}, \tag{B.1}$$

where $\boldsymbol{G}$ is the gradient and H is the Hessian, and superscript T denotes transpose. The gradient term gives the best linear approximation to the energy of the perturbed surface, whilst the second term gives the best quadratic approximation.

The simplest mode of iteration in Surface Evolver is a linear gradient-descent method that applies a force to each vertex which is proportional to the negative gradient of energy $-\boldsymbol{G}^T$. However, if the quadratic approximation $\frac{1}{2}(\Delta\boldsymbol{X})^T H\Delta\boldsymbol{X}$ is very close to the equilibrium then it is possible to find the equilibrium by solving for $\Delta\boldsymbol{X}$ such that $\boldsymbol{G}^T\Delta\boldsymbol{X} = 0$. This requires $\Delta\boldsymbol{X} = -H^{-1}\boldsymbol{G}$, so the Hessian matrix H needs to be invertible. The Newton-Raphson iteration to find such a $\Delta\boldsymbol{X}$ is handled internally by Surface Evolver. This method requires the surface to be close enough to the equilibrium that the quadratic approximation is valid. There is an alternative method that tries to minimize energy along the direction found by Newton's method using the Hessian, which can be used when the surface is much further from equilibrium.

The form of the quadratic term indicates the stability of configuration; the surface is at a local minimum if H is positive definite. Moreover, the eigenvectors and eigenvalues of H can also be used to check stability: the eigenvectors can be thought of as modes of perturbation of a surface, so negative eigenvalues lead to the growth of perturbations (because the force is the negative of the energy gradient).

Appendix C Finite difference matrix system

We show the matrix system for solving the linearised model as described in §3.2 for a very simplified case where $M = N = 1$. The system takes the form $A\mathbf{f} = \mathbf{b}$ where A is a matrix of size $((M+2)(N+2)+1) \times ((M+2)(N+2)+1)$, and $\mathbf{f}$ and $\mathbf{b}$ are vectors of length $(M+2)(N+2)+1$. We first show the matrix A of the coefficients of the discretised equations with $L = \left(\frac{1}{R^2} - 2\frac{1}{R^2}\frac{1}{\Delta\theta^2} - 2\frac{1}{\Delta y^2}\right)$ and $a = \sin\tilde{\theta}$, $b = \cos\tilde{\theta}$:

$$A = \left[\begin{array}{ccc|ccc|ccc|c}
a - b\left(\frac{-3}{2\Delta\theta}\right) & (-b)\left(\frac{2}{\Delta\theta}\right) & (-b)\left(\frac{-1}{2\Delta\theta}\right) & 0 & 0 & 0 & 0 & 0 & 0 & \gamma_0 \\
0 & \frac{-3}{2\Delta y} & 0 & 0 & \frac{2}{\Delta y} & 0 & 0 & \frac{-1}{2\Delta y} & 0 & 0 \\
b\left(\frac{1}{2\Delta\theta}\right) & b\left(\frac{-2}{\Delta\theta}\right) & a + b\left(\frac{3}{2\Delta\theta}\right) & 0 & 0 & 0 & 0 & 0 & 0 & \gamma_2 \\
\hline
0 & 0 & 0 & a - b\left(\frac{-3}{2\Delta\theta}\right) & (-b)\left(\frac{2}{\Delta\theta}\right) & (-b)\left(\frac{-1}{2\Delta\theta}\right) & 0 & 0 & 0 & \gamma_0 \\
0 & \frac{1}{\Delta y^2} & 0 & \frac{1}{R^2}\frac{1}{\Delta\theta^2} & L & \frac{1}{R^2}\frac{1}{\Delta\theta^2} & 0 & \frac{1}{\Delta y^2} & 0 & \gamma_1 \\
0 & 0 & 0 & b\left(\frac{1}{2\Delta\theta}\right) & b\left(\frac{-2}{\Delta\theta}\right) & a + b\left(\frac{3}{2\Delta\theta}\right) & 0 & 0 & 0 & \gamma_2 \\
\hline
0 & 0 & 0 & 0 & 0 & 0 & a - b\left(\frac{-3}{2\Delta\theta}\right) & (-b)\left(\frac{2}{\Delta\theta}\right) & (-b)\left(\frac{-1}{2\Delta\theta}\right) & \gamma_0 \\
0 & \frac{1}{2\Delta y} & 0 & 0 & \frac{-2}{\Delta y} & 0 & 0 & \frac{3}{2\Delta y} & 0 & 0 \\
0 & 0 & 0 & 0 & 0 & 0 & b\left(\frac{1}{2\Delta\theta}\right) & b\left(\frac{-2}{\Delta\theta}\right) & a + b\left(\frac{3}{2\Delta\theta}\right) & \gamma_2 \\
\hline
1 & 2 & 1 & 2 & 4 & 2 & 1 & 2 & 1 & 0
\end{array}\right]. \tag{C.1}$$

Here,

$$\gamma_0 = \sin\tilde{\theta}\cos(\theta_0) - \cos\tilde{\theta}\left(\frac{-3\cos\theta_0 + 4\cos\theta_1 - \cos\theta_2}{2\Delta\theta}\right), \tag{C.2}$$

$$\gamma_1 = \frac{1}{R^2\Delta\theta^2}(\cos\theta_0 + \cos\theta_2) + \left(\frac{2}{\Delta y^2} + L\right)\cos\theta_1, \tag{C.3}$$

$$\gamma_2 = \sin\tilde{\theta}\cos(\theta_2) + \cos\tilde{\theta}\left(\frac{\cos\theta_0 - 4\cos\theta_1 + 3\cos\theta_2}{2\Delta\theta}\right). \tag{C.4}$$

The first and last block rows contain the coefficients of the discretised Neumann boundary conditions, (3.8) and (3.9) respectively, the middle block row contains the coefficients of the discretised Helmholtz equation (3.5) and the first and last rows of each block row contain the coefficients of the discretisation of the Robin boundary conditions, (3.6) and (3.7) respectively.

The vector $\mathbf{f}$ is

$$\mathbf{f} = \begin{bmatrix} f_0^0 & f_1^0 & f_2^0 & f_0^1 & f_1^1 & f_2^1 & f_0^2 & f_1^2 & f_2^2 & \lambda \end{bmatrix}^T. \tag{C.5}$$

The vector $\mathbf{b}$ is

$$\mathbf{b} = \begin{bmatrix} K_-^{x_0}(0) & 0 & K_+x_0(0) & K_-x_0(\Delta y) & p^{x_0} & K_+x_0(\Delta y) & K_-x_0(2\Delta y) & 0 & K_+x_0(2\Delta y) & \mathscr{V}^{x_0} \end{bmatrix}^T, \tag{C.6}$$

where

$$K_\pm^{x_0}(y) = \pm b_\pm(x_0 + R\cos\tilde{\theta}, y) \mp R\cos\tilde{\theta} \left.\frac{\partial b_\pm}{\partial x}\right|_{(x_0+R\cos\tilde{\theta}, y)}. \tag{C.7}$$

Appendix

3.A An alternative implementation of the Surface Evolver solution

In the problem described in Chapter 3 we implement the Surface Evolver solution by meshing the perturbed walls. As Brakke (1994) explains, evolving with facets constrained on a curved wall is difficult in Surface Evolver due to trying to fit the facets to a curved constraint, and issues with refining. Thus we might anticipate that our solution does not work well for larger amplitude or sharper perturbations. To avoid these problems, and to increase computational efficiency, we can instead only mesh the liquid-vapour interface. That is, the upper and lower perturbed walls ($z = \pm 1/2 + B_{\pm}(x, y)$), the side walls ($y = \pm W$) and the end wall ($x = 0$) are not meshed. However we still need to account for the energy and volume contributions associated with these surfaces. We do this by calculating the energy and volume contributions via a line integral and performing this integration around oriented edges which are specified by the user. The result is added on to the total energy/volume of the surface.

Accounting for the energy of the missing facets

First we consider the energy associated with the removed surfaces. We write the surface energy integral as

$$\iint_S -\cos(\alpha_w)\ \mathrm{d}A = \iint_S -\cos(\alpha_w)\hat{\boldsymbol{v}} \cdot \hat{\boldsymbol{v}}\ \mathrm{d}A, \tag{3.A.1}$$

where, as in Chapter 3, $\hat{\boldsymbol{v}}$ is the outward pointing unit normal to the wetted surface S. We now wish to write this as a line integral using Stokes' Theorem: for a solenoidal

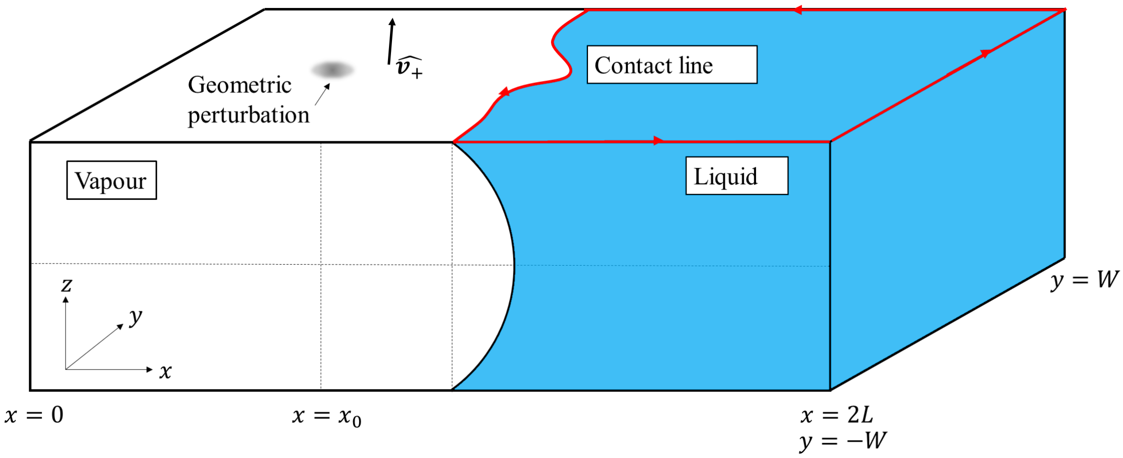

Figure 3.A.1: Sketch showing the orientation of the line integral around the wetted surface of the upper wall S_+, together with the orientation of the outward-pointing unit normal $\hat{\boldsymbol{v}}_+$. The function $\boldsymbol{w}_+$ is integrated around the red edges in the direction indicated by the arrows.

vector $\boldsymbol{u}$,

$$\iint_S -\cos(\alpha_w)\boldsymbol{u}\cdot\hat{\boldsymbol{v}}\,\mathrm{d}A = \iint_S -\cos(\alpha_w)(\nabla\times\boldsymbol{w})\cdot\hat{\boldsymbol{v}}\,\mathrm{d}A = \oint_{\partial S} -\cos(\alpha_w)\boldsymbol{w}\cdot\mathrm{d}\boldsymbol{r}, \tag{3.A.2}$$

where $\boldsymbol{w}$ is a vector field that has continuous first-order partial derivatives in a region containing S. Thus we first need a $\boldsymbol{u}$ such that $\boldsymbol{u}\cdot\hat{\boldsymbol{v}} = 1$ and $\boldsymbol{\nabla}\cdot\boldsymbol{u} = 0$ on S. Then we find a $\boldsymbol{w}$ such that $\boldsymbol{\nabla}\times\boldsymbol{w} = \boldsymbol{u}$. We are free to choose any $\boldsymbol{w}$ which satisfies these constraints, however the resulting function $\boldsymbol{w}$ cannot contain any singularities on S or its boundary.

To find the specific $\boldsymbol{w}$ required, we consider each surface in turn. Firstly, on the side walls and the end walls, the contact angle is $\alpha_w = \pi/2$ so there are no energy contributions from these walls. Next we consider the upper and lower wetted surfaces $S_\pm$, where $z = \pm 1/2 + B_\pm(x,y)$. We define $\boldsymbol{w}_\pm = w_{x\pm}\hat{\boldsymbol{x}} + w_{y\pm}\hat{\boldsymbol{y}} + w_{z\pm}\hat{\boldsymbol{z}}$. The integration region for the upper wall is shown in figure 3.A.1. The outward-pointing unit normal to the upper and lower channel walls is:

$$\hat{\boldsymbol{v}}_\pm = \pm\frac{1}{\sqrt{1+\left(\frac{\partial B_\pm}{\partial x}\right)^2+\left(\frac{\partial B_\pm}{\partial y}\right)^2}}\left(-\frac{\partial B_\pm}{\partial x}\hat{\boldsymbol{x}} - \frac{\partial B_\pm}{\partial y}\hat{\boldsymbol{y}} + \hat{\boldsymbol{z}}\right). \tag{3.A.3}$$

Therefore, we need a $\boldsymbol{u}_\pm = u_{x\pm}\hat{\boldsymbol{x}} + u_{y\pm}\hat{\boldsymbol{y}} + u_{z\pm}\hat{\boldsymbol{z}}$ and a $\boldsymbol{w}_\pm = w_{x\pm}\hat{\boldsymbol{x}} + w_{y\pm}\hat{\boldsymbol{y}} + w_{z\pm}\hat{\boldsymbol{z}}$

such that

$$u_{x\pm}\left(\mp\frac{\partial B_\pm}{\partial x}\right)+u_{y\pm}\left(\mp\frac{\partial B_\pm}{\partial y}\right)+u_{z\pm}(\pm 1)=\pm\sqrt{1+\left(\frac{\partial B_\pm}{\partial x}\right)^2+\left(\frac{\partial B_\pm}{\partial y}\right)^2}, \tag{3.A.4}$$

$$\frac{\partial u_{x\pm}}{\partial x}+\frac{\partial u_{y\pm}}{\partial y}+\frac{\partial u_{z\pm}}{\partial z}=0, \tag{3.A.5}$$

$$\left(\frac{\partial w_{z\pm}}{\partial y}-\frac{\partial w_{y\pm}}{\partial z}\right)=u_{x\pm},\quad \left(\frac{\partial w_{x\pm}}{\partial z}-\frac{\partial w_{z\pm}}{\partial x}\right)=u_{y\pm},\quad \left(\frac{\partial w_{y\pm}}{\partial x}-\frac{\partial w_{x\pm}}{\partial y}\right)=u_{z\pm} \tag{3.A.6}$$

We have thus far not been able to find a $\boldsymbol{u}$ and $\boldsymbol{w}$ satisfying this system with $\boldsymbol{w}$ having no singularities. Some examples of solutions that we considered are detailed below.

3.A.1 Radially axisymmetric perturbations

If we assume the perturbations on the upper and lower walls are radially axisymmetric then a $\boldsymbol{w}$ with a singularity at the centre of the bump can be found. The isolated Gaussian bump perturbations described in Chapter 3 are radially axisymmetric about $x = x_c^\pm$, $y = y_c^\pm$. Therefore, it is convenient to work in cylindrical polar coordinates $x = x_c + \rho\sin\varphi$, $y = y_c + \rho\cos\varphi$, $z = z$ so that the upper and lower walls are given by $z = \pm z_0 + B_\pm(\rho)$. Then the outward unit normal to the upper and lower channel walls is:

$$\hat{\boldsymbol{v}}_\pm = \pm\frac{1}{\sqrt{1+B_{\pm_\rho}^2}}\left(-\frac{\mathrm{d}B_\pm}{\mathrm{d}\rho}\hat{\boldsymbol{\rho}}+\hat{\boldsymbol{z}}\right). \tag{3.A.7}$$

Thus we can take

$$\boldsymbol{u}_\pm = \pm\sqrt{1+\left(\frac{\mathrm{d}B_\pm}{\mathrm{d}\rho}\right)^2}\,\hat{\boldsymbol{z}}. \tag{3.A.8}$$

To find the corresponding $\boldsymbol{w}_\pm$ for the upper and lower walls, we then solve for $\boldsymbol{\nabla}\times\boldsymbol{w}_\pm = \boldsymbol{u}_\pm$ in cylindrical polar coordinates. Thus, we solve

$$\frac{1}{\rho}\left(\frac{\partial(\rho w_{\pm\varphi})}{\partial\rho}-\frac{\partial w_{\pm\rho}}{\partial\varphi}\right)=\pm\sqrt{1+\left(\frac{\mathrm{d}B_\pm}{\mathrm{d}\rho}\right)^2}. \tag{3.A.9}$$

We are free to choose $w_{\pm\varphi} = 0$ which allows us to integrate analytically. We obtain

$$\boldsymbol{w}_\pm = \mp\rho\varphi\sqrt{1+\left(\frac{\mathrm{d}B_\pm}{\mathrm{d}\rho}\right)^2}\,\hat{\boldsymbol{\rho}}. \tag{3.A.10}$$

Transforming back to Cartesian coordinates and defining bump-centred coordinates $X = x - x_c$, $Y = y - y_c$, this vector is

$$\boldsymbol{w}_\pm = \mp \arctan\left(\frac{X}{Y}\right)\sqrt{1 + \left(\frac{\partial B_\pm}{\partial X}\right)^2 + \left(\frac{\partial B_\pm}{\partial Y}\right)^2}(X\hat{\boldsymbol{x}} + Y\hat{\boldsymbol{y}}), \tag{3.A.11}$$

which we integrate around the edges enclosing the upper and lower perturbed walls, $0 \leq x \leq x_\pm(y; x_0)$, $-W \leq y \leq W$, with $x_\pm(y; x_0)$ the contact line location. However this function is singular at $X = Y = 0$ which is at the centre of the bump. As shown in figure 3.A.2(a, b), this method works when the meniscus is far away from the bump and thus the method can be validated for a large portion of the domain. However we cannot compute contact line solutions as the contact line approaches the top of the bump, because the integrand becomes singular. A minimum energy solution satisfying all the boundary conditions cannot be computed as shown in figure 3.A.2(c, d).

To avoid the singluarity, we could introduce a branch cut so that we perform keyhole contour integration around the centre of the bump, as shown in figure 3.A.3, and add the resulting contribution onto the energy of the surface. However, this is difficult to implement in Surface Evolver as the integration requires knowledge of the location of the contact line which is unknown. Moreover, the branch cut solution allows us to compute solutions up to the bump on each side of the bump, but we cannot compute contact lines that lie over the top of the bump. Finally, the aim is to eventually use the code to caluclate solutions for offset and scattered bump perturbations which may not be radially axisymmetric, therefore this solution would no longer be straightforward to implement.

3.A.2 Taylor series approximation for small-amplitude perturbations

Another approach is to approximate the magnitude of the normal vector, that is, the right hand side of (3.A.4), by the first two terms of a Taylor expansion for small-amplitude perturbations so that a solution can be found. When the amplitude of the bump perturbations $B_\pm(x, z)$ is small so that $B_\pm(x, z) = \epsilon b_\pm(x, z)$ with $\epsilon \ll 1$, the right hand side equation (3.A.4) is approximated by

$$\pm\sqrt{1 + \left(\frac{\partial B_\pm}{\partial x}\right)^2 + \left(\frac{\partial B_\pm}{\partial y}\right)^2} \approx \pm\left\{1 + \frac{\epsilon^2}{2}\left(\frac{\partial b_\pm}{\partial x}\right)^2 + \epsilon^2\left(\frac{\partial b_\pm}{\partial y}\right)^2\right\}. \tag{3.A.12}$$

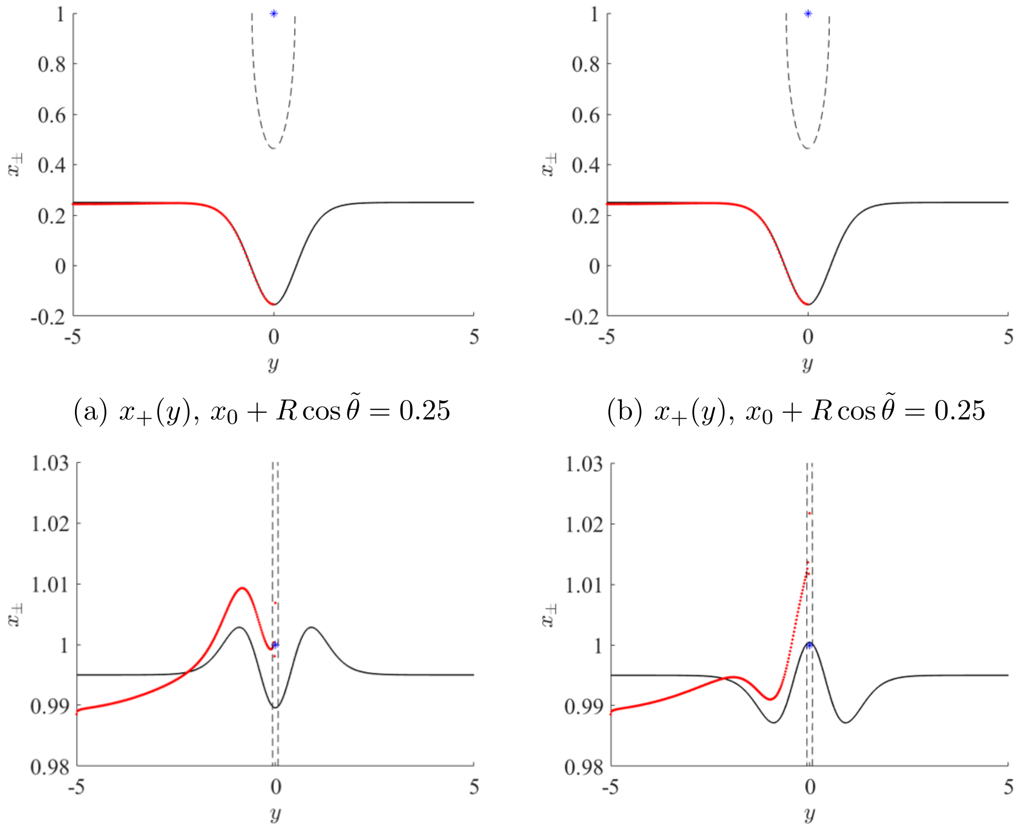

(a) $x_+(y)$, $x_0 + R\cos\tilde{\theta} = 0.25$ (b) $x_+(y)$, $x_0 + R\cos\tilde{\theta} = 0.25$

(c) $x_-(y)$, $x_0 + R\cos\tilde{\theta} = 0.995$ (d) $x_-(y)$, $x_0 + R\cos\tilde{\theta} = 0.995$

Figure 3.A.2: Contact line solutions for a bump at $x = 1$. Panels (a)–(b) and (c)–(d) show solutions for unperturbed contact lines far away from and close to the bump respectively. The blue star denotes the centre of the bump. In panels (a) and (b) the black dashed line denotes 75% of the maximum amplitude of the bump whereas in panels (c) and (d) it is a contour at 99.5% of the maximum bump amplitude. The black and red lines denote the linear and Surface Evolver solutions respectively. The channel width is $W = 5$, the amplitude of the bump is $\epsilon = 2$ and the width of the bump is $s = 0.25$, with contact angle $\phi = 85°$.

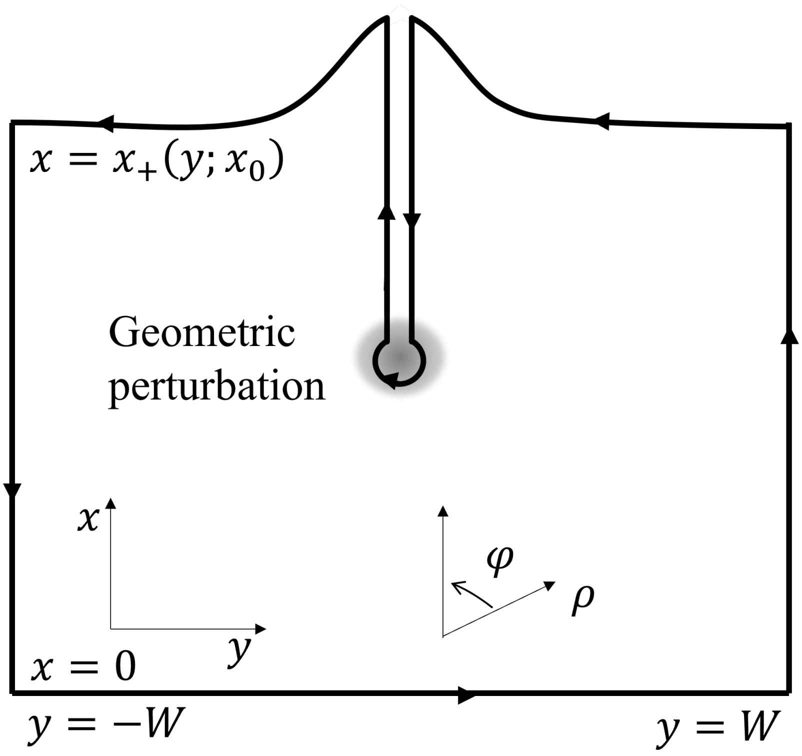

Figure 3.A.3: Sketch showing keyhole contour integration on the upper wall to avoid the singularity at the centre of the bump, together with the orientation of the bump-centred coordinates. The function $\boldsymbol{w}_+$ given in (3.A.11) is integrated around the edges in the direction shown by the arrows.

Therefore, we require a $\boldsymbol{u} = u_{x\pm}\hat{\boldsymbol{x}} + u_{y\pm}\hat{\boldsymbol{y}} + u_{z\pm}\hat{\boldsymbol{z}}$ such that

$$u_{x\pm}\left(\mp\frac{\partial B_\pm}{\partial x}\right) + u_{y\pm}\left(\mp\frac{\partial B_\pm}{\partial y}\right) + u_{z\pm}(\pm 1) = \pm\left\{1 + \frac{\epsilon^2}{2}\left(\frac{\partial b_\pm}{\partial x}\right)^2 + \epsilon^2\left(\frac{\partial b_\pm}{\partial y}\right)^2\right\}. \tag{3.A.13}$$

We can take

$$u_x = 0, \quad u_y = 0, \quad u_z = 1 + \frac{\epsilon^2}{2}\left(\frac{\partial b_\pm}{\partial x}\right)^2 + \epsilon^2\left(\frac{\partial b_\pm}{\partial y}\right)^2, \tag{3.A.14}$$

Then using (3.A.6) this leads to, for example,

$$w_x = -\int\left\{1 + \frac{\epsilon^2}{2}\left(\frac{\partial b_\pm}{\partial x}\right)^2 + \epsilon^2\left(\frac{\partial b_\pm}{\partial y}\right)^2\right\}\,\mathrm{d}y, \tag{3.A.15}$$

where

$$b_\pm(x, y) \propto \exp\left(-\frac{(x - x_c^\pm)^2}{s} - \frac{(y - y_c^\pm)^2}{s}\right), \tag{3.A.16}$$

so that the solution is given in terms of error functions and exponentials. We use an approximation of the error function from Abramowitz and Stegun (1948). For

$0 \leq X < \infty$,

$$\operatorname{erf}(X) \approx 1 - (a_1 t + a_2 t^2 + a_3 t^3 + a_4 t^4 + a_5 t^5)\, \mathrm{e}^{-X^2} + \varepsilon(X), \tag{3.A.17}$$

where

$$t = \frac{1}{1+pX}, \quad |\varepsilon(X)| \leq 1.5 \times 10^{-7}, \quad p = 0.3275911, \tag{3.A.18}$$

$$a_1 = 0.254829592,\ a_2 = -0.284496736,\ a_3 = 1.421413741, \tag{3.A.19}$$

$$a_4 = -1.453152027,\ a_5 = 1.061405429. \tag{3.A.20}$$

However, this solution also did not work in our implementation; we believe that this is because the approximation to the energy is not sufficiently accurate for the scales involved. We have not had time to experiment with more accurate approximations.

Accounting for the volume of the missing facets

As described in Chapter 3, the volume contribution is first written as an integral over the wetted surface S by using the divergence theorem:

$$V_L^{x_0} = \iiint_{V_L^{x_0}} 1 \,\mathrm{d}V = \iiint_{V_L^{x_0}} \boldsymbol{\nabla} \cdot \boldsymbol{F} \,\mathrm{d}V = \iint_S \boldsymbol{F} \cdot \hat{\boldsymbol{v}} \,\mathrm{d}A, \tag{3.A.21}$$

To write this integral as a line integral using Stokes theorem, we first need to find a solenoidal vector $\boldsymbol{u}$ such that $\boldsymbol{F} \cdot \hat{\boldsymbol{v}} = \boldsymbol{u} \cdot \hat{\boldsymbol{v}}$ on S where $F = x\hat{\boldsymbol{x}}$.

So firstly on the upper and lower perturbed wetted surfaces $S_\pm$, in Cartesian co-ordinates, the outward-pointing unit normal to the wetted surface is given by

$$\hat{\boldsymbol{v}}_\pm = \pm \frac{1}{\sqrt{1 + B_{\pm_x}^2 + B_{\pm_y}^2}} \left(-\frac{\partial B_\pm}{\partial x} \hat{\boldsymbol{x}} - \frac{\partial B_\pm}{\partial y} \hat{\boldsymbol{y}} + \hat{\boldsymbol{z}} \right). \tag{3.A.22}$$

Therefore, choosing

$$\boldsymbol{u}_\pm = x \frac{\partial B_\pm}{\partial x} \hat{\boldsymbol{z}} \tag{3.A.23}$$

satisfies the above conditions. We then find a $\boldsymbol{w}_\pm$ such that $\boldsymbol{\nabla} \times \boldsymbol{w}_\pm = \boldsymbol{v}_\pm$. Thus, if $\boldsymbol{w}_\pm = w_{\pm_x} \hat{\boldsymbol{x}} + w_{\pm_y} \hat{\boldsymbol{y}} + w_{\pm_z} \hat{\boldsymbol{z}}$, we solve

$$\left(\frac{\partial w_{-_y}}{\partial x} - \frac{\partial w_{-_x}}{\partial y} \right) = x \frac{\partial B_-}{\partial x} = -2\epsilon\, x(x - x_c^-) \exp\left(-\frac{(x - x_c^-)^2}{s} - \frac{(y - y_c^-)^2}{s} \right), \tag{3.A.24}$$

$$\left(\frac{\partial w_{+_y}}{\partial x} - \frac{\partial w_{+_x}}{\partial y} \right) = x \frac{\partial B_+}{\partial x} = -2a\epsilon\, x(x - x_c^+) \exp\left(-\frac{(x - x_c^+)^2}{s} - \frac{(y - y_c^+)^2}{s} \right). \tag{3.A.25}$$

We choose $w_{\pm_x} = 0$ then we obtain

$$\boldsymbol{w}_- = a\epsilon \exp\left(-\frac{(y-y_c^-)^2}{s}\right)\left\{x\exp\left(-\frac{(x-x_c^-)^2}{s}\right) - \frac{\sqrt{\pi}}{2}\mathrm{erf}(x-x_c^-)\right\}\hat{\boldsymbol{y}}, \quad (3.A.26)$$

$$\boldsymbol{w}_+ = \epsilon \exp\left(-\frac{(y-y_c^+)^2}{s}\right)\left\{x\exp\left(-\frac{(x-x_c^+)^2}{s}\right) - \frac{\sqrt{\pi}}{2}\mathrm{erf}(x-x_c^+)\right\}\hat{\boldsymbol{y}}, \quad (3.A.27)$$

where again we use the approximation from Abramowitz and Stegun (1948) to compute the error function in Surface Evolver. We integrate $\boldsymbol{w}_\pm$ around the upper and lower perturbed walls.

The wetted surfaces $S_{\pm W}$ on the side walls ($y = \pm W$) do not contribute to the volume constraint as the normal to these walls is $\pm\hat{\boldsymbol{y}}$, so that $\boldsymbol{F}\cdot\hat{\pm}\hat{\boldsymbol{y}} = \pm x\hat{\boldsymbol{x}}\cdot\hat{\boldsymbol{y}} = 0$. The end wall also does not contribute to the volume integral as $x = 0$ on this surface, so that $\boldsymbol{F} = 0$. Therefore we do not need to consider contributions from these walls.

This method for calculating the volume associated with the missing facets presents no problems and can be implemented without issue. However it cannot be used without also being able to account for the energy of the missing facets as explained in §3.A.1, §3.A.2.

Chapter 4

Free-stream coherent structures in the unsteady Rayleigh boundary layer

The work for this paper was started towards the end of my MSci year at Imperial College London, was continued during postgraduate research at Monash University, Melbourne and was completed during my studies at the University of Manchester. A very early draft of the asymptotic work for the basic flow and the production layer (sections 2-3) was submitted as part of my MSci and can therefore not be examined here. The work presented for examination is the asymptotic analysis of the adjustment-layer solution (Section 4), the results (Section 5) and the discussion (Section 6), together with the introduction (Section 1). The paper has a self-contained introduction, discussion, appendices and bibliography. It appears as:

E. C. Johnstone and P. Hall (2020). “Free-stream coherent structures in the unsteady Rayleigh boundary layer”. *IMA J. Appl. Math.* 85.6, pp. 1021–1040.

Statement of Contributions

EJ derived the model, performed the asymptotic analysis and the numerical computations, created the figures and wrote the paper. PH suggested the initial problem, provided guidance on the asymptotic analysis and numerical computations (particularly on the scalings in each layer) and provided editorial suggestions.

IMA Journal of Applied Mathematics (2020) **85**, 1021–1040
doi:10.1093/imamat/hxaa038
Advance Access publication on 9 October 2020

Free-stream coherent structures in the unsteady Rayleigh boundary layer

Eleanor C. Johnstone*
Department of Mathematics, University of Manchester, Manchester M13 9PL, UK
*Corresponding author: eleanor.johnstone@manchester.ac.uk

and

Philip Hall
School of Mathematics, Monash University, Melbourne, VIC 3800, Australia

[Received on 4 February 2020; revised on 9 July 2020; accepted on 13 September 2020]

Results are presented for nonlinear equilibrium solutions of the Navier–Stokes equations in the boundary layer set up by a flat plate started impulsively from rest. The solutions take the form of a wave–roll–streak interaction, which takes place in a layer located at the edge of the boundary layer. This extends previous results for similar nonlinear equilibrium solutions in steady 2D boundary layers. The results are derived asymptotically and then compared to numerical results obtained by marching the reduced boundary-region disturbance equations forward in time. It is concluded that the previously found canonical free-stream coherent structures in steady boundary layers can be embedded in unbounded, unsteady shear flows.

Keywords: transition to turbulence, unsteady transition, boundary layer stability.

1. Introduction

There are fundamental differences in the instability and transition processes in steady and unsteady flows. The asymptotic description of nonlinear equilibrium solutions of the Navier–Stokes equations, which has been suggested gives an insight into transition in shear flows, has previously only been conducted in the context of steady flows. We present results for nonlinear equilibrium solutions in the unsteady boundary layer set up by a flat plate moved impulsively from rest, hereafter referred to as the Rayleigh problem.

The solutions we are interested in are equilibrium solutions of the Navier–Stokes equations as fixed points or periodic orbits for shear flows. Their underlying physics is very similar to that described by vortex–wave interaction (VWI) theory (Hall & Smith, 1991): a streak is unstable to a 3D wave that interacts with itself in a critical layer to produce a roll via Reynolds stresses. This roll then drives the streak, resulting in a 'self-sustaining process' (Waleffe, 1997). These types of solutions, which are often referred to as 'exact coherent structures', have been found both numerically and asymptotically in the high Reynolds number limit for a range of steady flows (see, e.g. Faisst & Eckhardt, 2003; Waleffe 2001, 2003; Wedin & Kerswell, 2004; Wang *et al.*, 2007, Hall & Sherwin, 2010, Deguchi & Hall 2014a).

However, the solutions discussed here differ from the exact coherent structures because the roll–streak interaction takes place in a layer that sits just below the free stream. This layer is termed as the 'production layer' by Deguchi & Hall (2014b), who first observed these 'free-stream coherent structures' in parallel asymptotic suction boundary layer (ASBL) flow, and replaces the traditional critical layer in VWI theory that sits in the boundary layer.

Deguchi & Hall (2014b) solve the full Navier–Stokes equations within the production layer as a nonlinear eigenvalue problem of unit Reynolds number; this solution then motivates an asymptotic description of the flow above and below the layer. Above the layer, all disturbances decay, while below the layer the interaction of the perturbation with the background flow produces a streak disturbance that grows exponentially below the layer via a nonlinear interaction between the roll and the mean flow, before obtaining its maximum size in the near-wall boundary layer. The existence of the structures relies upon the fact that the background state is of boundary-layer form and that in the production layer the difference between the streamwise velocity and the free-stream speed is exponentially small, which allows the nonlinear interaction to take place. The key implication is that streak disturbances seen at the wall could have their origin much further away.

Free-stream coherent structures have since been described in a wide range of general steady shear flows such as the Burger's vortex sheet (Deguchi & Hall, 2014a); spatially growing 2D boundary layers such as Blasius flow (Deguchi & Hall, 2015); and planar jets (Deguchi & Hall, 2018). The asymptotic description of free-stream coherent structures in the Rayleigh problem is very similar to those described by Deguchi & Hall (2015) for spatially growing 2D boundary layers that approach their free-stream form exponentially. They show that the production layer problem for these flows can, remarkably, be reduced to exactly that of the ASBL flow, albeit with local values of the wavenumbers. However, below the production layer, non-parallel effects came into play to give a rich asymptotic structure comprising two 'adjustment layers' and an irrotational layer connected by diffusion fronts. These curves arise due to the coalescing of different Wentzel–Kramers–Brillouin (WKB) phases. As in the ASBL problem, the streak disturbance grows exponentially beneath the production layer towards the wall but this time obtains its maximum in the lower adjustment layer where the WKB amplitude is a minimum. The asymptotic results for large Reynolds numbers agree well with numerical solutions of the parabolic boundary-region equations for the disturbance.

We now describe free-stream coherent structures in the unsteady boundary layer arising from a flat plate set in impulsive motion from rest. The importance of unsteady effects on the stability of time-dependent flows has been studied for a wide range of problems, including an impulsively started rotating cylinder (Chen & Christensen, 1967); time-dependent rotational Couette flow (Kirchner & Chen, 1970); and the flow around a cylinder immersed in a fluid that is impulsively spun up (Otto, 1993). Of particular interest is the reconciliation of the onset of transition in unsteady flows with predictions of instability from linear stability analysis; Moss (1992) showed that for impulsively started pipe flow the onset of transition occurs at lower Reynolds numbers than linear predictions of instability. The effect of unsteadiness on the onset of transition and instability is attributed to an upstream travelling turbulent front leading to finite-amplitude disturbances.

Even for slowly-varying flows that can be studied using a quasi-static approach, the stabilizing effect of the quasi-static assumption is often not enough to overcome instabilities arising from the time-dependent nature of the flow (Seminara & Hall, 1975; Shen, 1961; Von Kerczek & Davis, 1974). Unsteady effects have been shown to be particularly important in the linear stability of the Stokes problem (an impulsively started flat plate in oscillatory motion), which is governed by unstable Floquet modes (and non-Floquet modes appear at high Reynolds numbers) (Cowley, 1987; Hall, 1978, 2003; Von Kerczek & Davis, 1974); when unsteady effects are amplified, such as a skewed acceleration of the plate, the problem becomes linearly unstable at lower Reynolds number (Thomas, 2020). Unsteadiness also changes the nature of the route to turbulence for the Stokes problem through the presence of a finite-time singularity and the growth of 3D disturbances interacting with 2D waves using a critical layer approach (Wu, 1992; Wu *et al.*, 1993). In fact, Wu *et al.* (1993) link the unsteady critical-layer approach and the VWI theory of Hall & Smith (1991) in the context of a linear disturbance evolving to an unsteady critical-layer type interaction, and then further evolving into a VWI-type state. It has been suggested that these VWI states, i.e. the exact and free-stream coherent structures described above, are a key building block of shear-flow transition processes; for a more complete discussion of this suggestion, the reader is referred to Jiménez (2018) and the introduction by Deguchi & Hall (2015). Therefore, a key implication of the problem discussed in this paper is that there may be a connection between transition in steady and unsteady flows.

The unsteady boundary-region equations that appear in this paper are also discussed by Ricco *et al.* (2011) where they are found to govern the evolution of streaky boundary-layer disturbances from unsteady free-stream turbulence. Unlike the case for steady disturbances, streaky boundary layers generated by unstable disturbances are inviscidly unstable, and thus boundary layer transition can occur without separation (Goldstein & Sescu, 2008). The unsteady boundary-region equations considered in this paper are reduced, through a suitable transformation, to the well-known Görtler vortex equations of Hall (1983) with zero Görtler number; these also appear as the governing equations for 3D boundary-layer perturbations in the problem studied by Luchini (1996). Their numerical solution is discussed thoroughly by Hall (1983); for extensive numerical studies of more complex nonlinear boundary-region equations the reader is referred to Martin & Martel (2012) and Sescu & Afsar (2018).

Little is known about the stability of fluid flows with a general time dependence; the meaning of stability is not clear when the magnitude of the basic flow changes over time. That being said, using the assumptions of Hall & Parker (1976) and Cowley (1987) that quasi-steady flow is justified at high Reynolds number with a fast convective time scale, then Rayleigh flow may be considered quasi-steady; indeed the time dependence of the free-stream coherent structure problem is absorbed in the similarity variable so that instantaneously the flow sees the disturbance as steady. Under this assumption, it could be suggested that there exists a similar mechanism for the transition process in steady and quasi-steady flows.

In this paper, we apply the approach of Deguchi & Hall (2015) for spatially growing boundary layers to the Rayleigh problem. The study of the unsteady problem is motivated by the Gaussian approach of the unperturbed flow to its free-stream form. Deguchi & Hall (2014b) show that for the ASBL problem this approach actually needs to be an exponential function of distance from the wall. We show that the unsteadiness in the Rayleigh problem can mimic the suction of ASBL flow to force the flow to instantaneously decay with the required exponential behaviour using a scaled variable.

We see that through an appropriate transformation the production-layer problem can be reduced to exactly the ‘parallel’ problem of ASBL flow through the introduction of a similarity variable that captures the time dependence of the problem. However, as with the spatially developing case, below the layer unsteady effects come back into play, and the problem has to be considered instantaneously at each time step, with instantaneous values of the frequency and wavenumbers. This gives rise to a complex asymptotic structure due to the changing dominance of the different WKB solutions; however, it also means that full numerical simulations would be very computationally demanding. This is not necessary, however, as the results of the locally parallel nonlinear eigenvalue problem of Deguchi & Hall (2014b) can be used to determine the instantaneous wavenumbers at each time step, thereby allowing the parabolic boundary-region equations to be marched forward in time to give a comparison to the analytical results. The procedure adopted for the rest of this paper is as follows: in §2 we outline the problem for Rayleigh flow before the production layer problem is derived in §3 and the flow beneath the production layer is described in §4. In §5, numerical results are computed. In §6, a general discussion of our results in the context of existing research is given, as well as comments on further questions to be explored.

2. The basic flow for the Rayleigh problem

Consider a viscous flow with viscosity ν above an infinitely long flat plate at $y^* = 0$ with respect to Cartesian co-ordinates (x^*, y^*, z^*). At time $t^* = 0$, the plate is impulsively set into motion and continues moving with constant velocity $-U_1$, where the sign is chosen to allow an easier comparison to the Deguchi & Hall (2014b) ASBL problem. Therefore, if the velocity of the flow is $\boldsymbol{u}^* = (u^*, v^*, w^*)$, then the boundary conditions are $\boldsymbol{u}^* \to (0, 0, 0)$ a long way from the plate, and $\boldsymbol{u}^* = (-U_1, 0, 0)$ at the plate. Taking τ as a typical time scale for the development of the flow, the width of the boundary layer that forms on the plate surface is found to be $\sqrt{\nu\tau}$. If we non-dimensionalize using this length scale and U_1 as a typical flow speed, the Reynolds number of the problem is found to be $Re = U_1\sqrt{\tau/\nu}$. Then, the equations of motion describing the non-dimensional flow field are

$$\frac{1}{Re}\boldsymbol{u}_t + (\boldsymbol{u}\cdot\nabla)\boldsymbol{u} = -\nabla p + \frac{1}{Re}\nabla^2\boldsymbol{u}, \tag{2.1}$$

$$\nabla\cdot\boldsymbol{u} = 0. \tag{2.2}$$

For the Rayleigh problem, the flow is uniform in the x-direction as the plate is moving with constant speed and there is no velocity in the spanwise direction. Hence, the flow is transient but only changes in the y-direction. Under these assumptions, the high-Reynolds-number equations of motion reduce to $u_t = u_{yy}$, where subscript represents partial derivative. This equation can be solved via the introduction of a similarity variable $\eta = y(2t)^{-1/2}$, where the scaling is chosen for convenience, so that we seek solutions in the form $u = \bar{u}(\eta)$. Thus, we solve

$$\bar{u}'' + \eta\bar{u}' = 0, \quad \bar{u}(0) = -1, \quad \bar{u}(\infty) = 0, \tag{2.3}$$

where prime denotes derivative, to find that

$$\bar{u} = \operatorname{erf}(\eta/2) - 1. \tag{2.4}$$

Therefore, at large values of η, i.e. as the free-stream is approached, the streamwise velocity is given by

$$u(t, y) \approx -A_0\eta^{-1}\mathrm{e}^{-\eta^2/2} = -A_0 y^{-1}\sqrt{2t}\mathrm{e}^{-y^2/4t}, \tag{2.5}$$

where $A_0 = \sqrt{2/\pi}$.

3. The production layer problem

If the Reynolds number is large, the equations of motion allow for other solutions including the free-stream coherent structures described in Deguchi & Hall (2014b). The production layer, where the nonlinear interaction that produces the structures takes place, is completely distinguished from the near-wall boundary layer. In this layer, waves, rolls and streaks interact in a self-sustaining manner to produce a coherent structure that is convected downstream with almost the free-stream speed. The interaction of the roll flow and the mean flow enables the streak disturbance to grow exponentially beneath the layer.

3.1 *Free-stream coherent structures in parallel boundary-layer flows*

We will show that we are able to reduce the production-later problem for the unsteady Rayleigh flow to the production layer problem for parallel ASBL flow. Therefore, in order to give some context to the results for free-stream coherent structures in the Rayleigh problem, we shall very briefly summarize the results of Deguchi & Hall (2014b) for the canonical parallel ASBL problem. These were described completely in that paper and summarized in Deguchi & Hall (2015), therefore only a brief description shall be given here.

ASBL flow is a viscous flow over an infinitely long flat plate; the basic flow is therefore independent of x and z with respect to Cartesian co-ordinates (x, y, z). The plate has small perforations where a low pressure gradient is maintained so the fluid is sucked downwards through the plate at constant velocity. The suction forces a parallel boundary layer on the plate surface. The basic flow is given by

$$\boldsymbol{u}_b = (u_b, -Re^{-1}, 0) = (1 - \mathrm{e}^{-y}, -Re^{-1}, 0), \tag{3.1}$$

with the Reynolds number Re based on the free-stream speed and the unperturbed boundary-layer thickness. If we perturb the flow at high Reynolds numbers we find a nonlinear interaction taking place in a layer located at $Y = y - \ln Re$. This layer is situated just below the free-stream and the structure created is convected downstream with speed differing from the free-stream speed by $O(Re^{-1})$ so that the wave dependence in the layer is defined as $X = x - ct$, $c = 1 - Re^{-1}c_1 + \cdots$. The equations describing the interaction form a nonlinear eigenvalue problem at unit Reynolds number for the wavespeed c_1 and are given by

$$([\boldsymbol{U} + c_1\hat{\boldsymbol{i}}] \cdot \nabla)\boldsymbol{U} = -\nabla P + \nabla^2\boldsymbol{U}; \quad \nabla \cdot \boldsymbol{U} = 0, \tag{3.2}$$

where $\boldsymbol{U} = (U, V, W)$ and P are the perturbation velocity and pressure scaled on Re^{-1} and Re^{-2}, respectively. This system is to be solved subject to boundary and periodicity conditions given by

$$\begin{gathered}\boldsymbol{U} \to (0, -1, 0) \text{ as } Y \to \infty; \quad \boldsymbol{U} \to (-\mathrm{e}^{-Y}, -1, 0) \text{ as } Y \to -\infty,\\ \boldsymbol{U}(X, Y, Z) = \boldsymbol{U}(X + 2\pi/\alpha, Y, Z), \quad \boldsymbol{U}(X, Y, Z) = \boldsymbol{U}(X, Y, Z + 2\pi/\beta).\end{gathered} \tag{3.3}$$

Here, α and β are the streamwise and spanwise wavenumbers, respectively. The key point to notice here is that the boundary condition as $Y \to -\infty$ allows for the possibility of higher-order X-independent terms of U to grow exponentially beneath the production layer, although the growth would be at a slower rate than the leading order growth $\sim e^{-Y}$. Below the layer the disturbance field adjusts to become compatible with the basic flow, therefore this layer is termed the ‘adjustment layer’. In order to analyse the growth of the higher-order terms in the adjustment layer, the flow is split into its mean flow, vortex and wave components. The mean flow is the average in X and Z of the flow, while the vortex component is the average in X of the disturbance only. The streak is the vortex component of U and the roll is the vortex component of (V, W). The equations for the leading order vortex components are then Fourier analysed to yield the form of the solution beneath the production layer:

$$U \to -\mathrm{e}^{-Y} + J_1\mathrm{e}^{(\omega_1 - 1)Y}\cos(2\beta Z) + \ldots; \quad V \to -1 + K_1\mathrm{e}^{\omega_1 Y}\cos(2\beta Z) + \ldots, \tag{3.4}$$

where $K_1 = K_1(\alpha, \beta)$ is to be found as part of the numerical eigenvalue problem in the production layer and

$$\omega_1 = (\sqrt{1 + 16\beta^2} - 1)/2 > 0, \quad J_1 = -K_1/2\omega_1. \tag{3.5}$$

Hence, we see that exponential growth of the streak only occurs for spanwise wavenumbers in the range $\beta < 1/\sqrt{2}$. It is found that as the wall is approached, where all disturbances must ultimately be reduced to zero, the streak disturbance takes its maximum within the unperturbed near-wall boundary layer. Thus the crucial conclusion is that a nonlinear interaction in the free-stream involving a velocity field of size $O(Re^{-1})$ can produce a much larger streak disturbance that is felt most strongly in the boundary layer, away from the production layer where it is generated. It should be noted that the wave and roll field decay below the production layer as the self-sustaining mechanism, which provides the forcing to the roll flow via the Reynolds stresses associated with the wave, is localized in the production layer. Numerical results at finite Reynolds number shown in Deguchi & Hall (2014b) agree well with the asymptotic theory shown above.

3.2 *The production layer problem for Rayleigh flow*

The free-stream coherent structures in ASBL flow described in §3.1 owe their existence to the fact that the basic flow approaches its free-stream form through an exponential function of distance from the wall. Deguchi & Hall (2015) show that an arbitrary 2D spatially developing boundary layer, which instead approaches its free-stream form via an exponential function of the square of distance from the wall (Brown & Stewartson, 1965), can also support the structures through an appropriate transformation that forces the decay to be of the required form locally around the production layer. This effect of boundary-layer growth is crucial to the interaction mimicking the ASBL structure in the production layer. We shall see that the same holds true of the Rayleigh problem, but with unsteady effects replacing the effect of boundary layer growth. We first find the location and scalings required to define the nonlinear eigenvalue problem to be solved in the production layer for the Rayleigh problem, and then show how this can be transformed into the canonical production-layer problem (3.2)–(3.3) in §3.1.

3.2.1 *Location and scalings*

We seek a structure that is periodic in the streamwise and spanwise directions, with wavenumbers α_0 and β_0, respectively. It is located in a layer of unknown thickness δ_p situated at an unknown distance K from the wall; the layer is situated just below the free-stream so $K \gg 1$. Writing $y(2t)^{-1/2} = K + \delta_p \tilde{Y}(2t)^{-1/2}$, we see that for large K, in order for the flow to decay locally as a function of exponential distance from the wall, we must take $\delta_p = K^{-1}$. In this case,

$$u \approx -A_0 K^{-1} e^{-K^2/2} e^{-\tilde{Y}/\sqrt{2t}}. \tag{3.6}$$

We now fix K by considering a balance of terms in the streamwise momentum equation. Previous work by Deguchi & Hall (2014b, 2015) has shown that the free-stream coherent structures in the production layer are nonlinear wave structures with wavelengths comparable to the boundary layer scale. Therefore, with respect to the scaling for y in the production layer and the boundary-layer scalings in §2, the structure will operate in a cube of sides length $\delta_p = K^{-1}$ within the viscous production layer. The nonlinear terms and viscous terms will thus balance if

$$\frac{1}{K}\exp\left[\frac{-K^2}{2}\right] = \frac{K^2}{Re} \qquad \Rightarrow K \approx \sqrt{2\ln Re}. \tag{3.7}$$

We now restrict any streamwise dependence to be in the form of a wave moving downstream with almost the free-stream speed; because the boundary-layer is growing in time, the wavespeed must also change in time. If the streamwise wavelength is also to remain comparable with the depth of the layer and the convective balance $\partial_t + u\partial_x \sim O(K^2/Re)$ is to be maintained, then in the production layer we write

$$\tilde{\Phi} = K\alpha_0\left[x - K\int^t c(\tilde{t})\,\mathrm{d}\tilde{t}\right], \quad \frac{y}{\sqrt{2t}} = K + \frac{\tilde{Y}}{K\sqrt{2t}}, \quad \tilde{Z} = Kz. \tag{3.8}$$

Here α_0 is the streamwise wavenumber, which is constant because the base flow of Rayleigh problem is not spatially dependent. Therefore, unlike the growing boundary layer problem studied in Deguchi & Hall (2015), where local streamwise wavenumbers $\alpha_0(x)$ were defined in terms of the (non-zero) free-stream speed $U_1(x)$, there are no difficulties if the free-stream speed is zero. We also note that if $c(t)$ is constant then the phase variable $\tilde{\Phi}$ reduces to the wave dependence seen in ASBL flow in §3.1. The scalings for the velocity field can be found by considering the continuity equation (2.2). We find $u \sim v \sim w \sim O(KRe^{-1})$, then the pressure must be $O(K^2Re^{-2})$ to be kept in play, so we seek a solution in the form

$$\boldsymbol{u} = KRe^{-1}\tilde{\boldsymbol{U}}(t,\tilde{\Phi},\tilde{Y},\tilde{Z}), \qquad p = K^2Re^{-2}\tilde{P}(t,\tilde{\Phi},\tilde{Y},\tilde{Z}). \tag{3.9}$$

We substitute this expansion into the equations of motion (2.1) and (2.2) to find the nonlinear eigenvalue problem for the instantaneous wavespeed to be solved in the production layer:

$$\left[\left(\tilde{\boldsymbol{U}} - c(t)\hat{\boldsymbol{i}} - \frac{1}{\sqrt{2t}}\hat{\boldsymbol{j}}\right)\cdot\tilde{\boldsymbol{\nabla}}\right]\tilde{\boldsymbol{U}} = -\tilde{\boldsymbol{\nabla}}\tilde{P} + \tilde{\nabla}^2\tilde{\boldsymbol{U}}, \tag{3.10}$$

$$\tilde{\boldsymbol{\nabla}}\cdot\tilde{\boldsymbol{U}} = 0, \tag{3.11}$$

where $\tilde{\boldsymbol{\nabla}} = (\alpha_0\partial_{\tilde{\Phi}}, \partial_{\tilde{Y}}, \partial_{\tilde{Z}})$ and $\tilde{\nabla}^2 = \alpha_0^2\partial^2_{\tilde{\Phi}} + \partial^2_{\tilde{Y}} + \partial^2_{\tilde{Z}}$, and the equations are to be solved subject to boundary conditions

$$\tilde{U} \to 0 \quad \text{as} \quad \tilde{Y} \to \infty, \tag{3.12a}$$

$$\tilde{U} \to -A_0\mathrm{e}^{-\tilde{Y}/\sqrt{2t}} \quad \text{as} \quad \tilde{Y} \to -\infty, \tag{3.12b}$$

and periodicity conditions

$$(\tilde{\boldsymbol{U}},\tilde{P})(t,\tilde{\Phi},\tilde{Y},\tilde{Z}+2\pi/\beta_0) = \boldsymbol{U}(t,\tilde{\Phi},\tilde{Y},\tilde{Z}), \tag{3.13a}$$

$$(\tilde{\boldsymbol{U}},\tilde{P})(t,\tilde{\Phi}+2\pi,\tilde{Y},\tilde{Z}) = \boldsymbol{U}(t,\tilde{\Phi},\tilde{Y},\tilde{Z}), \tag{3.13b}$$

where β_0 is the spanwise wavenumber. It is of crucial importance to notice the $(2t)^{-1/2}\partial_{\tilde{Y}}$ term in the momentum equation (3.10); this represents a 'suction-like' effect that has been produced by unsteady effects in the boundary layer. The portion of the flow travelling closest to the wall is subject to this suction-like effect that serves to thicken the velocity profile. The effect here gets weaker as time increases, and hence forces the production-layer flow to be quasi-steady.

3.4 *Reduction to the ASBL production layer problem*

The problem above looks similar to the nonlinear eigenvalue problems (3.2)–(3.3) described in §3.1 for ASBL flow. Indeed, if we consider the transformation

$$\tilde{\Phi} = \alpha_0\sqrt{2t}\Phi, \quad \tilde{Y} = \sqrt{2t}\left[Y + \ln(A_0\sqrt{2t})\right], \quad \tilde{Z} = \sqrt{2t}Z,$$
$$c = -c_1/\sqrt{2t}(\tilde{U}, \tilde{V}, \tilde{W}, \tilde{P}) = (\sqrt{2t})^{-1}(U, V+1, W, P), \tag{3.14}$$

then (3.10)–(3.13) become exactly the ASBL nonlinear eigenvalue problems (3.2)–(3.3) but with time-dependent values of the effective wavenumbers $\alpha = \alpha_0\sqrt{2t}$ and $\beta = \beta_0\sqrt{2t}$ (we note that the wavenumbers for the Rayleigh problem are constant). This means that at each timestep, solutions of the Rayleigh problem can be extracted by using the solution of the ASBL problem with instantaneous values of α and β at that time. This allows a significant computational reduction as rather than having to solve for a slowly varying time-dependent eigenvalue $c(t)$, only the steady eigenvalue problem needs to be solved to be able to determine the unsteady solution. The steady (parallel) problem was solved for a range of values of α and β in Deguchi & Hall (2014b).

3.5 *The roll–streak flow exiting the production layer*

The roll–streak flow exiting the production layer for ASBL flow is given by (3.4). Using the transformation above and the production-layer scalings (3.9), for the Rayleigh problem, we see that the roll–streak flow exiting the production layer is given by

$$u \to -A_0\frac{K}{Re}e^{-y/\sqrt{2t}} + \frac{K}{Re}\frac{J_1}{\sqrt{2t}}e^{(\omega_1-1)y/\sqrt{2t}}(\sqrt{2t}A_0)^{(1-\omega_1)}\cos(2K\beta_0 z) + \dots, \tag{3.15}$$

$$v \to \frac{K}{Re}\frac{K_1}{\sqrt{2t}}e^{\omega_1 y/\sqrt{2t}}(\sqrt{2t}A_0)^{-\omega_1}\cos(2K\beta_0 z) + \dots, \tag{3.16}$$

where J_1, K_1 and ω_1 are functions of the instantaneous effective spanwise wavenumber β and are therefore updated at each time step. From (3.4), for growth in ASBL flow the local spanwise wavenumber must satisfy $omega_1 - 1 < 0$, or equivalently, $\beta < 1/\sqrt{2}$ at each time step. Therefore for a given β_0, the length of time for which growth occurs in the Rayleigh problem is specified by $\beta_0\sqrt{2t} < 1/\sqrt{2}$. Hence, the free-stream coherent structures only produce an exponentially growing streak for a finite time. We also note that as with the ASBL problem, above the production layer, the wave, roll and streak all decay and the flow returns to its free-stream value given by (3.12a), as with no forcing the self-sustaining mechanism breaks down away from the critical layer that produces the Reynolds stresses. Finally we now see that if we had taken the velocity at the plate to be $(U_1, 0, 0)$ in §2 rather than $(-U_1, 0, 0)$ then we would change the sign of the streamwise velocity in (3.12b). Although the physics of the problem would be unchanged, the transformation to the ASBL problem in Deguchi & Hall (2014b) would be more complex.

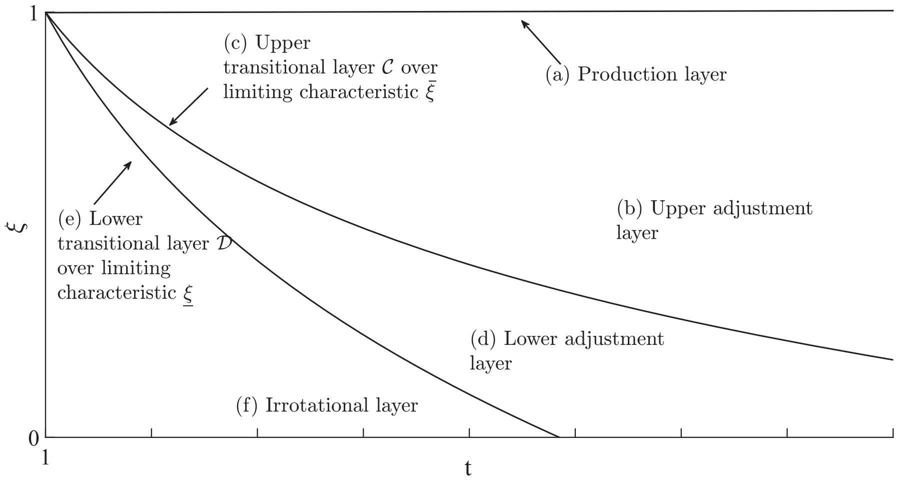

FIG. 1. The structure beneath the production layer for the unsteady problem showing the diffusion fronts, over which the WKB phase changes. Characteristics emanate from the initial point of forcing $(t, \xi) = (1, 1)$.

4. The adjustment layer problem

We now turn our attention to what happens beneath the production layer as the disturbance produced by the nonlinear interaction in the production layer interacts with the mean flow. For the ASBL problem this is relatively simple: the streak grows exponentially all the way down to the unperturbed boundary layer, where it is ultimately reduced to zero to satisfy the wall conditions. For the Rayleigh problem, we find that the solution is much more complicated and takes on a structure related to that found for spatially growing flow by Deguchi & Hall (2015). This is because beneath the production layer the unsteady effects, which could be forced to act in a quasi-steady manner in the production layer, come back into play. This leads to a rich asymptotic structure with two adjustment layers and an irrotational layer separated by diffusion fronts that arise when different WKB phase solutions become dominant; see Fig. 1. From the three layers we can form a composite solution by matching the solution across the diffusion fronts. We first derive the boundary-region equations, valid from the wall to the production layer, and then solve them using the WKB method. We find that the forcing from the solution exiting the production layer (region a in Fig. 1) dominates in an upper adjustment layer (region b) above a diffusion front $\mathscr{C}$ (region c), which arises due to a singularity from the onset of production-layer forcing. Below this curve a different WKB phase dominates in a lower adjustment layer (region d). The solution then becomes singular leading to a second diffusion front $\mathscr{D}$ (region e), below which the flow is irrotational (region f).

4.1 *The boundary-region equations*

We first find the equations describing the interaction between the production-layer solution and the basic flow and which are to be solved between the wall and the production layer. We decompose the flow field (u, v, w) into its basic flow, vortex and wave components to analyse how the disturbances exiting the production layer interact with the mean flow. The vortex component of u is called the streak flow (subscript s), and the vortex components of v and w are called the roll flow (subscript r). So if $\boldsymbol{u}_b = (u_b(t, y), 0, 0)$ is the basic flow in the unperturbed boundary layer, then the flow is disturbed by the production layer forcing as

$$(u, v, w) = [u_b + u_s \cos(2K\beta_0 z), Re^{-1} v_r \cos(2K\beta_0 z), Re^{-1} w_r \sin(2K\beta_0 z)], \tag{4.1}$$

$$p = Re^{-2} p_r \cos(2K\beta_0 z). \tag{4.2}$$

We note that the spanwise wavenumber of the perturbation is taken to be β_0 to allow matching with the solution exiting the production layers (3.15)–(3.16). We then find that the linearized boundary-region equations for the disturbance are

$$\frac{\partial}{\partial t}\begin{bmatrix} u_s \\ v_r \\ w_r \end{bmatrix} + v_r \frac{\partial}{\partial y}\begin{bmatrix} u_b \\ 0 \\ 0 \end{bmatrix} = \begin{bmatrix} 0 \\ -\partial p_r/\partial y \\ 2K\beta_0 p_r \end{bmatrix} + \left(\frac{\partial^2}{\partial y^2} - 4K^2\beta_0^2\right)\begin{bmatrix} u_s \\ v_r \\ w_r \end{bmatrix}, \tag{4.3}$$

$$\frac{\partial v_r}{\partial y} + 2K\beta_0 w_r = 0. \tag{4.4}$$

These equations are parabolic in t and can therefore be solved by integrating in y over the region from the wall to the production layer then marching forwards subject to boundary conditions at the wall and the production layer and an initial velocity imposed at some initial value of t. Without loss of generality, it is assumed that the production-layer forcing begins at $t = 1$. We also note that the wavenumbers are dependent on t and so the problem must be solved with instantaneous values of the wavenumbers. Considering the production-layer scalings (3.8), we now introduce a scaled variable $\xi = y/K\sqrt{2t}$ and seek a solution where $\xi = O(1)$. To enable matching with the solution exiting the production layers (3.15)–(3.16), we also adopt the production-layer scalings (3.9) for the roll–streak flow so that

$$(u_s, v_r, w_r, p_r) = (KRe^{-1} U_s, KV_r, KW_r, K^2 P_r). \tag{4.5}$$

Then, the basic flow (2.5) becomes $u_b \approx A_0 K Re^{-1} \xi^{-1} \mathrm{e}^{-K^2(\xi^2-1)/2}$, so that the equation for u_s in (4.3) becomes

$$K^{-2}\left[K^{-2}\partial_\xi^2 + \xi\,\partial_\xi - 2t\left(\partial_t + 4K^2\beta_0^2\right)\right] U_s - A_0\sqrt{2t}V_r \mathrm{e}^{-K^2(\xi^2-1)/2} = 0. \tag{4.6}$$

The second equation for the roll–streak field can be found by eliminating the pressure p_r and spanwise disturbance velocity w_r from (4.3) and (4.4) to give

$$\left[K^{-2}\partial_\xi^2 + \xi\,\partial_\xi - 2t\left(\partial_t + 4K^2\beta_0^2\right)\right] \mathscr{V}_r = 0, \tag{4.7}$$

where

$$\mathscr{V}_r = [K^{-2}\partial_\xi^2 - 2t(4K^2\beta_0^2)]\,[V_r(2t)^{-1/2}]. \tag{4.8}$$

The equations (4.6)–(4.7) are solved subject to the boundary conditions

$$u \to -A_0 \frac{K}{Re} \mathrm{e}^{-K^2(\xi-1)} + \frac{K}{Re}\frac{J_1}{\sqrt{2t}} \mathrm{e}^{(\omega_1-1)K^2(\xi-1)} (A_0\sqrt{2t})^{(1-\omega_1)} \cos(2K\beta_0 z) + \dots, \tag{4.9}$$

$$v \to \frac{K}{Re}\frac{K_1}{\sqrt{2t}} e^{\omega_1 K^2(\xi-1)} (A_0\sqrt{2t})^{-\omega_1} \cos(2K\beta_0 z) + \dots . \tag{4.10}$$

as $\xi \to \infty$. The roll–flow equation (4.7) suggests that we use the WKB method to find $\mathscr{V}_r$; this solution can then be used to find V_r and U_s from (4.8) and (4.6), respectively. W_r can be then be found from the continuity equation (4.4).

4.2 *The WKB solution in the upper adjustment layer*

We now find the solution in the upper adjustment layer, region (b) in Fig. 1. We seek a WKB solution for $\mathscr{V}_r$ in the form

$$\mathscr{V}_r = K^2 \mathscr{V}(t,\xi,K) e^{K^2\theta(t,\xi)}, \tag{4.11}$$

with $\mathscr{V}$ being the amplitude and θ being the phase in the usual notation. Substitution into the roll–flow equation (4.7) yields

$$\left[\theta_{\xi\xi} + \xi\theta_\xi - 2t\left(\theta_t + 4\beta_0^2\right)\right]\mathscr{V} + \left[K^{-4}\mathscr{V}_{\xi\xi} + K^{-2}\left(2\mathscr{V}_\xi\theta_\xi + \xi\mathscr{V}_\xi + \mathscr{V}\,\theta_{\xi\xi} - 2t\mathscr{V}_t\right)\right] = 0. \tag{4.12}$$

So at high Reynolds numbers, i.e. as $K \to \infty$, the leading order terms give the eikonal equation for the phase,

$$\theta_{\xi\xi} + \xi\theta_\xi - 2t\left(\theta_t + 4\beta_0^2\right) = 0, \tag{4.13}$$

while at the next order the terms of order K^{-2} give an equation for the amplitude. The forcing from the production layer initially diffuses into the adjustment layer through the phase function θ, therefore we initially consider the eikonal equation (4.13). This is a nonlinear partial differential equation and can be solved using Charpit's method of characteristics. Defining $\hat{p} = \theta_t$ and $\hat{q} = \theta_\xi$, we seek a solution to $F(\hat{p},\hat{q},\theta,t,\xi) = 0$. The Charpit equations for the eikonal equation (4.13) are

$$\frac{dt}{2t} = \frac{d\xi}{-(2\hat{q}+\xi)} = \frac{d\hat{p}}{-(2\hat{p}+8\beta_0^2)} = \frac{d\hat{q}}{\hat{q}} = \frac{d\theta}{2\hat{p}-\hat{q}(2\hat{q}+\xi)} = d\zeta, \tag{4.14}$$

subject to the initial Cauchy data

$$\zeta = 0,\ \theta_0(s) = \hat{p}_0(s) = 0,\ \hat{q}_0(s) = \omega_1(s),\ \mathscr{V} = \mathscr{V}_0(s) \text{ on } t_0(s) = s,\ \xi_0(s) = 1 \text{ for } s \geq 1, \tag{4.15}$$

where s is the parametrization of the initial data, ζ is the parametrization of the characteristics and

$$\mathscr{V}_0(s) = K_1(2t)^{-1}(A_0\sqrt{2t})^{-\omega_1}[\omega_1^2 - 2t(4\beta_0^2)] \tag{4.16}$$

from (4.8) and (4.10). We note that $F_{\hat{p}}t_0' - F_{\hat{q}}\xi_0' \neq 0$ (where prime represents derivative) and therefore the initial data are never tangent to the solution surface; that is to say, the integrability condition is satisfied and thus the characteristics will not cross away from $\zeta = 0$. Solving the Charpit equations (4.14) yields the solution

$$t = s\mathrm{e}^{2\zeta}, \quad \hat{q} = \omega_1(s)\mathrm{e}^{\zeta}, \quad \hat{p} = 4\beta_0^2[\mathrm{e}^{-2\zeta} - 1], \quad \xi = [1 + \omega_1(s)]\mathrm{e}^{-\zeta} - \omega_1(s)\mathrm{e}^{\zeta},$$

$$\theta = \left[\frac{1 - \mathrm{e}^{2\zeta}}{2}\right][2s(4\beta_0^2) + \omega_1^2(s)], \quad \frac{\partial^2\theta}{\partial\xi^2} = \frac{-\mathrm{e}^{2\zeta}}{\frac{1+\omega_1(s)}{\omega_1(s)} + \mathrm{e}^{2\zeta}}, \quad \mathscr{V} = \mathscr{V}_0(s)\sqrt{\frac{B(s) + 1}{B(s) + \mathrm{e}^{2\zeta}}}, \qquad (4.17)$$

where $B(s) = (1 + \omega_1(s))/\omega_1(s)$. For each value of s we can find an explicit solution for $\theta(t, \xi)$. This solution is valid for $t > 1$ where the production layer forcing begins. The characteristic emanating from that point separates what we shall define as the upper adjustment layer from the rest of the flow beneath the production layer. The limiting characteristic is at $s = 1$ and is given by

$$\bar{\xi}(t) = [1 + \omega_1(1)]t^{-1/2} - \omega_1(1)\sqrt{t}; \qquad (4.18)$$

the corresponding amplitude on this characteristic is given by

$$\mathscr{V} = \bar{\mathscr{V}}(t) = \mathscr{V}_0(1)\sqrt{(B(1) + 1)(B(1) + t)^{-1}} = \mathscr{V}^+. \qquad (4.19)$$

To continue the solution below the upper adjustment layer, we stipulate that all characteristics must now pass through the singular point of initial forcing $(t, \xi) = (1, 1)$.

4.3 *The WKB solution in the lower adjustment layer*

We seek a solution in the lower adjustment layer (region d in Fig. 1) to the Charpit equations (4.14) subject to the initial data

$$\zeta = 0, \quad \hat{p}_0(s) = 0, \quad \theta_0(s) = 0, \quad \hat{q}_0(s) = \hat{q}_0(s) \quad \text{at} \quad t = 1,\ \xi = 1 \quad \text{for} \quad s \geq \omega_1(1). \qquad (4.20)$$

We can think of this as the initial data, which was previously parametrized along t, degenerating into a point in the (t, ξ) plane. We therefore continue the initial data curve in θ_ξ as this carries the information about how the phase changes along each characteristic curve in the lower adjustment layer. We again solve the Charpit equations to give

$$\mathrm{e}^{\zeta} = \sqrt{t}, \quad \hat{q} = q_0(s)\sqrt{t}, \quad \hat{p} = 4\beta_0^2[t^{-1} - 1], \quad \xi = \frac{1 + q_0(s)}{\sqrt{t}} - q_0(s)\sqrt{t},$$

$$\theta = [q_0(s)^2 + 2(4\beta_0^2)]\left[\frac{1 - t}{2}\right], \frac{\partial^2\theta}{\partial\xi^2} = \frac{-t}{t - 1}, \quad \mathscr{V} = g(s)\frac{1}{\sqrt{\mathrm{e}^{2\zeta} - 1}}, \qquad (4.21)$$

where $g(s)$ is some as yet unknown function as we cannot prescribe initial data on $\mathscr{V}$ at the singular point. We note that $q_0(s)$ can be eliminated to give an explicit solution for $\theta(t, \xi)$.

4.4 *The WKB solution in the first transitional layer*

The solutions for $\theta_{\xi\xi}$ in (4.17) and (4.21) do not match at the limiting characteristic $\bar{\xi}$ given by (4.18). Therefore we introduce a diffusion front $\mathscr{C}$ to smooth out this discontinuity, shown by region (c) in

Fig. 1. Mathematically, this diffusion front arises as the two different WKB phases of the roll–flow equation (4.7) meet. The thickness of the transitional layer is fixed by observing that because only $\theta_{\xi\xi}$ is discontinuous across the layer, upon passing through the layer the exponential dependence must change by a factor

$$\exp[K^2(\xi-\bar{\xi})^2(\bar{\theta}^+_{\xi\xi}-\bar{\theta}^-_{\xi\xi})/2]=\exp[K^2(\xi-\bar{\xi})^2 J/2], \tag{4.22}$$

where plus and minus represent the upper and lower adjustment layer solutions, and the overbar denotes a quantity evaluated on $\mathscr{C}$, so ξ is thus $O(K^{-1})$. Thus in the diffusion front we look for a WKB solution of the form

$$\mathscr{V}_r=K^2\mathscr{V}^C(t,\phi)\mathrm{e}^{K^2\theta^C(t,\phi,K)}, \quad \phi=K(\xi-\bar{\xi})/\Delta, \quad \Delta=\sqrt{2/J}, \tag{4.23}$$

where superscript C represents the Taylor-series expansion truncated at $O(\xi^2)$ around the limiting characteristic $\xi = \bar{\xi}$. In this layer the higher order terms of the roll–flow equation (4.12), which were previously ignored, are reintroduced to smooth out the discontinuity. After some manipulation (for further details see Deguchi & Hall, 2015), we find that

$$\mathscr{V}^C=\bar{\mathscr{V}}(t)(\mathrm{erf}(\phi)+1)/2, \tag{4.24}$$

where $\bar{\mathscr{V}}(t)$ is given in (4.19). Then we can find the full solution in the lower adjustment layer; by matching with the solution in the lower adjustment layer (4.21)g, we obtain

$$g(s)=-\mathscr{V}_0(1)/[K\sqrt{2\pi}(s-\omega_1(1))]. \tag{4.25}$$

Thus we find that in the lower adjustment layer the amplitude is given by

$$\mathscr{V}=\frac{\mathscr{V}_0(1)\sqrt{t-1}}{K\sqrt{2\pi}[\xi\sqrt{t}-1+\omega_1(1)(t-1)]}=\mathscr{V}^-, \tag{4.26}$$

with $\mathscr{V}_0(1)$ given by (4.16). So in particular, we see that the amplitude falls by a factor of K^{-1} when crossing the diffusion front $\mathscr{C}$.

4.5 *The roll–streak flow in the upper and lower adjustment layers*

The roll and streak flows can now be found from (4.7) and (4.6), respectively. We obtain

$$V_r=\frac{\sqrt{2t}\mathscr{V}\mathrm{e}^{K^2\theta}}{\theta_\xi^2-2t(4\beta_0^2)}, \quad U_s=-\frac{A_0\xi^{-1}\sqrt{2t}}{2\theta_\xi}\mathrm{e}^{-\frac{K^2}{2}(\xi^2-1)}V_r, \tag{4.27}$$

where in the upper adjustment layer θ and $\mathscr{V}$ are as given in (4.17), whereas for the lower adjustment layer θ is as given in (4.21) and $\mathscr{V}$ is as given in (4.26). We see that this solution becomes singular when $s=\sqrt{2}(2\beta_0)$. This corresponds to a second limiting characteristic

$$\xi=\frac{1+2\sqrt{2}\beta_0}{\sqrt{t}}-2\sqrt{2}\beta_0\sqrt{t}\equiv\underline{\xi}(t). \tag{4.28}$$

4.6 *The WKB solution in the second transitional layer*

To smooth out the singularity we introduce a second diffusion front $\mathscr{D}$, which separates the upper and lower adjustment layers from the rest of the flow (region e in Fig. 1). Mathematically this curve arises because the homogeneous terms of the WKB solution have become as large as the inhomogeneous terms. Again the thickness of the layer is defined by insisting that the second-derivative amplitude terms in (4.7) are as large as the phase terms; once again this requires that the layer is of thickness $O(K^{-1})$. Thus in the diffusion front we seek a WKB solution of the form

$$V_r = V^D(t,\varphi)\mathrm{e}^{K^2\theta^D(t,\varphi,K)}; \quad \varphi = K(\xi - \underline{\xi})/\delta(t), \quad \delta(t) = \sqrt{-2/\theta^-_{\xi\xi}}, \tag{4.29}$$

where θ_D is the Taylor expansion truncated at $O(\xi^2)$ of the phase (4.21) in the lower adjustment layer. By considering the limiting form of V^D, we can obtain a match with the lower adjustment layer solution. We find that the amplitude of the roll in $\mathscr{D}$ is given by

$$V^D = V^i \mathrm{e}^{\varphi^2}\left[\frac{\mathrm{erf}(\varphi) - 1}{2}\right], \tag{4.30}$$

where

$$V^i(t) = -\frac{\mathscr{V}_0(1)}{4\beta_0[2\sqrt{2t}\beta_0 - \omega_1(1)\sqrt{t}]}. \tag{4.31}$$

So in particular, we see that the amplitude is once again $O(1)$; i.e. the amplitude grows by a factor K across the second diffusion layer.

4.7 *The WKB solution in the irrotational layer*

Beneath $\mathscr{D}$ the flow is irrotational because the forcing from the production layer cannot reach this part of the flow. By again using the roll–streak equations (4.6) and (4.7), we find that the streak and roll flows in this irrotational layer are given by

$$V_r = -V^i(t)\mathrm{e}^{K^2\theta^i(t,\xi)}, \quad U_s = -\frac{\sqrt{2t}A_0\mathrm{e}^{-\frac{K^2}{2}(\xi^2-1)}V_r}{2\xi\theta^i_\xi}, \tag{4.32}$$

where

$$\theta^i(t,\xi) = 2(4\beta_0^2)(1-t) + 2\sqrt{2\tau}\beta_0(\xi - \underline{\xi}). \tag{4.33}$$

4.8 *The full composite roll–streak solution*

We now combine the solutions from each of the three layers, along with the limiting solutions from each diffusion front, to produce a composite solution for the phase that is valid for the entire flow beneath the production layer. We define the composite solution so that under taking the logarithm it becomes (inner solution) + (outer solution) - (common part). Firstly, the WKB phase solution θ is continuous everywhere beneath the production layer and is defined as

$$\theta = \begin{cases} \theta^{+} \text{ from (4.17)} & \xi \geq \bar{\xi}, \\ \theta^{-} \text{ from (4.21)} & \bar{\xi} > \xi \geq \underline{\xi}, \\ \theta^{i} \text{ from (4.33)} & \xi < \underline{\xi}. \end{cases} \tag{4.34}$$

Then, to smooth out the singularities of the amplitude when crossing the lower adjustment layer, we define a composite solution for the roll flow in terms of the limiting forms as

$$V_r = \begin{cases} \frac{\mathscr{V}^C}{\mathscr{V}^C_\infty}\frac{\mathscr{V}^D}{\mathscr{V}^D_\infty}\frac{\sqrt{2t}\mathscr{V}^{+}\mathrm{e}^{K^2\theta}}{\theta_\xi^2-2t(4\beta_0^2)} \text{ from (4.19)} & \xi \geq \bar{\xi}, \\ \dfrac{\mathscr{V}^C}{\mathscr{V}^C_{-\infty}}\dfrac{\mathscr{V}^D}{\mathscr{V}^D_\infty}\dfrac{\sqrt{2t}\mathscr{V}^{-}\mathrm{e}^{K^2\theta}}{\theta_\xi^2-2t(4\beta_0^2)} \text{ from (4.26)} & \bar{\xi} > \xi \geq \underline{\xi}, \\ \dfrac{-\mathscr{V}^C}{\mathscr{V}^C_{-\infty}}\dfrac{\mathscr{V}^D}{\mathscr{V}^D_{-\infty}}V_i(t)\mathrm{e}^{K^2\theta^i(t,\xi)} \text{ from (4.31)} & \xi < \underline{\xi}. \end{cases} \tag{4.35}$$

The limiting forms $\mathscr{V}^C_\infty$, $\mathscr{V}^C_{-\infty}$, $\mathscr{V}^D_\infty$ and $\mathscr{V}^C_{-\infty}$ are the limits as $\phi \to \pm\infty$ and $\varphi \to \pm\infty$ of (4.24) and (4.30), respectively. The roll flow then completely defines the streak flow as

$$U_s = -\frac{A_0\xi^{-1}\sqrt{2t}}{2\theta_\xi}\mathrm{e}^{-\frac{K^2}{2}(\xi^2-1)}V_r, \tag{4.36}$$

where θ is defined in each layer by (4.34). Then W_r can be found from the continuity equation (4.4).

4.9 *The location of the streak maximum*

The streak flow in each layer, given by (4.36) for each θ as in (4.34), has exponential dependence with argument $K^2(\theta - \xi^2/2 - 1/2)$. This exponential dependence dominates the size of the streak. Therefore, defining $M = M(t,\xi) = K^2(\theta - \xi^2/2 - 1/2)$, the streak maximum occurs where $M_t = M_\xi = 0$. Thus, using the eikonal equation (4.13), we find that the streak maximum occurs where

$$\xi = 2\beta_0\sqrt{t}; \quad 2\beta_0 = \frac{1}{2t-1}. \tag{4.37}$$

Thus, the maximum of the streak occurs in the lower adjustment layer, i.e. $\bar{\xi} > \xi_M \geq \underline{\xi}$. This means that the maximum occurs well after the onset of forcing, and far away from the wall at $\xi = 0$. Hence, the streak structure is more dominant in the lower adjustment layer where $\xi = O(1)$ than in the unperturbed main boundary layer where $\xi = O(K^{-1})$. Surprisingly, this is the layer where the WKB amplitude is a minimum. This is because the dominant forcing from the production layer occurs through the phase.

5. Numerical results

We now present numerical solutions of the boundary-region equations (4.3)–(4.4) and compare them against the composite solution (4.35)–(4.36) found in §4. To calculate the numerical solution of the boundary-region equations (4.3)–(4.4), we march the equations forward in time from an initial condition, subject to boundary conditions at the wall and at the production layer. At each time step we evaluate the boundary conditions (3.15)–(3.16) using the instantaneous value of $K_1(\alpha, \beta)$ given by the solution of the numerical eigenvalue problem for ASBL flow, (3.2)–(3.3), solved for a range of (α, β) in Deguchi & Hall (2014b). Here we recall α and β are the instantaneous wavenumbers $\alpha = \alpha_0\sqrt{2t}$, $\beta = \beta_0\sqrt{2t}$. We solve for values of β lying between the left and right saddle nodes of the numerical eigenvalue solutions from Deguchi & Hall (2014b) for the production layer problem; taking the left saddle node to correspond to $t = 1$, this then fixes a time interval on which to compute the solution and thus also fixes the range of spanwise wavenumbers β. We find that there is good agreement between the asymptotic results and the numerical solutions. The boundary-region equations (4.3) are parabolic and therefore, given values of the Reynolds number and the spanwise wavenumber, can be solved numerically by marching forwards in time subject to initial forcing from the production layer. Following Hall (1983) we first rearrange the boundary-region equations (4.3)–(4.4) and eliminate the pressure and spanwise velocity disturbances to give a fourth-order equation for the roll flow v_r and a second-order equation for the streak flow u_s. Then, after writing the equations in terms of the similarity variable $\eta = y/\sqrt{2t}$, the equations are discretized in η using a second-order-accurate central finite-difference scheme. We then use a second-order-accurate Crank–Nicholson scheme to march the equations forward in time. We use a step size of $h = 10^{-3}$ in the t direction, and a grid of 2000 points in the η direction. We apply an initial condition $u_s = v_r = 0$ at $t = 1$ for all η. At the wall we apply no-slip and impenetrability, so that $u_s = v_r = \partial v_r/\partial y = 0$ at $\eta = 0$. At the production layer, corresponding to $\eta = K$, we apply the boundary conditions (3.15)–(3.16) and no-slip.

In Fig. 2 we present results for the numerical solution for $Re = 10^4$, 10^7 and 10^{10}. In Figs 2b, 2c and 2e we show the streak part of the numerical solution of the boundary-region equations, together with the limiting characteristics shown in Fig. 1. In addition we show the asymptotic prediction of the streak maximum in t and ξ given by (4.37). We see that as the Reynolds number increases the numerical results agree increasingly well with the asymptotic results; this is shown by the observed maximum of the numerical solution falling increasingly close to the predicted location of the maximum of M in t and ξ, marked by a black diamond (⧫). The numerical solution also improves over long times as the Reynolds number increases; for $Re = 10^4$ there is some error at larger values of t; however, here the expansion parameter K used is only approximately 4. However, in all cases, the numerical solution has captured the predicted overall flow structure; i.e. $O(Re^{-1})$ interactions taking place in the production layer produce a large amplitude streak appearing in the boundary layer, albeit for a finite time. In Figs 2b, 2d and 2f we show the disturbance streamwise velocity in the $y - z$ plane at the predicted time for the streak maximum to occur from (4.37). We see that the location of the predicted streak maximum agrees increasingly well with the numerical results as the Reynolds number is increased. We also clearly see the streak, having grown away from the production layer, obtaining its maximum well away from the production layer where it was generated.

6. Discussion

We have shown that free-stream coherent structures can exist in unsteady Rayleigh boundary-layer flow. The structures were mathematically similar to those derived in Deguchi & Hall (2015), with the flow unsteadiness replacing non-parallel effects. An $O(Re^{-1})$ nonlinear interaction in a layer situated just below the free-stream, where disturbances were convected with almost free-stream speed, produced a disturbance involving rolls, waves and streaks. The streak part of this disturbance interacted with the basic flow in the main part of the boundary layer and continued to grow through the ‘lift-up‘ mechanism, adjusting to the non-parallel nature of the basic flow via continuation through two transitional layers

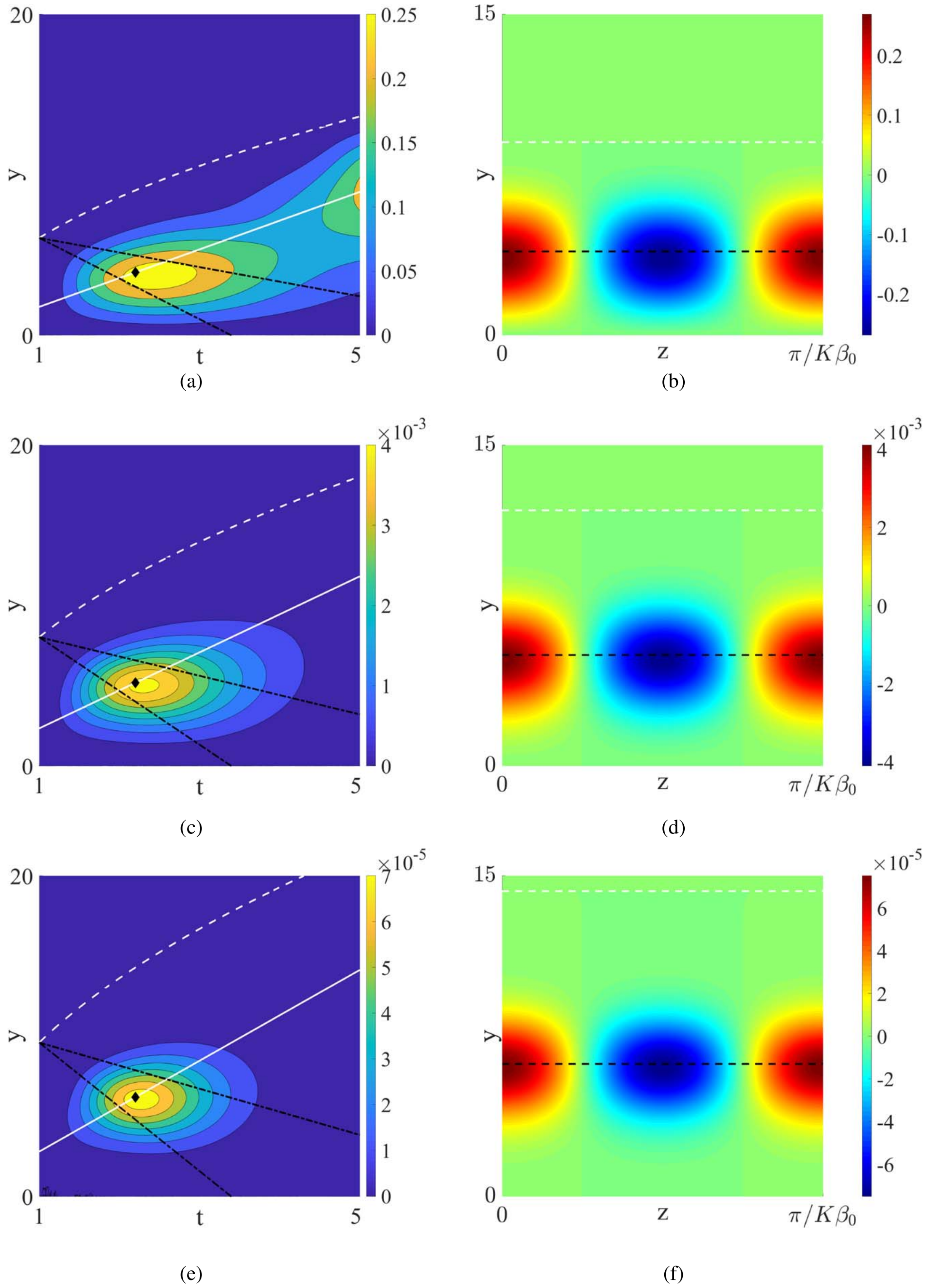

FIG. 2. The numerical solution for $Re = 10^4$ (a, b), 10^7 (c, d) and 10^{10} (e, f). (a, c, e): the streak part of the solution $-u_s$. The black dashed lines are the upper and lower limiting characteristics $\bar{\xi}$ and $\underline{\xi}$ from (4.18) and (4.28), respectively. The white line corresponds to the predicted location of the maximum of M in t and ξ from (4.37), with the corresponding time marked by a black diamond (♦). The white dashed line is $\xi = 1$ (at the production layer). (b, d, f): the disturbance streamwise velocity $-u_s \cos(2K\beta_0 z)$ at the predicted time of the streak maximum, $t \approx 2.21$. The black dashed line is the predicted location of the maximum of M in ξ at this time. The white dashed line is $\xi = 1$.

where discontinuities were smoothed to produce a composite solution. The streak maximum was predicted to be in the lower of the two adjustment layers. The asymptotically reduced boundary-region equations were then solved numerically via a Crank–Nicholson time-marching scheme. The numerical results were found to be in increasingly good agreement with the predicted asymptotic results as the Reynolds number was increased. In particular, as the Reynolds number was increased, the streak maximum in the numerical solution appeared earlier, in better agreement with the asymptotic prediction.

Unsteady flows are ubiquitous in nature and have many applications in engineering and science. The unsteadiness is mainly classed as non-periodic, e.g. the sudden opening and closing of valves in a flow through a pipe system or periodic, e.g. a turbine blade rotating through water. The Rayleigh problem studied here is non-periodic, but the laminar flow allows a similarity solution. Experimental results for transition to turbulence in non-periodic unsteady flows by Mathur *et al.* (2018) have shown that if the flow is persistently accelerated the critical Reynolds number associated with transition increases. In addition, for periodic unsteadiness flows or flows where the unsteadiness is changing, e.g. by acceleration, the flow history is important: the way in which instantaneous flow behaves is based on past history. In light of those results variations on the Rayleigh problem in which the quasi-steady approximation is not valid would provide interesting areas of further study. These include an oscillating flat plate (Stokes' second problem), and a flat plate accelerated uniformly from rest. The first of these has an analytic solution for the basic flow that approaches its free-stream value through an exponentially small correction so it could be particularly interesting to study in light of the results above. However, since it is not exponential throughout the main boundary layer, the interaction of a streak disturbance with the basic flow could be very different and may not support growth.

We also note here that we have not solved the unsteady production layer problem; such solutions, if they exist, could be used to analyse the small-time development of the problem studied here. We have not gone into detail here on the solution at the immediate point of forcing, when a singularity occurs. Here, the characteristics described in §4 pile up and a shock in the solution occurs. However, since the maximum of the streak disturbance occurs in the adjustment layer well away from the initial forcing at $t = 1$, it is anticipated that nothing new would be learnt about the solution by examining this region. Nevertheless, for a periodic or accelerating unsteadiness where, as discussed above, flow history is important, the shock at the initial point of forcing could have great implications at later times.

Laminar Rayleigh flow is often used to show how vorticity spreads in a boundary layer. The basic flow and the vorticity both satisfy the heat equation for the conduction of heat on a semi-infinite rod. In the context of fluid flow, the wall becomes a plane source of vorticity and the Rayleigh problem shows how fluid momentum is diffused away from the plate, with the region affected by viscosity (i.e. the boundary layer) growing in time; we earlier showed the width of the boundary layer to be $\sim \sqrt{\nu t}$. In addition, one can show that the shear stress at the wall decays as $t^{-1/2}$. With the free-stream coherent structures we now have high levels of vorticity entering the boundary layer from the free stream. It would be interesting to examine the interaction of the basic underlying vorticity field with the vorticity originating in the production layer; this could be done asymptotically in a similar manner to the problem described above.

The flat plate studied in this problem was infinitely long and therefore the free-stream coherent structures found were independent of the point x from the flow was viewed. An interesting problem to study further would be that of a semi-infinite flat plate moving with constant unit velocity. For time $t < x$, where x is the distance measured downstream from the leading edge, Rayleigh flow is observed. However beyond that point the flow is radically different; at $t = x$ the disturbance at the leading edge begins to affect the flow and for $t \to \infty$, Blasius flow is observed. Therefore we have a remarkable situation where an x-independent, time-dependent flow can smoothly change (this is a physical requirement) into a time-independent, x-dependent flow. There are conflicting explanations as to how this occurs; Smith (1972) and Stewartson (1951) claim that it occurs through an essential singularity, whereas Tokuda (1968) claims that the solution can be found without a singularity through the use of stretched variables. The question of how the free-stream coherent structures develop at this point is particularly intriguing; in particular, whether the transition point could provide any forcing to sustain the structures past the point where no growth occurs in these results.

Acknowledgements

The authors very much appreciate the constructive marks of the referees.

References

Brown, S. N. & Stewartson, K. (1965) On similarity solutions of the boundary-layer equations with algebraic decay. *J. Fluid Mech.*, **23**, 673–687.

Chen, C. & Christensen, D. K. (1967) Stability of flow induced by an impulsively started rotating cylinder. *Phys. Fluids*, **10**, 1845–1846.

Cowley, S. (1987) High frequency Rayleigh instability of stokes layers. *Stability of Time Dependent and Spatially Varying Flows* (D. Dwoyer & M. Hussaini eds). Springer, New York, NY, pp. 261–275.

Deguchi, K. & Hall, P. (2014a) Canonical exact coherent structures embedded in high Reynolds number flows. *Phil. Trans. Roy. Soc. A*, **372**, 20130352.

Deguchi, K. & Hall, P. (2014b) Free-stream coherent structures in parallel boundary-layer flows. *J. Fluid Mech.*, **752**, 602–625.

Deguchi, K. & Hall, P. (2015) Free-stream coherent structures in growing boundary layers: a link to near-wall streaks. *J. Fluid Mech.*, **778**, 451–484.

Deguchi, K. & Hall, P. (2018) Free-stream coherent structures in a planar jet. *J. Fluid Mech.*, **837**, 916.

Faisst, H. & Eckhardt, B. (2003) Traveling waves in pipe flow. *Phys. Rev. Lett.*, **91**, 224502.

Goldstein, M. & Sescu, A. (2008) Boundary-layer transition at high free-stream disturbance levels-beyond Klebanoff modes. *J. Fluid Mech.*, **613**, 95.

Hall, P. (1978) The linear stability of flat stokes layers. *P. Roy. Soc. A*, **359**, 151–166.

Hall, P. (1983) The linear development of Görtler vortices in growing boundary layers. *J. Fluid Mech.*, **130**, 41–58.

Hall, P. (2003) On the instability of stokes layers at high Reynolds numbers. *J. Fluid Mech.*, **482**, 1.

Hall, P. & Parker, K. H. (1976) The stability of the decaying flow in a suddenly blocked channel. *J. Fluid Mech.*, **75**, 305–314.

Hall, P. & Sherwin, S. (2010) Streamwise vortices in shear flows: harbingers of transition and the skeleton of coherent structures. *J. Fluid Mech.*, **661**, 178–205.

Hall, P. & Smith, F. T. (1991) On strongly nonlinear vortex/wave interactions in boundary-layer transition. *J. Fluid Mech.*, **227**, 641–666.

Jiménez, J. (2018) Coherent structures in wall-bounded turbulence. *J. Fluid Mech.*, **842**, P1.

Kirchner, R. & Chen, C. (1970) Stability of time-dependent rotational Couette flow. Part 1. Experimental investigation. *J. Fluid Mech.*, **40**, 39–47.

Luchini, P. (1996) Reynolds-number-independent instability of the boundary layer over a flat surface. *J. Fluid Mech.*, **327**, 101–115.

Martin, J. & Martel, C. (2012) Nonlinear streak computation using boundary region equations. *Fluid Dyn. Res.*, **44**, 045503.

Mathur, A., Seddighi, M. & He, S. (2018) Transition of transient channel flow with high Reynolds number ratios. *Entropy*, **20**.

Moss, E. (1992) The stability of spatially developed pipe flows impulsively started from rest. *Eleventh Australasian Fluid Mechanics Conference, Univ. of Tasmania, Hobart, Australia, 14–18 December 1992*, pp. 703–706.

Otto, S. R. (1993) Stability of the flow around a cylinder: the spin-up problem. *IMA J. Appl. Math.*, **51**, 13–26.

Ricco, P., Luo, J. & Wu, X. (2011) Evolution and instability of unsteady nonlinear streaks generated by free-stream vortical disturbances. *J. Fluid Mech.*, **677**, 1.

Seminara, G. & Hall, P. (1975) Linear stability of slowly varying unsteady flows in a curved channel. *P. Roy. Soc. A*, **346**, 279–303.

Sescu, A. & Afsar, M. (2018) Hampering Görtler vortices via optimal control in the framework of nonlinear boundary region equations. *J. Fluid Mech.*, **848**, 5–41.

Shen, S. (1961) Some considerations on the laminar stability of time-dependent basic flows. *J. Aerospace Sci.*, **28**, 397–404.

Smith, S. H. (1972) On the impulsive flow of a viscous liquid past a semi-infinite flat plate. *SIAM J. Appl. Math.*, **22**, 148–154.

Stewartson, K. (1951) On the impulsive motion of a flat plate in a viscous fluid. *Q. J. Mech. Appl. Math*, **4**, 182–198.

Thomas, C. (2020) The linear stability of an acceleration-skewed oscillatory stokes layer. *J. Fluid Mech.*, 895.

Tokuda, N. (1968) On the impulsive motion of a flat plate in a viscous fluid. *J. Fluid Mech.*, **33**, 657–672.

Von Kerczek, C. & Davis, S. H. (1974) Linear stability theory of oscillatory stokes layers. *J. Fluid Mech.*, **62**, 753–773.

Waleffe, F. (1997) On a self-sustaining process in shear flows. *Phys. Fluids*, **9**, 883–900.

Waleffe, F. (2001) Exact coherent structures in channel flow. *J. Fluid Mech.*, **435**, 93–102.

Waleffe, F. (2003) Homotopy of exact coherent structures in plane shear flows. *Phys. Fluids*, **15**, 1517–1534.

Wang, J., Gibson, J. & Waleffe, F. (2007) Lower branch coherent states in shear flows: transition and control. *Phys. Rev. Lett.*, **98**, 204501.

Wedin, H. & Kerswell, R. R. (2004) Exact coherent structures in pipe flow: travelling wave solutions. *J. Fluid Mech.*, **508**, 333–371.

Wu, X. (1992) The nonlinear evolution of high-frequency resonant-triad waves in an oscillatory stokes layer at high Reynolds number. *J. Fluid Mech.*, **245**, 553–597.

Wu, X., Lee, S. & Cowley, S. J. (1993) On the weakly nonlinear three-dimensional instability of shear layers to pairs of oblique waves: the stokes layer as a paradigm. *J. Fluid Mech.*, **253**, 681–721.

Chapter 5

Free-stream coherent structures in parallel compressible boundary-layer flows at subsonic and moderate supersonic Mach numbers

The work for this paper was started while I was doing postgraduate research at Monash University, Melbourne and was completed during my studies at the University of Manchester, but has not in any part been assessed for a previous degree. The paper has a self-contained introduction, discussion, appendices and bibliography. It appears as:

E. C. Johnstone and P. Hall (2021). "Free-stream coherent structures in parallel compressible boundary-layer flows at subsonic and moderate supersonic Mach numbers". *J. Fluid Mech.* 924, A27.

The version that was originally submitted to the Journal of Fluid Mechanics was shortlisted for the IMA Lighthill-Thwaites award in 2021.

Statement of Contributions

EJ derived the model, performed the asymptotic analysis and the numerical computations, created the figures and wrote the paper. PH suggested the initial problem, provided guidance on the asymptotic analysis (particularly on the scalings in each layer) and provided editorial suggestions.

J. Fluid Mech. (2021), *vol.* 924, A27, doi:10.1017/jfm.2021.617

Free-stream coherent structures in parallel compressible boundary-layer flows at subsonic and moderate supersonic Mach numbers

Eleanor C. Johnstone[1],† and Philip Hall[2]

[1]Department of Mathematics, University of Manchester, Manchester M13 9PL, UK

[2]School of Mathematics, Monash University, Melbourne, VIC 3800, Australia

(Received 6 November 2020; revised 31 March 2021; accepted 4 July 2021)

As a first step towards the description of coherent structures in compressible shear flows, we present an asymptotic description of nonlinear travelling-wave solutions of the Navier–Stokes equations in the compressible asymptotic suction boundary layer (ASBL). We consider free-stream Mach numbers M_∞ in the subsonic and moderate supersonic regime so that $0 \leqslant M_\infty \leqslant 2$. We extend the large-Reynolds-number asymptotic theory of Deguchi & Hall (*J. Fluid Mech.*, vol. 752, 2014, pp. 602–625) describing 'free-stream' coherent structures in incompressible ASBL flow to describe a nonlinear interaction in a thin layer situated just below the free stream. Crucially, the nonlinear interaction equations for the velocity field in this layer are identical to those obtained in the incompressible problem, and thus the asymptotic analysis supporting free-stream coherent structures in compressible ASBL is easily deduced from its incompressible counterpart. The nonlinear interaction produces streaky disturbances to both the velocity and temperature fields, which can grow exponentially towards the wall. We complete the description of the growth of the velocity and thermal streaks throughout the flow by solving the compressible boundary-region equations numerically. We show that the velocity and thermal streaks obtain their maximum amplitude in the unperturbed boundary layer. Increasing the free-stream Mach number enhances the thermal streaks and suppresses the velocity streaks, whereas varying the Prandtl number suppresses the velocity streaks, and can either enhance or suppress the thermal streaks depending on whether the flow is in the subsonic or moderate supersonic regime. Such nonlinear equilibrium states have been implicated in shear transition in incompressible flows; therefore, our results indicate that a similar mechanism may also be present in compressible flows.

Key words: compressible boundary layers, transition to turbulence, nonlinear instability

† Email address for correspondence: eleanor.johnstone@manchester.ac.uk

1. Introduction

It has been known since Kline *et al.* (1967) that transitional and turbulent flows exhibit clear structure within the boundary layer in the form of vortical structures coupled to high- and low-speed streaks in the plane perpendicular to the unperturbed flow. Recent understanding of these structures has been aided by the identification of three-dimensional, nonlinear invariant solutions of the Navier–Stokes equations which may take the form of equilibria, periodic orbits or travelling-wave solutions. These states, now commonly known as exact coherent structures, have been found in a wide range of canonical shear flows where the key parameter governing the dynamics is the Reynolds number; see, for e.g. Faisst & Eckhardt (2003), Waleffe (2001, 2003), Wedin & Kerswell (2004) and Wang, Gibson & Waleffe (2007). The study of exact coherent structures in two-parameter space has previously only been conducted in the context of stably stratified flows (Eaves & Caulfield 2015; Deguchi 2017; Lucas & Caulfield 2017; Lucas, Caulfield & Kerswell 2017; Olvera & Kerswell 2017), where it is shown that the Prandtl number plays a key role in the structure of the states found (Langham, Eaves & Kerswell 2020).

The present work is confined to a special type of coherent structure in asymptotic suction boundary-layer (ASBL) flow, in which a parallel, streamwise-invariant basic flow is maintained via constant suction far from the leading edge. In the incompressible case, Hocking (1975) showed that the flow is linearly stable up to a Reynolds number of 54 370; Fransson & Alfredsson (2003) subsequently showed experimentally that transition could occur at much lower Reynolds numbers. It has been very recently shown that it is possible to experimentally realise a turbulent ASBL (Ferro, Fallenius & Fransson 2021). Several three-dimensional, fully nonlinear invariant solutions of the Navier–Stokes equations have been identified in incompressible ASBL flow. Periodic-orbit-type solutions have been obtained by Kreilos *et al.* (2013) and Khapko *et al.* (2013) via edge tracking. Travelling-wave-type solutions have also been identified in the ASBL by Deguchi & Hall (2014), who found structures localised in the wall-normal direction but periodic in the streamwise and spanwise directions, and by Kreilos, Gibson & Schneider (2016), who found spanwise-localised travelling-wave solutions. In both cases, two types of solution were found: a 'wall mode' coherent structure with the streaks and vortex structure concentrated near the wall region; and a 'free-stream' coherent structure with the streak flow still mainly concentrated in the near-wall region but with the vortical structure residing in the free stream.

Deguchi & Hall (2014) showed that the spanwise-periodic wall modes could be described by high-Reynolds-number vortex–wave interaction theory (Hall & Smith 1991; Hall & Sherwin 2010), in which forcing in the critical layer of the wave drives a roll flow which produces a streak; the streaky flow is then itself unstable to the wave. This tripartite interaction is also known as a self-sustaining process (Waleffe 1997). Meanwhile, the free-stream coherent structures can be described by a distinct asymptotic theory which relies on the exponential approach of the boundary-layer flow to its free-stream form. A nonlinear interaction between tiny waves, rolls and streaks satisfies the unit-Reynolds-number three-dimensional Navier–Stokes equations within a 'production' layer, which is located at the edge of the free stream and which is of the same depth as the unperturbed boundary layer. The nonlinear production-layer interaction allows a streak disturbance to the velocity field to grow exponentially beneath the production layer. An analysis of the induced roll–streak flow shows that the streak obtains its maximum size in the near-wall boundary layer. This high-Reynolds-number asymptotic framework to describe free-stream coherent structures has subsequently been extended to non-parallel (Deguchi & Hall 2015, 2018) and unsteady (Johnstone & Hall 2020) flows.

Free-stream turbulence is known to play a key role in boundary-layer transition (Fransson, Matsubara & Alfredsson 2005; Fransson & Shahinfar 2020). It is hypothesised that free-stream coherent structures may play a key role in linking the coherent structures observed in the inner region (near-wall region of intense turbulence production) and outer (large-scale, less active) regions of boundary-layer flow (Deguchi & Hall 2014). This detail would be particularly relevant in the context of jet acoustics for compressible flows, when disturbances originating in the free stream may be implicated in the high frequency sound often referred to as 'screeching' which is observed in high-speed jet flows (Deguchi & Hall 2018).

There has been little work, however, into the asymptotic description of coherent structures in the context of compressible flows despite the importance of transitional and turbulent compressible flows to many industrial problems, particularly in the fields of aerospace engineering and acoustics. Past experimental and numerical studies have focused on laminar–turbulent transition in compressible boundary layers in the context of the effect of free-stream vortical disturbances, with particular focus on bypass transition (see, for e.g. Laufer 1954; Kendall 1975; Demetriades 1989; Graziosi & Brown 2002; Mayer, von Terzi & Fasel 2011). By extending the incompressible theory of Leib, Wundrow & Goldstein (1999), Ricco & Wu (2007) show that free-stream vortical disturbances can induce temperature fluctuations that lead to the formation of 'thermal streaks'; the growth of these streaks is enhanced at larger free-stream Mach numbers, although nonlinear effects were found to inhibit the growth of the streaks (Marensi, Ricco & Wu 2017). Short-wavelength free-stream vortical disturbances have also been found to concentrate in the 'edge layer' Wu & Dong (2016), which is akin to the production layer for free-stream coherent structures described above.

However, the organised streaky structures observed experimentally in incompressible flows have been identified in supersonic compressible flows both experimentally (for a thorough review see Spina, Smits & Robinson 1994) and numerically (Pirozzoli, Bernardini & Grasso 2008; Ringuette, Wu & Martín 2008). The structures found are consistent with the hairpin loop model of wall turbulence, with low-speed, elongated streaks observed in the logarithmic region. Thus there exists compelling evidence for the similarity between compressible and incompressible coherent structures. Indeed, the main effect of compressibility in turbulent shear boundary layers lies in the density fluctuations (Morkovin 1962), and it is generally accepted that for moderate free-stream Mach numbers $M_\infty \leqslant 2$, the dynamics of compressible shear boundary layers does not differ greatly from its incompressible counterpart (Spina *et al.* 1994).

The aim of the present work is to ask: (*a*) Can we use the high-Reynolds-number asymptotic theory describing free-stream coherent structures in incompressible ASBL flow (Deguchi & Hall 2014) to describe free-stream coherent structures in compressible ASBL flow in the subsonic and moderate supersonic regimes? And (*b*), what is the influence of the additional physical parameters, namely the Mach number M_∞ and the Prandtl number σ?

Assuming a perfect gas, the basic flow for the compressible ASBL approaches its free-stream form exponentially and thus has the underlying structure required to support the free-stream coherent structures described in Deguchi & Hall (2014). We find that compressibility effects shift the location of the production layer by a constant proportional to M_∞^2. However, the key result is that the leading-order equations for the velocity field in the production layer are identical to those for the incompressible problem. Since the asymptotics and numerical solutions agreed well for the incompressible case we expect that this is true for the compressible problem. Moreover, this also represents a significant computational reduction as the solution of the nonlinear eigenvalue production-layer problem, which was computed by direct numerical simulation by Deguchi & Hall (2014), can also be used for the compressible problem. However, as discussed at the end of this paper, we expect that this reduction will not hold in general for other compressible regimes at higher free-stream Mach number due to the presence of non-parallel effects and shocks.

The equations for the thermal field in the production layer are passive and driven by the velocity field. This effect arises due to the location of the thin production layer being just below the free stream, where compressibility effects are negligible because the density and viscosity are close to their constant free-stream values. As in the incompressible problem, the nonlinear interaction in the production layer produces a disturbance to the streamwise velocity field (a 'streak') that grows exponentially down towards the wall through interaction with the mean flow. However, the nonlinear interaction also induces a disturbance to the temperature field, a 'thermal streak', which also grows exponentially down towards the wall. The amplitude of the thermal streaks is enhanced as the Mach number is increased whilst the amplitude of the velocity streaks is suppressed. In the subsonic regime the amplitude of the velocity streaks is in general one order of magnitude larger than that of the thermal streaks but the amplitudes become of comparable size in the moderate supersonic regime. At the wall, both the velocity and thermal streaks vanish so as to satisfy the wall boundary conditions. The location where the thermal and velocity streaks attain their maximum amplitude relative to the velocity streak is controlled by the Prandtl number.

The rest of this paper is presented as follows: in § 2, we provide a brief description of free-stream coherent structures in incompressible ASBL flow. We then define the governing equations for compressible ASBL flow in § 3 and find the basic flow in § 4. The production-layer problem is then described in § 5. We present the solution below the production layer and down to the wall in § 6. We then present results for a variety of parameters in § 7 and finally in § 8 we draw some conclusions.

2. Free-stream coherent structures in incompressible parallel boundary-layer flows

To provide some context for the discussion of free-stream coherent structures in the compressible ASBL flow, we briefly summarise the results of Deguchi & Hall (2014) for free-stream coherent structures in incompressible ASBL flow.

Incompressible ASBL flow describes viscous, incompressible flow (u^*, v^*, w^*) with respect to Cartesian coordinates (x^*, y^*, z^*), with dynamic viscosity μ and kinematic viscosity ν, over a flat plate at $y^* = 0$. Uniform flow exists in the free stream, so denoting free-stream values by subscript ∞, at the free-stream $(u^*, v^*, w^*) = (u_\infty, -v_\infty, 0)$. The plate is subject to constant suction, so the velocity at the plate is $(u^*, v^*, w^*) = (0, -v_\infty, 0)$. Non-dimensionalising the velocity components on the free-stream speed u_∞ and the coordinates on the length scale ν/v_∞, and defining the Reynolds number $Re = u_\infty/v_\infty$, the basic flow is given by

$$(u_b, v_b, w_b) = (1 - \mathrm{e}^{-y}, -Re^{-1}, 0). \tag{2.1}$$

Deguchi & Hall (2014) showed that, at high Reynolds numbers, the incompressible Navier–Stokes equations allow for nonlinear equilibrium solutions taking the form of a roll–wave–streak interaction propagating in a viscous layer at the outer edge of the boundary layer; this layer is termed the production layer and the solutions are known as free-stream coherent structures. The interaction in the production layer is characterised by nonlinear travelling-wave solutions propagating with wave speed c; numerical computations suggest that the asymptotic behaviour of the wave speed is

$1 - c = O(Re^{-1})$, so that the wave propagates downstream with almost free-stream speed. The solutions also have streamwise length scales comparable to the spanwise length scales, and the thickness of production layer is comparable to the boundary-layer thickness. Seeking a solution with these scalings, which is periodic in the streamwise and spanwise directions with respective wavenumbers α and β, shows that the production layer in ASBL flow is located at $y = \ln Re$.

The solution inside the production layer is $\boldsymbol{U}(X, Y, z) = (U, V, W)$, where $(x, y, z) = (X - ct, Y - \ln Re, z)$, $c = 1 - Re^{-1}c_1$, and is determined by numerically solving the full Navier–Stokes equations at unit Reynolds number as a nonlinear eigenvalue problem for the perturbed wave speed c_1 of the travelling wave:

$$([\boldsymbol{U} + c_1\hat{\boldsymbol{i}}] \cdot \nabla)\boldsymbol{U} = -\nabla P + \nabla^2 \boldsymbol{U}, \tag{2.2}$$

$$\nabla \cdot \boldsymbol{U} = 0. \tag{2.3}$$

The asymptotic structure of the solution emerging from the lower side of the production layer shows that, below the layer, the disturbance to the streamwise velocity (termed the streak), which occurs as a result of the nonlinear interaction in the production layer, can grow exponentially like e^{-Y} as $Y \to -\infty$ while the other velocity components decay. Thus moving beneath the production layer,

$$u \to 1 - \mathrm{e}^{-y} + \frac{d_0}{Re} + \frac{J_1}{Re^{\omega_1}}\mathrm{e}^{(\omega_1-1)y}\cos(2\beta z) + \frac{J_1 K_1}{Re^{2\omega_1}4\omega_1}\mathrm{e}^{(2\omega_1-1)y} + \cdots, \tag{2.4}$$

$$v \to -\frac{1}{Re} + \frac{K_1}{Re^{\omega_1+1}}\mathrm{e}^{\omega_1 y}\cos(2\beta z) + \cdots, \tag{2.5}$$

$$w \to -\frac{K_1\omega_1}{2\beta Re^{\omega_1+1}}\mathrm{e}^{\omega_1 y}\sin(2\beta z) + \cdots, \tag{2.6}$$

where

$$J_1 = \frac{K_1}{(\omega_1 - 1)^2 + (\omega_1 - 1) - 4\beta^2}, \quad \omega_1 = \frac{-1 + \sqrt{1 + 16\beta^2}}{2} \geqslant 0, \tag{2.7a,b}$$

for spanwise wavenumber β, and where K_1 is found as part of the numerical solution of the eigenvalue problem in the production layer. These solutions are valid as the wall layer is approached, i.e. when $1 \ll y \ll \ln Re$. The constant of integration d_0 is found by matching with the numerical solution of the eigenvalue problem (2.2)–(2.3) which was computed for a range of spanwise wavenumbers β in Deguchi & Hall (2014). Thus the term d_0/Re is the next order correction to the mean flow due to the nonlinear interaction in the production layer. Therefore in general the streamwise velocity solution is only given up to a constant, however, the correction does not influence the vortex field which is the quantity of interest. By solving for the induced flow throughout the boundary region between the production layer and the wall, Deguchi & Hall (2014) show that for $\beta < 1/\sqrt{2}$ the streak disturbance grows down to the main part of the boundary layer, before being reduced to zero at the wall to satisfy the boundary conditions.

3. Governing equations for compressible ASBL flow

We now consider the compressible counterpart of ASBL flow. Consider a viscous, compressible perfect gas with density, temperature and dynamic viscosity ρ^*, θ^* and μ^* respectively, flowing with velocity $\boldsymbol{u}^* = (u^*, v^*, w^*)$ with respect to Cartesian coordinates

(x^*, y^*, z^*) over an infinitely long flat plate at $y^* = 0$. Uniform suction exists at the plate boundary so that, denoting free-stream values by subscript ∞, the velocity is $\boldsymbol{u}^* = (0, -v_\infty, 0)$ at the plate. Meanwhile, a long way from the plate at the free stream, $\boldsymbol{u}^* \to (u_\infty, -v_\infty, 0)$ and $(\rho^*, \theta^*, \mu^*, p^*) \to (\rho_\infty, \theta_\infty, \mu_\infty, p_\infty/\rho_\infty u_\infty^2)$. The suction at $y^* = 0$ does not allow for zero heat transfer over the plate due to the transfer of kinetic energy across it, and therefore we assume the temperature at the plate is fixed so that $\theta^* = \theta_p$ at $y^* = 0$.

We non-dimensionalise by scaling the coordinates (x^*, y^*, z^*) on the velocity-boundary-layer thickness $\delta = \mu_\infty/\rho_\infty v_\infty$, the velocity components (u^*, v^*, w^*) on u_∞, the pressure on $\rho_\infty u_\infty^2$ and the quantities ρ^*, θ^* and μ^* on their free-stream values. We define the Reynolds number Re by

$$Re = u_\infty/v_\infty. \tag{3.1}$$

Throughout the analysis that follows, we assume the Reynolds number is large. We also define the following physical constants:

(i) c_v, c_p, are the specific heats at constant volume and constant pressure respectively;
(ii) $\gamma = c_p/c_v$ is the ratio of specific heats; for air, $\gamma \approx 1.4$;
(iii) R is the molecular gas constant which is approximately 286 $\mathrm{m^2\,s^{-2}\,K^{-1}}$ for air;
(iv) $a_\infty = \sqrt{\gamma R\theta_\infty}$ is the speed of sound in the free stream;
(v) $M_\infty = u_\infty/a_\infty$ is the free-stream Mach number;
(vi) k is the thermal diffusivity of the gas;
(vii) $\sigma = \mu_\infty c_p/k$ is the Prandtl number which defines the ratio of momentum diffusivity to thermal diffusivity; for air, $\sigma \approx 0.71$.

We consider values of u_∞ and a_∞ such that we obtain Mach numbers M_∞ in the subsonic and moderate supersonic regimes so that $M_\infty \leqslant 2$. In the moderate supersonic regime we assume that the plate is sufficiently thin so that shocks are not present. We choose parameters γ and σ that are appropriate for the ideal gas assumption; in particular, this means that $\sigma < 2$, which will become important in the scaling arguments below.

Then, using mixed notation so that (x_1, x_2, x_3) represents (x, y, z), $\boldsymbol{\nabla} = (\partial_{x_1}, \partial_{x_2}, \partial_{x_3})$ and $\boldsymbol{u} = (u_1, u_2, u_3)$ represents (u, v, w), the Navier–Stokes equations have the form

$$\rho\frac{\mathrm{D}u_i}{\mathrm{D}t} = -\frac{\partial p}{\partial x_i} + \frac{1}{Re}\left\{\frac{\partial}{\partial x_i}\left(-\frac{2}{3}\mu\boldsymbol{\nabla}\boldsymbol{\cdot}\boldsymbol{u}\right) + \frac{\partial}{\partial x_j}\left(\mu\frac{\partial u_j}{\partial x_i}\right) + \frac{\partial}{\partial x_j}\left(\mu\frac{\partial u_i}{\partial x_j}\right)\right\} \quad (i, j = 1, 2, 3), \tag{3.2}$$

$$\frac{\partial\rho}{\partial t} + \boldsymbol{\nabla}\boldsymbol{\cdot}(\rho\boldsymbol{u}) = 0, \tag{3.3}$$

$$\rho\frac{\mathrm{D}\theta}{\mathrm{D}t} = \frac{(\gamma-1)M_\infty^2}{Re}\varPhi + (\gamma-1)M_\infty^2\frac{\mathrm{D}p}{\mathrm{D}t} + \frac{1}{Re}\frac{1}{\sigma}\frac{\partial}{\partial x_i}\left(\mu\frac{\partial\theta}{\partial x_i}\right), \tag{3.4}$$

$$p = \theta_\infty U_\infty^{-2}\rho R\theta, \tag{3.5}$$

where the dissipation function $\varPhi$ is defined by

$$\varPhi = \tfrac{1}{2}\mu e_{ij}e_{ij} - \tfrac{2}{3}\mu(\boldsymbol{\nabla}\boldsymbol{\cdot}\boldsymbol{u})^2, \tag{3.6}$$

and $e_{ij} = \partial u_i/\partial x_j + \partial u_j/\partial x_i$ is the rate of strain tensor.

We close the equations of motion with a power-law viscosity law, so that after non-dimensionalisation

$$\mu = \theta^{\zeta}. \tag{3.7}$$

The index $\zeta = 1$ gives the Chapman–Rubesin viscosity law (Chapman & Rubesin 1949) which is suitable for the subsonic regime; for the moderate supersonic regime a slightly more accurate model has $\zeta = 0.76$ (Cebeci 2002). If we were to extend the analysis to higher Mach numbers then a more realistic viscosity model, such as Sutherland's law (Sutherland 1893), would be required.

4. The basic flow

We now solve the equations of motion for the basic boundary-layer flow state. The ASBL flow is steady, two-dimensional and independent of x. Therefore we seek a boundary-layer solution in the form

$$(u, v, w, p) = \left(\hat{u}(y), Re^{-1}\hat{v}(y), 0, \hat{p}(y)\right), \tag{4.1a}$$

$$(\theta, \rho, \mu) = \left(\hat{\theta}(y), \hat{\rho}(y), \hat{\mu}(y)\right), \tag{4.1b}$$

where the scaling for the normal velocity arises from the need to retain viscous effects in the boundary layer. The boundary conditions at the plate and the free stream are given by

$$(\hat{u}, \hat{v}, \hat{w}) = (0, -1, 0)\,, \quad \hat{\theta} = \theta_p/\theta_\infty \quad \text{at } y = 0, \tag{4.2a}$$

$$(\hat{u}, \hat{v}, \hat{w}) \to (1, -1, 0)\,, \quad \hat{p} \to p_\infty/\rho_\infty u_\infty^2, \quad (\hat{\theta}, \hat{\rho}, \hat{\mu}) \to (1, 1, 1) \quad \text{as } y \to \infty. \tag{4.2b}$$

We substitute the expansion (4.1) into the governing equations (3.2)–(3.5) and, assuming that the Reynolds number is large, retain leading-order terms. The y-momentum equation from (3.2) with $i = 2$ reduces to $\partial\hat{p}/\partial y = 0$, which means that the pressure $\hat{p}$ is constant across the boundary layer and equal to its free-stream value of $p_\infty/\rho_\infty u_\infty^2$. It follows that the equation of state (3.5) reduces to $\hat{\rho}\hat{\theta} = 1$. Then the continuity equation (3.3) reduces to $\partial_y(\hat{\rho}\hat{v}) = 0$; integrating and applying free-stream boundary conditions (4.2) gives $\hat{\rho}\hat{v} = -1$ across the boundary layer. Thus, $\hat{v} = -\hat{\theta}$, so in particular, the suction condition at the plate gives $\theta_p/\theta_\infty = 1$.

We now use the Dorodnitsyn–Howarth transformation (Dorodnitsyn 1942; Howarth 1948) given by

$$\xi = \int_0^y \hat{\rho}(y')\,\mathrm{d}y', \tag{4.3}$$

so that y-derivatives d_y are replaced by $\hat{\rho}(\xi)\,\mathrm{d}_\xi$. The equations of motion then reduce to

$$\hat{u}' + (\hat{\theta}^{\zeta-1}\hat{u}')' = 0, \quad \hat{\theta}' + \sigma^{-1}(\hat{\theta}^{\zeta-1}\hat{\theta}')' + (\gamma-1)M_\infty^2(\hat{u}')^2 = 0, \tag{4.4a,b}$$

where a prime denotes derivative with respect to ξ. In general, these equations must be solved numerically subject to the boundary conditions (4.2). An analytic solution can be found in the special case of the Chapman–Rubesin law when $\zeta = 1$, and is given by

$$\hat{u}(\xi) = 1 - \mathrm{e}^{-\xi}, \quad \hat{\theta}(\xi) = 1 + \frac{(\gamma-1)M_\infty^2\sigma}{2(2-\sigma)}(\mathrm{e}^{-\sigma\xi} - \mathrm{e}^{-2\xi}), \tag{4.5a,b}$$

$$\hat{v}(\xi) = -\hat{\theta}(\xi), \quad \hat{w}(\xi) = 0, \quad \hat{p}(\xi) = p_\infty/\rho_\infty u_\infty^2, \tag{4.6a–c}$$

$$\hat{\rho}(\xi) = \left(\hat{\theta}(\xi)\right)^{-1}, \quad \hat{\mu}(\xi) = \hat{\theta}(\xi). \tag{4.7a,b}$$

For large ξ, when the temperature and streamwise velocity are approaching their (non-dimensional) free-stream values of 1, this analytical basic solution can be used regardless of the index in the viscosity law (3.7). We can invert the Dorodnitsyn–Howarth transformation (4.3) as

$$y = \int_0^\xi \hat{\theta}(\xi')\,\mathrm{d}\xi'. \tag{4.8}$$

Thus if ξ is large, then we can approximate the Dorodnitsyn–Howarth variable by

$$\xi \approx g(y) = y + C_0; \quad C_0 = \frac{(1-\gamma)M_\infty^2}{4}. \tag{4.9a,b}$$

Consequently, in the free stream, we can write the basic flow in terms of the physical variable y. For the interior region we find $\xi = g(y)$ by solving the inversion equation (4.8) numerically.

Thus for large ξ, i.e. large y, the basic streamwise velocity is given by $\hat{u} \approx 1 - \mathrm{e}^{-C_0}\mathrm{e}^{-y}$. Thus the streamwise velocity approaches its free-stream form exponentially as a function of distance from the wall. Therefore the free-stream coherent structure theory of Deguchi & Hall (2014) can be applied. The basic solution for the temperature field also approaches its free-stream form exponentially, with the rate of decay being dependent on the value of the Prandtl number. As discussed above in § 3, gases which provide a good approximation to the ideal gas assumption have Prandtl numbers $\sigma < 2$, and therefore the decay of the basic state to its free-stream form will be dominated by the $\exp(-\sigma\xi)$ term in the basic flow (4.5*a*,*b*). Hence, the decay will be slower than that of the streamwise velocity field $\hat{u}$ if $\sigma < 1$. Thus the thermal boundary layer is thicker than the velocity boundary layer if $\sigma < 1$, and *vice versa* if $\sigma > 1$; this is consistent with laminar boundary-layer theory which suggests that the thickness of the thermal boundary layer δ_θ scales relative to the thickness of the velocity boundary layer δ_v as $\delta_\theta \sim \delta_v\sigma^{-1/3}$ (Schlichting 1968, p. 307).

5. The production-layer problem for compressible ASBL flow

Using the inversion of the Dorodnitsyn–Howarth transformation for large ξ (4.8), at the production layer we obtain $\xi \approx y + C_0$, and therefore the solution in the production layer can be expressed in terms of the physical variable y. To find the location of the production layer and the scalings of the flow components in the layer, following Deguchi & Hall (2014), we seek a travelling-wave solution propagating with almost the free-stream speed with wavelengths comparable to the boundary-layer scalings of § 4 so that $\partial_x = \partial_y = \partial_z = O(1)$. Then, if viscosity is to play a role in the interaction, $v = O(Re^{-1})$, and by the continuity equation (3.3), $1 - u = w = O(Re^{-1})$. To retain convective terms in the x-momentum equation (3.2) the $\rho(\partial_t + u\partial_x)$ term must also be $O(Re^{-1})$; this defines the wave dependence in the production layer. The pressure must then be $O(Re^{-2})$ to stay in play.

The streamwise component of the velocity field in the production layer must include the basic flow component (4.5*a*,*b*) for matching. For large ξ, the basic flow $\hat{u}$ has the form $1-\hat{u} = \exp(-y - C_0)$, therefore, in the production layer, $\mathrm{e}^{-y-C_0} = Re^{-1}$. Thus the location of the production layer is given by $y = y_{PL} = \ln Re - C_0$; this allows us to define a production-layer variable $Y = y - \ln Re + C_0$. The thickness of the production layer must then be $O(1)$ to ensure that the streamwise velocity u can only vary on an $O(1)$ length scale in the production layer.

Thus since $C_0 < 0$ for $\gamma = 1.4$, a key feature of the compressible problem is that the location of the production layer where the waves and rolls are concentrated moves further away from the wall as both the Reynolds number and the Mach number increase. Since $C_0 \propto M_\infty^2$, it is anticipated that the Mach number may have a strong influence on the hypersonic (large Mach number) production-layer problem; this is discussed further in the conclusion. However, our choice of parameters means that $|C_0| \ll \ln Re$. Therefore the values of σ and M_∞ do not strongly influence the location of the production layer.

Under the scalings described above, the basic states for the streamwise velocity and temperature (4.5*a*,*b*) in the production layer are given by

$$\hat{u} = 1 - \frac{1}{Re}\mathrm{e}^{-Y}, \quad \hat{\theta} = 1 + \lambda\left(\frac{1}{Re^{\sigma}}\mathrm{e}^{-\sigma Y} - \frac{1}{Re^{2}}\mathrm{e}^{-2Y}\right), \tag{5.1a,b}$$

where

$$\lambda = \frac{(\gamma-1)M_\infty^2\sigma}{2(2-\sigma)}. \tag{5.2}$$

Thus the largest deviation of the temperature field from its free-stream value at the production layer is controlled by the value of the Prandtl number σ. In particular, if $\sigma < 1$, then the deviation of the temperature field from its free-stream value is greater than the streamwise velocity deviation; this is again due to the relative thickness of the thermal and velocity boundary layers as discussed in § 4.

It is also important to stress that, although the $\exp(-\sigma\xi)$ exponential in the basic temperature state (4.5*a*,*b*) dominates the decay of the basic state to its free-stream value, upon exiting the production layer towards the wall as $Y \to -\infty$, any growing temperature disturbances will be dominated by the $\exp(-2Y)$ term in (5.1) and thus both exponentials need to be retained in the production-layer scalings.

Based on the discussion above, in the production layer we seek a solution of the Navier–Stokes equations in the form

$$\left.\begin{aligned} (X, Y, z) = (x - ct, y - \ln Re + C_0, z); \quad c = 1 - Re^{-1}c_1 + \dots,\\ \boldsymbol{u} = (1,0,0) + Re^{-1}\bar{\boldsymbol{u}}(X,Y,z) + \dots, \quad p = p_\infty/\rho_\infty u_\infty^2 + Re^{-2}\bar{p}(X,Y,z) + \dots,\\ (\theta,\rho,\mu) = 1 + Re^{-\sigma}(\bar{\theta}_1,\bar{\rho}_1,\bar{\mu}_1)(X,Y,z) + Re^{-2}(\bar{\theta}_2,\bar{\rho}_2,\bar{\mu}_2)(X,Y,z). \end{aligned}\right\} \tag{5.3a–e}$$

We substitute these scalings into the Navier–Stokes equations (3.2)–(3.5) and, at leading order, we obtain the production-layer problem

$$\mathcal{L}\bar{\boldsymbol{u}} = -\boldsymbol{\nabla}\bar{p} + \nabla^2\bar{\boldsymbol{u}}, \text{ at order } Re^{-1}, \tag{5.4}$$

$$\boldsymbol{\nabla}\cdot\bar{\boldsymbol{u}} = 0, \text{ at order } Re^{-1}, \tag{5.5}$$

$$\mathcal{L}\bar{\theta}_1 = \sigma^{-1}\nabla^2\bar{\theta}_1, \text{ at order } Re^{-(\sigma+1)}, \tag{5.6}$$

$$\mathcal{L}\bar{\theta}_2 = (\gamma-1)M_\infty^2\mathcal{L}\bar{p} + (\gamma-1)M_\infty^2\bar{\Phi} + \sigma^{-1}\nabla^2\bar{\theta}_2, \text{ at order } Re^{-3}, \tag{5.7}$$

$$\bar{\rho}_1 + \bar{\theta}_1 = 0, \text{ at order } Re^{-\sigma}, \tag{5.8}$$

$$\bar{p} = R\theta_\infty u_\infty^{-2}(\bar{\rho}_2 + \bar{\theta}_2), \text{ at order } Re^{-2}, \tag{5.9}$$

$$\bar{\mu}_1 = \zeta\bar{\theta}_1, \text{ at order } Re^{-\sigma}, \tag{5.10}$$

$$\bar{\mu}_2 = \zeta\bar{\theta}_2, \text{ at order } Re^{-2}, \tag{5.11}$$

where the operator $\mathcal{L} = ([\bar{\boldsymbol{u}} + c_1\hat{\boldsymbol{i}}] \cdot \nabla)$, $\nabla = (\partial_X, \partial_Y, \partial_z)$ and the dissipation function $\bar{\Phi}$ is found by substituting the production-layer scalings into (3.6).

We see that the production-layer equations for the velocity field $\bar{\boldsymbol{u}}$ (5.4)–(5.5) are the same as the equations (2.2)–(2.3) for the incompressible production-layer problem in Deguchi & Hall (2014), which describe a unit-Reynolds-number eigenvalue problem for the wave speed c_1. The only difference in the compressible problem is that the equations are solved at a slightly different value of y. Therefore, the solution to the incompressible eigenvalue problem, which was calculated in Deguchi & Hall (2014), can now also be used for the compressible problem. The velocity field then drives the temperature field through the heat equations (5.6)–(5.7); (5.6), which is obtained at $O(Re^{-\sigma})$, is dominant in the production layer, but we require the solution of the equation at $O(Re^{-2})$ as the production layer is exited towards the wall.

The production-layer problem (5.4)–(5.11) is solved subject to boundary conditions specifying that the flow exiting the production layer on either side must match asymptotically onto the basic solution (4.5*a*,*b*),

$$\bar{\boldsymbol{u}} \to (0, -1, 0), \quad \bar{\theta}_1 \to \lambda e^{-\sigma Y}, \quad \bar{\theta}_2 \to -\lambda e^{-2Y} \quad \text{as } Y \to \infty, \tag{5.12}$$

$$\bar{\boldsymbol{u}} \to (-e^{-Y}, -1, 0), \quad \bar{\theta}_1 \to \lambda e^{-\sigma Y}, \quad \bar{\theta}_2 \to -\lambda e^{-2Y} \quad \text{as } Y \to -\infty, \tag{5.13}$$

and periodicity conditions; defining α and β as the streamwise and spanwise wavenumbers, respectively,

$$(\bar{\boldsymbol{u}}, \bar{\theta}_{1,2})(X, Y, z) = (\bar{\boldsymbol{u}}, \bar{\theta}_{1,2})(X + 2\pi/\alpha, Y, z), \tag{5.14}$$

$$(\bar{\boldsymbol{u}}, \bar{\theta}_{1,2})(X, Y, z) = (\bar{\boldsymbol{u}}, \bar{\theta}_{1,2})(X, Y, z + 2\pi/\beta). \tag{5.15}$$

Thus, boundary condition (5.13) allows for the streamwise velocity disturbance $\bar{u}$ to grow exponentially beneath the production layer. However, it also allows for the disturbances to the temperature field $\bar{\theta}_1$, $\bar{\theta}_2$ to grow exponentially, and at a faster rate than the streamwise velocity disturbance. Coming out of the production layer $\bar{\theta}_2$ is dominant, however, $\bar{\theta}_1$, which satisfies a homogeneous equation, must be retained as it is needed at the wall. All disturbances must be reduced to zero at the wall and therefore, as in the incompressible problem, the maximum value of the disturbances will occur in a layer between the wall and the production layer where the basic flow adjusts to accommodate the disturbance.

6. The adjustment-layer problem

Below the production layer, the flow returns to the unperturbed boundary-layer flow (4.5*a*,*b*)–(4.7*a*,*b*) at leading order. However, the nonlinear production-layer interaction produces exponentially growing disturbances to the streamwise velocity and temperature fields that interact with the basic flow beneath the production layer. The flow between the production layer and the wall adjusts to accommodate the disturbances; we thus refer to this region as the adjustment layer. The solution in the upper part of this layer is dominated by the solution exiting the production layer. Then as the wall is approached, the solution is described by the boundary-region equations.

6.1. *The solution exiting the production layer*

Firstly, above the production layer as $Y \to \infty$, the velocity must eventually return to its free-stream form $\bar{\boldsymbol{u}} = (0, -1, 0)$. As in Deguchi & Hall (2014), the decay of the streamwise velocity u will be proportional to e^{-Y-C_0}, however, the nonlinear interaction in the production layer gives a constant of proportionality which differs from unity. Thus the production-layer interaction can give at most an $O(1)$ effect on the amplitude of the streamwise velocity displacement. Since the temperature field in the production layer is entirely driven by the equations for the velocity (5.4)–(5.5), any temperature disturbances will also decay above the production layer as there is no interaction to sustain them.

We now consider $Y \to -\infty$. To analyse the flow beneath the production layer, we decompose the velocity disturbance $\bar{\boldsymbol{u}}$ into vortex and wave components. The wave is associated with the X-dependent components of the velocity field. The X-independent components of the velocity are split into a roll flow, which is associated with the components $\bar{v}$ and $\bar{w}$, and the streak, which is the downstream velocity component $\bar{u}$. The combination of the roll and streak constitutes a streamwise vortex. At leading order, the flow must satisfy the basic ASBL flow given by (5.13), and therefore we split the streak into a mean in z and a z-dependent component (there is no mean in z of the roll flow due to symmetry). In addition to the z-dependent components, we allow the z-independent term to grow exponentially in the adjustment layer as $Y \to -\infty$, but it must eventually at leading order reduce to $-\mathrm{e}^{-Y}$ in order to match onto the unperturbed basic flow at the wall.

We decompose the temperature disturbances $\bar{\theta}_1$ and $\bar{\theta}_2$ in the same way. Following the nomenclature outlined in Ricco & Wu (2007), we refer to the X-independent component of the temperature disturbance as a 'thermal streak' and the corresponding streamwise velocity disturbance shall be termed a 'velocity streak'. Hence, in the adjustment layer, we seek a solution in the form

$$\bar{\boldsymbol{u}} = (\bar{u}_s(Y), -1, 0) + (u_s(Y, z), v_r(Y, z), w_r(Y, z)) + \boldsymbol{u}_w(X, Y, z), \tag{6.1}$$

$$\bar{\theta}_{1,2} = \bar{\theta}_{s_{1,2}}(Y) + \theta_{s_{1,2}}(Y, z) + \theta_{w_{1,2}}(X, Y, z), \tag{6.2}$$

where subscripts s, r and w refer to streak, roll and wave components respectively.

As in the incompressible ASBL study of Deguchi & Hall (2014), outside of the production layer the roll flow decays as there is no longer any forcing from the Reynolds stresses associated with the wavefield to sustain it. The wave $\boldsymbol{u}_w$ also decays faster than the roll; this can be seen through a balance of advection–diffusion terms and is confirmed by the numerical results of Deguchi & Hall (2014). Since the temperature field is driven entirely by the velocity field, the same is true of the corresponding temperature components $\theta_{w_{1,2}}$ and $\theta_{w_{1,2}}$. However, the velocity streak $\bar{u}_s + u_s$ can grow exponentially through interaction with the roll. The growth or decay of the velocity streak depends on the spanwise wavenumber β through the periodicity conditions (5.15). The new feature for the compressible problem is that the interaction of the roll flow with the temperature field drives the growth of the thermal streak.

We substitute the decomposition of the disturbances (6.1)–(6.2) into the production-layer equations (5.4)–(5.11). After introducing the roll-flow streamfunction ψ such that

$\partial_z \psi = v_r$ and $\partial_y \psi = -w_r$, the resulting equations for the roll-velocity-streak flow are given by

$$\left(\frac{\partial^2}{\partial Y^2} + \frac{\partial}{\partial Y} + \frac{\partial^2}{\partial z^2}\right) u_s = \mathrm{e}^{-Y} v_r, \tag{6.3}$$

$$\left(\frac{\partial^2}{\partial Y^2} + \frac{\partial}{\partial Y} + \frac{\partial^2}{\partial z^2}\right)\left(\frac{\partial^2}{\partial Y^2} + \frac{\partial^2}{\partial z^2}\right) \psi = 0, \tag{6.4}$$

$$\left(\frac{\mathrm{d}}{\mathrm{d}Y} + \frac{\mathrm{d}^2}{\mathrm{d}Y^2}\right) \bar{u}_s = \frac{\beta}{2\pi}\frac{\mathrm{d}}{\mathrm{d}Y}\int_{z=0}^{2\pi/\beta} (u_s v_r)\,\mathrm{d}z, \tag{6.5}$$

where the final equation for the mean velocity streak disturbance $\bar{u}_s$ has been found by taking the mean in z of the production-layer x-momentum equation (5.4). It is important to note the ∂_Y terms in the equations above which arise from the suction in the flow. It is these terms that allow the interaction of the mean part of the basic flow with the roll flow to produce growth.

The roll-velocity-streak equations (6.3)–(6.5) are solved together with the equations for the thermal streak,

$$\left(\frac{\partial^2}{\partial Y^2} + \frac{1}{\sigma}\frac{\partial}{\partial Y} + \frac{1}{\sigma}\frac{\partial^2}{\partial z^2}\right)\theta_{s_1} = -\sigma\lambda \mathrm{e}^{-\sigma Y} v_r, \tag{6.6}$$

$$\left(\frac{\partial^2}{\partial Y^2} + \frac{1}{\sigma}\frac{\partial}{\partial Y} + \frac{1}{\sigma}\frac{\partial^2}{\partial z^2}\right)\theta_{s_2} = -2\lambda v_r \mathrm{e}^{-2Y} - 2(\gamma-1)M_\infty^2 \mathrm{e}^{-Y}\frac{\partial u_s}{\partial Y}, \tag{6.7}$$

$$\left(\frac{\mathrm{d}}{\mathrm{d}Y} + \frac{1}{\sigma}\frac{\mathrm{d}^2}{\mathrm{d}Y^2}\right)\bar{\theta}_{s_1} = \frac{\beta}{2\pi}\frac{\mathrm{d}}{\mathrm{d}Y}\int_{z=0}^{2\pi/\beta} (v_r\theta_{s_1})\,\mathrm{d}z, \tag{6.8}$$

$$\left(\frac{\mathrm{d}}{\mathrm{d}Y} + \frac{1}{\sigma}\frac{\mathrm{d}^2}{\mathrm{d}Y^2}\right)\bar{\theta}_{v_2} = \frac{\beta}{2\pi}\frac{\mathrm{d}}{\mathrm{d}Y}\int_{z=0}^{2\pi/\beta} \left(v_r\theta_{s_2} - (\gamma-1)M_\infty^2 \varPhi_v\right)\mathrm{d}z, \tag{6.9}$$

where the dissipation function $\varPhi_v$ associated with the vortex flow is

$$\begin{aligned}\varPhi_v = {} & \frac{4}{3}\left(\frac{\partial v_r}{\partial Y}\right)^2 + \frac{4}{3}\left(\frac{\partial w_r}{\partial z}\right)^2 + \left(\frac{\mathrm{d}\bar{u}_s}{\mathrm{d}Y} + \frac{\partial u_s}{\partial Y}\right)^2 + \left(\frac{\partial u_s}{\partial z}\right)^2 + \left(\frac{\partial v_r}{\partial z}\right)^2 \\ & + 2\frac{\partial v_r}{\partial z}\frac{\partial w_r}{\partial Y} + \left(\frac{\partial w_r}{\partial Y}\right)^2 - \frac{4}{3}\frac{\partial v_r}{\partial Y}\frac{\partial w_r}{\partial z}.\end{aligned} \tag{6.10}$$

These equations are solved by Fourier expansion in z. The numerical results of Deguchi & Hall (2014) show that the vortex wavelength is half that of the wave part of the flow, and therefore the wavelength of the vortex is π/β, which sets the wavenumbers of the Fourier expansion. Therefore, we seek a solution for ψ in the form

$$\psi = \sum_{n=0}^{\infty} a_n \cos(2n\beta z) + \sum_{n=1}^{\infty} b_n \sin(2n\beta z). \tag{6.11}$$

The roll-velocity-streak equations (6.3)–(6.5) are the same as those for the incompressible equation in Deguchi & Hall (2014), with $Y = y - \ln Re + C_0$ where $C_0 = 0$ (corresponding to $M_\infty = 0$) in the incompressible problem. Thus, the solution of (6.3)–(6.5) is the same as that for the incompressible problem; the incompressible solution with $C_0 = 0$ is given in (2.4)–(2.6). Thus upon exiting the production layer in the compressible problem, the leading order solution of (6.3)–(6.5) in original boundary-layer coordinates (x, y, z) and associated flow quantities (u, v, w) is

$$u \to 1 - \exp(-(y + C_0)) + \frac{d_0}{Re} + \frac{J_1}{Re^{\omega_1}} \exp((\omega_1 - 1)(y + C_0)) \cos(2\beta z) + \frac{J_1 K_1}{Re^{2\omega_1} 4\omega_1} \exp((2\omega_1 - 1)(y + C_0)) + \cdots , \tag{6.12}$$

$$v \to -\frac{1}{Re} + \frac{K_1}{Re^{\omega_1+1}} \exp(\omega_1 (y + C_0)) \cos(2\beta z) + \cdots , \tag{6.13}$$

$$w \to -\frac{K_1 \omega_1}{2\beta Re^{\omega_1+1}} \exp(\omega_1 (y + C_0)) \sin(2\beta z) + \cdots , \tag{6.14}$$

where

$$J_n = \frac{K_n}{(\omega_n - 1)^2 + (\omega_n - 1) - 4n^2\beta^2}, \quad \omega_n = \frac{-1 + \sqrt{1 + 16n^2\beta^2}}{2} \geqslant 0, \tag{6.15a,b}$$

for $n \geqslant 1$. The terms represented by '$\cdots$' represent more slowly growing harmonics in z, with constants J_n, K_n and ω_n for $n > 1$. The constants d_0 and K_1 are found as part of the nonlinear eigenvalue production-layer problem; K_1 was reported for a range of β in Deguchi & Hall (2014). Thus we only give the full streamwise velocity solution up to a constant d_0/Re, but this constant does not affect the streaks. As required, the flow returns to its unperturbed basic state at leading order, with exponentially growing disturbances that can become larger than the velocities involved in the nonlinear interaction in the production layer where the disturbances originated.

The solutions for u_s, v_r and $\bar{u}_s$ are then used as forcing for the equations (6.6)–(6.9) for the thermal streak. In the original boundary-layer variables, $\theta = 1 + Re^{-\sigma}\bar{\theta}_1 + Re^{-2}\bar{\theta}_2$, we find that upon exiting the production layer,

$$\begin{aligned}\theta &\to 1 + \lambda \exp(-\sigma (y + C_0)) - \lambda \exp(-2(y + C_0)) + \frac{d_1}{Re^{\sigma}} + \frac{d_2}{Re^2} \\ &+ \frac{1}{Re^{\omega_1}} (L_1 \exp((\omega_1 - \sigma)(y + C_0)) + Q_1 \exp((\omega_1 - 2)(y + C_0))) \cos(2\beta z) \\ &+ \frac{1}{Re^{2\omega_1}} \left(\frac{L_1 K_1 \sigma}{4\omega_1} \exp((2\omega_1 - \sigma)(y + C_0)) + R_1 \exp((2\omega_1 - 2)(y + C_0)) \right) + \cdots ,\end{aligned} \tag{6.16}$$

where again the terms represented by '$\cdots$' denote more slowly growing harmonics in z, with constants K_n, J_n, L_n, Q_n, R_n and ω_n for $n > 1$ and where

$$L_n = \frac{-K_n \lambda \sigma}{(\omega_n - \sigma) + \sigma^{-1}(\omega_n - \sigma)^2 - \sigma^{-1} 4n^2\beta^2}, \tag{6.17a}$$

$$Q_n = \frac{-2\lambda K_n - 2(\gamma - 1)M_\infty^2 J_n(\omega_n - 1)}{(\omega_n - 2) + \sigma^{-1}(\omega_n - 2)^2 - \sigma^{-1} 4n^2\beta^2}, \tag{6.17b}$$

$$\begin{aligned}R_n = &-2\,\frac{\sigma \left(\frac{1}{4} M_\infty^2 {J_n}^2 (\gamma - 1)\, {\omega_n}^3 - \frac{1}{2} M_\infty^2 {J_n}^2 (\gamma - 1)\, {\omega_n}^2 - \frac{1}{4} J_n M_\infty^2 K_n (\gamma - 1) \right)}{\omega_n (\sigma + 2\,\omega_n - 2)} \\ &-2\,\frac{\sigma \left(M_\infty^2 \left(\beta^2 n^2 + \frac{1}{4} \right) (\gamma - 1)\, {J_n}^2 + \frac{1}{2} J_n M_\infty^2 K_n (\gamma - 1) - \frac{1}{4} Q_n K_n \right)}{\sigma + 2\,\omega_n - 2}.\end{aligned} \tag{6.17c}$$

	(*a*) $\beta < \frac{\sqrt{3}}{4}$	(*b*) $\frac{\sqrt{3}}{4} < \beta < \frac{1}{\sqrt{2}}$	(*c*) $\frac{1}{\sqrt{2}} < \beta < \sqrt{\frac{3}{2}}$	(*d*) $\beta > \sqrt{\frac{3}{2}}$
u_s	G	G	D	D
$\bar{u}_s$	G	D	D	D
θ_s	G	G	G	D
$\bar{\theta}_v$	G	G	D	D

Table 1. The growth and decay of the disturbances for different values of the spanwise wavenumber β. Growth is represented by 'G' and decay by 'D'. The growth and decay is shown for the both the mean in z and the z-dependent parts of the flow.

The constants d_1 and d_2 are constants of integration; again, we only find the solution for the temperature field up to a constant, but this constant does not affect the growth of the thermal streaks beneath the production layer.

The asymptotic solution (6.12)–(6.13) for u and v beneath the production layer shows that the roll flow always decays as the wall layer is approached, whereas the mean part of the velocity streak flow (6.12) can grow beneath the production layer if $2\omega_1 < 1$, corresponding to values of $\beta < \sqrt{3}/4$. The z-dependent part of the velocity streak can grow if $\omega_1 < 1$, corresponding to values of $\beta < 1/\sqrt{2}$, and therefore these latter modes are the fastest growing. If $\beta > 1/\sqrt{2}$, then the velocity streak disturbance decays exponentially, and the nonlinear interaction in the production layer simply produces an $O(Re^{-1})$ correction to the flow.

Meanwhile, the asymptotic solution for the temperature (6.16) beneath the production layer shows that the thermal streaks can grow if $\omega_1 < \sigma$ or if $\omega_1 < 2$. For the range of values of Prandtl number $\sigma < 2$ considered, the modes proportional to $\exp((\omega_1 - 2)(y + C_0))$ will dominate the growth, and therefore the nonlinear interaction in the production layer will always produce growing temperature disturbances for $\beta < \sqrt{3}/\sqrt{2}$.

The structure of the solution with varying β is summarised in table 1. The asymptotic results suggest that there exists a case where the thermal streaks can grow while the velocity streak decays. However, solutions of the production-layer problem (5.4)–(5.5) have not been found for values of $\beta \gtrsim 0.47$ (Deguchi & Hall 2014, 2015), and therefore cases (*c*) and (*d*) are possibly not relevant.

We see that, in all cases, a nonlinear interaction in the production layer of size $O(Re^{-1})$, which drives $O(Re^{-2})$, $O(Re^{-\sigma})$ temperature perturbations, can induce much larger changes to the velocity and temperature fields of $O(Re^{-\omega_1})$ in the main part of the boundary layer. We now consider the solution as it approaches the wall layer, where all disturbances are eventually reduced to zero to satisfy the wall boundary conditions.

6.2. *Boundary-layer analysis*

The solutions exiting the production layer, (6.12)–(6.14) and (6.16), do not satisfy the wall boundary conditions. We now find the solution for the induced flow which is valid all the way down to the wall. This solution should also match onto the solution exiting the production layer given by (6.12)–(6.14) and (6.16). An examination of this solution shows that in the boundary layer, disturbances can grow exponentially. The z-dependent part of the disturbance grows faster than the z-independent part; therefore, to match onto the solution exiting the production layer, the boundary-region solution will have z-dependence in the form of $\cos(2\beta z)$. However, the solution must also satisfy conditions (4.2*a*), and therefore any disturbances must ultimately be reduced to zero at the wall.

The solution in the boundary region is described in terms of the Dorodnitsyn–Howarth variable ξ; since disturbances are always small compared with the basic flow, the definition of the variable in (4.3) is valid throughout the flow, and in particular, $\partial_y = \hat{\rho}(\xi)\partial_\xi$. The inversion of the Dorodnitsyn–Howarth transformation for $y(\xi)$ is given in (4.8), however, unlike near the wall and in the production layer, we cannot generally find an explicit relationship for $\xi(y)$ as it cannot be assumed that the exponential terms involving ξ are smaller than the linear terms. Therefore, to find the solution for the physical variable y, we first solve the boundary-region equations in terms of ξ, and then use the monotonic relationship $y(\xi)$ in (4.8) to plot the solutions for each corresponding value of y.

Based on this discussion, in the boundary region we seek a solution in terms of the fundamental harmonics of the solution exiting the production layer (6.12)–(6.14), (6.16) in the form

$$u = \hat{u}(\xi) + Re^{-\omega_1}\tilde{u}(\xi)\cos(2\beta z), \tag{6.18a}$$

$$v(\xi) = Re^{-1}\hat{v}(\xi) + Re^{-(1+\omega_1)}\tilde{v}(\xi)\cos(2\beta z), \tag{6.18b}$$

$$w = Re^{-(1+\omega_1)}\tilde{w}(\xi)\sin(2\beta z), \quad p = \hat{p}(\xi) + Re^{-(2+\omega_1)}\tilde{p}(\xi)\cos(2\beta z), \tag{6.18c}$$

$$(\theta, \rho, \mu) = \left(\hat{\theta}(\xi), \hat{\rho}(\xi), \hat{\mu}(\xi)\right) + Re^{-\omega_1}\left(\tilde{\theta}(\xi), \tilde{\rho}(\xi), \tilde{\mu}(\xi)\right)\cos(2\beta z), \tag{6.18d}$$

where the basic solution (hat quantities) is given by the solution of (4.4*a,b*). We use the same velocity streak and thermal streak terminology to refer to the disturbances to the streamwise velocity and temperature fields respectively, and again the roll flow is associated with the disturbances to the (v, w) components of the velocity.

We substitute this expansion into the Navier–Stokes equations (3.2)–(3.5), which leads to a set of ordinary differential equations in ξ for the leading-order disturbance amplitudes (tilde quantities). Following Hall (1983), we eliminate the pressure $\tilde{p}$ and the spanwise disturbance velocity $\tilde{w}$; then we also eliminate the viscosity $\tilde{\mu}$ and the density $\tilde{\rho}$ using the equation of state (3.5) and the linearised power-law viscosity law (3.7). We are then left with three coupled differential equations for $\tilde{u}$ (from the x-momentum equation), $\tilde{v}$ (from the y-momentum equation) and $\tilde{\theta}$ (from the temperature equation)

$$A_1\tilde{u} + A_2\tilde{u}' + A_3\tilde{u}'' = A_4\tilde{v} + A_5\tilde{\theta} + A_6\tilde{\theta}', \tag{6.19}$$

$$B_1\tilde{v} + B_2\tilde{v}' + B_3\tilde{v}'' + B_4\tilde{v}^{(3)} + B_5\tilde{v}^{(4)} = B_6\tilde{\theta} + B_7\tilde{\theta}' + B_8\tilde{\theta}'' + B_9\tilde{\theta}^{(3)} + B_{10}\tilde{\theta}^{(4)}, \tag{6.20}$$

$$C_1\tilde{\theta} + C_2\tilde{\theta}' + C_3\tilde{\theta}'' = C_4\tilde{u}' + C_5\tilde{v}. \tag{6.21}$$

Here, the superscripts represent derivatives in the usual way. The coefficients A_k, B_k and C_k depend on the basic solution and are too long to write here; details are available from the authors on request. These coupled equations are solved subject to zero-disturbance and no-slip boundary conditions at the wall, and matching to the solution exiting the production layer (6.12), (6.13), (6.16) at $\xi = \xi_{PL} = \ln Re$, so that

$$\tilde{u}(0) = 0, \quad \tilde{u}(\xi_{PL}) = J_1\exp((\omega_1 - 1)\xi_{PL}), \tag{6.22a}$$

$$\tilde{v}(0) = \tilde{v}'(0) = 0, \quad \tilde{v}(\xi_{PL}) = K_1\exp(\omega_1\xi_{PL}), \quad \tilde{v}'(\xi_{PL}) = K_1\omega_1\exp(\omega_1\xi_{PL}), \tag{6.22b}$$

$$\tilde{\theta}(0) = 0, \quad \tilde{\theta}(\xi_{PL}) = (L_1\exp((\omega_1 - \sigma)\xi_{PL}) + Q_1\exp((\omega_1 - 2)\xi_{PL}))\,. \tag{6.22c}$$

Altitude (m)	θ_∞ (K)	a_∞ (m s^{-1})	u_∞ (m s^{-1})	v_∞ (m s^{-1})
0	288.2	340	34–679	$2.4 \times 10^{-4} - 8.5 \times 10^{-3}$
5000	255.7	320	32–640	$2.3 \times 10^{-4} - 8.0 \times 10^{-3}$
11 000	216.8	295	29–589	$2.1 \times 10^{-4} - 7.4 \times 10^{-3}$

Table 2. The range of dimensional values of free-stream velocity u_∞ and suction velocity v_∞ at free-stream temperature θ_∞ for the range of Mach numbers $0.1 \leqslant M_\infty \leqslant 2$ and Reynolds numbers $80\,000 \leqslant Re \leqslant 140\,000$.

The reduced boundary-region equations are discretised on a grid with N interior points and we use second-order accurate centred finite differences to approximate the derivatives with step size $\Delta\xi$; see Appendix A for details. We then solve the resulting matrix equation for $\tilde{u}$, $\tilde{v}$ and $\tilde{\theta}$.

7. Results

We solve the matrix system for $\tilde{u}$, $\tilde{v}$ and $\tilde{\theta}$ on a grid containing $N = 2000$ points. To compute the boundary conditions (6.12), (6.13) and (6.16), we require the value of $K_1 = K_1(\alpha, \beta)$ which is determined as part of the numerical solution of the production-layer nonlinear eigenvalue problem (5.4)–(5.5) for the wave speed c_1. For wavenumber values $(\alpha, \beta) = (0.2, 0.4)$, which by table 1 is in the regime where both the velocity and thermal streaks are expected to grow, Deguchi & Hall (2014) find $K_1 = 16.9$; we use these parameter values in our computations.

We explore the behaviour of the velocity and thermal streaks as the Reynolds number Re, Mach number M_∞ and Prandtl number σ vary. The Reynolds number and Mach number are defined using the dimensional quantities u_∞ (the streamwise velocity), v_∞ (the suction velocity) and θ_∞ (the free-stream temperature). Using the International Standard Atmosphere (International Organization for Standardization 1975) value for temperature at a fixed altitude, we describe in table 2 the range of free-stream velocities u_∞ and suction velocities v_∞ required to obtain Reynolds numbers in the range 80 000–140 000 and Mach numbers in the subsonic to moderate supersonic range, $0.1 \leqslant M_\infty \leqslant 2$.

Next, to examine the development of the flow disturbances beneath the production layer, we define the amplitudes of the leading-order velocity streak, roll and thermal streak solutions exiting the production layer (6.12)–(6.14), (6.16) and the numerical solution in the boundary region

$$A_{u_s} = Re^{-1}\sqrt{\frac{\beta}{2\pi}\int_0^{2\pi/\beta} u_s^2\,\mathrm{d}z}, \quad A_{\tilde{u}} = Re^{-\omega_1}\sqrt{\frac{\tilde{u}^2}{2}}, \tag{7.1a,b}$$

$$A_{v_r,w_r} = Re^{-1}\sqrt{\frac{\beta}{2\pi}\int_0^{2\pi/\beta} (v_r^2 + w_r^2)\,\mathrm{d}z}, \quad A_{\tilde{v},\tilde{w}} = Re^{-(\omega_1+1)}\sqrt{\frac{\tilde{v}^2+\tilde{w}^2}{2}}, \tag{7.2a,b}$$

$$A_{\theta_s} = \sqrt{\frac{\beta}{2\pi}\int_0^{2\pi/\beta} \left(Re^{-\sigma}\theta_{s_1} + Re^{-2}\theta_{s_2}\right)^2\,\mathrm{d}z}, \quad A_{\tilde{\theta}} = Re^{-\omega_1}\sqrt{\frac{\tilde{\theta}^2}{2}}. \tag{7.3a,b}$$

We first consider the validity of the upper adjustment-layer solution (6.12)–(6.14), (6.16). In figure 1 we plot the amplitudes of the velocity streaks, roll flow and thermal streaks for both the asymptotic solution (6.12)–(6.14), (6.16) and the numerical solution of the

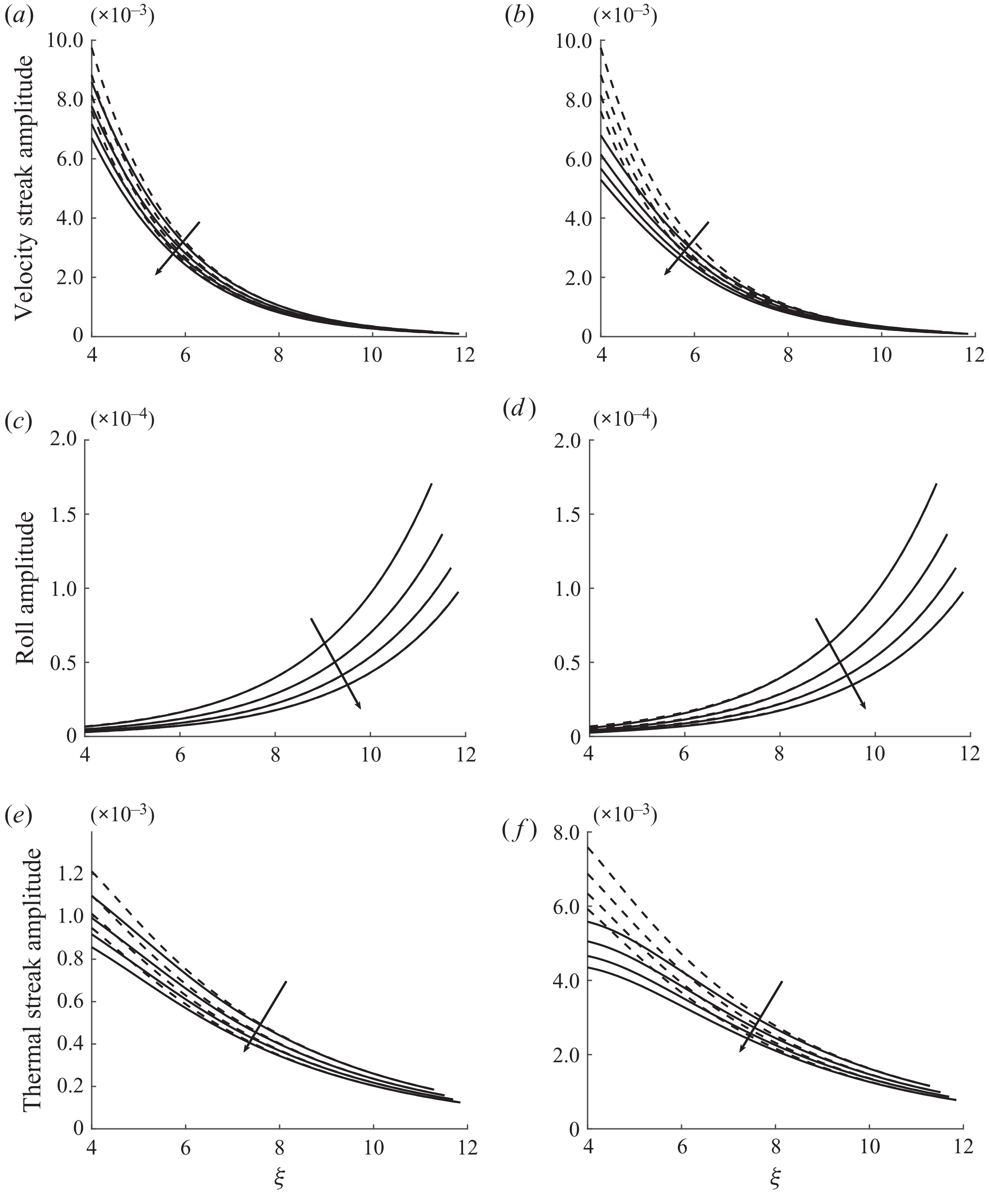

Figure 1. The amplitudes of the velocity streak (a,b), roll flow (c,d) and thermal streak (e,f). The solid black lines denote the amplitudes of the boundary-region solution ($A_{\tilde{u}}$, $A_{\tilde{v},\tilde{w}}$, $A_{\tilde{\theta}}$) whilst the dashed lines denote the amplitudes of the asymptotic production-layer solution (A_{u_s}, A_{v_r,w_r}, A_{θ_s}) as functions of the Dorodnitsyn–Howarth variable ξ. The four lines denote the amplitudes calculated for Reynolds numbers $Re = 80\,000$, $100\,0000$, $120\,000$ and $140\,000$, corresponding to production-layer locations $\xi_{PL} = 11.29$, 11.51, 11.70 and 11.85 respectively. The black arrow denotes the direction of increasing Reynolds number. The amplitudes in (a,c,e) were calculated using a subsonic free-stream Mach number $M_\infty = 0.8$ whilst (b,d,f) are the amplitudes for the moderate supersonic regime with $M_\infty = 2$. The Prandtl number is $\sigma = 0.71$ and we have used $\zeta = 0.76$ in the power-law viscosity law (3.7) to calculate the basic flow.

boundary-region equations (6.19)–(6.21) in terms of the Dorodnitsyn–Howarth variable ξ, so that the production layer is located at $\xi_{PL} = \ln Re$. For both the subsonic (a,c,e) and moderate supersonic (b,d,f) regimes, the asymptotic solution describing the roll flow is valid all the way to the wall, whereas the solution for the velocity and thermal streaks

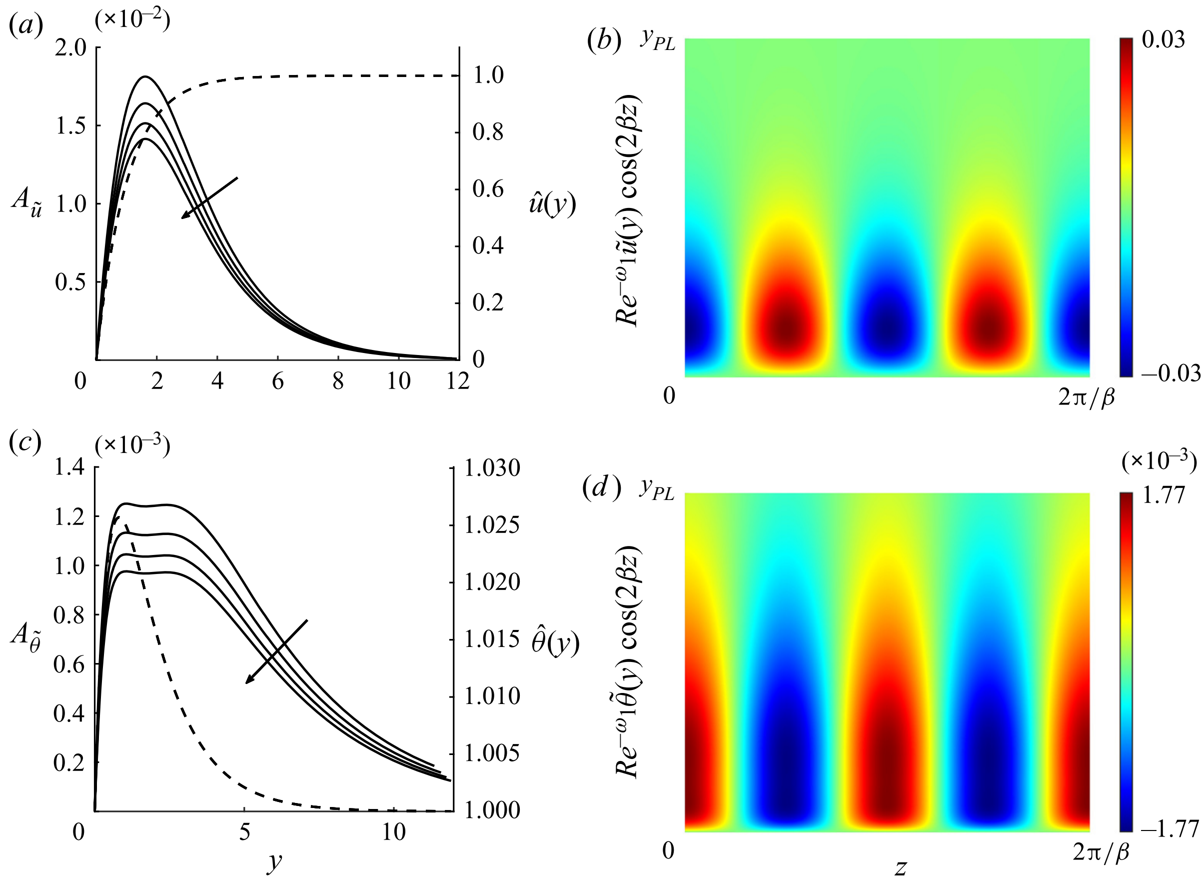

Figure 2. The numerical solution of boundary-region equations (6.19)–(6.21) at subsonic Mach number $M_\infty = 0.8$. The Prandtl number is $\sigma = 0.71$ and we have used $\zeta = 0.76$ in the power-law viscosity law (3.7) to calculate the basic flow. The amplitudes of the velocity streak $A_{\tilde{u}}$ (a) and the thermal streak $A_{\tilde{\theta}}$ (c) (left axis) are denoted by solid black lines together with the basic flow profile $\hat{u}(y)$ (a) and $\hat{\theta}(y)$ (c) (right axis), which are denoted by dashed lines. The four solid lines denote the amplitudes calculated for Reynolds numbers $Re = 80\,000$, $1\,000\,000$, $120\,000$ and $140\,000$, corresponding to production-layer locations $y_{PL} = 11.35$, 11.58, 11.76 and 11.91 respectively. The black arrow denotes the direction of increasing Reynolds number. The velocity (b) and thermal (d) streaks are shown over two vortex wavelengths at a Reynolds number $Re = 80\,000$, with $y_{PL} = 11.35$.

breaks down as the wall is approached; the location of this breakdown indicates the thickness of the upper adjustment layer. This breakdown occurs further from the wall in the moderate supersonic regime, indicating a thinner upper adjustment layer. We also note that the amplitude of the thermal streaks for subsonic free-stream Mach numbers is approximately one order of magnitude smaller than that of velocity streaks, whereas in the moderate supersonic regime the amplitudes are comparable.

As the wall is approached, the numerical solution of the boundary-region equations describes the flow induced by the disturbances from the production layer. In figure 2 we show the development of the amplitudes of the velocity and thermal streaks as the walls is approached, for subsonic free-stream Mach number $M_\infty = 0.8$, as a function of the physical variable y which is related to the Dorodnitsyn–Howarth variable by (4.8). As in the incompressible case, the velocity streak grows throughout the boundary region before taking its maximum in the near-wall boundary layer. In the compressible problem, the nonlinear interaction in the production layer also produces a thermal streak which similarly grows throughout the boundary layer; the rate growth of the thermal streak is higher than that of the velocity streak so that the effect of the thermal streak is felt both further from the wall and more uniformly across the flow compared with the

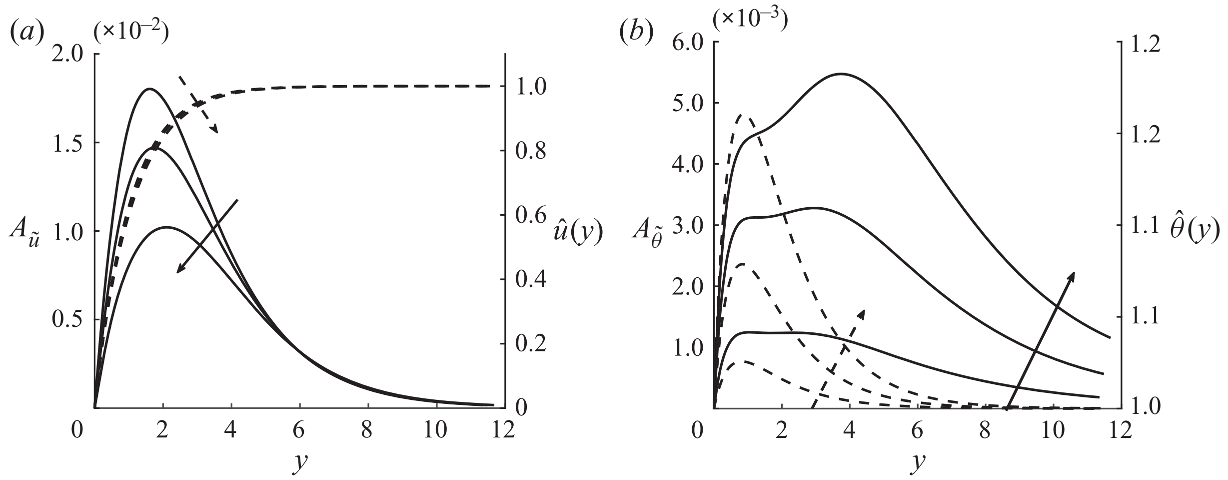

Figure 3. The amplitude of the velocity streaks (*a*) and thermal streaks (*b*) (solid lines, left axis), together with the basic flows $\hat{u}(y)$ and $\hat{\theta}(y)$ (dashed lines, right axis) for free-stream Mach numbers $M_\infty = 0.8$, 1.4 and 2. The arrow indicates the direction of increasing Mach number. The Prandtl number is $\sigma = 0.71$ and we have used $\zeta = 0.76$ in the power-law viscosity law (3.7) to calculate the basic flow.

velocity streak. In figure 2(*b*,*d*) we show the velocity and thermal streaks over two vortex wavelengths. Note that the velocity and thermal streaks shown in figure 2(*b*,*d*) are in phase, but the functions of y multiplying $\cos(2\beta z)$ have opposite sign.

The variation of the amplitude of the velocity and thermal streaks for varying Mach number is shown in figure 3, for a Reynolds number of $Re = 80\,000$. The amplitude of the thermal streak is enhanced as the free-stream Mach number is increased whilst the amplitude of the velocity streaks decreases; as noted above, for moderate supersonic M_∞ the amplitudes are of comparable magnitude. This is consistent with the idea of compressibility effects becoming more important as the free-stream Mach number is increased (Morkovin 1962), but also suggests that the amplitude of the velocity streaks could be become larger than that of the thermal streaks in more compressible regimes. The location of the maximum amplitude of the thermal streak occurs further from the wall as M_∞ is increased, with the structure of the amplitude solution changing from two local maxima to one more pronounced peak. Thus unlike the incompressible case, the growth of the thermal streak is not uniform in y.

Meanwhile, the effect of Prandtl number on the streak amplitude is shown in figure 4 for both the subsonic and moderate supersonic regimes. Increasing the Prandtl number from 0.7 to 1.3 leads to velocity streaks with smaller maximum amplitude where the maximum occurs further from the wall; these effects are more pronounced in the moderate supersonic regime than the subsonic regime. Meanwhile, for the thermal streaks, the effect of increasing the Prandtl number is to decrease the amplitude of the streak exiting the production layer, inhibit the growth of the streak further from the wall, but increase the eventual rate of growth. In the subsonic case the streaks eventually have a larger maximum amplitude; this is not the case in the moderate supersonic regime.

8. Discussion

Our results show the existence of free-stream coherent structures in the compressible ASBL at $O(1)$ Mach number. The solutions take the form of a roll–wave–streak interaction at the edge of the boundary layer, in a production layer whose location is dependent on both the Prandtl number and the Mach number. The interaction produces both a streaky disturbance and a temperature disturbance. These grow exponentially out of the production

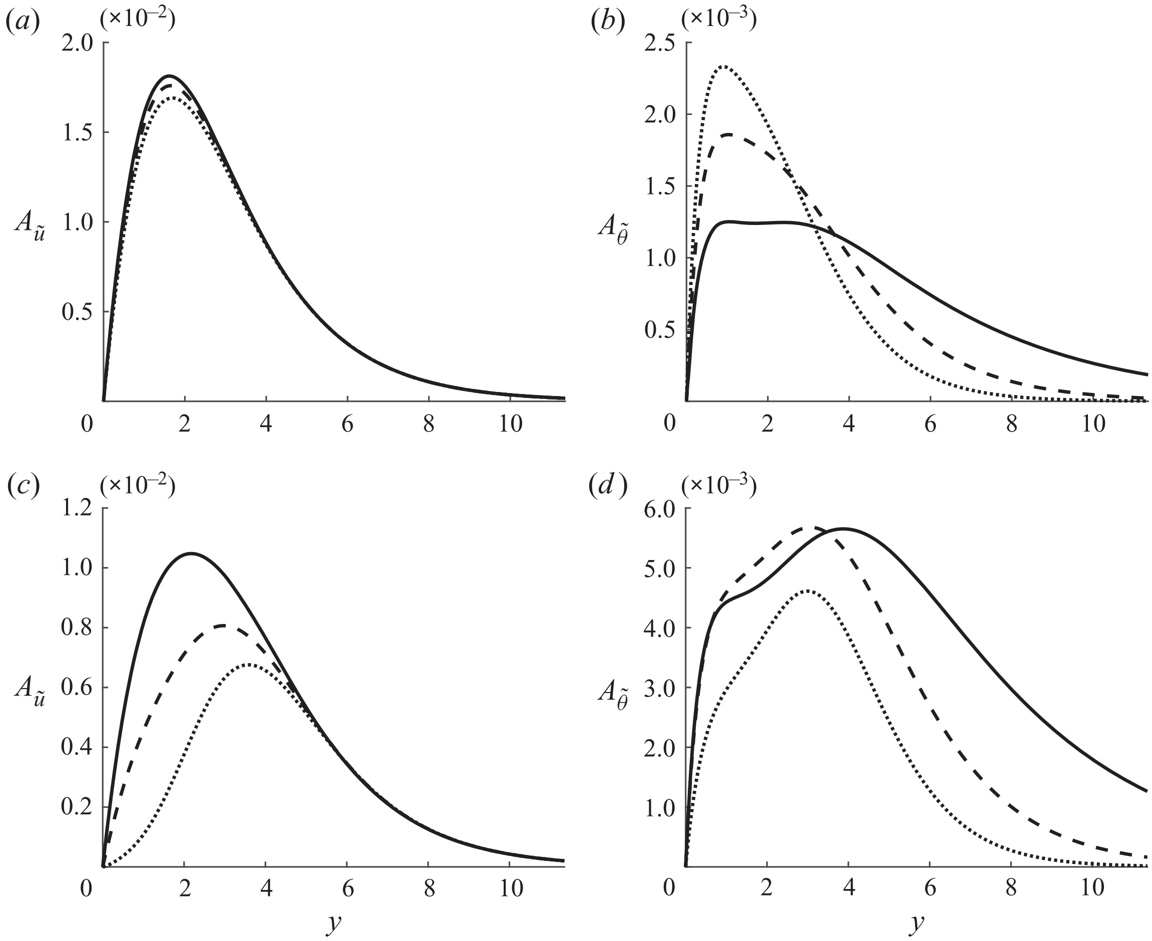

Figure 4. The amplitude of the velocity streaks (*a*,*c*) and thermal streaks (*b*,*d*) for Prandtl number $\sigma = 0.71$ (solid black line), 1 (dashed line) and 1.3 (dotted line). The amplitudes in (*a*,*c*) are for a subsonic free-stream Mach number $M_\infty = 0.8$ whilst (*b*,*d*) are for the moderate supersonic regime with $M_\infty = 2$. The Reynolds number is $Re = 80\,000$ and we have used $\zeta = 0.76$ in the power-law viscosity law (3.7) to calculate the basic flow.

layer, with the rate of growth being controlled by the spanwise wavenumber and, for the temperature disturbance, the Prandtl number. Above the layer, the disturbances decay rapidly to zero. For the compressible case considered here, the main difference from the incompressible case is the development of a spanwise varying temperature field beneath the production layer. The amplitude of the induced temperature field disturbances depends on both the Prandtl number and the free-stream Mach number, with the amplitude of the velocity and thermal streaks being comparable in the moderate supersonic regime. We might anticipate that in practice the induced temperature and streak fields could be big enough to lead to secondary instabilities. In the incompressible case we know from Dempsey, Hall & Deguchi (2017) that the streak generated by the free-stream coherent structure acts as a receptivity mechanism in curved flows, so for curved compressible flows, such as those over turbine blades, we anticipate that the structures described here might trigger transition through the Görtler vortex mechanism.

Our results show that the fundamental mechanism described by Deguchi & Hall (2014) for incompressible flows is also operational in compressible flows. In particular, this suggests the mechanism will occur in compressible jets and therefore might have important consequences for sound production in compressible jet flows. Extension of the work of Deguchi & Hall (2015) on swept wing flows is also possible.

Our analysis has assumed that the viscosity can be described by the power-law viscosity law, that the effect of shocks in the moderate supersonic regime is negligible with a sufficiently thin plate and that the gas in question is an ideal gas. Extension of the work to account for a more realistic viscosity model, for example Sutherland's law (Sutherland 1893), is straightforward but we believe that for the Mach numbers considered here that is not necessary. At hypersonic speeds beyond the regime covered here both real gas effects and more realistic viscosity models must be used and an intriguing question is the relationship between the production-layer problem and the temperature adjustment layer for the basic state at hypersonic speeds. Certainly, we know from for example Cowley & Hall (1990), Blackaby, Cowley & Hall (1993) and Fu, Hall & Blackaby (1993) that real gas effects, realistic viscosity models and indeed shocks present in the flow can significantly alter streamwise vortex or travelling-wave instabilities, so it is to be expected that the free-stream coherent structure mechanism at hypersonic speeds will be significantly different from that in the moderate supersonic case.

It is not yet known whether the class of exact coherent structures described by Hall & Sherwin (2010) can be extended to compressible flows. However, the fundamental asymptotic analysis supporting the structure is the vortex–wave interaction theory of Hall & Smith (1991) which in fact was given in the context of compressible flows so it would appear likely that it is operational in compressible flows. Moreover, the inviscid stability equation for many boundary-layer compressible flows has unstable solutions when the incompressible counterpart has none (Mack 1975, 1984) so it may well be that vortex–wave interactions in compressible flows may have a richer structure than their incompressible counterparts. Taken together with the extension of the free-stream coherent structure mechanism to compressible flows, it suggests that compressible flows might well have a significant family of possible exact coherent states.

Acknowledgements. The authors would like to thank the referees for their helpful and constructive comments.

Declaration of interests. The authors report no conflict of interest.

Author ORCIDs.
Eleanor C. Johnstone https://orcid.org/0000-0002-2166-5859;
Philip Hall https://orcid.org/0000-0001-5175-3115.

Appendix A. The finite-difference approximation to the boundary-region equations

We denote the values of $\tilde{u}$, $\tilde{v}$ and $\tilde{\theta}$ at $\xi_i = (i-1)\Delta\xi$, $\Delta\xi = 1/N$ by $\tilde{u}(\xi_i) = \tilde{u}_i$, $\tilde{v}(\xi_i) = \tilde{v}_i$ and $\tilde{\theta}(\xi_i) = \tilde{\theta}_i$, respectively, where $0 \leqslant i \leqslant N+1$. The wall is at $\xi_1 = 0$ and the production layer is at $\xi_N = (N-1)\Delta\xi = \xi_{PL}$.

The discretised boundary-region equations are

$$\alpha_1\tilde{u}_{i+1} + \alpha_2\tilde{u}_i + \alpha_3\tilde{u}_{i-1} = \alpha_4\tilde{v}_i + \alpha_5\tilde{\theta}_{i+1} + \alpha_6\tilde{\theta}_i + \alpha_7\tilde{\theta}_{i-1}, \tag{A1}$$

$$\begin{aligned}&\beta_1\tilde{v}_{i+2} + \beta_2\tilde{v}_{i+1} + \beta_3\tilde{v}_i + \beta_4\tilde{v}_{i-1} + \beta_5\tilde{v}_{i-2}\\ &\quad= \beta_6\tilde{\theta}_{i+2} + \beta_7\tilde{\theta}_{i+1} + \beta_8\tilde{\theta}_i + \beta_9\tilde{\theta}_{i-1} + \beta_{10}\tilde{\theta}_{i-2},\end{aligned} \tag{A2}$$

$$\gamma_1\tilde{\theta}_{i+1} + \gamma_2\tilde{\theta}_i + \gamma_3\tilde{\theta}_{i-1} = \gamma_4\tilde{u}_{i+1} + \gamma_5\tilde{u}_{i-1} + \gamma_6\tilde{v}_i. \tag{A3}$$

The coefficients α_k, β_k and γ_k depend on the coefficients A_k, B_k and C_k. The coefficients of the finite-difference approximation to the x-momentum equation (6.19) are given by

$$\alpha_1 = A_2/\Delta\xi + A_3/\Delta\xi^2, \quad \alpha_2 = A_1 - 2A_3/\Delta\xi^2, \quad \alpha_3 = -A_2/\Delta\xi + A_3/\Delta\xi^2, \tag{A4a}$$

$$\alpha_4 = A4, \quad \alpha_5 = A_6/2\Delta\xi, \quad \alpha_6 = A_5, \quad \alpha_7 = -A_6/2\Delta\xi. \tag{A4b}$$

The coefficients of the finite-difference approximation to the y-momentum equation (6.20) are given by

$$\beta_1 = B4/2\Delta\xi^3 + B5/\Delta\xi^4, \tag{A5a}$$

$$\beta_2 = B2/2\Delta\xi + B3/\Delta\xi^2 - 2B4/2\Delta\xi^3 - 4B5/\Delta\xi^4, \tag{A5b}$$

$$\beta_3 = B1 - 2B3/\Delta\xi^2 + 6B5/\Delta\xi^4, \tag{A5c}$$

$$\beta_4 = -B2/2\Delta\xi + B3/\Delta\xi^2 + 2B4/2\Delta\xi^3 - 4B5/\Delta\xi^4, \tag{A5d}$$

$$\beta_5 = -B4/2\Delta\xi^3 + B5/\Delta\xi^4, \quad \beta_6 = B9/2\Delta\xi^3 + B10/\Delta\xi^4, \tag{A5e}$$

$$\beta_7 = B7/2\Delta\xi + B8/\Delta\xi^2 - 2B9/2\Delta\xi^3 - 4B10/\Delta\xi^4, \tag{A5f}$$

$$\beta_8 = B6 - 2B8/\Delta\xi^2 + 6B10/\Delta\xi^4, \tag{A5g}$$

$$\beta_9 = -B7/2\Delta\xi + B8/\Delta\xi^2 + 2B9/2\Delta\xi^3 - 4B10/\Delta\xi^4, \tag{A5h}$$

$$\beta_{10} = -B9/2\Delta\xi^3 + B10/\Delta\xi^4. \tag{A5i}$$

The coefficients of the finite-difference approximation to the temperature equation (6.21) are given by

$$\gamma_1 = C1/2\Delta\xi, \quad \gamma_2 = -C1/2\Delta\xi, \quad \gamma_3 = C2, \quad \gamma_4 = C4/2\Delta\xi + C5/\Delta\xi^2, \tag{A6a}$$

$$\gamma_5 = C3 - 2C5/\Delta\xi^2, \quad \gamma_6 = -C4/2\Delta\xi + C5/\Delta\xi^2. \tag{A6b}$$

The coefficients A1–A6, B1–B10 and C1–C5 are available from the authors on request.

These finite-difference approximations are then encoded in a 3×3 block matrix A where each block is of size $(N+2)^2$. The first, second and third block rows contain the discretisations of the x-momentum, y-momentum and temperature equations respectively. To find the solution $\tilde{\boldsymbol{u}} = (\tilde{u}(\xi_i), \tilde{v}(\xi_i), \tilde{\theta}(\xi_i))^{\mathrm{T}}$ for $0 \leqslant i \leqslant N+1$ we solve $A\tilde{\boldsymbol{u}} = \boldsymbol{b}$, where $\boldsymbol{b}$ contains the values of the solution and its derivatives at the boundaries.

References

Blackaby, N.D., Cowley, S.J. & Hall, P. 1993 On the instability of hypersonic flow past a flat plate. *J. Fluid Mech.* **247**, 369–416.

Cebeci, T. 2002 *Convective Heat Transfer*, vol. 2. Springer.

Chapman, D.R. & Rubesin, M.W. 1949 Temperature and velocity profiles in the compressible laminar boundary layer with arbitrary distribution of surface temperature. *J. Aero. Sci.* **16** (9), 547–565.

Cowley, S. & Hall, P. 1990 On the instability of hypersonic flow past a wedge. *J. Fluid Mech* **214**, 17–42.

Deguchi, K. 2017 Scaling of small vortices in stably stratified shear flows. *J. Fluid Mech* **821**, 582–594.

Deguchi, K. & Hall, P. 2014 Free-stream coherent structures in parallel boundary-layer flows. *J. Fluid Mech.* **752**, 602–625.

Deguchi, K. & Hall, P. 2015 Free-stream coherent structures in growing boundary layers: a link to near-wall streaks. *J. Fluid Mech.* **778**, 451–484.

Deguchi, K. & Hall, P. 2018 Free-stream coherent structures in a planar jet. *J. Fluid Mech.* **837**, 916–930.

Demetriades, A. 1989 Growth of disturbances in a laminar boundary layer at Mach 3. *Phys. Fluids* A **1** (2), 312–317.

DEMPSEY, L.J., HALL, P. & DEGUCHI, K. 2017 The excitation of Görtler vortices by free-stream coherent structures. *J. Fluid Mech.* **826**, 60–96.

DORODNITSYN, A.A. 1942 Boundary layer in a compressible gas. *Prikl. Mat. Mekh.* **6** (6), 449–486.

EAVES, T.S. & CAULFIELD, C.P. 2015 Disruption of SSP/VWI states by a stable stratification. *J. Fluid Mech.* **784**, 548–564.

FAISST, H. & ECKHARDT, B. 2003 Traveling waves in pipe flow. *Phys. Rev. Lett.* **91** (22), 224502.

FERRO, M., FALLENIUS, B.E.G. & FRANSSON, J.H.M. 2021 Experimental study on turbulent asymptotic suction boundary layers. *J. Fluid Mech.* **915**, A80.

FRANSSON, J.H.M. & ALFREDSSON, P.H. 2003 On the disturbance growth in an asymptotic suction boundary layer. *J. Fluid Mech.* **482**, 51–90.

FRANSSON, J.H.M., MATSUBARA, M. & ALFREDSSON, P.H. 2005 Transition induced by free-stream turbulence. *J. Fluid Mech.* **527**, 1–25.

FRANSSON, J.H.M. & SHAHINFAR, S. 2020 On the effect of free-stream turbulence on boundary-layer transition. *J. Fluid Mech.* **899**, A23.

FU, Y., HALL, P. & BLACKABY, N. 1993 On the Görtler instability in hypersonic flows: Sutherland law fluids and real gas effects. *Phil. Trans. R. Soc. Lond.* A **342** (1665), 325–377.

GRAZIOSI, P. & BROWN, G.L. 2002 Experiments on stability and transition at Mach 3. *J. Fluid Mech.* **472**, 83–124.

HALL, P. 1983 The linear development of Görtler vortices in growing boundary layers. *J. Fluid Mech.* **130**, 41–58.

HALL, P. & SHERWIN, S. 2010 Streamwise vortices in shear flows: harbingers of transition and the skeleton of coherent structures. *J. Fluid Mech.* **661**, 178–205.

HALL, P. & SMITH, F.T. 1991 On strongly nonlinear vortex/wave interactions in boundary-layer transition. *J. Fluid Mech.* **227**, 641–666.

HOCKING, L.M. 1975 Non-linear instability of the asymptotic suction velocity profile. *Q. J. Mech. Appl. Maths* **28** (3), 341–353.

HOWARTH, L. 1948 Concerning the effect of compressibility on laminar boundary layers and their separation. *Proc. R. Soc. Lond.* A **194** (1036), 16–42.

INTERNATIONAL ORGANIZATION FOR STANDARDIZATION 1975 *Standard Atmosphere*. ISO 2533:1975.

JOHNSTONE, E.C. & HALL, P. 2020 Free-stream coherent structures in the unsteady Rayleigh boundary layer. *IMA J. Appl. Maths* **85** (6), 1021–1040.

KENDALL, J.M. 1975 Wind tunnel experiments relating to supersonic and hypersonic boundary-layer transition. *AIAA J.* **13** (3), 290–299.

KHAPKO, T., KREILOS, T., SCHLATTER, P., DUGUET, Y., ECKHARDT, B. & HENNINGSON, D.S. 2013 Localized edge states in the asymptotic suction boundary layer. *J. Fluid Mech.* **717**, R6.

KLINE, S.J., REYNOLDS, W.C., SCHRAUB, F.A. & RUNSTADLER, P.W. 1967 The structure of turbulent boundary layers. *J. Fluid Mech.* **30** (4), 741–773.

KREILOS, T., GIBSON, J.F. & SCHNEIDER, T.M. 2016 Localized travelling waves in the asymptotic suction boundary layer. *J. Fluid Mech.* **795**, R3.

KREILOS, T., VEBLE, G., SCHNEIDER, T.M. & ECKHARDT, B. 2013 Edge states for the turbulence transition in the asymptotic suction boundary layer. *J. Fluid Mech.* **726**, 100–122.

LANGHAM, J., EAVES, T.S. & KERSWELL, R.R. 2020 Stably stratified exact coherent structures in shear flow: the effect of Prandtl number. *J. Fluid Mech.* **882**, A10.

LAUFER, J. 1954 Factors affecting transition Reynolds numbers on models in supersonic wind tunnels. *J. Aero. Sci.* **21** (7), 497–498.

LEIB, S.J., WUNDROW, D.W. & GOLDSTEIN, M.E. 1999 Effect of free-stream turbulence and other vortical disturbances on a laminar boundary layer. *J. Fluid Mech.* **380** (1), 169–203.

LUCAS, D. & CAULFIELD, C.P. 2017 Irreversible mixing by unstable periodic orbits in buoyancy dominated stratified turbulence. *J. Fluid Mech.* **832**, R1.

LUCAS, D., CAULFIELD, C.P. & KERSWELL, R.R. 2017 Layer formation in horizontally forced stratified turbulence: connecting exact coherent structures to linear instabilities. *J. Fluid Mech.* **832**, 409–437.

MACK, L.M. 1975 Linear stability theory and the problem of supersonic boundary-layer transition. *AIAA J.* **13** (3), 278–289.

MACK, L.M. 1984 Boundary-layer linear stability theory. In *Special Course on Stability and Transition of Laminar Flow, AGARD Rep.* 709. Jet Propulsion Laboratory.

MARENSI, E., RICCO, P. & WU, X. 2017 Nonlinear unsteady streaks engendered by the interaction of free-stream vorticity with a compressible boundary layer. *J. Fluid Mech.* **817**, 80–121.

MAYER, C.S.J., VON TERZI, D.A. & FASEL, H.F. 2011 Direct numerical simulation of complete transition to turbulence via oblique breakdown at Mach 3. *J. Fluid Mech.* **674**, 5–42.

MORKOVIN, M.V. 1962 Effects of compressibility on turbulent flows. In *Mécanique de la Turbulence* (ed. A. Favre), pp. 367–380. CNRS.

OLVERA, D. & KERSWELL, R.R. 2017 Exact coherent structures in stably stratified plane Couette flow. *J. Fluid Mech.* **826**, 583–614.

PIROZZOLI, S., BERNARDINI, M. & GRASSO, F. 2008 Characterization of coherent vortical structures in a supersonic turbulent boundary layer. *J. Fluid Mech.* **613**, 205–231.

RICCO, P. & WU, X. 2007 Response of a compressible laminar boundary layer to free-stream vortical disturbances. *J. Fluid Mech.* **587**, 97–138.

RINGUETTE, M.J., WU, M. & MARTÍN, M.P. 2008 Coherent structures in direct numerical simulation of turbulent boundary layers at Mach 3. *J. Fluid Mech.* **594**, 59–69.

SCHLICHTING, H. 1968 *Boundary Layer Theory*, vol. 960. Springer.

SPINA, E.F., SMITS, A.J. & ROBINSON, S.K. 1994 The physics of supersonic turbulent boundary layers. *Annu. Rev. Fluid Mech.* **26** (1), 287–319.

SUTHERLAND, W. 1893 LII. The viscosity of gases and molecular force. *Lond. Edin. Dublin Phil. Mag. J. Sci.* **36** (223), 507–531.

WALEFFE, F. 1997 On a self-sustaining process in shear flows. *Phys. Fluids* **9** (4), 883–900.

WALEFFE, F. 2001 Exact coherent structures in channel flow. *J. Fluid Mech.* **435**, 93–102.

WALEFFE, F. 2003 Homotopy of exact coherent structures in plane shear flows. *Phys. Fluids* **15** (6), 1517–1534.

WANG, J., GIBSON, J. & WALEFFE, F. 2007 Lower branch coherent states in shear flows: transition and control. *Phys. Rev. Lett.* **98** (20), 204501.

WEDIN, H. & KERSWELL, R.R. 2004 Exact coherent structures in pipe flow: travelling wave solutions. *J. Fluid Mech.* **508**, 333–371.

WU, X. & DONG, M. 2016 Entrainment of short-wavelength free-stream vortical disturbances in compressible and incompressible boundary layers. *J. Fluid Mech.* **797**, 683–728.

Chapter 6

Conclusions

6.1 Summary

This thesis has explored how asymptotic methods can be used as a powerful tool in understanding how geometric perturbations affect static menisci in channel geometries, and how unsteady and compressible high Reynolds-number flows can support free-stream coherent structures which are thought to form part of the scaffold of turbulent flows. These problems were motivated by issues arising in industry, but have been explored from a theoretical and idealised perspective.

In Chapters 2 and 3 we used computational and asymptotic methods to find and describe equilibrium solutions for static liquid-vapour interfaces in perturbed rectangular channels. Chapter 2 focused on configurations with the perturbations taking the form of ridges and grooves. We used asymptotic methods for a linearised model for small-amplitude perturbations to show that perturbations that change the channel volume induce a change in the mean curvature of the meniscus. This leads to a contact line displacement that can be matched onto the arc of a catenoid with the same mean curvature as the meniscus. Channel-volume-preserving perturbations induced a deflection of the contact line leading to piecewise-linear displacement; it is, therefore, possible to obtain large-amplitude displacement for small-amplitude perturbations in a sufficiently wide channel. This knowledge allowed us to choose suitable patterns of perturbations to engineer specific contact line shapes.

We did not observe contact angle hysteresis or stick-slip behaviour when imposing ridge and groove perturbations. However Cox (1983) and Jansons (1985) have observed these behaviours for drops on surfaces with periodic and random roughness. Motivated by these studies, in Chapter 3 we considered channels with mirror-symmetric and mirror-anti-symmetric configurations of isolated Gaussian bump perturbations. The bumps caused the same qualitative deformation of the meniscus and contact line. Again, we used asymptotic methods for a linearised model for small-amplitude perturbations to show that perturbations that change the channel volume induce a change in the mean curvature of the meniscus. However, the position of the contact line relative to the bump affects the direction and amplitude of the contact line displacement and deformation of the meniscus. By computing quasi-static equilibrium solutions for a meniscus advancing over a bump, we showed that the meniscus bulges as it approaches the bump, then the meniscus flattens before the direction of deformation changes as it passes over the bump. Due to time constraints, only preliminary results were presented and further analysis is needed to develop an understanding of this problem.

The combination of these studies shows that even small-amplitude geometric perturbations to rectangular channels can significantly affect the shape of the equilibrium solution. Computations of slowly-moving menisci in perturbed rectangular channels need to account for this deformation of the equilibrium solution when computing the base state. The insight gained from using asymptotic methods to understand the numerical computations allowed us to the predict of the behaviour of the equilibrium solution from the shape of the channel walls. Crucially, for small-amplitude perturbations ridge and groove perturbations we were able to predict the far-field behaviour of the contact line without solving the Young–Laplace equation at all. These tools could be exploited to achieve desired behaviour of fluids in microchannels.

Chapters 4 and 5 explored a very different reduction of the Navier–Stokes equations to describe free-stream coherent structure wave-roll-streak-type solutions of the Navier–Stokes equations in the high-Reynolds number asymptotic limit. In Chapter 4 we considered the unsteady Rayleigh boundary layer. We used scaling arguments to derive Reynolds-number-independent equations governing the wave-roll-streak interaction equations in a production layer whose location relative to the wall depends on the Reynolds number. Through a suitable transformation, these equations were reduced to the interaction equations for free-stream coherent structures in parallel boundary layers given in Deguchi and Hall (2014a). The solution to these equations was given in that paper. We then used the solution of these equations as boundary conditions to solve the boundary-region equations numerically, to show that the structures could persist for a finite time. The maximum amplitude of the disturbance produced in the production layer was felt in the near-wall boundary layer. Thus we showed that free-stream coherent structures can be supported by unsteady boundary-layer flows in an analagous way to the mechanism already described by Deguchi and Hall (2015a) for spatially growing boundary layers and were therefore somewhat unsurprising. Nevertheless it furthered our understanding of how free-stream coherent structures can be embedded in a wide range of boundary-layer flows, and paved the way for the more novel results of Chapter 5.

Motivated by industrial applications, particularly a wish to understand and control turbulent flows in aeronautical situations, in Chapter 5 we considered compressible parallel boundary layer flows. Here we showed that the location of the production layer depended on both the Reynolds number and the free-stream Mach number. However, surprisingly, the interaction equations for the wave-roll-streak velocity field in the production layer reduce to exactly those for the incompressible problem. This interaction then drives a passive thermal field. Numerical solutions of the boundary-region equations showed that the maximum amplitude of the disturbances was dependent on the Mach number and the Prandtl number.

Although exact coherent structures and self-sustaining process (SSP) states have been widely studied in incompressible flows, little is known about their compressible counterparts. The existence of free-stream coherent structure solutions of the Navier–Stokes equations gives strong evidence that compressible flows may support a significant family of exact coherent structures. Moreover, it suggests that the structure underpinning turbulence in compressible flow is of the same type as in incompressible flows. Of course, the asymptotic results presented here need to be confirmed by computation of SSP states in compressible flows via direct numerical simulation. However, the remarkable agreement between asymptotic theory and numerical computations in the incompressible case (as shown in e.g. (Deguchi and Hall, 2014a)) is encouraging in suggesting that the agreement might be equally good in compressible flows.

From a broader perspective, the essential features of free-stream coherent structures are that their existence relies completely on the exponential decay of boundary-layer flow to its free-stream form and that the disturbance induced by the structure is most strongly felt in the near-wall boundary layer. Thus, direct numerical simulations of turbulent flow would reveal the structure in the boundary layer but not necessarily link its origin to the free-stream coherent structures. Asymptotic methods are crucial in elucidating this relationship. Moreover, free-stream coherent structures allow a way for disturbances to get from the free-stream to the boundary layer. This is particularly relevant in compressible parallel boundary-layer flows, where we may wish to understand the interaction between noise disturbances and turbulent flows.

6.2 Extensions

A key question that we have only briefly touched upon across the studies is that of stability. In the studies of capillary equilibria in Chapters 2 and 3, we have thus far only studied static solutions. The stability of the equilibrium solutions can be examined using Surface Evolver by checking the eigenvalues of the Hessian of the energy function of the computed solution as described in Appendix B of Chapter 3. Solutions for ridge perturbations in Chapter 2 had single solution branches which gave no evidence of loss of stability, e.g. via turning points. However, we anticipate the possibility of multiple solution branches for bumps of sufficiently large amplitude or sharpness that may induce large-amplitude deflections of the contact line.

Furthermore, having computed static solutions for ridge and groove perturbations and quasi-static solutions for a contact line moving over a bump, a natural step would be to compute a finger or bubble moving steadily slowly through a rectangular channel with geometric perturbations. In the case of a zero contact angle meniscus in a tube, this is an extension of the well-known Bretherton problem (Bretherton, 1961); more complex confining geometries have been discussed by Wong, Radke and Morris (1995a,b). A finite contact angle would require a contact angle slip condition which has been discussed in the context of surface roughness by Miksis and Davis (1994). The question then is whether geometric heterogeneity introduced by localised geometric perturbations induces contact angle hysteresis in the channel geometry. Jansons

(1985) demonstrated that moving contact lines on a random or periodic rough surface exhibit phenomena such as stick-slip and contact angle hysteresis. Additionally, chemical heterogeneity has been found to induce contact angle hysteresis (Hatipogullari et al., 2019); since in the linear problem the geometrical perturbation problem is analogous to using chemicals to locally change the contact angle, it is, therefore, reasonable to expect that such effects might also be seen for geometrically perturbed channels.

We have also not discussed the stability of the free-stream coherent structures described in Chapters 4 and 5. The instability of vortex-wave interaction states has been studied by Deguchi and Hall (2016) in incompressible flows and by Ozcakir, Hall and Tanveer (2019) for pipe flows. However, this analysis has not been extended to compressible flows where the existence of the temperature field may impact the stability. More recently attention has been focused on the instability generated by wall roughness in channel flows where Hall (2020, 2021) and Hall and Ozcakir (2021) have shown that a vortex-wave type mechanism controls the instability in channel flows, growing boundary layers and pipe flows respectively. However, an open question remains whether the streamwise vortex instability is absolute (so that any instabilities lead to the flow being unstable everywhere) or convective (so that disturbances only amplify downstream of the noise); this work is ongoing.

Finally, we would like to suggest how the ideas presented in this thesis could be useful in practice. Chapter 2 showed how it is possible to engineer contact line shapes for static menisci in rectangular channels using small localised perturbations. This could be used as a tool to design microfluidic devices with prescribed initial states for low capillary number dynamical flow. However in practice, microfluidic devices may not be rectangular or may contain non-rectangular components; for example, microfluidic tubing is used to connect microfluidic devices to external equipment (Wang, Chen, et al., 2014). In this case, the basic solution would be a spherical cap, and a relevant problem to study could be a droplet or catenoid trapped between two parallel plates. For the droplet, the two radii of curvature have the same sign so the Gaussian curvature is positive; whereas for the catenoid they have opposite signs leading to negative Gaussian curvature. A study by Vaziri and Mahadevan (2008) into the nonlinear response of elastic surfaces with different curvatures to perturbations suggests that the signature of the Gaussian curvature determines the nature of the response with positive Gaussian curvatures inducing global but well-bounded responses, whereas negative Gaussian curvatures lead to non-local deformation. A caveat is that elastic shells may show sensitivity to Gaussian curvature that is not shared by interfaces with isotropic tension. However, we might expect that the droplet problem (positive Gaussian curvature), which is elliptic, could lead to a very localised response, whereas we might not expect this for the hyperbolic catenoid problem. The problems we have studied above for a cylindrical meniscus in a rectangular channel, in which we obtain a long-range divergent response that is unbounded in the far-field, are degenerate in this framework because the Gaussian curvature is zero. Therefore we might anticipate that the Gaussian curvature determines the distance of the long-range response to perturbations in the confining geometry. This could be important when choosing geometries of microchannels for specific purposes.

Meanwhile, a source of great frustration and cost in aeronautical design is how to design aerofoils to reduce noise disturbances in high-speed compressible flows (see e.g. Brooks, Pope and Marcolini (1989) and Pando, Schmid and Sipp (2014)). To investigate the role of the free-stream coherent structures described in Chapter 5 in noise generation, the nonlinear solutions found in compressible boundary layers could be used as a source term in the linearised Euler equations. We note, however, that our asymptotic theory does not cover the generation of the source term. Indeed, in Chapters 4 and 5 we have not addressed how the production layer interaction starts and ends; the asymptotic theory used to describe these solutions relies on an initial disturbance that is consistent with the asymptotic structure of the resulting states. However, as discussed in §1, evidence of the importance of coherent structures in high Reynolds number transition has been observed extensively in experiments and numerical simulations.

As discussed in Chapter 5, the question of whether free-stream coherent structures can be described in hypersonic boundary-layer flows is a natural extension of the subsonic and moderate supersonic problem, but presents technical difficulties due to the highly non-parallel nature of the base flow.

6.3 Conclusion and Outlook

Starting with the Navier–Stokes equations (1.1)–(1.2) and appropriate boundary conditions, we have used simplifications to obtain and solve governing equations for two specific but very different types of flow: static fluid-fluid interfaces and high-Reynolds-number boundary-layer flows. From a purely mathematical viewpoint, it is remarkable that one system of partial differential equations can describe phenomena in two extremely different physical configurations. In both cases we have demonstrated that while computations can be used to find solutions of the governing equations, asymptotic methods give a much stronger insight into why the solution behaves a certain way.

Our understanding of physical phenomena in interfacial and boundary-layer flows is far from complete. While direct numerical simulations are widely used to understand such phenomena, computing solutions is expensive and time-consuming. The asymptotic methods used in this thesis demonstrate how insights into flow behaviour can predict behaviour without expensive computations, and enhance understanding of existing solutions. Ultimately, it is reasonable to assume that sufficiently powerful computers will exist to be able to compute high resolution direct numerical simulations of fluid phenomena with relative ease. However, such computing power is currently almost inconceivable. Moreover, computation of solutions does not guarantee an understanding of the physics underpinning them. For this reason, asymptotic methods like those used in this thesis will still have a crucial role to play in our future understanding and should be considered a fundamental tool to be used in harmony with computational and experimental work.

Bibliography

Abramowitz, M. and Stegun, I. A. (1948). *Handbook of Mathematical Functions with formulas, graphs, and mathematical tables.* Vol. 55. US Government printing office.

Ajaev, V. S. and Homsy, G. (2006). “Modeling shapes and dynamics of confined bubbles”. *Annu. Rev. Fluid Mech.* 38, pp. 277–307.

Anna, S. L. (2016). “Droplets and bubbles in microfluidic devices”. *Annu. Rev. Fluid Mech.* 48, pp. 285–309.

Batchelor, G. (2000). *An Introduction to Fluid Dynamics.* Cambridge University Press.

Benney, D. (1984). “The evolution of disturbances in shear flows at high Reynolds numbers”. *Stud. in Appl. Math.* 70, pp. 1–19.

Brakke, K. A. (1994). “Surface Evolver Manual”. *Mathematics Department, Susquehanna Univerisity, Selinsgrove, PA.*

Bretherton, F. P. (1961). “The motion of long bubbles in tubes”. *J. Fluid Mech.* 10.2, pp. 166–188.

Brooks, T. F., Pope, D. S. and Marcolini, M. A. (1989). *Airfoil self-noise and prediction.* Tech. rep. NASA Reference Publication.

Buckingham, E. (1914). “On physically similar systems; illustrations of the use of dimensional equations”. *Physical review* 4.4, p. 345.

Cassie, A. B. D. and Baxter, S. (1944). “Wettability of porous surfaces”. *Trans. Faraday Soc.* 40 (0), pp. 546–551.

Cox, R. G. (1983). “The spreading of a liquid on a rough solid surface”. *J. Fluid Mech.* 131, pp. 1–26.

Darband, G. B., Aliofkhazraei, M., Khorsand, S., Sokhanvar, S. and Kaboli, A. (2020). “Science and engineering of superhydrophobic surfaces: review of corrosion resistance, chemical and mechanical stability”. *Arabian Journal of Chemistry* 13.1, pp. 1763–1802.

De Gennes, P.-G. (1985). "Wetting: statics and dynamics". *Reviews of Modern Physics* 57.3, p. 827.

Deguchi, K. and Hall, P. (2018). "Free-stream coherent structures in a planar jet". *J. Fluid Mech.* 837, pp. 916–930.

Deguchi, K. and Hall, P. (2015a). "Free-stream coherent structures in growing boundary layers: a link to near-wall streaks". *J. Fluid Mech.* 778, pp. 451–484.

Deguchi, K. and Hall, P. (2014a). "Free-stream coherent structures in parallel boundary-layer flows". *J. Fluid Mech.* 752, pp. 602–625.

Deguchi, K. and Hall, P. (2016). "On the instability of vortex–wave interaction states". *J. Fluid Mech.* 802, pp. 634–666.

Dussan, V. (1976). "The moving contact line: the slip boundary condition". *J. Fluid Mech.* 77, pp. 665–684.

Dussan V., E. B. and Davis, S. H. (1974). "On the motion of a fluid-fluid interface along a solid surface". *J. Fluid Mech.* 65.1, pp. 71–95.

Faisst, H. and Eckhardt, B. (2003). "Traveling waves in pipe flow". *Phys. Rev. Lett.* 91.22, p. 224502.

Finn, R. (2012). *Equilibrium Capillary Surfaces.* Vol. 284. Springer Science & Business Media.

Franco-Gómez, A., Thompson, A. B., Hazel, A. L. and Juel, A. (2016). "Sensitivity of Saffman–Taylor fingers to channel-depth perturbations". *J. Fluid Mech.* 794, pp. 343–368.

Franco-Gómez, A., Thompson, A. B., Hazel, A. L. and Juel, A. (2018). "Bubble propagation in Hele–Shaw channels with centred constrictions". *Fluid Dyn. Res.* 50.2, p. 021403.

Graham, M. D. and Floryan, D. (2021). "Exact coherent states and the nonlinear dynamics of wall-bounded turbulent flows". *Ann. Rev. Fluid Mech.* 53, pp. 227–253.

Hall, P. and Sherwin, S. (2010). "Streamwise vortices in shear flows: harbingers of transition and the skeleton of coherent structures". *J. Fluid Mech.* 661, pp. 178–205.

Hall, P. and Smith, F. T. (1991). "On strongly nonlinear vortex/wave interactions in boundary-layer transition". *J. Fluid Mech.* 227, pp. 641–666.

Hall, P. (2020). "An instability mechanism for channel flows in the presence of wall roughness". *J. Fluid Mech.* 899.

Hall, P. (2021). "On the roughness instability of growing boundary layers". *J. Fluid Mech.* 922.

Hall, P. and Ozcakir, O. (2021). "Poiseuille flow in rough pipes: linear instability induced by vortex–wave interactions". *J. Fluid Mech.* 913.

Hatipogullari, M., Wylock, C., Pradas, M., Kalliadasis, S. and Colinet, P. (2019). "Contact angle hysteresis in a microchannel: Statics". *Phys. Rev. Fluids* 4.4, p. 044008.

Herminghaus, S., Brinkmann, M. and Seemann, R. (2008). "Wetting and dewetting of complex surface geometries". *Annu. Rev. Mater. Res.* 38, pp. 101–121.

Homsy, G. M. (2008). *Multimedia Fluid Mechanics.*

Jansons, K. (1985). "Moving contact lines on a two-dimensional rough surface". *J. Fluid Mech.* 154, pp. 1–28.

Jia, J., Song, Q., Liu, Z. and Wang, B. (2019). "Effect of wall roughness on performance of microchannel applied in microfluidic device". *Microsystem Technologies* 25.6, pp. 2385–2397.

Jiménez, J. (2018). "Coherent structures in wall-bounded turbulence". *J. Fluid Mech.* 842, P1.

Johnstone, E. C. and Hall, P. (2020). "Free-stream coherent structures in the unsteady Rayleigh boundary layer". *IMA J. Appl. Math.* 85.6, pp. 1021–1040.

Johnstone, E. C. and Hall, P. (2021). "Free-stream coherent structures in parallel compressible boundary-layer flows at subsonic and moderate supersonic Mach numbers". *J. Fluid Mech.* 924, A27.

Johnstone, E. C., Hazel, A. L. and Jensen, O. E. (2022). "The effect of isolated ridges and grooves on static menisci in rectangular channels". *J. Fluid Mech.* 935, A32.

Kawahara, G. and Kida, S. (2001). "Periodic motion embedded in plane Couette turbulence: regeneration cycle and burst". *J. Fluid Mech.* 449, pp. 291–300.

Kline, S. J., Reynolds, W. C., Schraub, F. A. and Runstadler, P. W. (1967). "The structure of turbulent boundary layers". *J. Fluid Mech.* 30.4, pp. 741–773.

Kreilos, T., Gibson, J. and Schneider, T. M. (2016). "Localized travelling waves in the asymptotic suction boundary layer". *J. Fluid Mech.* 795, R3.

Ladyzhenskaya, O. A. (2003). “Sixth problem of the millennium: Navier-Stokes equations, existence and smoothness”. *Russian Mathematical Surveys* 58.2, p. 251.

Lin, C. (1955). *The Theory of Hydrodynamic Stability*. Cambridge University Press.

Liu, K. and Jiang, L. (2012). “Bio-inspired self-cleaning surfaces”. *Ann. Rev. Materials Research* 42, pp. 231–263.

Lohse, D. (2022). “Fundamental fluid dynamics challenges in inkjet printing”. *Ann. Rev. Fluid Mech.* 54, pp. 349–382.

Miksis, M. J. and Davis, S. H. (1994). “Slip over rough and coated surfaces”. *J. Fluid Mech.* 273, pp. 125–139.

Nagata, M. (1990). “Three-dimensional finite-amplitude solutions in plane Couette flow: bifurcation from infinity”. *J. Fluid Mech.* 217, pp. 519–527.

Newton, I. (1833). *Philosophiae Naturalis Principia Mathematica*. Vol. 1. G. Brookman.

Ozcakir, O., Hall, P. and Tanveer, S. (2019). “Nonlinear exact coherent structures in pipe flow and their instabilities”. *J. Fluid Mech* 868, pp. 341–368.

Pando, M. F. de, Schmid, P. J. and Sipp, D. (2014). “A global analysis of tonal noise in flows around aerofoils”. *J. Fluid Mech.* 754, pp. 5–38.

Quéré, D. (2008). “Wetting and roughness”. *Annu. Rev. Mater. Res.* 38, pp. 71–99.

Riley, N. (2001). “Steady streaming”. *Ann. Rev. Fluid Mech.* 33.1, pp. 43–65.

Robinson, S. K. (1991). “Coherent motions in the turbulent boundary layer”. *Ann. Rev. Fluid Mech.* 23.1, pp. 601–639.

Schneider, T. M., Gibson, J., Lagha, M., De Lillo, F. and Eckhardt, B. (2008). “Laminar-turbulent boundary in plane Couette flow”. *Phys. Rev. E* 78.3, p. 037301.

Stewartson, K. (1964). *The Theory of Laminar Boundary Layers in Compressible Fluids*. Clarendon Press Oxford.

Stone, H. A., Stroock, A. D. and Ajdari, A. (2004). “Engineering flows in small devices: microfluidics toward a lab-on-a-chip”. *Annu. Rev. Fluid Mech.* 36, pp. 381–411.

Stuart, J. (1966). “Double boundary layers in oscillatory viscous flow”. *J. Fluid Mech.* 24.4, pp. 673–687.

Tabeling, P., Zocchi, G. and Libchaber, A. (1987). “An experimental study of the Saffman–Taylor instability”. *J. Fluid Mech.* 177, pp. 67–82.

Taylor, G. I. (1923). "VIII. Stability of a viscous liquid contained between two rotating cylinders". *Phil. Trans. Roy. Soc. Lond. A* 223.605-615, pp. 289–343.

Thompson, A. B., Juel, A. and Hazel, A. L. (2014). "Multiple finger propagation modes in Hele-Shaw channels of variable depth". *J. Fluid Mech.* 746, pp. 123–164.

Vaziri, A. and Mahadevan, L. (2008). "Localized and extended deformations of elastic shells". *Proc. National Acad. Sci. USA* 105.23, pp. 7913–7918.

Venkatesan, S., Jerald, J., Asokan, P. and Prabakaran, R. (2020). "A comprehensive review on microfluidics technology and its applications". *Recent Advances in Mechanical Engineering*, pp. 235–245.

Waleffe, F. (1997). "On a self-sustaining process in shear flows". *Phys. Fluids* 9.4, pp. 883–900.

Waleffe, F. (2003). "Homotopy of exact coherent structures in plane shear flows". *Phys. Fluids* 15.6, pp. 1517–1534.

Wang, J., Gibson, J. and Waleffe, F. (2007). "Lower branch coherent states in shear flows: transition and control". *Phys. Rev. Lett.* 98.20, p. 204501.

Wang, J., Chen, W., Sun, J., Liu, C., Yin, Q., Zhang, L., Xianyu, Y., Shi, X., Hu, G. and Jiang, X. (2014). "A microfluidic tubing method and its application for controlled synthesis of polymeric nanoparticles". *Lab on a Chip* 14.10, pp. 1673–1677.

Wedin, H. and Kerswell, R. R. (2004). "Exact coherent structures in pipe flow: travelling wave solutions". *J. Fluid Mech.* 508, pp. 333–371.

Wenzel, R. N. (1936). "Resistance of solid surfaces to wetting by water". *Industrial & Engineering Chemistry* 28.8, pp. 988–994.

Wong, H., Radke, C. and Morris, S. (1995a). "The motion of long bubbles in polygonal capillaries. Part 1. Thin films". *J. Fluid Mech.* 292, pp. 71–94.

Wong, H., Radke, C. and Morris, S. (1995b). "The motion of long bubbles in polygonal capillaries. Part 2. Drag, fluid pressure and fluid flow". *J. Fluid Mech.* 292, pp. 95–110.

Young, T. (1805). "III. An essay on the cohesion of fluids". *Phil. Trans. Roy. Soc. Lond.* 95, pp. 65–87.